

AD-A134 457

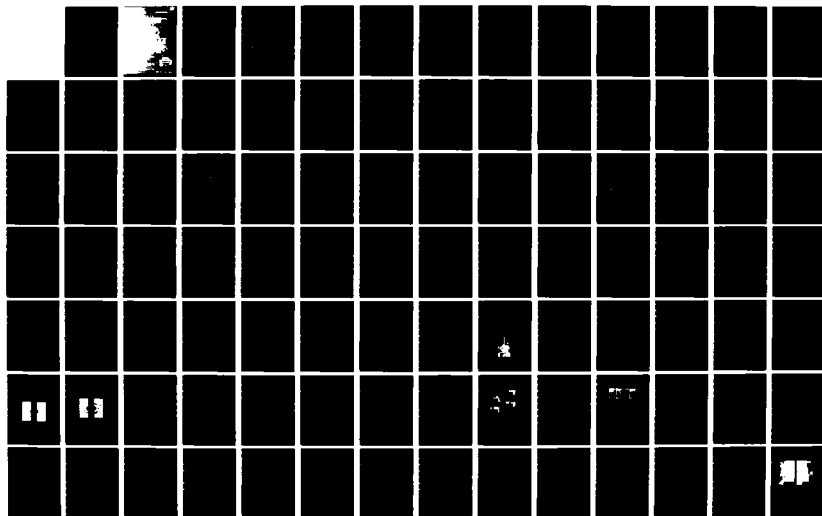
THE USE OF ION IMPLANTATION FOR MATERIALS PROCESSING
(U) NAVAL RESEARCH LAB WASHINGTON DC F A SMIDT
28 SEP 83 NRL-MR-5177

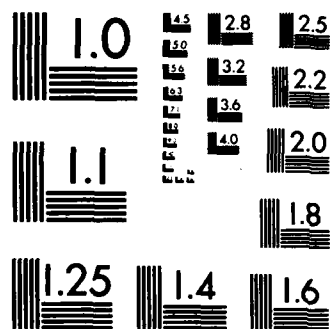
1/2

UNCLASSIFIED

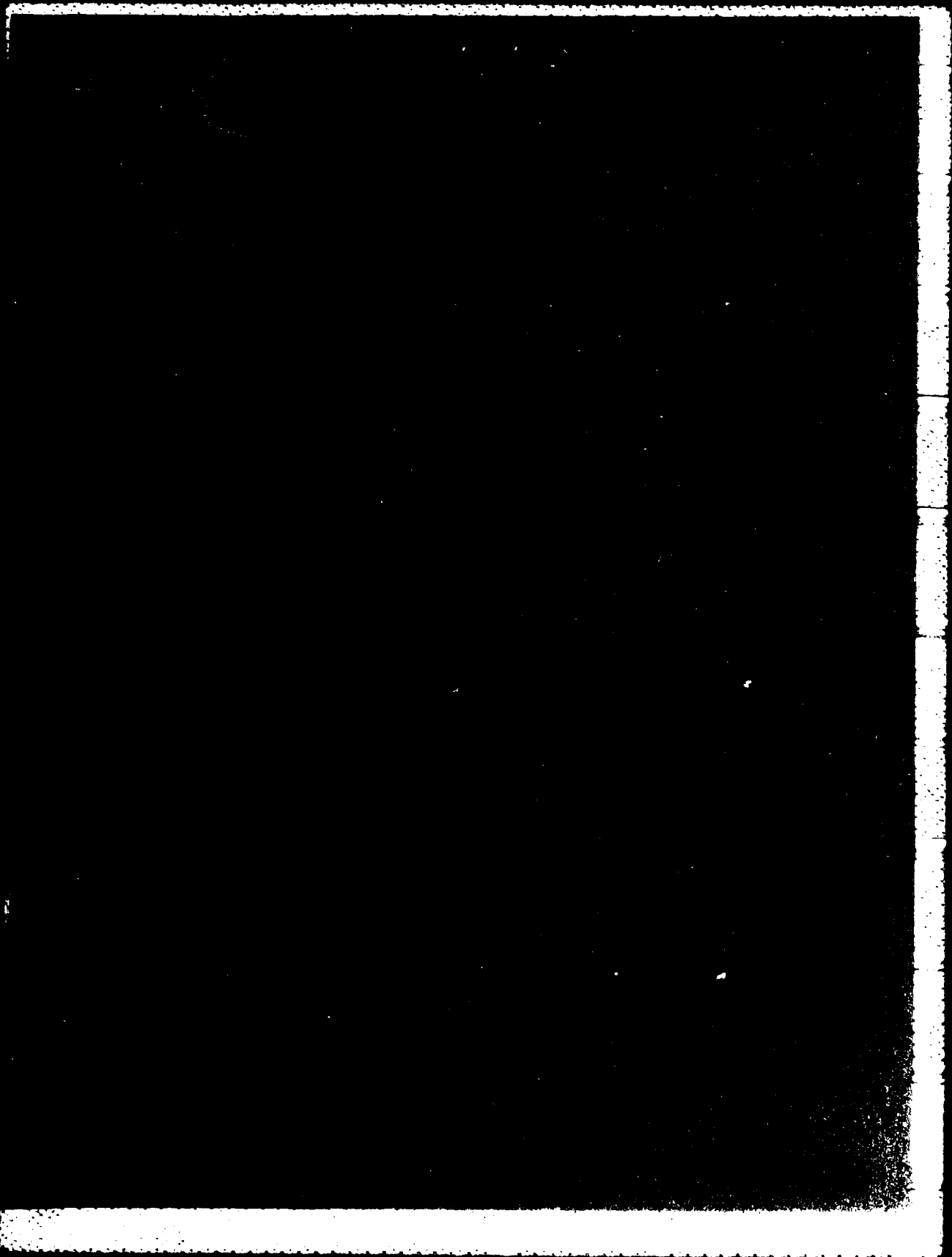
F/G 20/8

NL





MICROCOPY RESOLUTION TEST CHART
NATIONAL BUREAU OF STANDARDS-1963-A



REPORT DOCUMENTATION PAGE		READ INSTRUCTIONS BEFORE COMPLETING FORM	
1. REPORT NUMBER NRL Memorandum Report 5177		2. GOVT ACCESSION NO. AI 34457	
4. TITLE (and Subtitle) THE USE OF ION IMPLANTATION FOR MATERIALS PROCESSING — ANNUAL PROGRESS REPORT FOR THE PERIOD 1 OCTOBER 1981 — 30 SEPTEMBER 1982		5. TYPE OF REPORT & PERIOD COVERED Progress report for the period 1 Oct. 1981 — 30 Sept. 1982	
7. AUTHOR(s) F.A. Smidt		6. PERFORMING ORG. REPORT NUMBER	
9. PERFORMING ORGANIZATION NAME AND ADDRESS Naval Research Laboratory Washington, DC 20375		8. CONTRACT OR GRANT NUMBER(s)	
11. CONTROLLING OFFICE NAME AND ADDRESS Office of Naval Research Arlington, VA 22217		10. PROGRAM ELEMENT, PROJECT, TASK AREA & WORK UNIT NUMBERS Complete list follows on next page	
14. MONITORING AGENCY NAME & ADDRESS (if different from Controlling Office)		12. REPORT DATE September 28, 1983	
		13. NUMBER OF PAGES 185	
		15. SECURITY CLASS. (of this report) UNCLASSIFIED	
		15a. DECLASSIFICATION/DOWNGRADING SCHEDULE	
16. DISTRIBUTION STATEMENT (of this Report) Approved for public release; distribution unlimited.			
17. DISTRIBUTION STATEMENT (of the abstract entered in Block 20, if different from Report)			
18. SUPPLEMENTARY NOTES			
19. KEY WORDS (Continue on reverse side if necessary and identify by block number)			
Auger electron spectroscopy	Ion implantation	Ti-6Al-4V	Oxidation
Corrosion	Materials processing	M50	304SS
Fatigue	Wear	Bearings	
Rutherford backscattering	Sputtering	Friction	
Index of refraction	AISI 52100	Beryllium	
20. ABSTRACT (Continue on reverse side if necessary and identify by block number)			
An interdisciplinary program on the use of ion implantation for materials processing is being conducted at NRL. This report describes the important factors in ion implantation science and technology and reports progress in the use of ion implantation to modify friction, wear, fatigue, corrosion, and optical properties of materials.			

10. Program Element, Project, Task Area & Work Unit Numbers

ONR RR012-02-43 66-0445-0-2
 ONR RR012-01-42 66-0446-0-2
 ONR RR012-01-42 66-0446-0-2
 ONR RR012-01-42 66-0418-0-2
 NAVSEA; WR 30827 66-1663-0-2
 ONR RR012-01-42 66-0447-0-2
 ONR RR022-06-42 61-0037-0-2
 ONR RR022-06-42 63-1020-0-2
 ONR RR012-02-43 66-0445-0-2
 ONR RR022-06-42 61-0037-0-2
 ONR RR022-06-42 63-1020-0-2
 ONR RR022-06-42 66-0423-0-2
 ONR RR022-06-42 66-0467-0-2
 ONR RR022-06-42 66-0467-0-2
 ONR RR012-01-42 66-0447-0-2
 ONR RR012-01-42 66-0447-0-2

Accession For	
NTIS GRA&I	<input checked="" type="checkbox"/>
DTIC TAB	<input type="checkbox"/>
Unannounced	<input type="checkbox"/>
Justification	
By	
Distribution/	
Availability Codes	
Dist	Avail and/or Special
A-1	



CONTENTS

PREFACE - F.A. Smidt	v
SUMMARY	1

RESEARCH PROGRESS

I. ION IMPLANTATION SCIENCE AND TECHNOLOGY	
A. NEAR SURFACE ANALYSIS WITH ENERGETIC ION BEAMS	9
C.R. Gossett	
B. SPUTTERING ANALYSIS WITH PIXE.....	31
J.M. Lambert, P.A. Treado, D. Trbojevic, R.G. Allas, A.R. Knudson, G.W. Reynolds and F.R. Vozzo	
C. THE SURFACE BEHAVIOR OF A BINARY ALLOY DURING.....	39
PRODUCTION BY ION IMPLANTATION G.W. Reynolds, F.R. Vozzo, R.G. Allas, A.R. Knudson, J.M. Lambert and P.A. Treado	
D. COMPUTER STUDY OF SELF-SPUTTERING OF Cu and Ni at 90 keV	47
M. Rosen, G.P. Mueller and W.A. Fraser	
E. METHODS TO CONTROL TARGET HEATING DURING ION IMPLANTATION.....	53
K.S. Grabowski and R.A. Kant	
II. WEAR AND FATIGUE	
A. THE EFFECT OF NITROGEN IMPLANTATION ON MARTENSITE IN 304 STAINLESS STEEL	65
R.G. Vardiman, R.N. Bolster, and I.L. Singer	
B. MECHANICAL AND MICROSTRUCTURAL PROPERTIES OF BORON IMPLANTED BERYLLIUM	73
R.A. Kant, A.R. Knudson, and K. Kumar	
C. EFFECTS OF CARBON ON THE FRICTION AND WEAR OF TITANIUM-IMPLANTED 52100 STEEL	81
I.L. Singer and R.A. Jeffries	

- D. A TECHNIQUE FOR STUDYING THE EFFECT OF ION IMPLANTATION
ON DISLOCATION STRUCTURES DEVELOPED DURING THE FATIGUE
OF NICKEL.....93
R.G. Vardiman

III. CORROSION AND OXIDATION

- A. ION IMPLANTATION EFFECTS ON THE THERMAL OXIDATION OF
METALS101
K.S. Grabowski and L.E. Rehn
- B. ELECTROCHEMICAL AND A.E.S. STUDIES OF Fe-Cr SURFACE
ALLOYS FORMED ON A.I.S.I. 52100 STEEL BY ION BEAM
MIXING133
W.K. Chan, C.R. Clayton, R.G. Allas,
C.R. Gossett and J.K. Hirvonen
- C. RHEED, AES AND XPS STUDIES OF THE PASSIVE FILMS FORMED
ON ION IMPLANTED STAINLESS STEEL.....143
C.R. Clayton, K.G.K. Doss, Y-F Wang,
J.B. Warren and G.K. Hubler

IV. OTHER EXPLORATORY RESEARCH AREAS

- A. INFRARED STUDIES OF ISOTHERMAL ANNEALING OF ION-
IMPLANTED SILICON: REFRACTIVE INDICES, REGROWTH RATES,
AND CARRIER PROFILES.....155
C.N. Waddell, W.G. Spitzer, G.K. Hubler,
and J.E. Fredrickson
- B. PROPERTIES OF AMORPHOUS SILICON PRODUCED BY ION
IMPLANTATION: THERMAL ANNEALING.....169
W.G. Spitzer, G.K. Hubler and T.A. Kennedy

- V. BIBLIOGRAPHY174

THE USE OF ION IMPLANTATION FOR MATERIALS PROCESSING

Preface - F. A. Smidt

This report is the fourth in a series of Progress Reports of work, conducted at the Naval Research Laboratory (NRL) on the use of ion implantation for materials processing. The objective of the programs is to develop ion implantation as a viable surface treatment technique for use in applications of interest to the Navy. Attainment of this objective requires both applications oriented research, to demonstrate the benefits of ion implantation, and fundamental research, to provide an understanding of the physical and metallurgical changes taking place in the implanted region of a material.

The work reported here represents a coordinated effort in three divisions at NRL, the Condensed Matter and Radiation Sciences Division (Code 6600), the Chemistry Division (Code 6100) and the Material Science and Technology Division (Code 6300). The work includes in-house basic research conducted under the auspices of the Office of Naval Research, applied research performed for several Navy and DOD sponsors (NAVAIR, NAVSEA) and collaborative work with scientists at other laboratories.

The purpose of this report is to make available in one source the results from all studies at NRL related to the use of ion implantation for materials processing so as to provide a more comprehensive picture of the scope and interrelationship of the research. The report consists of four sections describing the research and a cumulative bibliography of published papers and reports.

THE USE OF ION IMPLANTATION FOR MATERIALS PROCESSING

ANNUAL PROGRESS REPORT
FOR THE PERIOD
1 OCTOBER 1981 to 30 SEPTEMBER 1982

SUMMARY

I. ION IMPLANTATION SCIENCE AND TECHNOLOGY

Research reported in this section contributes to our general understanding of the ion implantation process and the development and refinement of techniques for ion implantation processing.

A. Near Surface Analysis With Energetic Ion Beams

C.R. Gossett

A review is given of some representative methods and results for near surface analysis of elemental composition vs. depth as determined by Rutherford backscattering and related ion beam techniques. Examples are given from new applications in the areas of thin film and ion implantation technologies, which are used to tailor the near-surface composition to beneficially modify such surface-sensitive properties as friction, wear, oxidation and resistance to corrosion. Profiling by energetic ion beam methods is useful in optimizing the effect or in studies to understand the mechanisms. The advantages and limitations of this analysis method are explored with discussion of ion-excited x-ray analysis and nuclear reaction analysis as alternative or auxiliary approaches.

B. Sputtering Analysis With PIXE

J.M. Lambert, P.A. Treado, D. Trbojevic, R.G. Allas, A.R. Knudson, G.W. Reynolds, and F.R. Vozzo

The applicability of the particle induced x-ray emission (PIXE) in the determination of sputtering distributions and yields was studied. Sputtered particles were caught on foils for the 45 keV to 125 keV self sputtering of Fe, Ni, Cu, Ti, Mo and

Au and for the 90 keV self sputtering of both target and implanted particles of $\text{Ni}^+ + \text{Cu}$, $\text{Cu}^+ + \text{Ni}$, $\text{Ni}^+ + \text{Fe}$, and $\text{As}^+ + \text{Ag}$, and for the target particles of $\text{Ar}^+ + \text{Au}$.

Sputtered particles were collected in an ultra high vacuum (UHV) and in a poorer vacuum system with 99.99% pure Al catcher foils. PIXE data, the x-ray yields from 1 MeV proton and 2 MeV alpha particle beam bombardments, were used to determine the angular distribution of the sputtered products. The sputtering yield was calculated from the angular distribution data by integration over a hemisphere assuming azimuthal symmetry. The efficiency of the PIXE systems was calibrated with a standardized target such as $18 \mu\text{g}/\text{cm}^2$ Fe on the same 99.99% Al foil material. The Al x-ray yield of the catcher foils provided a normalization of all data from a given catcher foil. For a number of samples studied, we have been able to compare the distribution and yields obtained with PIXE to those measured by the Rutherford backscattering (RBS) technique. Also separate RBS analysis of Xe markers in the sputtering targets provided yield values. Comparison of the PIXE and RBS results indicate that the PIXE sputtering distribution and yield measurements are comparable.

C. The Surface Behavior of a Binary Alloy During Production by Ion Implantation

G.W. Reynolds, F.R. Vozzo, R.G. Allas, A.R. Knudson, J.M. Lambert and P.A. Treado

Thin surface copper-nickel alloys were prepared by ion implantation at 90 keV. During the implantation of one pure element by the other the sputtered products were collected on catcher foils at different stages from the beginning of the implant through to the steady state configuration of the target surface. The collector foils and targets were analyzed to determine the behavior of the sputtering yields during implantation and for the change in surface composition at the selected fluence. The total sputtering yield for the target and the effective elemental sputtering yields for each component appear to be functions of the changing surface fractions, the self ion sputtering yield of the implanted species, and the elemental sputtering yield of the initial target species. A model relating these parameters is presented.

D. Computer Study of Self-Sputtering of Cu and Ni at 90 keV

M. Rosen, G.P. Mueller and W.A. Fraser

The self-sputtering of 90 keV Cu (Ni) ions incident on polycrystalline Cu (Ni) targets has been studied using the code MARLOWE. Experimental values of the sputtering yields and the angular distribution of sputtered atoms are reproduced with the Moliere potential using the screening length of Torrens and

Robinson. Particular attention is paid to those subcascades which have sputtered atoms as their end products. The distribution of the depths at which these subcascades are initiated is presented, together with the distribution of the frequency and length of replacement sequences they contain. A comparison is made of self-sputtering from amorphous and polycrystalline targets at this energy.

E. Methods to Control Target Heating During Ion Implantation

K.S. Grabowski and R.A. Kant

The use of high-current ion implanters with beam powers in excess of 1 kw requires improved methods of target cooling. This paper casts well-known mathematical solutions [4] to heat conduction problems in terms of ion implantation parameters, and discusses the different regimes of conduction cooling. Examples illustrate that for most applications: (1) scanning of the ion beam and/or targets is necessary, (2) storing energy in target heat capacity is insufficient to limit target temperature rise, and (3) producing good sample contact with a heat sink is essential. Methods of producing adequate contacts are discussed, based on experimental measurements of the interface contact conductance, h , for various combinations of materials. Finally, as an example of successful target cooling by conduction techniques, the device used at the Naval Research Laboratory to cool tool-steel bearing races is briefly described.

II. WEAR AND FATIGUE

Research reported in this section involves the application of ion implantation processing to the improvement of wear and fatigue properties of surface and fundamental investigations conducted to improve our understanding of the effects of implantation on wear and fatigue mechanisms.

A. The Effect of Nitrogen Implantation on Martensite in 304 Stainless Steel

R.G. Vardiman, R.N. Bolster, and I.L. Singer

Martensite will form in austenitic 304 stainless steel when it is deformed. Transmission electron microscope studies show that nitrogen ion implantation causes a reversion of the martensite to austenite. Specimens containing martensite resulting from fine surface polishing and heavy rolling are examined. The transformation is shown not to occur because of temperature increases during implantation. The effect is related to recent wear results in 304 stainless steel.

B. Mechanical and Microstructural Properties of Boron Implanted Beryllium

R.A. Kant, A.R. Knudson and K. Kumar

High dose boron implantation into instrument grade I-400 beryllium has been found to produce a substantial increase of its wear resistance. A comparison of the friction and wear behavior resulting from two shapes of the boron depth distribution is made. The wear resistance provided by a boron layer of constant (flat) concentration was found to be superior to that of a gradually decreasing (graded) profile. Rutherford backscattering was used to determine the boron depth distribution profiles and transmission electron microscopy was used to examine the microstructure. Electron diffraction pattern analysis provides evidence for the formation of beryllium borides.

C. Effects of Carbon on the Friction and Wear of Titanium-Implanted 52100 Steel

I.L. Singer and R.A. Jeffries

Auger spectroscopy, EDX and optical microscopy have been used to analyze friction and wear behavior of 52100 steel implanted with Ti to a fluence of $2 \times 10^{17}/\text{cm}^2$. Three implantation conditions were chosen to produce different C concentration profiles at the surface: disk 1 - Ti^+ implanted at 190 keV produced a partially carburized layer; disk 2 - Ti^+ at 190 keV followed by C($2 \times 10^{17}/\text{cm}^2$) at 50 keV produced equal and overlapping Ti and C profiles; disk 3 - Ti^+ implanted at 50 keV produced a more fully carburized layer than disk 1 but had less Ti and a smaller C/Ti ratio than disk 2. Disk 3 had the best tribological surface; the friction coefficient was $\mu=0.3$ and no wear was detected. Disk 2 displayed stick slip with an average $\mu=0.5$ and showed mild wear. Disk 1 showed high friction and severe wear. We conclude that the improved tribological surface of Ti-implanted steel results from vacuum carburization and not just the presence of excess C.

D. A Technique for Studying the Effect of Ion Implantation on Dislocation Structures Developed During the Fatigue of Nickel

R.G. Vardiman

A method has been developed for the study of dislocation structures produced during the fatigue of nickel wires. Carefully prepared specimens are nickel plated so that transverse TEM samples can be made. In this way near surface effects and depth variation, particularly important for ion implantation studies, can be observed. For pure nickel, carbon implantation gave a relatively small increase in fatigue life. Dislocation

structures likewise varied little, mainly due to the cellular structure developed during the first cycle. This structure occurs because the maximum fatigue stresses were well above the yield point of nickel. The techniques which have been developed are being extended to a nickel-chromium alloy where fatigue stresses below the yield point should allow better differentiation of implantation effects.

III. CORROSION AND OXIDATION

Research reported in this section involves the application of ion implantation processing to improvement of the corrosion and oxidation resistance of surfaces and fundamental investigations conducted to improve our understanding of the effects of the implantation on corrosion and oxidation mechanisms.

A. Ion Implantation Effects on the Thermal Oxidation of Metals

K.S. Grabowski and L.E. Rehn

In the past decade, ion implantation has been shown to reduce oxide thicknesses up to tenfold in survey experiments on Ti, Zr, Ni, Cu, and Cr, and to enhance the long-term oxidation resistance of some high-temperature alloys. This review summarizes the major results of previous work. Important concepts are illustrated using recent experimental results obtained from a He-implanted Ni-1 at.% Pt alloy. Collectively, the results indicate that ion implantation has considerable potential for reducing oxidation, and as a research tool to investigate the mechanisms of thermal oxidation in metals. However, more thorough work needs to be done before the influences of ion implantation on the oxidation of metals can be understood.

B. Electrochemical and A.E.S. Studies of Fe-Cr Surface Alloys Formed On AISI 52100 Steel by Ion Beam Mixing

W.K. Chan, C.R. Clayton, R.G. Allas, C.R. Gossett and J.K. Hirvonen

Fe-Cr surface alloys have been formed on AISI 52100 steel by Ion Beam Mixing in order to improve localized corrosion resistance. Three implant species were considered in this work, namely: Cr^+ , Xe^{++} and Kr^{++} . Ion implantation was carried out on Cr surface layers, of 30 and 50 nm, deposited onto 52100 steel coupons. The resulting surface alloys were chemically characterized by Auger electron spectroscopy. Electrochemical pitting studies were carried out in deaerated 0.01M NaCl solution buffered to pH6. Each of the surface alloys formed by the ion beam mixing technique exhibited a significantly higher resistance

to localized corrosion compared to 52100 steel. The possible influence on the localized corrosion resistance of the surface alloys of oxidation, carbide formation and sputtering, resulting from the ion implantation treatments, is discussed.

C. RHEED, AES and XPS Studies of the Passive Films Formed on Ion Implanted Stainless Steel

C.R. Clayton, K.G.K. Doss, Y-F. Wang, J.B. Warren and G.K. Hubler

P-implantation (10^{17} ions cm^{-2} , 40 Kev) into 304 stainless steel (ss) has been carried out, and an amorphous surface alloy was formed. Polarization studies in deaerated 1N H_2SO_4 + 2% NaCl showed that P-implantation improved both the general and localized corrosion resistance of 304 ss. A comparative study has been carried out between the implanted and unimplanted steel to determine what influence P-implantation has upon the properties of the passive film formed in 1N H_2SO_4 . The influence of Cl ions on pre-formed passive films was also studied. RHEED, XPS and AES were used to evaluate the nature of the passive films formed in these studies.

IV. OTHER EXPLORATORY RESEARCH AREAS

Research reported in this section includes exploratory investigations to assess the potential of ion implantation in areas other than wear/fatigue and corrosion/oxidation.

A. Infrared Studies of Isothermal Annealing of Ion-Implanted Silicon: Refractive Indices, Regrowth Rates, and Carrier Profiles

C.N. Waddell, W.G. Spitzer, G.K. Hubler, and J.E. Fredrickson

A model-dependent computer analysis technique developed previously has in this work been applied to the infrared reflection data of a number of (111) and (100) oriented Si samples which were implanted with high fluences of Si or P ions and then taken through an isothermal annealing process. The physical properties deduced from this analysis are (i) Dielectric properties including the frequency dependent refractive indices of the recrystallized Si and of the α -Si as a function of annealing temperature and time; (ii) structural information including the amorphous layer depth, widths of transition regions, and the epitaxial regrowth rates; and (iii) electrical properties including the depth profile of the carrier density, the carrier mobility near the maximum carrier density, and the carrier activation efficiency. The physical interpretation of

the results is discussed and, where possible, comparisons with results of other experiments are made.

B. Properties of Amorphous Silicon Produced by Ion Implantation:
Thermal Annealing

W.G. Spitzer, G.K. Hubler and T.A. Kennedy

The refractive index, electron paramagnetic resonance (EPR) signal strength and density of amorphous silicon were measured as a function of 500°C isothermal annealing time. The EPR signal was found to be correlated with two distinct optical states of amorphous silicon that were previously reported. One state is the as-implanted state which has a refractive index 12% larger than crystalline silicon. The other state is stabilized after thermal annealing and has a refractive index 8% larger than crystalline silicon and an EPR signal strength a factor of three smaller than the first state. This state is stable until epitaxial recrystallization occurs. No correlation is found with the amorphous silicon density.

BIBLIOGRAPHY

A cumulative bibliography of papers related to ion implantation for materials processing authored or co-authored by NRL staff members is provided.

Section I.A

NEAR SURFACE ANALYSIS WITH ENERGETIC ION BEAMS

C. R. Gossett

Materials Modification and Analysis Branch
Condensed Matter and Radiation Sciences Division
Naval Research Laboratory

This work was supported by the Office of Naval Research.

Near Surface Analysis with Energetic Ion Beams

C. R. GOSSETT

Naval Research Laboratory, Condensed Matter and Radiation Sciences Division,
Washington, DC 20375

A review is given of some representative methods and results for near surface analysis of elemental composition vs. depth as determined by Rutherford backscattering and related ion beam techniques. Examples are given from new applications in the areas of thin film and ion implantation technologies, which are used to tailor the near-surface composition to beneficially modify such surface-sensitive properties as friction, wear, oxidation and resistance to corrosion. Profiling by energetic ion beam methods is useful in optimizing the effect or in studies to understand the mechanisms. The advantages and limitations of this analysis method are explored with discussion of ion-excited x-ray analysis and nuclear reaction analysis as alternative or auxiliary approaches.

The field of materials analysis by energetic ion beams has begun to mature in the last decade after arising within the nuclear physics community. The basic method, Rutherford backscattering, has been the subject of a text (1), and the field has also engendered a useful handbook (2). Publications are scattered throughout the literature with much of the output in articles relating to the properties of materials. In these the ion beam analysis may form only a part of the work. New developments in technique and applications continue and have been the subject of a series of international conferences (see for example (3) for the latest of these).

For the purposes of this symposium this paper will attempt to summarize the main features of the technique, drawing on the author's own work to demonstrate both the range of applicability and the limitations. In addition to Ruther-

ford backscattering two auxiliary ion beam techniques will also be discussed.

A principal distinction between energetic ion beam analysis and other analysis techniques presented at this symposium is one of the energy scale involved. While chemical binding effects are in the range of electron volts and the "surface-sensitive" techniques are at most restricted to within a few orders of magnitude of this, most energetic ion beam analyses are conducted in the range of a few million electron volts for the primary ions. This vast difference in the energy range has a number of important consequences for the analysis method.

First, because of the large energy difference, this method is completely insensitive to chemical binding effects. While other conventional surface analysis techniques which are sensitive to the chemical state are unquestionably frequently required, it is also true that methods thus dependent on the chemical state may suffer from difficulties in calibration, particularly in transition regions where an element is found in more than one chemical state. Energetic ion beam analysis, on the other hand, offers an absolute technique independent of these effects. As such, this technique and other conventional techniques (e.g. Auger, ESCA etc.) may often prove to be complementary, each supplying information not available by the other techniques.

Second, because the high energies provide penetration of solid materials to depths of several micrometers, this technique is not strictly a "surface analysis" method so much as a "near-surface analysis." When information is required on the composition, not only of the outermost surface, but also of the depth region within a few micrometers below the surface, such as in cases where the surface may be expected to be removed in use by wear or corrosion, then the composition in immediately underlying regions may be of importance. In these cases where a composition vs. depth (profile) is required, surface-sensitive techniques may of course be applied, provided that a method of successively removing surface layers by abrasion, etching, or sputtering is supplied to determine the profile. The greater penetration of the energetic ion beam, on the other hand, does not require removal of material to obtain a profile, as it depends only upon the relatively well understood energy loss phenomena for ions in matter to determine the depth at which atoms of a particular species are located. In this sense, this method is not destructive, although it may in some circumstances affect the material under study and may not always qualify as totally "nondestructive".

Third, the requirement of accelerating an ion to the MeV range of energies must necessarily entail a larger size, more expensive and often more complex acceleration apparatus. Thus, the technique of energetic ion beam analysis grew in the

environment of nuclear physics laboratories where such accelerators proliferated in the past few decades in support of the low energy nuclear physics research. This same environment was responsible for generating much of the available information on specific useful nuclear reactions and on the energy loss of ions in materials which is so important to the applications of the technique. In more recent years, as the technique has become better established, many of these older facilities have been converted to materials analysis and much of the current accelerator production is dedicated to this field and the related field of modification of materials by ion implantation.

Elastic Backscattering Analysis

The use of elastic backscattering, which is the primary technique for energetic ion beam analysis, is the normal method of choice when it will produce satisfactory results. Some other ion beam techniques which may be useful in supplementing backscattering in specific cases will be discussed later in this paper.

Backscattering analysis requires the previously mentioned accelerator and the associated energy selection, focusing and positioning apparatus. The incident ions, usually a stable isotope of hydrogen or helium, are formed into a well collimated beam of monoenergetic particles. Beyond this the requirements are relatively simple. Generally analyses are conducted in a moderately high (e.g. 10^{-6} Torr) vacuum, because of the energy losses even in gaseous matter, although in special cases of volatile substances or even liquids, analyses have been provided in partial atmospheres of inert gasses. The other required apparatus for the experiment are: (1) a small surface barrier diode detector for detecting the scattered ions and for measuring their energy; (2) associated electronics, including a multichannel analyzer system or equivalent on-line computer for converting the electrical pulses from the detector into a spectrum of count vs. energy; and (3) a means of positioning a sample to intercept the accelerated ion beam in a known relationship to the detector. The latter arrangement typically includes provision to place successively several samples in position without breaking the vacuum and usually a means of changing the orientation of the sample with respect to the beam direction.

The theoretical foundation upon which backscattering stands is extremely straight-forward. The primary mechanism is the elastic collision process. The conservation of energy and momentum provide nonrelativistically that the ratio of the energy of the scattered ion, E_1 , to that of the incident ion, E_0 , is:

$$\frac{E_1}{E_0} = \frac{M_1^2}{(M_1 + M_2)^2} \left\{ \cos \theta \pm \left[\left(\frac{M_2}{M_1} \right)^2 - \sin^2 \theta \right]^{1/2} \right\}^2, \quad (1)$$

where the subscripts 1 and 2 refer to the scattered ion and the scattering atom, respectively, M is the mass, and θ is the scattering angle. Scattering angles from about 135° to nearly 180° are generally used to enhance the separation in energy for different masses, but it will also be noted that the energy separation of adjacent mass numbers will become less sensitive at higher masses.

Thin Film Example. As an illustration of the method, Figure 1 shows a backscattering spectrum for a study of a thin MoS_2 film sputter-deposited for solid lubrication purposes. Since this analysis is of a relatively thin layer it provides a good example of the effect of the elastic collision process in identifying the elements present within the thin film. In this case the mass four isotope of helium (i.e., an alpha particle) scattered into a narrow angular range at a definite backward angle will have an energy uniquely dependent upon the mass of the nucleus from which it scattered as calculated by Equation 1. This determines the grouping of the energy of the scattered ions into the peaks, each labeled with the symbol for the relevant element.

A second consideration, not as apparent in Figure 1, where the film is very thin, is the role of energy loss considerations in defining the depth below the surface at which the particular scattering event took place. This energy loss is due to inelastic collisions of the ions with the electrons of the atoms present in the film. In the case illustrated in Figure 1 the atoms were all within a very thin near-surface layer and the peaks show an energy width not significantly greater than the energy resolution of the detector system. However, for thicker layers, both the incoming ion and the scattered ion lose energy in traversing the distance between the surface and the scattering site giving rise to a distribution of energies. There now exists a large amount of experimental and theoretical information on this energy loss process for passage of the commonly used analysis ion beams into most elements. Thus, with a knowledge of the stopping power known to an accuracy of 10-15% or better it is possible with a monoenergetic incident beam to quantify the depth at which the scattering event took place in terms of the energy loss of the scattered ion compared to an ion scattered at the surface, for which no inelastic losses occurred.

A large amount of information may be determined from energy spectra such as that shown in Figure 1. If the bombard-

ing energy is low enough (i.e., below about 3 MeV for helium ions for all but lightest elements) the elastic collision process giving rise to the backscattering is due entirely to the electrostatic repulsive forces between the ion and the nucleus and does not involve an actual contact of the two. In this case the backscattering is called Rutherford backscattering. The great advantage of the purely electrostatic scattering is that its probability depends only on the square of the atomic number of the nucleus and not on specific nuclear properties. Therefore for any given element the cross section or probability of scattering at the prescribed angle is directly and simply calculable. This means that comparisons with standards are not required other than for a single elemental sample to establish the solid angle subtended by the detector. The consequence of this is that given the beam energy, scattering angle, total integrated beam charge, and elemental identification from the peak positions, the number of atoms/cm² of each element present can be readily and directly calculated from the total number of counts in each peak.

It should be noted that a Z^2 dependence of the cross section makes the process very sensitive for heavier elements but proportionately less so for lighter elements. This effect can be observed in Figure 1 when it is noted that the Au peak indicates the presence of only about 0.04% Au compared to about 50% for the O peak. In the latter case the sensitivity is further degraded by the superposition of the O peak from the thin film with the distribution from the thick underlying Si substrate. It should be further noted here that the Si substrate is prevented from interfering with other elements by the special preparation of the substrate by placing a film of C on its surface before deposition of the sample thin film. This technique is useful when one has the opportunity to choose the substrate.

In thicker uniform samples the peaks at each mass broaden out with a relatively flat-topped distribution. By calculations based upon the energy loss process described above, it is possible to relate the energy of the scattered ion to the depth below the surface for the scattering interaction. In this way the observed distribution may be related to the composition vs. depth of the particular element within the sample layer.

Thick Film Example. As the peaks become thicker the possibility of interference of the distributions from two or more of the elements is also increased. This is particularly true for heavier elements which inherently appear closer together in terms of the energy of the scattered ions. A particularly difficult example of this situation is shown in Figure 2, again for a sputter-deposited solid lubricant film, in this case a thicker layer on a steel substrate. Figure 2

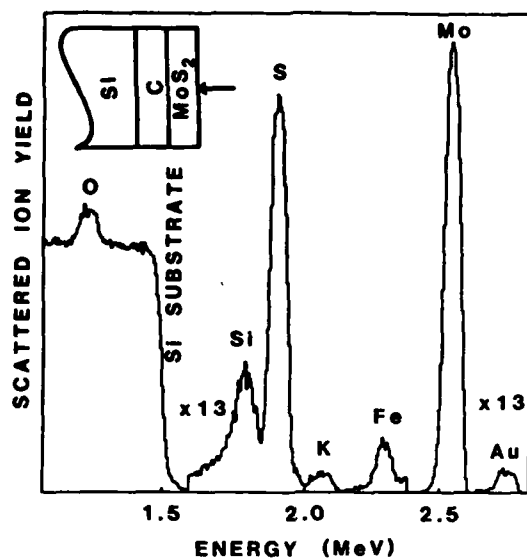


Figure 1. A Rutherford backscattering spectrum for a thin ($40 \mu\text{g}/\text{cm}^2$) MoS_2 sputter-deposited film. Conditions: $^4\text{He}^+$ ions normally incident at 3.0 MeV, and scattered ions detected at a 135° angle by a surface-barrier diode detector. Note the scale factor for other than the Mo peak and the Si substrate. The sample layer configuration is indicated at the upper left.

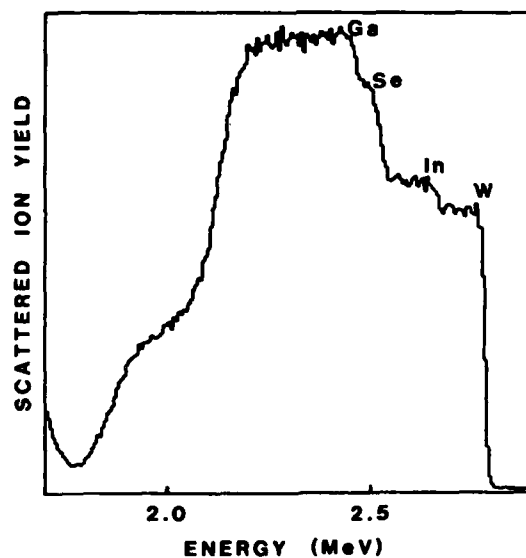


Figure 2. A partial Rutherford backscattering spectrum for a relatively thick ($430 \mu\text{g}/\text{cm}^2$) sputter-deposited solid lubricant thin film with conditions as in Fig. 1.

shows a higher energy portion of the spectrum and demonstrates discernable edges for the four (labeled) elements involved. It should be noted that in the case where the thickness of the layer is greater than the resolution of the detector, the height of the edges may be related to the number of atoms/cm³ of that particular element at the surface. Thus, it is possible even when the distributions overlap to determine from the edge heights the composition of the film, at least at or near the surface. Because in this spectrum the distributions from the four elements considerably overlap it is more difficult to determine the detailed profile. However, the appearance of the combined distribution suggests that the elements are nearly uniformly distributed throughout the depth of the film.

The problem of overlapping distributions arises from the fact that it is impossible to distinguish uniquely or simply from the energy of a single scattered ion, whether: (1) the scattering is from the lighter element near the surface, or (2) from a heavier element at a greater depth below the surface. Although individual scattered ions can not be thus distinguished, in the aggregate they can frequently be identified, as in the case of the edges shown in Figure 2 and discussed above.

Because all phases of the interaction of the incident energetic ion beam with materials, including kinematics and cross section of the elastic collision and the energy losses by means of inelastic interaction with the electrons are readily calculable, the analysis lends itself to computer simulation. One of the first such programs, developed at IBM (4), is used at NRL, while other programs have also been developed at a number of other laboratories.

Figure 3 shows a computer simulation for the spectrum shown in Figure 2 and illustrates how the individual distributions (i.e., the lower curves identified by involved element) add to produce the observed total distribution shown as the upper curve. It is seen that the computer fit is relatively good and that the assumption of uniformity (the individual elemental compositions do not vary by more than 10% throughout the depth except at the back edge) was warranted. Although the simulation conclusions are not necessarily unique they generally may give a reasonable description of even complex overlap situations. However, since the processes simulated require a fair amount of computation, the direct deconvolution of a spectrum by such techniques is not generally possible. In practice, computer fits such as those shown are determined by a series of trials of successive approximations to the observed distribution. As such, they are relatively time-consuming and may not be universally applied except where circumstances warrant.

Implantation Example. An even more complex example may be cited from the use of ion implantation as applied for modifying the surface-sensitive properties of metals. The use of ion implantation in the semiconductor industry is well known as a means of producing well controlled and reproducible doping of semiconductor materials. Also, for metals by means of ion implantation it is often possible to produce near the surface an entirely different alloy from that of the bulk, as in a stainless steel, by the addition of Cr or other common alloying elements. In such cases it is obviously necessary to know what concentration profile results from the implantation of one or more elements into the near surface region. Although the computational capabilities for predicting the distribution of an element implanted under given conditions have improved considerably in recent years, there are a number of factors which are not yet well understood or for which information may not be available in many cases. These effects may strongly influence the resulting depth concentration profile, particularly if more than one implantation is performed. These effects include, but are not limited to, dilution, ion induced mixing and surface sputtering. The latter may become a factor in these cases because of the relatively larger fluences required to change the near surface composition in the 1 - 50 at % range.

Figure 4 provides an example of the result of a duplex implantation into a commonly used bearing alloy. The small peak at the left of the diagram which is due to P, the lighter of the two implanted elements, is subject to easy interpretation. From this peak the conditions of the P implantation (i.e., the total atoms present and the parameters of its nearly Gaussian distribution) may be determined. As in earlier examples the presence of the peak on a large background from the bulk materials present in the alloy requires excellent statistics (through longer exposure to the analyzing beam) in order to reduce the statistical uncertainties in subtracting this background. Due to the proximity in mass of the major component of the steel, Fe, and the other implanted element, Cr, the interpretation of the major leading edge due to the Fe is not at all clear from initial inspection. The lower intensity distribution above the Fe edge is due to a small percentage (about 4 wt %) of Mo in the base alloy.

A solution of this problem is provided by the computer simulation shown in Figure 5, where the distributions of the individual elements are shown labeled in the bottom of the figure and the top curve is the sum of these for comparison with Figure 4. What is observed is a new phenomenon compared to the simpler thin film case shown earlier, i.e., the presence of a dilution effect in the base materials caused by the implantation of the two ion species. This may be readily

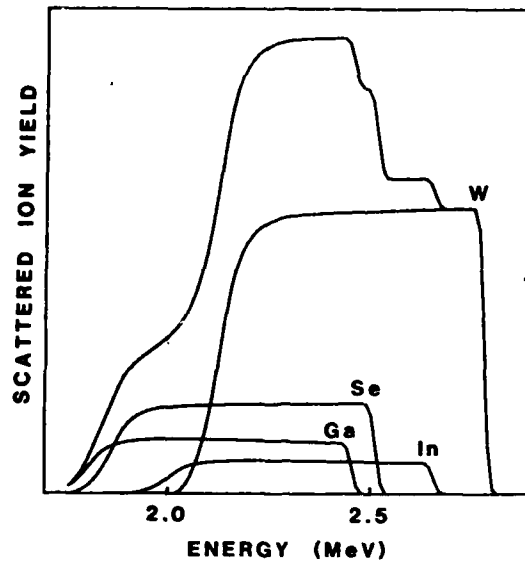


Figure 3. A computer simulation of the partial spectrum from Fig. 2. The lower labeled curves are the individual distributions, and the upper curve is their sum.

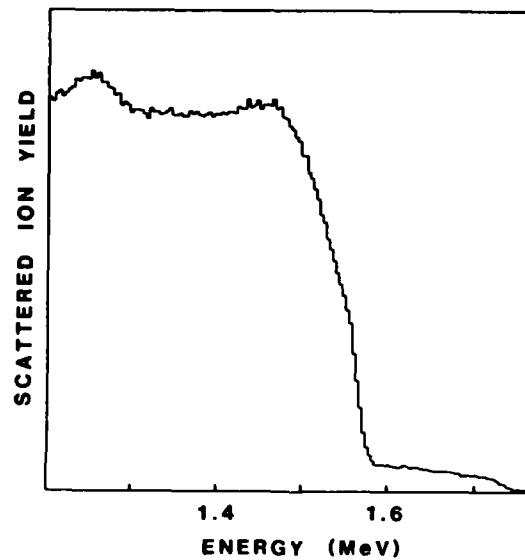


Figure 4. A partial Rutherford backscattering spectrum of an M-50 steel sample successively implanted with 2×10^{17} ^{52}Cr atoms/cm 2 at 150 keV and with 1×10^{17} ^{31}P atoms/cm 2 at 40 keV. Conditions: $^4\text{He}^+$ ions normally incident at an energy of 2.0 MeV, and scattered ions detected at a 135° angle by a surface-barrier diode detector.

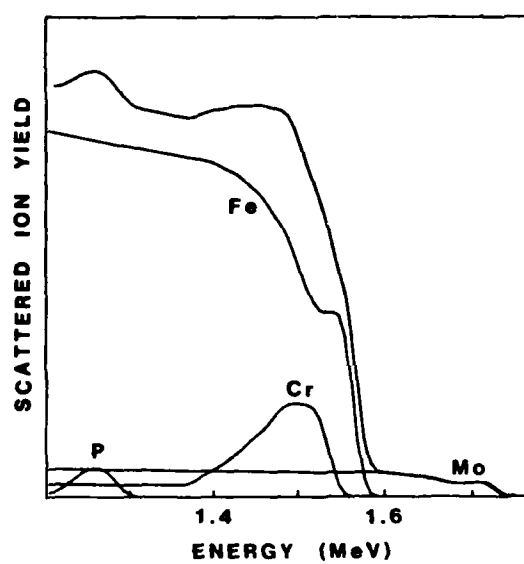


Figure 5. A computer simulation of the partial spectrum from Fig. 4.

observed in the Fe distribution and also in the weaker Mo distribution from the base components. The other small percentage component, Cr, in the original alloy is identical with one of the implanted ions, but its presence is manifest in the tail shown to the left of the Cr peak.

The P peak to the left shows the expected nearly Gaussian distribution with a width consistent with the relatively lower energy (40 keV) with which it was implanted, producing a distribution near the surface. The Cr distribution, on the other hand, is clearly considerably distorted from a Gaussian distribution, due in this case to sputtering which is significant for this fluence (2×10^{17} ^{52}Cr atoms/cm²). This sputtering results in raising the percentage of Cr at the surface relative to the peak as is apparent by the appearance of a definite edge at the high energy (surface) end of the Cr distribution. This edge is slightly displaced from the Fe edge due to their mass difference. It is the superposition of the displaced Cr peak with the dilution dip in the Fe distribution which gives rise to the peculiar shape of the observed distribution of Figure 4. Although the computer simulation shown here is instructive in explaining the effects leading to the observed distribution, it will in most cases produce sufficient uncertainties in the elemental composition profiles as to make other methods preferable in a case which proves this difficult for backscattering analysis. Fortunately in this case a specific nuclear reaction is available to profile the Cr and this reaction will be described later.

The examples of backscattering analysis that have been cited demonstrate some of the principal limitations of the method which are here summarized. (1) The energy separation of ions scattered from neighboring elements becomes smaller the higher the mass. This effect may lead to identification and/or overlap problems. (2) The cross section for elastic scattering varies with Z^2 , making it more difficult to observe lighter elements. This problem is exacerbated by the fact that distributions from light elements may frequently be superimposed on large distributions from the bulk materials or from a substrate, unless special substrate provision can be made. (3) When the thickness of layers of material are sufficiently great or constituent elements are insufficiently separated in mass the possibility of overlap exists which may degrade the quality of information on the depth distribution available, but may not necessarily prevent a determination of composition at least at the surface.

Ion Induced x-ray. Auxiliary techniques may be used to obviate some of the difficulties or limitations of backscattering analysis outlined above. One such technique is ion induced x-ray analysis, a relatively simple technique to apply in an

accelerator laboratory. The instrumentation consists of a cooled lithium drifted silicon detector, usually in its own vacuum container and separated from the accelerator vacuum by thin Be windows. The electronics and multichannel analyzer requirements are similar to those for ion energy detection, and if sufficient equipment is available, an x-ray spectrum may frequently be accumulated simultaneously with the backscattering spectrum. Unlike the backscattering, however, the energies of the observed x-rays are characteristic only of the elements present and not of their depth distribution. In this laboratory this method is used principally to provide positive elemental identifications in cases where high mass numbers cause difficulties using elastic backscattering or in some cases to identify weaker components which may be masked by other elements in overlapping backscattering distributions.

However, it is possible to get quantitative information on the total quantity of a given element present from the x-ray data. Generally corrections are necessary for decreasing cross section and increasing x-ray absorption as a function of depth in the material, except for cases of elements known to be present only in a thin layer near the surface. As this information is generally available from the backscattering analysis the two techniques may be used in conjunction and it may be possible to produce better results for the total quantity from the x-ray data, such as case of the sample for which a backscattering analysis is shown in Figures 2 and 3. The ion induced x-ray spectrum from this solid lubricant sample is shown in Figure 6 in a semi-logarithmic display. Although this spectrum shows considerable complexity due to multiple K, L, or M peaks from the several elements present, at least one well isolated peak is available for purposes of quantification for practically all elements. In any case, the presence of the particular peaks does provide positive identification of the elements in the sample.

Nuclear Reaction Analysis

An additional approach that may help when interferences occur in backscattering spectra or when weak lighter element distributions are obscured by large backgrounds is the use of a selective nuclear reaction to determine the profile of that particular element only. By careful selection of the bombarding ion species and energy it is often possible to find such a selective nuclear reaction so as to preclude interference from other elements which may cause problems in the backscattering case. Recourse to nuclear reactions is, however, resorted to only in cases of necessity, as nuclear reactions generally suffer from cross sections several orders of magnitude lower than the equivalent Rutherford elastic scattering. As a consequence of this and the added complexity of nuclear

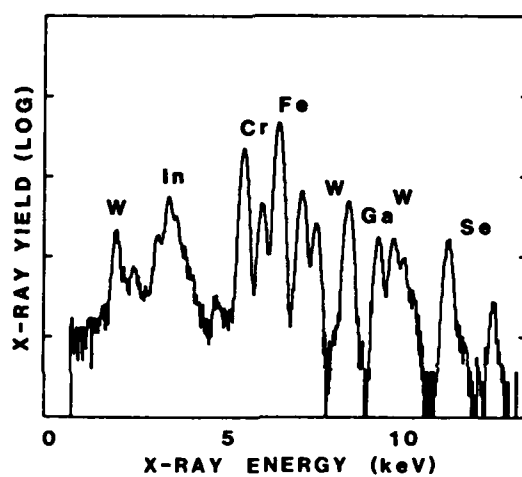


Figure 6. An ion induced x-ray spectrum for the sample shown in Fig. 2. Conditions: $^1\text{H}^+$ ions incident at an energy of 3.0 MeV, and scattered ions detected at a 45° angle to the normal sample. X-rays detected at a 90° angle to the beam with a Si(Li) detector.

reaction analysis, such methods are generally much more time consuming. The conceptually more difficult subject of nuclear reactions may be divided into two classes to simplify the discussion.

Nonresonant Reactions. The so-called "nonresonant" reactions in use bear a close resemblance to the backscattering techniques previously described. In this case the bombarding ion type and energy are selected to be sufficient to actually penetrate the nucleus and initiate a reaction, rather than remaining outside the nucleus as in the Rutherford backscattering case. The cross section for the reaction then becomes a complex function of the nuclear excited states and thus not subject to simple calculation. Indeed in this case it is necessary to experimentally measure the cross sections as a function of energy in the region of interest, or more usually to use a standard of a pure element or compound of known stoichiometry to calibrate the reaction yield for comparison. This is not completely straight forward in the case of moderately fluctuating cross sections as proper allowance must be taken computationally of the differing energy losses in the two different materials.

One of the primary distinctions of this type of reaction is the fact that usually the detected particle (this term rather than ion will be used henceforth in conformity to nuclear physics usage) is normally of a different element or isotope than the incident particle which initiates the reaction. Typical reactions may be (p,α) , (d,p) , (d,α) , $(^3\text{He},p)$, or $(^3\text{He},\alpha)$ where $p = ^1\text{H}^+$, $d = ^2\text{H}^+$, and $\alpha = ^4\text{He}^+$ or $^4\text{He}^{++}$. These reactions are largely restricted to light elements ($Z < 10$) by energy considerations in order to allow penetration of the nucleus with low energy (< 5 MeV) particle beams. Generally then, to profile a particular element a specific reaction will be chosen which fulfills as many as possible of the following factors: (1) the reaction must be exoergic with a large positive Q-value (energy release) to assure that the outgoing particle will have a large enough energy to place it higher in the energy spectrum than the elastically scattered particles from any elements in the sample. (2) The cross section must be as large as possible to provide good yield and must be as smooth or slowly varying as possible to facilitate comparison with the standard. Frequently, in addition to the choice of energy, a choice of the angle with respect to the beam at which the particles are observed may improve these factors. (3) Possible interference with particles from other light elements which may be present should be avoided. This is usually easy since other light elements are normally present only as surface contaminants except in organic materials, and in any event can usually be avoided by proper choice of bombarding particle and energy.

(4) If it is necessary to profile with good depth resolution it is preferable that one of the particles be an isotope of He, as the greater stopping power will increase the energy loss for this particle and thus enhance the depth resolution.

N Implantation Example. Experimentally the measurements are conducted similarly to the backscattering technique. The same type of detector is used, although often thicker to accommodate the higher energy and hence greater range of the particles, particularly for a hydrogen isotope. An example for a Si_3N_4 standard for the $^{14}\text{N}(\text{d},\alpha)^{12}\text{C}$ reaction is shown in Figure 7 in a semi-logarithmic representation. The detector does not distinguish between particle types and the various groups seen are due to competing (d,p) and higher-excited state (d, α) groups. The elastically scattered deuterons give rise to the highest peak at the extreme low energy end. The groups of interest are marked α_0 and α_1 , corresponding to reactions proceeding to the ground state and 4.43 MeV first excited state of ^{12}C , respectively. Because of very large Q values these groups stand out above the others and are suitable for use in profiling work. The α_1 group is often used because it has a relatively flat cross section over an extended energy range.

Figure 8 shows an application of this technique to a measurement of N implanted into a tool steel, specifically an end mill, to ascertain the stability of the N under the rigorous conditions at the cutting edge. The figure shows the same very small portion of the energy spectrum taken at two points on the end mill: one at the cutting end where overheating occurred (b) and the second on the cutting edge farther from the region which overheated (a). The portion of the spectra displayed in each case corresponds to only a small part of the spectrum of Figure 7, specifically from the higher energy edge of the α_1 group along the flat portion. As can be seen the cool end (a) retained the N in the nearly "as implanted" condition in a narrow layer near the surface, while for the hot end (b) the heat has caused the N to diffuse, greatly reducing the capability of the N in inhibiting wear.

C Implantation Example. Another example of using a light element to affect surface properties is the implantation of C into a Ti6Al4V alloy in an attempt to enhance fatigue characteristics. The (d,p) reaction is the usual standard for profiling C, but this reaction suffers from a lack of high depth resolution due to the fact that it utilizes only H isotopes which have lower stopping power. This provides a problem in that, in the relative "dirty" vacuum systems of accelerators, C is deposited as a ubiquitous surface contaminant in a graphitic form by the action of the beam, even with cryotrapping arrangements. The problem then is distinguishing

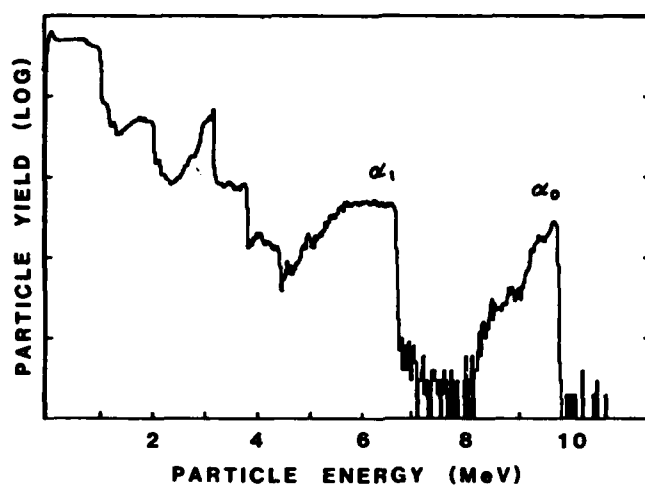


Figure 7. A spectrum of particles resulting from nuclear reactions and scattering from a thick Si_3N_4 standard. Conditions: $^2\text{H}^+$ ions normally incident at an energy of 1.41 MeV, and resulting reaction particles detected at a 165° angle by a surface-barrier diode detector. The particle group marked α_1 is from the $^{14}\text{N}(\text{d},\alpha)^{12}\text{C}$ reaction and is used to profile N in samples.

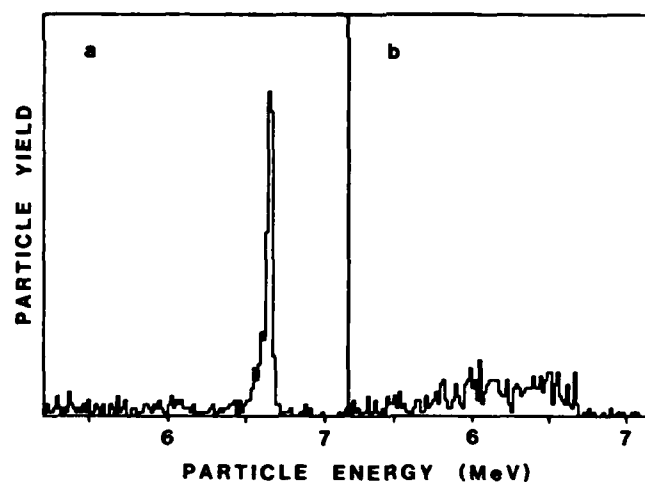


Figure 8. Partial spectra of particles resulting from the $^{14}\text{N}(\text{d},\alpha)^{12}\text{C}$ reaction at two positions on a ^{14}N implanted cutting edge of an end mill tool. Key: a, the end was not overheated and retains the as implanted N; and b, the end was overheated in use and caused diffusion of the N. Conditions are as in Fig. 7.

the surface C, added by the analysis technique, from that deliberately introduced into the near surface region of the sample.

The solution to the problem, which was reported recently (5), is the use of a ($^3\text{He},\alpha$) reaction which through the greater stopping power of the He isotopes provides enhanced depth resolution. The result is shown in Figure 9 which is a profile of a relatively shallow C implant in the Ti alloy.

The technique here is of particular interest since it utilizes a magnetic spectrometer with a position-sensitive detector rather than the usual surface-barrier energy detector. This double-focusing spectrometer, which has a very reasonable solid angle of acceptance, is sometimes used in profiling because of its inherently higher energy resolution. However, in this case the use of a magnetic momentum measuring device rather than a purely energy measuring device is necessary because for this reaction at backward angles the energy of the alpha particles is actually below that of the bombarding ^3He particles elastically scattered from the Ti alloy. However, because of the higher momentum due to the mass four observed reaction particle compared to the mass three scattered particles, the alpha particles may be observed in the region of interest, resulting in the spectrum shown.

Resonant Nuclear Reaction. A second class of nuclear reaction useful in profiling the near surface region is the so called "resonant" reaction, in which a narrow isolated resonance in the yield of the selected reaction is used to probe the number of atoms of this nucleus within a narrow depth interval of the sample. The profile is then generated by accumulating data at a series of different bombarding energies, each corresponding to a different depth below the surface of the sample for the resonance, according to the energy loss process for the incident particles.

This method is of course restricted to nuclei which provide a satisfactory resonance, usually with a (p, γ) or (p, α) reaction. These are most often found in the region of elements between $Z = 10$ and $Z = 28$, although a few examples exist for lighter elements. Unfortunately above Ni there are no nuclear reaction techniques which have proved satisfactory for profiling purposes.

Cr Implantation Example. Fortunately for those interested in profiling implanted elements in steels, the principal isotope of Fe contributes very little yield from the (p, γ) reaction in the energy region of interest, whereas at least Ti, Cr, and Ni (6) among others have an appropriate resonance. To measure the gamma-ray yield it is often necessary to use a high-resolution gamma-ray detector such as Ge(Li) or hyperpure

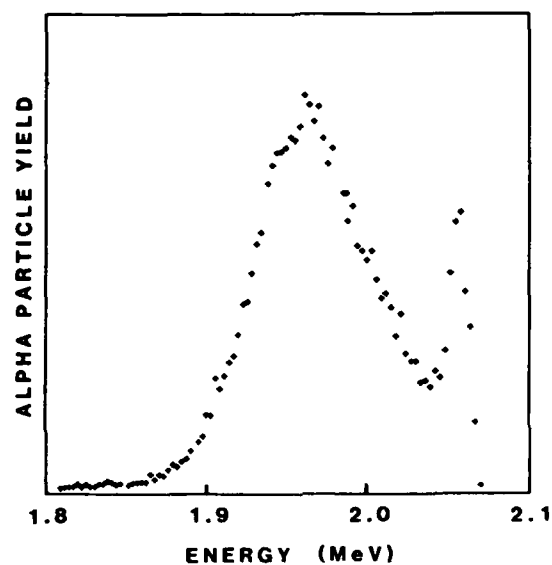


Figure 9. A partial spectrum of α particles resulting from the $^{12}\text{C}(^3\text{He},\alpha)^{11}\text{C}$ reaction as applied to a Ti6Al4V alloy sample implanted with 3×10^{17} ^{12}C atoms/cm² at 75 keV. Conditions: $^3\text{He}^+$ ions normally incident at an energy of 2.775 MeV, and resulting reaction particles detected at a 135° angle with a magnetic spectrometer. The higher energy peak is due to surface contamination and is resolved from the implanted distribution. (Reproduced, with permission, from Ref. 5. Copyright, North-Holland Publishing Co.)

Ge in order to be able to clearly distinguish only transitions produced by the resonance of interest. Such detectors, self contained in their own cryostat, again utilize electronics and multichannel analyzer similar to the other cases.

An example of this technique is shown in Figure 10 where distributions for Cr implanted in Fe are shown at two different fluences to demonstrate the effect of sputtering on the profile at higher fluences. The lower curve is for a fluence producing negligible effect from the sputtering whereas the upper curve shows the typical distortion effects characterized by a raising of the surface concentration due to sputtering.

Conclusions

It has been shown that energetic ion beams may be utilized to "nondestructively" determine the profile of composition vs. depth in a wide variety of near surface situations. The major difficulties and limitations of the method have been delineated with descriptions of alternative methods applicable in difficult cases. The advantages of using these techniques as complementary to other surface analysis methods has also been pointed out.

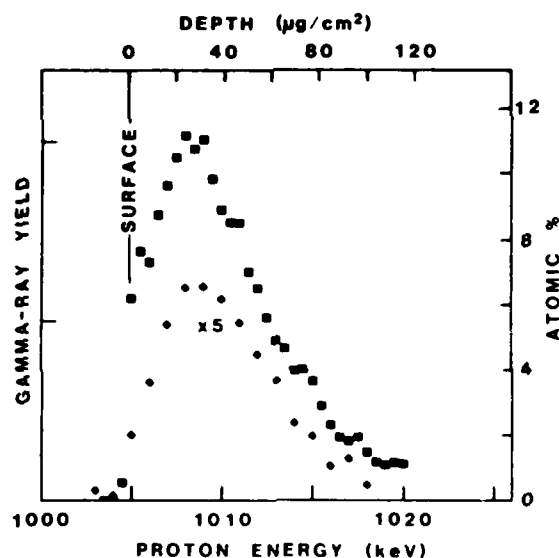


Figure 10. Profiles generated from the 1005-keV resonance of the $^{52}\text{Cr}(p,\gamma)^{53}\text{Mn}$ reaction in pure Fe samples implanted with fluences of 1×10^{17} and 1×10^{16} ^{52}Cr atoms/cm² at 150 keV. (Note the scale factor for the latter.) The incident energy at which the γ -ray yield for each point was obtained is on the lower abscissa scale and an equivalent depth scale is on the upper. Conditions: $^1\text{H}^+$ ions normally incident, and γ -rays detected at a 0° angle to the beam with a Ge(Li) detector. (Reproduced, with permission, from Ref. 6. Copyright 1980, North-Holland Publishing Co.)

Literature Cited

1. Chu, W-K.; Mayer, J. W.; Nicolet, M.-A. "Backscattering Spectrometry"; Academic Press: New York, NY, 1978.
2. Mayer, J. W.; Rimini, E., Eds.; "Ion Beam Handbook for Materials Analysis"; Academic Press, New York, NY, 1977.
3. King, B., Ed.; "Proceedings of the 5th International Conference on Ion Beam Analysis" (Sydney, Australia, 16-20 February 1981); to be published in Nucl. Instrum. Methods.
4. Zeigler, J. F.; Lever, R. F.; Hirvonen, J. K. "Computer Analysis of Nuclear Backscattering," p. 163 in "Ion Beam Surface Layer Analysis," ed. by O. Meyer, G. Linker, and F. Kappeler; Plenum Press: New York, NY, 1976.
5. Gossett, C. R.; to be published in (3).
6. Gossett, C. R. Nucl. Instrum. Methods 1980, 168, 217.

RECEIVED April 5, 1982

Reprinted from ACS SYMPOSIUM SERIES, NO. 199
INDUSTRIAL APPLICATIONS OF SURFACE ANALYSIS
Lawrence A. Casper and Cedric J. Powell, Editors

Section I.B

SPUTTERING ANALYSIS WITH PIXE

J. M. Lambert and P. A. Treado¹
D. Trbojevic²
R. G. Allas and A. R. Knudson³
G. W. Reynolds and F. R. Vozzo⁴

¹Georgetown University
Washington, D. C.
and

Materials Modification and Analysis Branch
Condensed Matter and Radiation Sciences Division
Naval Research Laboratory

²Georgetown University
Washington, D. C.

³Materials Modification and Analysis Branch
Condensed Matter and Radiation Sciences Division
Naval Research Laboratory

⁴State University of New York
Albany, NY
and

Materials Modification and Analysis Branch
Condensed Matter and Radiation Sciences Division
Naval Research Laboratory

This work was supported by the Office of Naval Research.

SPUTTERING ANALYSIS WITH PIXE

J.M. Lambert and P.A. Treado
Georgetown University and Naval Research Laboratory
Washington, D.C. 20057 and 20375

D. Trbojevic
Georgetown University, Washington, D.C. 20057

R.G. Allas and A.R. Knudson
Naval Research Laboratory, Washington, D.C. 20375

G.W. Reynolds and F.R. Vozzo
SUNY, Albany and Naval Research Laboratory
Albany, NY 12222 and Washington, D.C. 20375

Summary

The applicability of the particle induced x-ray emission (PIXE) in the determination of sputtering distributions and yields was studied. Sputtered particles were caught on foils for the 45 keV to 125 keV self sputtering of Fe, Ni, Cu, Ti, Mo and Au and for the 90 keV sputtering of both target and implanted particles of Ni⁺ + Cu, Cu⁺ + Ni, Ni⁺ + Fe, and As⁺ + Ag, and for the target particles of Ar⁺ + Au.

Sputtered particles were collected in an ultra high vacuum (UHV) and in a poorer vacuum system with 99.99% pure Al catcher foils. PIXE data, the x-ray yields from 1 MeV proton and 2 MeV alpha particle beam bombardments, were used to determine the angular distribution of the sputtered products. The sputtering yield was calculated from the angular distribution data by integration over a hemisphere assuming azimuthal symmetry. The efficiency of the PIXE systems was calibrated with a standardized target such as 18 µg/cm² Fe on the same 99.99% Al foil material. The Al x-ray yield of the catcher foils provided a normalization of all data from a given catcher foil. For a number of samples studied, we have been able to compare the distribution and yields obtained with PIXE to those measured by the Rutherford backscattering (RBS) technique. Also separate RBS analysis of Xe markers in the sputtering targets provided yield values. Comparison of the PIXE and RBS results indicate that the PIXE sputtering distribution and yield measurements are comparable.

Introduction

Studies of sputtering yields and of the angular distribution of the sputtered products provide valuable information for the development of more sophisticated models of sputtering processes and for the proper modification of materials by ion implantation. Sputtering yields are one of the most important parameters controlling the surface behavior of the target during ion implantation; they limit the maximum atomic fraction attainable at the surface during an implant¹. It has been shown that measured self-ion sputtering yield values²⁻⁴ can be significantly different from those predicted by theory⁵. Also, measurements of specific yields can vary significantly from one to the other²⁻⁴.

The parameters affecting sputtering are many. 1) incident beam energy, 2) target environment vacuum, 3) target surface condition, cleanliness and smoothness, 4) incident beam intensity, 5) beam fluence, 6) target materials, i.e., single element, binary alloy, tertiary alloy, etc., 7) target-beam geometry, and 8) uniformity of beam current density on target. Measurement techniques for determining yields and angular distributions are many, also¹.

We used the PIXE analysis of the sputtered products caught on foils and compared the PIXE results to RBS data for the same foils and to RBS data which provided the depth of Xe marker profiles before and after bombardment of the target.

Our goal was to determine the circumstances for the applicability of PIXE analysis in the determination of sputtering distributions and yields. When the target environment vacuum is in the 10⁻⁸ Torr region, the sticking coefficient for many sputtered products on the Al catcher foils is approximately one, the PIXE x-ray energy is sufficient to keep the attenuation from the PIXE target to the x-ray detector minimal, the PIXE beam intensity monitoring and recording is accurate and the PIXE cross section for a given x-ray is sufficient to allow data accumulation in a relatively short time, then the PIXE analysis technique is relatively easy to use and provides excellent results.

Experimental Arrangements

To accomplish our measurements, it was necessary to bombard the target from which sputtering occurred with heavy ions and to bombard the catcher foils from which the PIXE data were obtained with light ions. Various accelerators were used at three laboratories: Physics Department, Georgetown University (GU); Materials Modification and Analysis Branch of the Naval Research Laboratory (NRL); and the Institute for Particle-Solid Interactions (IPSI) at the State University of New York at Albany (SUNYA). Table I lists the accelerators, locations and use in this investigation.

TABLE I

Accelerators Used in This Work

Accelerator	Normal Voltage	Location	Application
VandeGraaff	2MV	GU	PIXE
VandeGraaff	5MV	NRL	PIXE, RBS, Xe
Dynamitron	4MV	IPSI	RBS, Xe
Danphysik	150kV	IPSI	Implants 10 ⁻⁷ Torr, ≤ 3 µA
LEIM	150kV	NRL	Implants 2x10 ⁻⁹ Torr, ≤ 2 µA
Extrion	200kV	NRL	Implants 10 ⁻⁶ Torr, ≤ 20 µA

Sputtering Apparatus

The sputtering samples were either 1 mm slices cut from high purity polycrystalline rods of 12 mm to 20 mm diameter or were samples from 0.5 mm foils approximately 15 mm square. The samples were mechanically polished to a mirror finish. Each type of sample was implanted at either 1 or 1.5 MeV with Xe markers to a fluence of 1×10^{16} ions/cm², whenever the RBS technique could distinguish between Xe and the substrate species.

Figure 1 depicts the target assembly used to bombard a target and collect the sputtered products on a portion of the catcher foil in the UHV condition. A system similar to that depicted in Fig. 1 was used with a poorer vacuum for high dose bombardments. In each system, the incident beam was normal to the target surface and the catcher foil formed a portion of a 3 cm radius circle centered on the center of the beam spot on the target. The angular region covered by the catcher foil extended from 6° to 90° with respect to the incident beam direction. The assembly connected to either of the "high-dose" implanters listed in Table I, i.e., the chamber, aperture and cold can/target suppressor assembly, has been previously described². For each target assembly, the incident beam was raster scanned across a 3 mm x 5 mm aperture. It should be noted that for some of the sputtering experiments, the optical emission from the sputtered neutral atoms was monitored to confirm that the sputtering yield was not changing with increased fluence during the bombardment³.

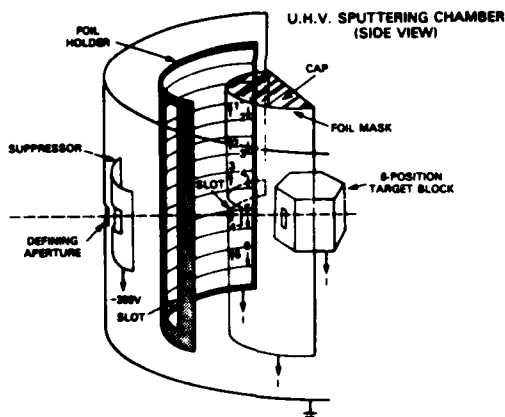


Fig. 1. Target and catcher foil assembly for UHV system

PIXE Analysis Apparatus

A 1 MeV proton beam and a 2 MeV alpha-particle beam from the GU and NRL accelerators, as listed in Table I, were used to provide the PIXE data.

The catcher foil target and PIXE beam and x-ray detector system, although slightly different for the two PIXE beams, are illustrated in Fig. 2, as a composite schematic. For the 1 MeV proton and 2 MeV alpha beams the solid angles subtended by the detectors were approximately 6 msr and 40 msr, respectively. In each case the x-ray detector was a LN₂ - cooled Si(Li) with 0.02 in. Be window. The

exit window from the target-vacuum was 5×10^{-4} in. mylar and the air gap was minimal, about 0.5 inch. For each system standard PIXE electronics provide signals to a data accumulation and analysis system, TN-1710 for the proton PIXE and SEL-840 for the alpha particle PIXE work, respectively. In each case, the data accumulation and analysis system included the capability of peak searching, background subtraction and peak fitting.

Each PIXE target could have a specific angular region of the catcher foil placed in the incident PIXE beam. Thus, data could be obtained as a function of the angle of emission of the sputtered ions with respect to the heavy ion beam. Post-irradiation PIXE beam positions were determined by the "vapor" technique. No data were accepted unless the incident PIXE beam was centered on the portion of the catcher foil which had been exposed during the implantation of the incident sputtering beam. Thus, the relative density of the sputtered atoms adhering to the Al catcher foil was measured by the x-ray yield from the species of interest.

Ancillary Apparatus

RBS measurements of the shift of Xe marker position and sputtered product density on the catcher foils were obtained. For the Xe marker data, the facilities at the NRL and the IPSI-SUNYA were used. The RBS data for each target, from which the Xe and substrate RBS signal could be spectrally separated, were taken from both the sputtered and the unsputtered regions of the target, i.e., the post-and prior-irradiation regions. The RBS data were then analyzed in a standard manner^{2,3}. The stopping powers, as given by Ziegler⁶ for ⁴He⁺, were used to convert the energy shift of the Xe peak to the number of atoms per cm² removed from (or added to) the target from which sputtering occurred.

PIXE Data Angular Distribution

The catcher foil with the sputtered products was placed in the charged particle beam such that a region of approximately 1.5 mm by 3.0 mm was struck by the light ion beam. The beam intensity was a few nA to a few hundred nA. Counting rates including the bremsstrahlung and the Al x-ray intensity, were kept to less than 20,000 cps. The x-ray spectrum for each spot on the foil was recorded and both straight-line background subtraction and resultant-peak fitting were accomplished. The data from a minimum of 6 spots and maximum of 18 spots on the foil provided the angular distribution data. A typical 1 MeV proton induced spectrum is shown in Fig. 3. Typical angular distribution data are depicted in Fig. 4a and 4b. To obtain the angular distribution of the sputtered products on a given foil, no knowledge of the thickness of the elemental product of interest is required for any spot on the foil; all data are normalized to that for the 6° position of the foil. Consequently, one of the major problems of elemental analysis by the PIXE technique is bypassed. However, the problem associated with secondary electron suppression, target charging and build up of unwanted species on the target could cause systematic errors. By using the Al K x-ray line in each spectrum to normalize the angular distribution measurements, and by passing pulses corresponding to an energy greater than the spectral structure of interest from a pulser through the total electronic system, system dead times are taken into account.

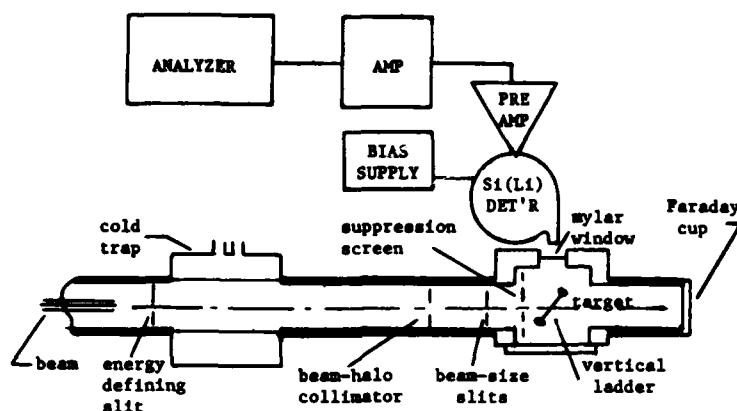


Fig. 2. Composite illustration of the catcher-foil target, PIXE beam collimation, and x-ray detection systems.

A thin $18 \mu\text{g}/\text{cm}^2$ layer of Fe on the 99.99% Al foil material provided an absolute standard target for determining system-reproducibility and for a specific PIXE cross section determination. Comparison of the measured cross section to tabulated values^{7,8}, provided a check of the solid angle subtended by the Si(Li) detectors and the ability to use the tabulated cross section values for other elements.

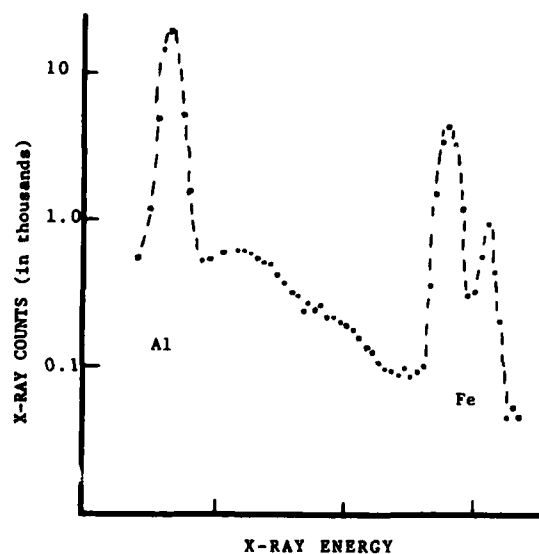
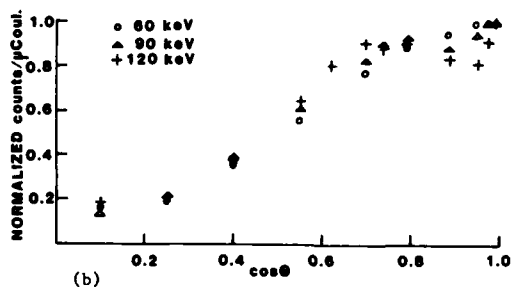
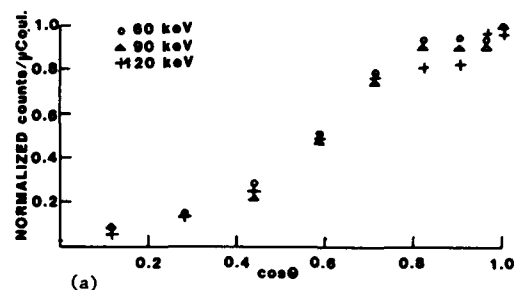


Fig. 3. Typical 1 MeV proton induced x-ray data. Al and Fe (alpha and beta) lines with bremsstrahlung structure.



Figs. 4a and 4b. PIXE determined angular distribution of sputtered product, (a) copper beam incident on copper and (b) nickel beam incident on nickel.

Sputtering Yields

The sputtering yield for a given implant target species is defined as $Y = N_s/N_i$ where N_s is the number of atoms removed from the implanted surface and N_i is the number of ions incident on the implant target. The number of atoms removed from the surface by sputtering is measured by catching a portion of the removed atoms on a foil and determining how many atoms are caught. Because of the geometry of the catcher foil - implant target arrangement, the catcher foil forms a cylindrical slice of a spheri-

cal surface around the target and the number of particles per unit area on the catcher foil is proportional to the number of x-rays emitted per unit solid angle from the species caught on the catcher foil.

Thus, the angular distribution of the sputtered particles caught on the catcher foil provides the sputtering yield by integration of the measured distribution over a hemisphere. Because our sputtered products come from normal incidence of the impinging implant beam on polycrystalline targets, azimuthal symmetry is assumed for integration over the hemisphere. Linear positions on the catcher foil, measured from the anti-implant-beam direction, are linearly proportional to the spherical angle, θ . We assume that the sticking coefficient for the sputtered products on the catcher foil is 1 for the UHV environment used.

With these assumptions, the quantity of interest is the number of sputtered-species particles per unit area on the catcher foil and not the depth distributions of the sputtered layer on the catcher foil. It should be pointed out that this amounts to the assumption that the atoms on the catcher foil form a "thin" PIXE target, i.e., that the thickness is no more than a few monolayers. Then we can investigate the areal density rather than the volume density and the number of x-rays in the K_α line N_x can be expressed as

$$N_x = \frac{Q_x}{Ze} N_a \sigma_x \frac{\Delta\Omega_x}{4\pi} \frac{1}{\cos \phi} K$$

where Q_x/Ze is the number of PIXE incident particles, Q_x is the accumulated PIXE beam charge, N_a is the areal density of particles on the catcher foil at the bombarded position, σ_x is the appropriate charged particle x-ray cross section for either 1 MeV protons⁷ or 2 MeV alphas^{7,8}, $\Delta\Omega_x$ is the solid angle subtended by the x-ray detector, ϕ is the angle between the PIXE beam and the normal to the catcher foil target, and K is the correction factor for absorption by the windows and air gap.

The x-rays are produced in an area, dA_x , on the catcher foil; thus, $N_a dA_x$ is the number of particles per unit solid angle on the catcher foil with respect to the implant beam causing the sputtering. If the foil is at a uniform distance R_s from the implant target, then dA_x subtends a solid angle dA_x/R_s^2 , and the number of ions emitted per unit solid from the sputtered target are,

$$N_\Omega(\theta) = (N_a dA_x)/dA_x/R_s^2 = N_a R_s^2.$$

It should be noted that $N_\Omega(\theta) \neq f(dA_x)$. Then, the total number of ions sputtered from the target is

$$N_s = \int N_\Omega(\theta) d\Omega = 2\pi N_\Omega(0) I,$$

where

$$I = \int_0^{\pi/2} f(\theta) \sin \theta d\theta,$$

and $f(\theta)$ is the angular distribution function normalized so the $f(0) = 1$, Fig. 5. For example, $f(\theta) = \cos^n \theta$ gives $I = 1/(n+1)$. From our results, $0.2 < I < 0.6$.

The sputtering yield, $Y = N_s/N_i$, with the proper constants, is

$$Y = 2027 \frac{N_x(0) R_s^2 I \cos \phi}{Q_x(0) Q_i \sigma_x \Delta\Omega_x} K$$

where $N_x(0)$ is the number of K_α x-rays at $\theta = 0$, $Q_x(0)$ is the μC of PIXE beam charge producing

$N_x(0)$, R_s is the radial distance from the implant target to the catcher foil in cm, Q_i is μC of implant beam charge, σ_x is in barns, $\Delta\Omega_x$ is in msr, and k is the x-ray attenuation factor.

Although reasonably good results have been obtained by using an appropriate $\Delta\Omega_i$ associated with each measured point, a computer program which fits the experimental points to an eighth order polynomial, with even terms only, in θ , and calculates the integral for $f(\theta)$ over θ was used to obtain I . It should be noted that the non-computer method provided results within $\pm 15\%$ of the computer generated results for I . A polynomial in $\cos \theta$, again with even order terms, provided results for I with standard deviations larger than that for the polynomial fit with θ .

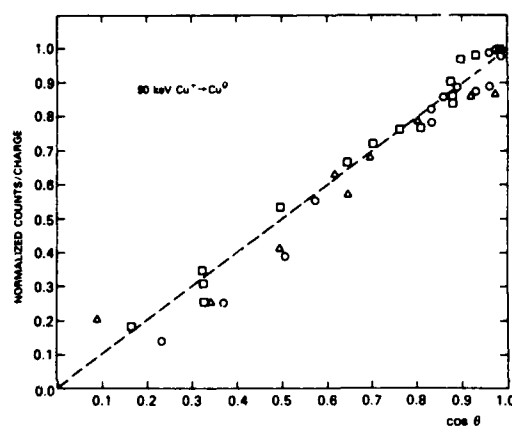


Fig. 5. Data from 90 keV Cu^+ on Cu, i.e. self sputtering, with dashed curve showing the $n = 1$, $f(\theta) = \cos \theta$, distribution.

Results

The data for the angular distribution of sputtered products were quite consistent with RBS measurements and provided reasonably smooth curves with $\cos^n \theta$ shapes where $0.8 \leq n \leq 4.0$. Thus, the PIXE data for angular distributions were quite acceptable. For some of the elemental species of interest, particularly when the PIXE cross section was small or the energy of the x-ray spectral structure was in the region of the bremsstrahlung, the uncertainties of the PIXE data were significantly larger than that of the RBS data. Elements such as Ag, Ti and As were difficult to work with, because the x-ray structure on the bremsstrahlung and/or the effective sticking coefficient was less than 1. The yield determinations, as described above and based on the PIXE angular distribution data, are as good as those obtained with RBS angular distribution data or RBS measurements of Xe markers in the implant samples. Table II lists the results of the distribution and yield determinations we have obtained. Clearly, PIXE measurements are applicable to sputtering angular distributions and yields determination.

TABLE II
Results of a Number of Sputtering Distribution
and Yield Measurements

Sputtered Element	Implant Beam Species (Target) and Energy in keV	Implant Condition	Distribution n of $\cos^2\theta$	Sputtering Yield (Y)	Measurement Technique (Place), Beam Particle and Energy in MeV
Ti	Ti(Ti), 125	hi-I, lo-V	2.0 ¹	0.09 \pm 0.07 ²	PIXE (GU) p,1
		hi-I, lo-V	---	0.2 \pm 0.15	RBS-Xe (NRL) α ,3
		hi-I, lo-V	---	0.3 \pm 0.2	RBS-Xe (NRL) α ,3
Fe	Fe(Fe), 60	UHV	1.0	4.4 \pm 0.9	PIXE (NRL) α ,2
		UHV	---	3.5 \pm 0.7	RBS-Xe (NRL) α ,3
		hi-I, lo-V	---	1.8 \pm 0.4	RBS-Xe (NRL) α ,3
	Fe(Fe), 90	UHV	1.3	3.5 \pm 0.7	PIXE (NRL) α ,2
		hi-I, lo-V	---	2.1 \pm 0.4	RBS-Xe (NRL) α ,3
	Fe(Fe), 120	UHV	1.3	2.7 \pm 0.6	PIXE (NRL) α ,2
		UHV	---	2.7 \pm 0.6	RBS-Xe (NRL) α ,3
Fe	Ni(Fe), 90	hi-I, lo-V	2.6 ¹	3.5 \pm 0.7	PIXE (NRL) α ,2
		hi-I, lo-V	2.7 ²	3.7 \pm 0.7	PIXE (NRL) α ,2
		UHV	1.0	2.8 \pm 0.6	PIXE (GU) p,1
Ni	Ni(Ni), 90	UHV	---	3.6 \pm 0.7	RBS-Xe (SUNYA) α ,3
		UHV	1.1	3.2 \pm 0.7	PIXE (GU) p,1
	Ni(Ni), 120	UHV	1.4	2.6 \pm 0.6	RBS-foil (NRL) α ,3
		UHV	---	3.4 \pm 0.7	RBS-Xe (SUNYA) α ,3
		UHV	---	3.4 \pm 0.7	RBS-Xe (SUNYA) α ,3
Ni	Cu(Ni), 90	UHV	1.2 ¹	2.3 \pm 0.5	PIXE (NRL) α ,2
		UHV	1.4 ¹	2.6 \pm 0.5	PIXE (GU) p,1
		UHV	1.2 ¹	2.7 \pm 0.5	PIXE (NRL) α ,2
		UHV	1.1 ²	2.7 \pm 0.5	PIXE (GU) p,1
		UHV	1.2 ²	2.7 \pm 0.5	PIXE (NRL) α ,2
		UHV	1.3 ²	2.5 \pm 0.5	PIXE (GU) p,1
		UHV	1.1 ²	2.1 \pm 0.5	PIXE (NRL) α ,2
		UHV	1.1 ²	2.1 \pm 0.5	PIXE (NRL) α ,2
Ni	Ni(Cu), 90	UHV	1.6 ²	0.6 \pm 0.2	PIXE (GU) p,1
		UHV	1.4 ²	0.5 \pm 0.2	PIXE (NRL) α ,2
Ni	Ni(Fe), 90	UHV	3.9 ¹	0.9 \pm 0.2	PIXE (NRL) α ,2
		UHV	5.0 ²	1.1 \pm 0.2	PIXE (NRL) α ,2
Cu	Cu(Cu), 60	UHV	0.9	4.1 \pm 0.8	PIXE (GU) p,1
		UHV	---	4.2 \pm 0.8	RBS-Xe (SUNYA) α ,3
	Cu(Cu), 90	UHV	1.0	4.2 \pm 0.8	PIXE (GU) p,1
		UHV	---	4.0 \pm 0.8	RBS-Xe (NRL) α ,3
		UHV	1.5	4.8 \pm 1.0	RBS-foil (NRL) α ,3
	Cu(Cu), 120	UHV	1.0	4.0 \pm 0.8	PIXE (GU) p,1
		UHV	---	4.2 \pm 0.8	RBS-Xe (SUNYA) α ,3
Cu	Ni(Cu), 90	UHV	1.2 ¹	2.1 \pm 0.4	PIXE (NRL) α ,2
		UHV	2.0 ¹	2.4 \pm 0.5	PIXE (GU) p,1
		UHV	1.2 ¹	2.3 \pm 0.5	RBS-foil (NRL) α ,3
		UHV	1.2 ²	2.4 \pm 0.5	PIXE (NRL) α ,2
		UHV	1.0 ²	2.8 \pm 0.6	PIXE (GU) p,1
		UHV	1.3 ²	2.5 \pm 0.5	RBS-foil (NRL) α ,3
Cu	Cu(Ni), 90	UHV	0.8 ²	0.6 \pm 0.3	PIXE (GU) p,1
Ag	As(Ag), 45	hi-I, lo-V	---	---	PIXE not applicable as Ag K x-ray on top of bremsstrahlung
	As(Ag), 90	hi-I, lo-V	---	---	PIXE not applicable as Ag K x-ray on top of bremsstrahlung
As	As(Ag), 45	hi-I, lo-V	---	---	PIXE applicable but not useful for these foils; too little As on foils.
Mo	Mo(Mo), 90	UHV	2.3 ¹	2.5 \pm 0.9 ²	PIXE (GU) p,1
		hi-I, lo-V	2.3 ¹	1.2 \pm 0.6 ²	PIXE (GU) p,1
Au	Au(Au), 90	hi-I, lo-V	1.3	29 \pm 5 ⁵	PIXE (GU) p,1
		hi-I, lo-V	2.0	34 \pm 4	RBS-foil (SUNY) α ,3

TABLE II - Cont.

Sputtered Species	Species Beam Species (Target) and Energy in keV	Implant Condition	Distribution n of $\cos^2\theta$	Sputtering Yield (Y)	Measurement Technique (Place, Beam Particle and Energy in MeV)
Au	Au(Au), 120	hi-I, lo-V	1.4	51 \pm 8 ⁵	PIXE (GU) p,1
		hl-I, lo-V	1.8	54 \pm 6	RBS-foil (SUNYA) α ,3
Au	Ar(Au), 90	hi-I, lo-V	2	5.8 \pm 1.0 ⁵	PIXE (GU) p,1

1. Preliminary value, assumed.
2. Preliminary values based on low angle (6°, 12°) data.
3. Sputtered particles caught from initiation of implant to steady state sputtering.
4. Sputtered particles caught after steady state sputtering reached.
5. Au L x-ray measured; cross section from ref. 9.

References

1. J.K. Hirvonen, (ed), Treatise on Materials Science and Technology, (Academic Press, New York, 1980).
2. G.W. Reynolds, A.R. Knudson and C.R. Gossett, Nucl. Instr. and Meth. 182/183, (1981) 197.
3. R.G. Allas, A.R. Knudson, J.M. Lambert, P.A. Treado and G.W. Reynolds, Nucl. Instr. and Meth. 194, (1982) 615.
4. H.H. Anderson and H.L. Bay, Sputtering by Ion Bombardment, (R. Behrisch, ed., Springer-Verlag, Berlin, 1980).
5. P. Sigmund, Sputtering by Ion Bombardment, (R. Behrisch, ed., Springer-Verlag, Berlin, 1980).
6. J.F. Ziegler, (ed.), Helium: Stopping Powers and Ranges in All Elemental Matter, (Pergamon Press, New York, 1977).
7. R.K. Gardner and Tom J. Gray, Atomic Data and Nuclear Data Tables 21, (1978) 515.
8. C.G. Soares, R.D. Lear, J.T. Sanders and H.A. Van Rinsvelt, Phys. Rev. A13, (1976) 953.
9. S. Shafroth, et al., Phys. Rev. A7, (1973) 566.

Section I.C

THE SURFACE BEHAVIOR OF A BINARY ALLOY
DURING PRODUCTION BY ION IMPLANTATION

G. W. Reynolds and F. R. Vozzo¹
R. G. Allas and A. R. Knudson²
J. M. Lambert and P. A. Treado³

¹State University of New York
Albany, NY

and

Materials Modification and Analysis Branch
Condensed Matter and Radiation Sciences Division
Naval Research Laboratory

²Materials Modification and Analysis Branch
Condensed Matter and Radiation Sciences Division
Naval Research Laboratory

³Georgetown University
Washington, D. C.

and

Materials Modification and Analysis Branch
Condensed Matter and Radiation Sciences Division
Naval Research Laboratory

This work was supported by the Office of Naval Research.

THE SURFACE BEHAVIOR OF A BINARY ALLOY DURING PRODUCTION BY ION IMPLANTATION

G. W. Reynolds and F. R. Vozzo
State University of New York at Albany and NRL

R. G. Allas and A. R. Knudson
Naval Research Laboratory, Washington, DC

J. M. Lambert and P. A. Treado
Georgetown University, Washington, DC and NRL

ABSTRACT

Thin surface copper-nickel alloys were prepared by ion implantation at 90 keV. During the implantation of one pure element by the other the sputtered products were collected on catcher foils at different stages from the beginning of the implant through to the steady state configuration of the target surface. The collector foils and targets were analyzed to determine the behavior of the sputtering yields during implantation and for the change in surface composition at the selected fluence. The total sputtering yield for the target and the effective elemental sputtering yields for each component appear to be functions of the changing surface fractions, the self ion sputtering yield of the implanted species, and the elemental sputtering yield of the initial target species. A model relating these parameters is presented.

1. INTRODUCTION

The development of techniques for the production of modified alloy structures by ion implantation is currently an expanding endeavor [1]. Current theoretical discussions and reviews of the sputtering process do not consider the changing surface fractions in the large fluence regime as an important factor affecting the overall sputtering behavior of the target material [2-9]. Recent experiments [10] where the alloy surface was optically monitored during implantation indicate that the changing surface fractions as the implantation approaches steady state are significant in describing the behavior of the ion implanted surface. The experiments presented in this paper are an attempt to verify this significance and to present a first order model which may be extended to describe the surface during ion implantation.

2. THE EXPERIMENT

Thin surface alloys of copper and nickel were prepared by implanting 90-keV copper ions into nickel targets or by implanting 90-keV nickel ions into copper. The fluence for each sample was calculated using the model presented in this paper. The fluence so calculated was used to modify the surface of the target in a particular manner. Table 1 incorporates the predicted surface composition for the specified fluence as well as the experimental results for that particular sample.

The implantation of the targets was performed in a UHV chamber at a vacuum of about 2×10^{-9} torr. The target assembly and associated collector foil

holder have been described in a previous paper [11]. During these experiments six targets were mounted on the holder and sequentially placed perpendicular to the beam axis for implantation. One target was the pure beam elemental material and was implanted to provide a reference signal for the optical monitoring apparatus. The other five targets were the pure elemental material in which the alloy was to be prepared. Five collector foils were arranged on the holder to collect the sputtered products from the surfaces at predicted atomic surface fractions for the beam species. The selected surface fractions represent various steps in the implantation process from the initial stage to the steady state surface configuration.

Subsequently the collector foils and the implanted targets were analyzed using particle induced x-ray emission (PIXE) and Rutherford backscattering (RBS). The collector foils were analyzed to obtain the angular distribution of the sputtered material collected for each element. This information was used to derive partial sputtering yields at different phases of the implantation process. The targets also were examined in the sputtered area for the atomic surface fractions by PIXE.

3. MODEL

The model presented here has been developed to include the effect of the implanted species as it appears in the surface during the implantation process, since the large fluences implanted in ion beam material modification require that the implanted beam species be a significant fraction of the surface composition. Many descriptions of the alloy sputtering process are valid only in the low fluence regime where the ratio of implanted species to the initial target species at the surface is very small. The present model relates the changing surface fractions of the alloy components to the total sputtering yield for the target surface and the partial sputtering yields of each of the alloy components.

At any time during the implantation process, the total sputtering yield, S_{tot} , for the target may be written

$$S_{tot} = \sum_i s_i \quad (1)$$

where s_i is the partial sputtering yield for the i th elemental component in the target surface. Each partial sputtering yield can be expressed as the sum of two terms, the first of which is a function of the surface atomic fraction, n_i , the elemental sputtering yield, $S(1)_i$, and a surface binding energy correction factor, f_i . This term is the familiar expression for the partial sputtering yield. The second term is a function of all of the surface fractions and represents the interaction of all the surface components to bring about the probable ejection of a particular atom from the surface. The partial sputtering yield for the i th component is given by:

$$s_i = [f_i n_i S(1)_i + n_i \sum_j f_j n_j S(1)_j] / 2 \quad (2)$$

where the summation over j includes all the surface components and the factor of 2 is an empirical normalization constant. Substitution of equation (2) into (1) yields

$$S_{tot} = \sum_i f_i n_i S(1)_i \quad (3)$$

$S(1)_i$, the elemental sputtering yield may be measured, or estimated from the Sigmund theory [2]. The factor f_i is given by the elemental surface binding energy, $U(o)$, divided by the instantaneous average binding energy, $U(ave)$, for that element in the surface,

$$r_1 = (U_0/U_{avg})_1 \quad (4)$$

effectively substituting the instantaneous average surface binding energy into the sputtering yield equation for that particular component. The behavior of the average surface binding energy as a function of fluence (i.e., changing surface fractions) is left for discussion in a subsequent paper, since in this discussion we assume that all f_i equal one during the implantation. This assumption appears reasonable as both copper and nickel have the same basic crystallographic system (fcc) and the individual atoms of both elements are nearly of the same size. Recent experimental measurements [11] of the self-ion sputtering yields exhibit small differences and the same small differences (about 20%) are exhibited in the respective binding energies of these elements [12,13].

In this experiment, using the assumptions indicated above, the partial sputtering yields for the implanted element, (1), and the initial target element, (2), (assuming $f_1 = f_2 = 1$) become

$$s_1 = \frac{n_1 S(1)_1 + n_1 (n_1 S(1)_1 + n_2 S(1)_2)}{2} \quad (5)$$

and

$$s_2 = \frac{n_2 S(1)_2 + n_2 (n_1 S(1)_1 + n_2 S(1)_2)}{2} \quad (6)$$

In particular at the beginning of the implantation $n_1 = 0$, $n_2 = 1.0$, $s_1 = 0$, and

$$S_{tot} = \frac{n_2 S(1)_2 + n_2^2 S(1)_2}{2} = S(1)_2 \quad (7)$$

At steady state (defined as the condition where beam species atoms are sputtered from the target surface at the same rate as they are being implanted into the target) s_1 equals 1 and equation (5) becomes

$$1 = \frac{n_1 ((1 + n_1) S(1)_1 + (1 - n_1) S(1)_2)}{2} \quad (8)$$

Since the elemental sputtering yields may be measured or calculated from theory, equation (8) can be solved for the surface fraction of the implanted species at the steady state condition, thus predicting the final surface composition. By using this solution the partial sputtering yield for the initial target element may be calculated which then determines the total sputtering yield for the surface at steady state conditions.

4. RESULTS

Tables 1 and 2 summarize the analyses of the collector foils and targets and present the predictions for the fluences based on the model presented. Figure 1 illustrates the normalized angular distributions of the sputtered products collected on a typical foil. Of particular note is the close similarity for both the copper atoms collected and the nickel atoms collected. This similarity suggests that the angular distribution of the sputtered materials is independent of species from a uniform surface matrix.

TABLE 1.
Calculated and Experimental Results for 90-keV Nickel Ions Implanted into Copper

1a. Steady-State Parameters Determined by Model ($s_1 = 1$)

	Theoretical	Experimental
S(1) Ni	6.45	$3.4 \pm .7$ Ref. (11)
S(1) Cu	7.37	$2.2 \pm .6^*$
n_1	.146	.33
n_2	.854	.67
s_2	6.24	1.7
S_{tot}	7.24	2.7
		*determined from lowest fluence foil

1b. Atomic Surface Fraction vs. Fluence

Foil Number	Fluence ions/cm ²	Model Calculations		Experimental		Experimental	
		Theoretical S(1)		Experimental S(1)		Foil Measurement	
		n_1	n_2	n_1	n_2	n_1^\dagger	n_2
1	1.2×10^{16}	.025	.975	.019	.981	.02	.98
2	4.2×10^{16}	.087	.913	.065	.935	.03	.97
3	6.8×10^{16}	.146	.854	.11	.89	.08	.92
4	1.1×10^{17}	.146	.854	.17	.83	.11	.89
5	1.5×10^{17}	.146	.854	.23	.77	.12	.88

1c. Partial and Total Sputtering Yields vs. Fluence

Foil Number	Fluence ions/cm ²	Model Calculations			Experimental			Experimental		
		Theoretical S(1)			Experimental S(1)			Foil Measurement		
		s_1	s_2	S_{tot}	s_1	s_2	S_{tot}	s_1^\dagger	s_2	S_{tot}
1	1.2×10^{16}	.17	7.17	7.34	.06	2.36	2.42	---	2.2	2.2
2	4.2×10^{16}	.66	6.68	7.34	.19	2.27	2.47	.14	2.6	2.74
3	6.8×10^{16}	1.0	6.24	7.24	.33	2.18	2.51	.21	2.4	2.61
4	1.1×10^{17}	1.0	6.24	7.24	.51	2.06	2.57	.25	2.3	2.55
5	1.5×10^{17}	1.0	6.24	7.24	.69	1.91	2.60	.32	2.3	2.62

† Relative error 30%

TABLE 2.
Calculated and Experimental Results for 90 keV Copper Ions Implanted into Nickel

2a. Steady-State Parameters Determined by Model ($s_1 = 1$)		
	Theoretical	Experimental
S(1) Cu	8.44	4.2 ± .8 Ref. (11)
S(1) Ni	7.11	2.8 ± .6*
n_1	.127	.27
n_2	.873	.73
s_2	6.28	2.2
S_{tot}	7.29	3.2
		*determined from lowest fluence foil

2b. Atomic Surface Fraction vs. Fluence

Foil Number	Fluence ions/cm ²	Model Calculations				Experimental	
		Theoretical S(1)		Experimental S(1)		Foil Measurement	
		n_1	n_2	n_1	n_2	n_1^\dagger	n_2
1	2.0 x 10 ¹⁶	.040	.960	.035	.965	.06	.94
2	4.7 x 10 ¹⁶	.094	.906	.082	.918	.06	.94
3	6.2 x 10 ¹⁶	.127	.873	.12	.88	.16	.84
4	8.2 x 10 ¹⁶	.127	.873	.15	.85	.18	.82
5	1.3 x 10 ¹⁷	.127	.873	.23	.77	.21	.79

2c. Partial and Total Sputtering Yields vs. Fluence

Foil Number	Fluence ions/cm ²	Model Calculations						Experimental		
		Theoretical S(1)			Experimental S(1)			Foil Measurement		
		s_1	s_2	S_{tot}	s_1	s_2	S_{tot}	s_1^\dagger	s_2	S_{tot}
1	2.0 x 10 ¹⁶	.31	6.85	7.16	.2	2.7	2.9	---	2.8	2.8
2	4.7 x 10 ¹⁶	.74	6.50	7.24	.3	2.6	2.9	.14	2.7	2.8
3	6.2 x 10 ¹⁶	1.0	6.28	7.28	.4	2.6	3.0	.4	2.4	2.8
4	8.2 x 10 ¹⁶	1.0	6.28	7.28	.6	2.5	3.1	.5	2.6	3.1
5	1.3 x 10 ¹⁷	1.0	6.28	7.28	.8	2.4	3.2	.7	2.2	2.9

†Relative error 30%

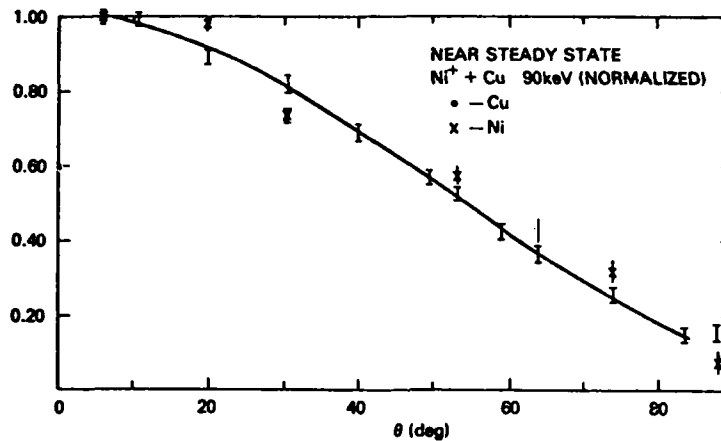


Figure 1. Angular distribution of sputtered products on collector foils.

In the literature the reciprocal of the elemental sputtering yield for the implanted species will be the atomic surface fraction at the steady-state condition [1], whereas this model predicts the surface fraction to be somewhat different at this same condition unless all of the elemental sputtering yields are equal. The atomic surface fractions for the implanted element, as predicted using the recently measured elemental sputtering yields for these elements, are naturally larger than the values obtained using the theoretical yields calculated after Sigmund [2], because the measured values are much less than those predicted by theory.

The atomic surface fractions as measured from the copper to nickel ratios on the collector foils tend to support the previous measurements of the elemental sputtering yields. The measured surface fractions and the partial sputtering yields as determined from the experiment indicate that the authors did not reach the steady-state condition for the implanted species in either experiment, although it was nearly reached for the copper-implanted-into-nickel case. In the nickel-implanted-into-copper case, it appears that the implantation is approaching half the steady state condition. This behavior suggests that as nickel appears at the surface of the implanted target, the nickel atoms strongly affect the average surface binding energy invalidating the assumption that it remain constant for this experiment. From the copper implanted into nickel results, it appears that as small amounts of copper appear in the surface of the nickel, the average surface binding energy is not affected as significantly.

5. SUMMARY

A preliminary model has been presented to describe the behavior of the surface of an elemental target during implantation by an additional atomic species. The copper-nickel alloy system was selected to test the model. The experimental results indicate:

1. that the elemental sputtering yields for polycrystalline metallic target materials are significantly lower than theory would predict;
2. that to first order the model predicts the results well for the copper implanted into nickel and only indicates the trend for the nickel implanted into copper case suggesting a strong interaction at the surface in the latter case;
3. that the angular distribution for the sputtered atoms from an alloy target appears to be independent of species and atomic surface fractions.

Additional target surface analysis measurement techniques are necessary to supplement the information derived from the collector foil measurements. The model presented here is a first order attempt to describe the surface during implantation including the effects of the implanted species. The authors plan to continue efforts to improve the model adding surface dependent factors such as surface binding energy changes due to the changing surface.

6. BIBLIOGRAPHY

1. J. K. Hirvonen (ed.), Treatise on Materials Science and Technology, (Academic Press, New York, 1980).
2. P. Sigmund, "Theoretical Concepts," chapter 2 of Sputtering by Ion Bombardment, R. Behrisch, ed., (Springer, 1981).
3. P. K. Haff, Caltech Preprint BAP-7 (1976).
4. P. K. Haff, Appl. Phys. Lett. 31(4), 259 (1977).
5. P. Sigmund, J. Vac. Sci. Technol. 17(1), 396 (1980).
6. P. K. Haff and Z. E. Switowski, Appl. Phys. Lett. 29(9), 549 (1976).
7. H. H. Andersen, "Sputtering of Multicomponent Metals and Semiconductors," SPIG 1980, M. Matini ed., (Boris Kidric Institute of Nuclear Sciences, Yugoslavia), pp. 421-83.
8. R. Kelly, Nucl. Instrum. Methods, 149, 553 (1978).
9. R. Collins, Radiat. Eff., 37, 19 (1979).
10. G. W. Reynolds, A. R. Knudson, and C. R. Gossett, Nucl. Instrum. Methods 181/183, 179 (1981).
11. R. G. Allas, A. R. Knudson, J. M. Lambert, P. A. Treado, and G. W. Reynolds, in Proc. 9th Int. Conf. on Atomic Collisions in Solids, Lyon (1981) (in press).
12. K. A. Gschneider, Solid State Phys. 16, 275 (1964).
13. D. P. Jackson, Radiat. Eff. 18, (1973) 185.

Section I.D

COMPUTER STUDY OF SELF-SPUTTERING OF Cu AND Ni AT 90 keV

M. Rosen, G. P. Mueller and W. A. Fraser

Radiation-Matter Interactions Branch
Condensed Matter and Radiation Sciences Division
Naval Research Laboratory

This work was supported by the Office of Naval Research.

COMPUTER STUDY OF SELF-SPUTTERING OF Cu and Ni AT 90 keV

M. ROSEN, G.P. MUELLER and W.A. FRASER

Naval Research Laboratory, Washington, DC 20375, USA

The self-sputtering of 90 keV Cu (Ni) ions incident on polycrystalline Cu (Ni) targets has been studied using the code MARLOWE. Experimental values of the sputtering yields and the angular distribution of sputtered atoms are reproduced with the Molière potential using the screening length of Torrens and Robinson. Particular attention is paid to those subcascades which have sputtered atoms as their end products. The distribution of the depths at which these subcascades are initiated is presented, together with the distribution of the frequency and length of replacement sequences they contain. A comparison is made of self-sputtering from amorphous and polycrystalline targets at this energy.

1. Introduction

Experimental results have recently been reported for the self-sputtering of high energy Cu and Ni ions from polycrystalline targets [1]. Sputtering yields and sputtered atom angular distributions were measured at several energies. We have examined the 90 keV data using the binary collision cascade simulation code MARLOWE [2-4]. We discuss this calculation in sect. 2 and examine the structure of the sputtering cascades (those subcascades which end with sputtered atoms) in greater detail in sect. 3. In sect. 4 we present the results of repeating the calculation with amorphous targets and discuss the significant differences found.

2. Self-sputtering yields and angular distributions

The computational model used by the code MARLOWE for sputtering calculations is amply described in ref. 3, 4. In order to keep computation time from becoming prohibitively large, we used targets of finite thickness. We found that bulk values for the sputtering yield were obtained (within calculational error) for a target width of 11 lattice constants. This was the thickness used in the calculation. This is a much larger value than that reported by Hou and Robinson [3,4] (~ 2 lattice spacings for heavy ion sputtering from a heavy target), and is a result of the fact that our incident energy is two orders of magnitude larger than theirs. For both Cu and Ni we took the

energy cut-off (the energy below which atoms are not followed) and the minimum displacement energy (the minimum energy transfer needed to set a lattice atom in motion) to be 5 eV. All calculations were done with the surface binding energy E_s set to zero. An auxiliary code was used to impose a planar surface binding energy condition on all atoms that had escaped the surface. In this way the sputtering yield and angular distributions could be determined as a function of E_s , without repeating the MARLOWE calculations. The self-sputtering yields for 90 keV Cu and Ni from polycrystalline targets measured by Allas et al. [1] ran from 4.0 to 4.8 and 2.8 to 3.9, respectively, with quoted errors of 20%. We have calculated Cu and Ni yields of 5.2 ± 0.6 and 4.1 ± 0.5 , in agreement with the experimental values, using surface binding energies of 5.0 eV and 6.0 eV, respectively. Both these energies are about 0.5 eV greater than the average of surface binding energies calculated by Jackson [6], but considering the general uncertainties in the knowledge of surface energies (see ref. 5) and the size of the experimental errors, they are not unreasonable.

The results of a calculation using the sputtering theory of Sigmund [7] were also presented in ref. 1. They calculated yields approximately twice the measured values. Sigmund uses a power-law approximation to the elastic scattering cross section for a Thomas-Fermi atomic interaction while we used the Molière potential, but with the smaller screening radius suggested by Torrens and Robinson (0.0738 Å) [2]. A Molière potential that approximates the Thomas-Fermi potential, at least

0167-5087/83/0000-0000/\$03.00 © 1983 N

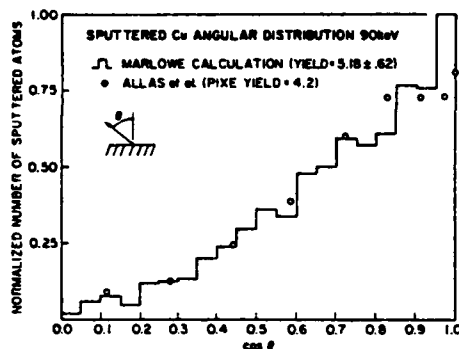


Fig. 1. Angular distribution of sputtered Cu atoms for normally incident 90 keV Cu beam.

out to nearest neighbor distances, has a screening radius twice this value (15 Å) [8]. This would result in a higher yield as it allows more large impact parameter, low energy collisions. Indeed a MARLOWE calculation using the larger screening radius resulted in a sputtering yield twice as large.

In fig. 1 we compare the experimental PIXE-determined angular distribution of the sputtered Cu atoms [1] with our calculated values. The results for Ni are presented in fig. 2. The calculated distributions were normalized to unity at an exit angle normal to the target surface. The experimental distributions were then normalized such that the ratio of the areas under the calculated and experimental curves was equal to the ratio of the calculated and experimental yields. The general agree-

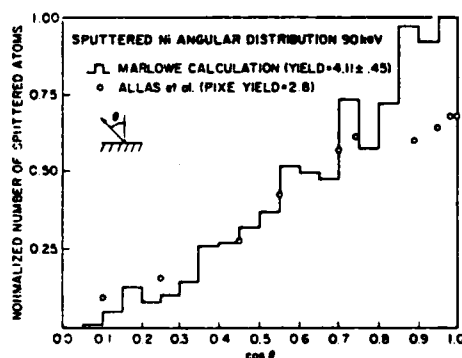


Fig. 2. Angular distribution of sputtered Ni atoms for normally incident 90 keV Ni beam.

ment is clear, particularly for Cu. Although the calculation appears to indicate a deviation from a $\cos \theta$ law for the sputtered atom distribution, it must be remembered that the statistical error associated with individual angle bins may be much larger than the error in the yield and it would be rash to draw any conclusion from this data. Having shown agreement for both Cu and Ni, we consider below further details of the calculation for Cu alone.

3. Structures of sputtering cascades

A calculation such as this has the advantage of examining aspects of the sputtering process not easily available to experiment and therefore can shed light on possible mechanisms. We have examined some aspects of the structure of what may be called sputtering cascades. We have traced the chain of collisions back from each sputtered atom, collision by collision, to its deepest point in the target. This string of collisions we term a sputtering trajectory.

In fig. 3 we show both the distributions of the depths of origin of the sputtered atoms and the distribution of the maximum depths of the sputtering trajectories. We see that the distribution of maximum depths of sputtering trajectories lies significantly deeper than the distribution of the sites of origin of the sputtered atoms themselves. Some 88% of the sputtered atoms originate within two atomic layers of the surface, while only 8% of the sputtering trajectories originate there. This is why such thick target was required in the calculation to reach bulk values of the yield. It is interesting that Robinson found for the sputtering of Xe from monocrystalline Au at much lower energy (700 eV) [5] that 99% of the sputtered atoms originated within two atomic layers of the surface. This is not very different from our result for Cu.

We looked at the number of collisions that occur along a sputtering trajectory from its origin out to the surface. The results are shown in table 1. The distribution of the number of collisions peaks around the relatively small number of 4. Some 77% of the trajectories contain six or fewer collisions: only 41% of the sputtering trajectories originate within six atomic layers of the surface.

We also investigated the frequency of occurrence of replacement sequences in sputtering

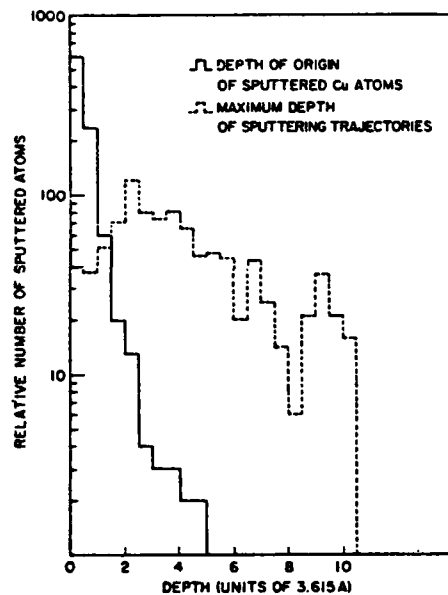


Fig. 3. Comparison of calculated depth distribution of sites of origin of sputtered Cu atoms to distribution of maximum depths of sputtering trajectories for 90 keV normally incident Cu ions.

trajectories. These are sequences of displacement collisions in which each displayed atom is replaced by the atom which displayed it. Although we gathered information on all such sequences, we shall count as meaningful only those replacement sequences of length greater than three. Indeed, when we looked at sputtering trajectories in amorphous targets, replacement sequences of length up to two occurred, but none greater than two. We looked at 932 sputtering trajectories; a number of these contained more than one sequence. In table 2 we show the distribution of replacement sequences as a function of the length of the sequence and also according to the number of sequences that occurred in the trajectory in which they appeared. For example the second column in the table says that there were 51 replacement sequences of length 3 in sputtering trajectories that contained only a single sequence, 8 of length 3 in trajectories that contained 2 sequences, and 1 of length 3 in a trajectory that contained 3 sequences. No trajectories were found that contained more than 2 sequences. It is seen that replacement sequences contribute to but certainly do not dominate the propagation of the sputtering trajectories. Only 20% of the sputtered atoms come from trajectories that contain any replacement sequences at all. The lack of such sequences in amorphous targets, therefore, cannot explain the low yield we found for such targets and which we discuss in the next section.

Table 1
Number of collisions along sputtering trajectories

	0	1	2	3	4	5	6	7	8	9	10
Number of collisions	0	6.4	11.8	15.2	17.0	14.8	11.5	6.9	4.8	3.0	2.3
Percent of trajectories	11	12	13	15	14	16	17	18	19	20+	
Percent of trajectories	1.6	0.9	1.5	0.3	0.4	1.0	0.2	0.2	0.2	0	

Table 2
Distribution of replacement sequences in sputtering trajectories

No. of sequences on trajectory	Length of replacement sequence												
	3	4	5	6	7	8	9	10	11	12	13	14	15
1	51	36	21	13	10	9	12	7	1	3	1	3	2
2	8	2	1	2	3	1	0	1	2	0	0	0	0
3	1	0	0	0	1	0	0	0	0	0	0	0	0

1. THEORY

Table 3
Distribution of yield values

Yield	0	1	2	3	4	5	6	7	8	9	10
Frequency (poly.)%	34	13	9.5	5.0	4.4	4.4	3.3	2.2	1.6	2.2	2.2
Frequency (amor.)%	57	10.5	6.5	6.0	4.0	3.5	1.0	2.0	1.5	1.5	1.5
Yield	11	12	13	14	15	16	17	18	19	20+	
Frequency (poly.)%	4.4	2.2	0.6	0	1.6	1.6	1.6	0.6	1.1	4.0	
Frequency (amor.)%	0.5	0	0	1.0	0.5	0.5	0.5	0.5	0.5	1.0	

4. Sputtering from amorphous targets

We also calculated the self-sputtering yield for 90 keV Cu atoms from an amorphous target, using the same parameters as in the polycrystalline case, and found the yield to be 2.31 ± 0.34 , less than half the polycrystalline target value. Now the sputtering yield is a statistical quantity with quoted values being averages over a large number of incident atoms. The number of particles sputtered when an incident atom strikes the target varies over a wide range of values. In table 3 we show the distribution of yield values for both the amorphous and polycrystalline cases. The greatest difference is that for amorphous targets no atoms at all are sputtered 57% of the time, while this occurs with a frequency of only 34% for polycrystalline targets. The reason for this is not immediately clear. The distribution of maximum depths of the sputtering trajectories is much the same as for polycrystalline targets. A possibility may be that although the range of an atom is the same for both amorphous and polycrystalline media (the densities being the same), the fluctuations are larger for polycrystals because of the ordered structure. Near the surface, these would allow more particles to escape in the case of polycrystals.

Parenthetically it should be noted that more than 36% of the polycrystalline sputtering yield arises from events in which 15 or more atoms are sputtered, even though they occur relatively rarely. Even for amorphous targets these events account for more than 27% of the yield. It is worth noting also that for amorphous targets essentially no sputtering trajectory contains more than seven collisions.

5. Conclusions

We have shown that high energy heavy atom self-sputtering yields and angular distributions can be accounted for by a binary collision cascade simulation code such as MARLOWE. Although calculated yields may be relatively insensitive to comparatively small variations in potential parameters [4], we have shown that this is not true for relatively large variation in the screening distance and one should choose these parameters with some care. We have also shown that although sputtered atoms come from sites very close to the surface, the mechanism originates with events significantly deeper. The large difference we have calculated between yields from amorphous and polycrystalline targets is not well understood and requires further elucidation.

References

- [1] R.G. Allas, A.R. Knudson, J.M. Lambert, P.A. Treado and G.W. Reynolds, Nucl. Instr. and Meth. 194 (1982) 615.
- [2] M.T. Robinson and I.M. Torrens, Phys. Rev. B9 (1974) 5008.
- [3] M. Hou and M.T. Robinson, Nucl. Instr. and Meth. 132 (1976) 641.
- [4] M. Hou and M.T. Robinson, Appl. Phys. 18 (1979) 381.
- [5] M.T. Robinson, Sputtering by ion bombardment, ed. R. Behrisch (Springer-Verlag, Berlin, 1980) ch. 3.
- [6] D.P. Jackson, Rad. Effects 18 (1973) 185.
- [7] P. Sigmund, Sputtering by ion bombardment, ed. R. Behrisch (Springer-Verlag, Berlin, 1980) ch. 2.
- [8] G.P. Mueller, Proc. 1st Albuquerque Informal Range/Energy Workshop, ed., D.K. Brice (Sandia National Laboratories, Albuquerque, 1981) SAND 79-2217.

Section I.E

METHODS TO CONTROL TARGET HEATING DURING ION IMPLANTATION

K. S. Grabowski and R. A. Kant

Materials Modification and Analysis Branch
Condensed Matter and Radiation Sciences Division
Naval Research Laboratory

This work was supported by the Office of Naval Research and Naval Sea Systems Command.

Methods to Control Target Heating During Ion Implantation

K.S. Grabowski and R.A. Kant

Naval Research Laboratory, Code 6671, Washington, DC 20375, USA

1. Introduction

The use of high-current ion implanters with beam powers in excess of 1kW requires improved methods of target cooling. This problem has already been addressed for ion implantation of Si wafers [1-3], but cooling of metallic targets needs further development. Compared to Si wafers, metallic targets typically have more awkward geometries, thicker cross sections, lower thermal conductivities, and in some cases (e.g., certain heat-treated steels) comparable temperature limitations during implantation ($T \leq 2000^\circ\text{C}$). In addition, since metallic targets typically require higher implantation doses than Si wafers, use of high-current implanters is highly desirable. Heat conduction to a sink will generally be necessary for cooling of metallic targets.

This paper casts well-known mathematical solutions [4] to heat conduction problems in terms of ion-implantation parameters, and discusses the different regimes of conduction cooling. Examples illustrate that for most applications: (1) scanning of the ion beam and/or targets is necessary, (2) storing energy in target heat capacity is insufficient to limit target temperature rise, and (3) producing good sample contact with a heat sink is essential. Methods of producing adequate contacts are discussed, based on experimental measurements of the interface contact conductance, h , for various combinations of materials. Finally, as an example of successful target cooling by conduction techniques, the device used at the Naval Research Laboratory to cool tool-steel bearing races is briefly described.

2. Radiation Cooling

Radiation cooling of the target is only sufficient for those applications where a high equilibrium temperature or large radiating surface area is acceptable. As Fig.1 shows, to limit surface temperature to 500°C for a rather typical effective total emissivity of 0.2 and an input power of 1kW, 0.25 m^2 of radiating surface area is needed. For lower temperatures, higher incident power densities, or lower effective emissivities, radiative heat transfer is clearly inadequate.

3. Conduction Cooling

The time-dependent temperature rise of a surface struck by a constant heat flux can be readily solved for the case of one-dimensional heat transfer [4]. Solutions expressed in dimensionless units are shown in Fig.2 for

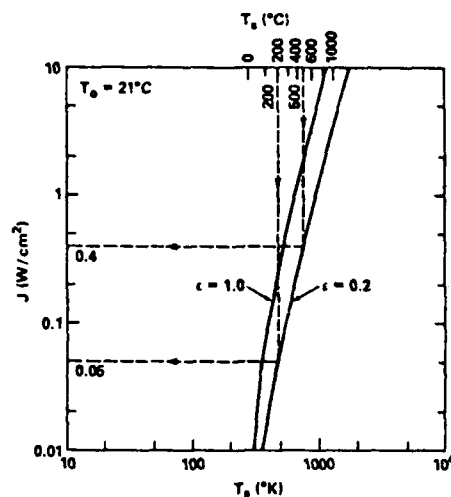


Fig. 1. Power radiated per unit surface area as a function of surface temperature and effective total emissivity, ϵ , for surroundings at 21°C. Strictly, ϵ should include the influence of viewfactors and the emissivity of surrounding material

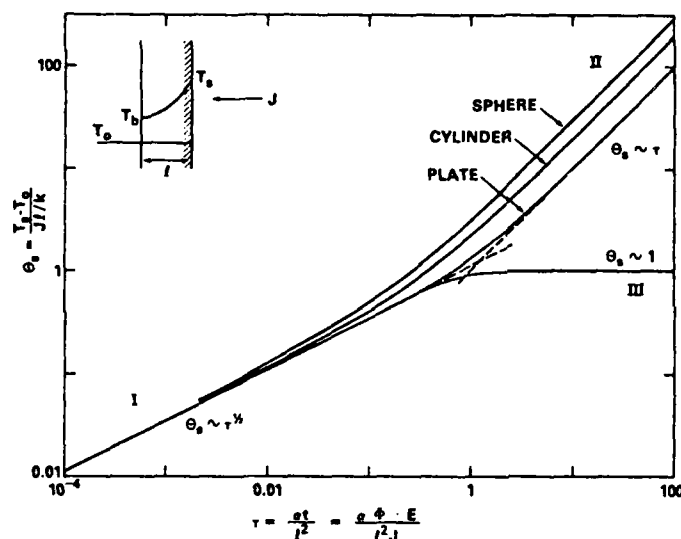


Fig. 2. Dimensionless surface temperature rise, θ_s , versus dimensionless time (or dose) τ , for incident power density J , assuming one-dimensional heat transfer. l represents plate thickness, or cylinder or sphere radius; k , thermal conductivity; α , thermal diffusivity; ϕ , ion dose; and E , ion energy. Heat is withdrawn from the target in region III by a heat sink

plate, cylinder, and sphere geometries where θ_s represents dimensionless surface temperature and τ represents dimensionless time (or implantation dose). As indicated in the figure inset: T_s represents the surface temperature, T_0 the initial temperature, and T_b the temperature either at the back of a plate of thickness l or at the center of a sphere or cylinder of radius l . J is the incident power density (W/cm^2). Other

important variables include: k , thermal conductivity ($W/(cm-K)$); α , thermal diffusivity (cm^2/s) equal to $k/(\rho C)$ where ρ is density (g/cm^3) and C is heat capacity ($Ws/(g-K)$); and t , duration of exposure (s) equal to $\phi E/J$ where ϕ is implantation fluence ($ions/cm^2$) and E is ion energy (Ws/ion). Nominal values of α , k , and ρC for selected materials are listed in Table I as taken from [5]. Actual values depend strongly on exact alloy composition and specific heat treatment.

Table 1. Thermal Properties of Selected Materials

Material	α (cm^2/s)	k ($W/(cmK)$)	ρC ($Ws/(cm^3K)$)
Cu	1.1	3.9	3.4
Al	0.95	2.3	2.4
Al (2024-T4)	0.50	1.2	2.4
Si	0.53	0.84	1.6
Brass (Cu - 30Zn)	0.38	1.2	3.2
Ta	0.24	0.54	2.3
Fe	0.23	0.80	3.5
Fe (0.10C)	0.18	0.65	3.5
Fe (M2 tool steel)	0.058	0.21	3.7
Fe (304 SS)	0.041	0.16	4.0
Ti	0.068	0.16	2.3
Ti (6Al - 4V)	0.026	0.068	2.6
Superalloy (IN 738)	0.035	0.12	3.4

Three different regimes of conduction heat transfer are indicated in Fig.2. In regions I and II all deposited heat is retained in the sample, whereas in region III a steady-state condition obtains where heat flow is constant through a plate sample to a heat sink. In region I the deposited energy has not yet diffused to the boundary of the sample (i.e., at t^2 and $T_b = T_0$), so the surface temperature rise is that for heat diffusion in a semi-infinite medium and $\theta_s = \tau^{1/2}$. In region II most of the deposited energy is distributed throughout the sample (i.e., at t^2 , $T_b = T_s$), so the temperature rise is limited by the heat capacity of the sample and $\theta_s = \tau$. In region III, for an ideal heat sink (i.e., $T_b = T_0$) $\theta_s = 1$, otherwise θ_s is constant but greater than 1.

The transition from region I to either II or III occurs quite sharply at $\tau=1$ for plate samples but more gradually for cylinder or sphere samples. The implantation conditions which produce $\tau=1$ are identified in Fig.3. Examination of this figure reveals that for most metals implantations, τ exceeds 1. For a typical energy and fluence (100-keV ions, $1 \times 10^{17}/cm^2$), a nominally maximum power density (1-kW beam into 10 cm^2) and even a poorly conducting metal (Ti-6Al-4V, $\alpha=0.026$ cm^2/s), τ will exceed 1 unless samples thicker than 0.5 cm are implanted. Use of thicker samples, highly focused unscanned beams, or low fluences are required to prevent τ from exceeding 1.

3.1 Region I (Heat-Diffusion Limited)

While this region is applicable for low doses of implantation, it is most relevant to cases of thick samples with low thermal diffusivity and/or for implantations conducted with high-current unscanned beams (see Fig.3). In these cases, large temperature increases may occur. In the low-dose limit, the temperature rise in region I can be expressed as:

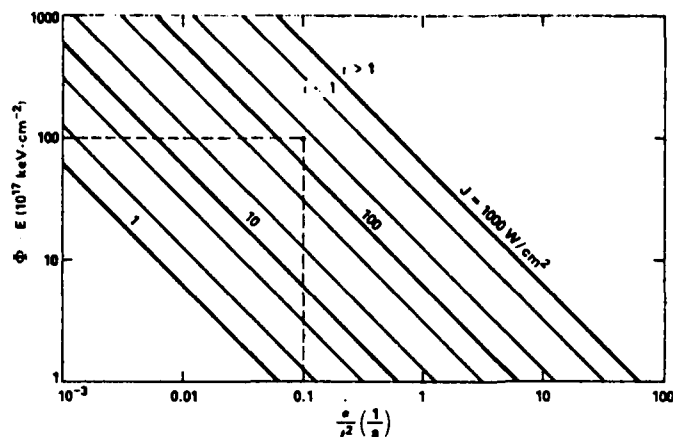


Fig. 3. Ion implantation conditions for which $\tau=1$, with $\tau<1$ occurring below a given power-density line and $\tau>1$ above it

$$\theta_s = \frac{2}{\sqrt{\pi}} \tau^{1/2}, \text{ or} \quad (1)$$

$$T_s - T_0 = \frac{2}{\sqrt{\pi}} \frac{(\phi E)^{1/2}}{\rho C} \left(\frac{J}{\alpha} \right)^{1/2}. \quad (2)$$

Since for ion implantation into most metals ϕ , E and ρC are nearly invariant, the ratio of power density input to heat diffusion output determines the target temperature rise.

As an example, the implantation of 100-keV ions to a dose of $1 \times 10^{17} \text{ cm}^{-2}$ into 1-cm-thick plate of 0.1-%C steel using an unscanned high-current beam (i.e., $J \approx 300 \text{ W/cm}^2$) maintains τ less than 1 and Eq.(2) predicts $T_s - T_0 \approx 530^\circ\text{C}$. To limit the temperature rise of this sample, the average incident power density must be reduced. Scanning the beam at an adequate rate can accomplish this.

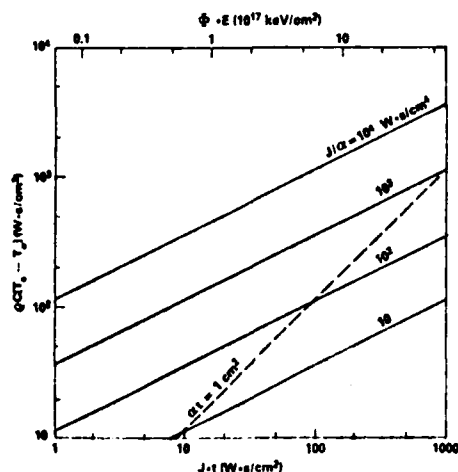


Fig. 4. Pseudo-temperature rise, $\rho C(T_s - T_0)$, as a function of both absorbed energy Jt (or ϕE), and the ratio J/α . This figure is only valid when $\tau < 1$, or to the left of the dashed line for a 1-cm-thick plate target. Dashed line for other target thicknesses can be drawn through other constant values of τ

Figure 4 graphically represents the square root dependence of $(T_s - T_0)$ in Eq.(2) on both J/α and Jt (or ϕE). This figure can be used to determine the minimum necessary scan speed. Using the previous example; to limit the steel-plate temperature increase to 100°C ($\rho C (T_s - T_0) = 350 \text{ Ws/cm}^3$) on a single pass of a 300 W/cm^2 ion beam ($J/\alpha = 1670 \text{ Ws/cm}^4$) the beam dwell time on a given spot must be less than 200 ms ($Jt < 60 \text{ Ws/cm}^2$). For a 1.5-cm-wide beam this translates into a minimum scan speed of 7.5 cm/s or about 7 rpm for the edge of a rotating 20-cm-diameter disk. At this moderate scan rate, approximately 27 passes will be needed to complete the implantation, and input heat should be able to diffuse to a suitable heat sink between passes.

3.2 Region II (Heat-Capacity Limited)

This region applies to samples which are thermally isolated and for which $\tau > 1$. In the high dose-limit:

$$\theta_s = n\tau, \text{ or} \quad (3)$$

$$T_s - T_0 = n \frac{\phi E}{\rho C \ell}. \quad (4)$$

The variables are the same used in Fig.2 except for the additional coefficient n , which equals 1, 2, or 3 for plate, cylinder, or sphere geometries, respectively. As before, ℓ represents either plate thickness, or cylinder or sphere radius.

For most implantation doses and typical target sizes, heat capacity alone is insufficient to cool the target. As a representative example, implantation of 100-keV ions to $1 \times 10^{17} \text{ cm}^{-2}$ into 0.1%-C steel will produce a uniform temperature rise of about 460°C in targets consisting of a 1-cm-thick plate, a 4-cm-diameter cylinder, or a 6-cm-diameter sphere. As this is a large temperature rise in these substantially sized samples it is clear that storage of implantation heat energy within many targets will not be acceptable. Heat storage could be augmented by attaching a small target to a massive heat sink, however, the heat sink would have to be cooled between subsequent implantations and heat diffusion throughout the large size would be limited.

3.3 Region III (Steady-State Conduction to Heat Sink)

The best method to limit target temperature rise is to secure the target to a good heat sink. For a plate target attached to an ideal heat sink $T_b = T_0$, so

$$T_s - T_0 = -\frac{J\ell}{k}. \quad (5)$$

Taking a 1-cm-thick plate of 0.1%-C steel as a representative implantation target, its temperature increase will exceed 200°C only for incident power densities in excess of 130 W/cm^2 . In other words, for a 1-kW ion beam scanned moderately well, an ideal heat sink would cool most targets adequately.

Unfortunately, ideal heat sinks cannot readily be attained in vacuum. In practice there are temperature drops across heat-conducting interfaces. These temperature drops can be expressed by

$$\Delta T = \frac{J}{h} \quad (6)$$

where h ($W/(cm^2K)$) represents the interface contact conductance for contacting solids. Using $h=0.05$ $W/(cm^2K)$ as representative of steel contacting steel in vacuum, one readily finds that a heat flux of only 5 W/cm^2 will produce a $100^\circ C$ temperature drop across the interface. Poor contact conductance is by far the greatest limitation to high incident power densities yet discussed.

Use of low incident power densities can help, but is not always practical. For example, to implant the inside groove of an outer race of a bearing (e.g., for corrosion resistance), only 1 or 2 bearings at a time can easily be implanted. For two 6-cm-diameter bearings with 1-cm-wide grooves, this means that only about 40 cm^2 are exposed to the beam, for an average incident power density of 25 W/cm^2 for a 1-kW ion beam. Each steel to steel contact interface would produce a temperature drop of about $500^\circ C$. Clearly, methods of improving interface contact conductance in vacuum are needed. Values of h near 1 $W/(cm^2K)$ would be desirable.

One further point on providing a good heat sink. Heat must ultimately be removed across the additional interface between metal and cooling fluid. Values of h for this interface typically range from about 0.01 to 1 $W/(cm^2K)$ for a cooling medium of water. The value depends somewhat upon water temperature and cooling geometry, but mostly upon the flow velocity. Flow velocities in excess of about 200 cm/s will produce an h near 1. By providing adequate contact area between metal and cooling fluid it is possible to limit the temperature drop across the metal/fluid interface to a few tens of degrees C, even for 1-kW power inputs.

4. Interface Contact Conductance

4.1 Empirical Values

Many interface-contact-conductance measurements have been performed on various materials over the years (see references in [6]) and some have been collected in handbooks such as that of Rohsenow and Hartnett [7]. However, many of these measurements were performed on samples with carefully prepared surface finishes. Partly in an attempt to provide practical engineering values, we measured h at NRL for selected materials having machined surfaces.

Washers (0.16-cm thick, 2.54-cm OD, 1.27-cm ID) were machined from selected stock material and clamped between two Al-alloy cylinders, pressed together using calibrated springs. Heat was applied to one end in vacuum by a Joule-type heater and removed from the other end by water cooling. The total temperature drop across clamped washers was measured using four thermocouples attached to the Al-alloy cylinders. The interfacial temperature drop was determined by subtracting the temperature drop expected from thermal conduction through the washers. Power levels up to 40 W were selected to produce interfacial temperature drops in excess of about $5^\circ C$.

Table II lists values of interface contact conductance h , measured using a contact pressure of 1.17 MPa (170 psi). The values listed with a "greater than" sign are lower-limit estimates due to the limited accuracy

Table 2. Interface Contact Conductance

INTERFACE	$h(W/(cm^2-K))$
SS/SS	0.04
SS/Al	0.19
SS/Al Foil/SS	> 0.3
SS/Indium/SS	> 0.6
SS/Silver Paint/SS	> 5
Al/Brass	0.5
Al/Cu	0.9
Al/OF-Cu	1.5
Al/Al	1.6
Brass/Brass	0.1
Cu/Cu	0.6
OF-Cu/OF-Cu	1.5

SS: 304 Stainless Steel

Cu: Tough-pitch Cu

Al: 6061, T6 Temper

OF-Cu: Oxygen-free Cu

Brass: Cu-30 Zn

obtainable with a 40 W heater. For like materials the contact conductance improved about 40 fold going from SS/SS to Al/Al, with unacceptably low h values ($h < 1 W/cm^2$) occurring for SS/SS and Brass/Brass couples. For dissimilar washer materials the contact conductance was somewhat below the mean value of the like-washer pairs. These results mean that Al fixtures and 1.2 MPa clamping pressures can provide a nearly acceptable contact conductance for clamping brass targets ($h=0.5$), but not SS targets ($h=0.2$). To clamp SS targets use of an interstitial material like indium or Ag paint may be necessary.

The semiconductor industry currently obtains poorer contact conductances for clamping Si wafers because wafer fragility limits the usable contact pressure to about 7kPa (1psi). Eaton/NOVA has obtained contact conductances of 0.018 - 0.024 $W/(cm^2K)$ using an elastomer-dome substrate and 0.020 - 0.050 using gaseous cooling [3]. More recently, Varian/Extrion has obtained $h=0.06 W/(cm^2-K)$ by introducing a small quantity of low-pressure gas to the interface between Si wafer and a computer-designed contoured Al dome [8].

4.2 Predicted Values

M.M. Yovanovich and V.W. Antonetti have recently found good correlation between the interface contact conductance measured in vacuum on samples with carefully controlled surface finishes, and specific physical parameters [6,9]. They found

$$h = 1.25 \frac{mk}{\sigma} \left(\frac{P}{H} \right)^{0.95} \quad (7)$$

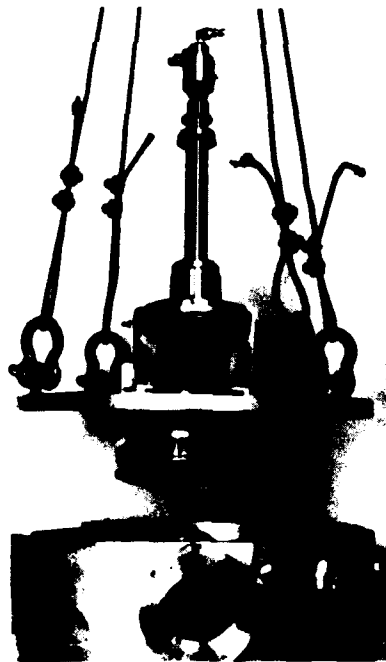
where P is contact pressure, H is microhardness of the surface region deformed during contact, k is thermal conductivity, σ is the root-mean-square surface roughness, and m is the mean surface slope, a number directly obtainable from surface profilometry measurements. This

correlation applies to vacuum ambients and for contact pressure greater than about 1 MPa (145 psi). The major point here is that contact conductance can be improved by (1) selecting materials with a large k/H ratio, (2) using large contact pressures P , and (3) carefully polishing the contacting surfaces.

Trends predicted by Eq.(7) were supported by the excellent improvement we observed in h when a thin foil of soft well-conducting metal was placed between two hard stainless steel washers. Even though an additional interface was produced by adding the foil, the net contact conductance was greatly improved. This technique is generally useful; however Yovanovich has shown [10] that using too thick a foil (i.e., >0.1 mm) can produce a temperature gradient in the foil sufficient to negate the improvement in h .

5. NRL Water-Cooled Heat Sink

The principles described in this paper were utilized in the design of a rotating water-cooled feedthrough presently in use at NRL. The water-cooled heat sink, viewed along the beam direction in Fig. 5, was designed to absorb 100 W of power while maintaining most rotating implantation targets at temperatures below 100°C. Attached to the heat sink is the outer race of a 22.5-cm-OD main-shaft ball-type bearing used in jet engines. The vacuum feedthrough can be tilted up to 22° and translated in and out of the vacuum chamber. It is typically rotated at 2 rpm, although speeds up to about 500 rpm are possible. Cooling water passes through the stainless-steel shaft into a Cu end plug. Samples are clamped onto an Al base plate bolted to the Cu plug, allowing considerably flexibility in target fixturing. With this design, a temperature difference of only 64°C was measured between the surface of an Al plate



80133(6)

Fig.5. Rotating water-cooled heat sink developed at NRL. The feedthrough can be tilted up to 22°, translated in or out, and is typically rotated at 2 rpm

and the water supply temperature when a 105 W beam was directly incident on the Al plate.

Obviously, to remove 1 kW of power, improvements in this heat sink are needed. Directly cooling the Al baseplate would eliminate the thermal resistance between Cu plug and Al baseplate and more interface area for cooling water would be available. These two components probably contributed nearly two-thirds of the observed 64°C temperature drop at 105 W of power.

6. Summary & Conclusions

This work has shown that in many cases radiation cooling of targets is insufficient when a high-current ion implanter is used. Conduction cooling techniques must then be utilized. Three different regimes of conduction cooling were described: (I) heat-diffusion limited, (II) heat-capacity limited, and (III) steady-state conduction to a heat sink. The first two regimes apply when the target is thermally isolated. For most implantations into metals, doses are large enough and samples small enough that transition from region I into either region II or III occurs, especially if even a small amount of beam scanning is utilized. Furthermore, since few samples are large enough to completely store implanted energy without undergoing an unacceptable temperature rise, most metallic targets should be implanted under the conditions of region III.

This work has shown that with region III conduction cooling, substantial target heating can occur from interfacial temperature drops unless good interface contact conductance is obtained or beam scanning over a large area is possible. Engineering values of contact conductance h , as well as its expected dependence on contact pressure, surface microhardness and finish, and thermal conductivity were presented. In some cases use of a conductance-promoting interstitial foil may be necessary. Since beam scanning and water cooling are generally required, guidelines for their satisfactory application were also briefly described.

In conclusion, this work has shown that to prevent excessive heating of most metallic targets: (1) conduction cooling by a heat sink is necessary since radiation cooling and the target's heat capacity alone usually are inadequate, (2) some scanning of either beam or target is necessary (to limit interfacial temperature drops and to prevent localized target heating), and (3) producing good contact conductances is extremely important.

Acknowledgements

The authors wish to thank E.T. Tildon for her assistance in measuring interface contact conductances and M.M. Yovanovich for his insight on the theory of contact conductance.

References

1. P.D. Parry: J. Vac. Sci. Technol. 13, 622 (1976)
2. M. Bruel, B. Berthet, M. Floccari, and J.F. Michand: Rad. Eff. 44, 173 (1979)

3. M. King and P.H. Rose: Nucl. Instrum. Methods Phys. Res. 189, 169 (1981)
4. H.S. Carslaw and J.C. Jaeger: Conduction of Heat in Solids, (Oxford Univ. Press, London 1959)
5. American Society for Metals: Metals Handbook, 9th ed., Vol. 1, Properties and Selection: Irons and Steels (Amer. Soc. Met., Metals Park 1978); ibid, Vol. 2, Properties and Selection: Nonferrous Alloys and Pure Metals, 1979; ibid, Vol.3, Properties and Selection: Stainless Steels, Tool Materials and Special-Purpose Metals, 1980; Y.S. Touloukian and C.Y. Ho, ed.: Thermophysical Properties of Matter, 13 Vols (IFI/Plenum, New York 1970-1974)
6. M.M. Yovanovich: Prog. Astronautics Aeronautics 83, 83 (1982)
7. W.R. Rohsenow and J.P. Hartnett: Handbook of Heat Transfer, (McGraw-Hill, New York 1973)
8. S.C. Holden; N.L. Turner and R.B. Bramhall: private communications, data to be published
9. M.M. Yovanovich: private communication
10. M.M. Yovanovich: Prog. Astronautics Aeronautics 31, 227 (1973)

Section II.A

THE EFFECT OF NITROGEN IMPLANTATION ON MARTENSITE
IN 304 STAINLESS STEEL

R. G. Vardiman¹
R. N. Bolster, and I. L. Singer²

¹Physical Metallurgy Branch
Material Science and Technology Division
Naval Research Laboratory

²Surface Chemistry Branch
Chemistry Division
Naval Research Laboratory

This work was supported by the Office of Naval Research.

THE EFFECT OF NITROGEN IMPLANTATION ON MARTENSITE IN 304 STAINLESS STEEL

R. G. VARDIMAN, R. N. BOLSTER, AND I. L. SINGER
U. S. Naval Research Laboratory, Washington, DC 20375

ABSTRACT

Martensite will form in austenitic 304 stainless steel when it is deformed. Transmission electron microscope studies show that nitrogen ion implantation causes a reversion of the martensite to austenite. Specimens containing martensite resulting from fine surface polishing and heavy rolling are examined. The transformation is shown not to occur because of temperature increases during implantation. The effect is related to recent wear results in 304 stainless steel.

INTRODUCTION

Many austenitic stainless steels undergo a diffusionless phase transformation to martensite when stressed or quenched to very low temperatures. The face centered cubic (FCC) austenite phase may be regarded as metastable under deformation. The martensite in stainless steel is usually body centered cubic (BCC), although some hexagonal martensite may be formed, particularly in low temperature deformation (1).

Martensite has inferior corrosion and fracture resistance compared with austenite (2-4). Surfaces are particularly vulnerable to its formation, either in finishing operations or from high contact stress in use, such as from wear or impact. These effects may be prevented by a finishing heat treatment or by increased amounts of alloying elements such as nickel, manganese, nitrogen, or carbon, but such steps are not always practical. Nitrogen and carbon have the greatest effect per weight added on austenite stabilization, but their amounts are limited by low solubility. Because of the very high concentrations which can be achieved by ion implantation, the potential exists for achieving effects impossible by other means. Ion implantation is known to induce phase transformations in the target material in some cases (5-9). In stainless steels, martensite has been produced by implantation of large atoms such as antimony (10).

In this paper, we show that martensite in 304 stainless can be transformed to austenite by nitrogen implantation. We have looked at martensite formed by heavy deformation and by abrasive wear using fine diamond particles. The microstructure has been characterized by x-ray diffraction, transmission electron microscopy (TEM) and electron diffraction. Composition of the surface layer was determined by Auger electron spectroscopy (AES). The observed results are consistent with recently published studies on the abrasive wear behavior of nitrogen implanted steels (11,12).

MATERIALS AND METHODS

Our starting material in all cases was 304 stainless steel; the analysis in Table I is from the supplier. Two types of specimen were used. For the first,

1.5 mm sheet was cold rolled to 0.05 mm, a reduction in area of approximately 97%. X-ray diffraction of this material showed that it was predominantly martensite (BCC) with remaining austenite of the order of 20%. The other type of specimen was in the form of 12.7 mm diameter buttons, as have been used in previous wear studies (11,12). These have a surface finish given by a vibratory polisher charged with 1-5 μ m diamond powder in paraffin oil.

TABLE I
Composition of the 304 Stainless Steel

Element	Cr	Ni	Mn	Mo	Si	P	S	L	N
Wt. pct.	18.18	8.48	1.75	0.36	0.50	0.03	0.005	0.055	0.05

For TEM examination, 3 mm discs were punched from the rolled foil. Specimens to be implanted were electrolytically polished on one side, then thinned through from the opposite side after implantation. The electrolyte was 6% perchloric acid in ethanol, used at -60°C. For the wear buttons, the polished surface was cut off in a thin slicing machine, mechanically polished on the cut side to 0.1 mm thickness and 3 mm discs punched out. These were then thinned through from the side opposite the original diamond polished face. In all cases, the surface of interest was protected from the electrolyte during thinning by a coating of a translucent masking compound. With this technique it was possible to preserve the implanted or worn surface in almost every case. Thinned layers of typically 100-200 nm thickness were examined in a 200 keV electron microscope.

For the rolled specimens, nitrogen implantation was done at 75 keV (150 keV N_2^+). In this case the thickness of the implanted layer (see Table II) is approximately the same as the thickness of the film which is examined in the electron microscope. The wear buttons were implanted at 40 keV, to correspond with the energy used in the wear studies (11,12). In both cases the total dose was 2×10^{17} at./cm². Power densities were normally in the range of 0.6 to 0.9 watts/cm². Samples were carefully heat sunk to limit the temperature rise during implantation.

Auger electron spectroscopy (AES) was used to determine concentration profiles in the oxide layer of implanted specimens, and nitrogen in the full implanted layer. The sputtering rate for 2 keV argon ion milling, and the concentration sensitivity factors were determined in previous work (13,14).

TABLE II
Experimental and theoretical values of the nitrogen implantation parameters for a dose of 2×10^{17} N⁺/cm²

		Projected range (nm)	Straggling range (nm)	Max Concentration (at. pct.)
40 keV	Theory	44	21	30
	Experiment	55 \pm 5	37 \pm 4	23 \pm 3
75 keV	Theory	83	34	22
	Experiment	87 \pm 14	47 \pm 7	17 \pm 3

RESULTS

The nitrogen concentration parameters as determined by AES, and as derived from modified LSS theory (15) are given in Table II for both the 40 keV and the 75 keV implants. The agreement is reasonable, particularly if sputtering effects, which broaden the profile (16), are taken into account. The measured total dose is within 5% of the nominal fluence of 2×10^{17} at./cm.²

Cold Rolled Material. The microstructure observed in TEM is in agreement with the x-ray results, that is, mostly martensite with only small scattered patches of austenite. A typical selected area diffraction pattern taken with a $1000 \mu\text{m}$ diffraction aperture giving a selected area of $11.6 \mu\text{m}$ diameter is shown on the left side of Fig. 1. Because of the high degree of deformation, diffraction occurs in rings or ring segments. As expected very little diffraction is seen at the austenite (γ) diffraction positions. After the nitrogen implant, the austenite diffraction rings are strong, while the martensite (α') rings are reduced in intensity, as seen on the right side of Fig. 1. Because the exact thickness of the film in a given area is unknown, the amount of martensite remaining in the implanted layer, as contrasted with martensite lying below the implanted layer, cannot be estimated. CrN, which we have found in annealed 304

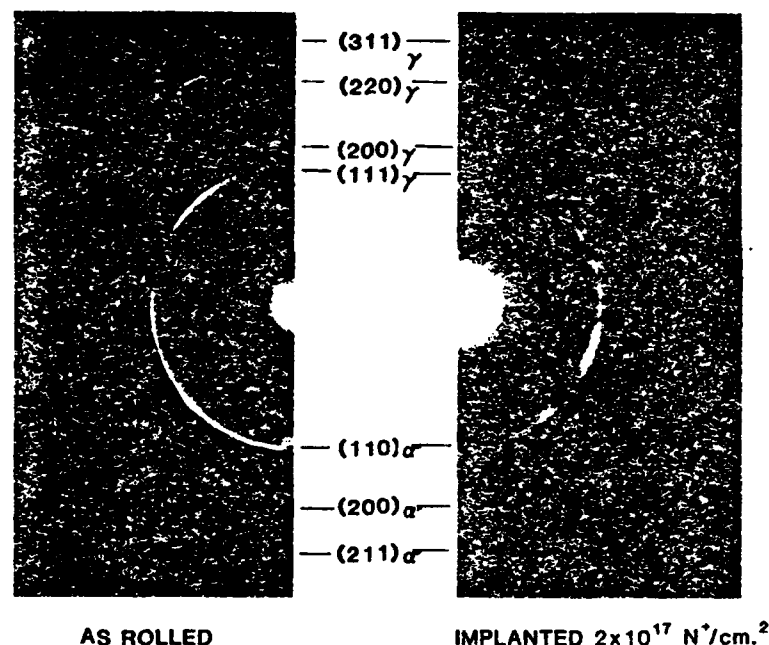


Fig. 1. Electron diffraction patterns of 97% R.A. material, $11.6 \mu\text{m}$ selected area.

stainless steel implanted with nitrogen, is not seen in any of the implanted specimens studied here.

Wear specimens. The deformation resulting from 3 μm diamond polishing is necessarily confined to a thin layer. The diffraction pattern on the left side of Fig. 2 shows strong continuous martensite rings, and segmented austenite rings, indicating a moderately deformed austenite layer beneath the martensite. After nitrogen implantation, martensite diffraction is completely absent, as seen on the right side of Fig. 2. The elimination of martensite by an implant which reached a maximum depth of 100 nm indicates that the martensitic layer itself had a thickness in the 50-100 nm range. The diffraction pattern of the implanted specimen shows short intense ring segments which correspond to austenite lying beneath the implanted layer. The nitrogen atoms cause an expansion of the austenite lattice, so that rings corresponding to the implanted material lie at slightly smaller radii. Most of the diffracted rings from implanted material are doublets, for which there is no present explanation.

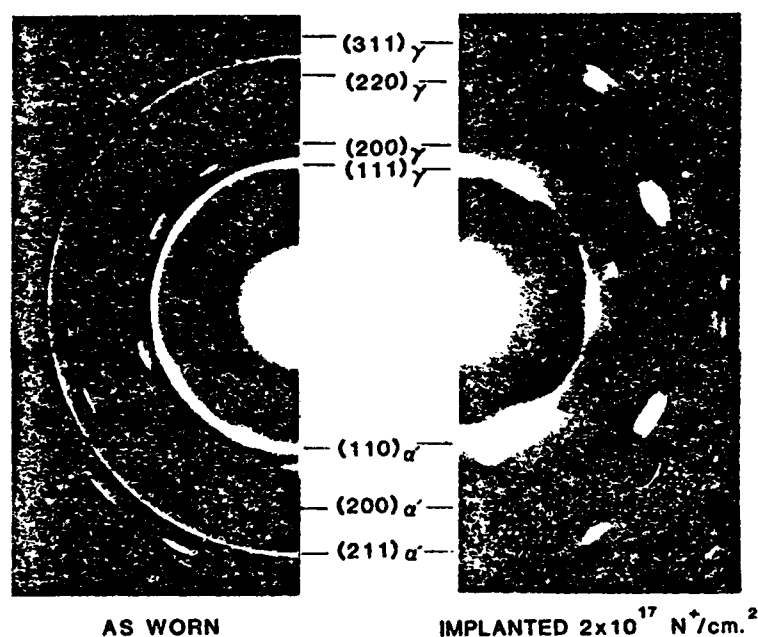


Fig. 2. Electron diffraction patterns of abrasive wear surfaces, 11.6 μm selected area.

DISCUSSION

We have evaluated the possibility that temperature increases during implanta-

tion could be sufficient to cause the martensite to transform. For martensite formed by quenching 304 stainless, the transformation temperature is 500°C (17), however, this may be lower for deformation martensite. Experience with implants done with comparable flux indicate temperatures in the 100-150°C range may develop. Auger analysis of the oxide layer on the surface of our implanted specimens shows a composition and thickness corresponding to an upper limit of 200°C during implantation. To check the effect of such a temperature on the martensite, a specimen of the 97% R.A. material was heated for one hour in an oil bath at 200°C. The x-ray diffraction spectra before and after heating were identical. Thus it does not appear that the observed transformation could have been caused by the temperature rise during implantation per se.

The stabilizing effect of nitrogen on the austenite phase is well known (1). The mixing and enhanced diffusivity developed by implantation are apparently sufficient to cause nucleation and growth of the austenite in the martensitic regions. Further work is required to determine the critical nitrogen dose, and the effect of other implants, both γ stabilizing (Ni, Mn) and nonstabilizing.

Recent work on abrasive wear by 3 μ m diamond particles on 304 stainless showed anomalous results, in that nitrogen implantation decreased wear resistance, where in other steels it increased wear resistance (11,12). The authors speculated that nitrogen implantation might affect the phase composition at the surface. The present results demonstrate clearly that this is the case. The ability to create a highly stabilized austenitic surface by ion implantation has practical implications, where a martensitic surface developed by finishing or use might reduce service life.

ACKNOWLEDGMENT

We would like to thank Dr. J. H. Hirvonen and his group for their help and cooperation in obtaining the implantations.

REFERENCES

1. Handbook of Stainless Steels, eds. D. Peckner and I. M. Bernstein (McGraw-Hill, N.Y., 1977), ch. 4.
2. H. Hanninen and T. Hakarainen, Corrosion 36, 47 (1980).
3. H. Kamide and H. Sugarawa, Corrosion 35, 456 (1979).
4. K. L. Hsu, T. M. Ahn, and D. A. Rigney, Wear 60, 13 (1980).
5. V. N. Bykov, V. A. Troyan, G. G. Zdovtseva, and V. ... Khaimovich, Phys. Stat. Sol. (a) 32, 53 (1975).
6. E. Johnson, T. Wohlenberg, W. A. Grant, P. Hansen, and L. T. Chadderton, J. Microscopy 116, 77 (1979).
7. E. Johnson, T. Wohlenberg, and W. A. Grant, Phase Trans. 1, 23 (1979).
8. P. V. Pavlov, E. I. Zorin, D. I. Tetelbaum, V. P. Lesnikov, G. M. Ryzhkov, and A. V. Pavlov, Phys. Stat. Sol. (a) 19, 373 (1973).
9. M. R. Skokan, E. F. Skelton, and E. Cukauskas, J. Phys. Chem. Sol. 41, 977 (1980).

10. E. Johnson, U. Littmark, A. Johansen, and C. Christodoulides, Report No. 81-07, ISSN 0106-7222, H. C. Orsted Institute, Copenhagen (1981).
11. R. N. Bolster and I. L. Singer, *Appl. Phys. Lett.* 36, 208 (1980).
12. R. N. Bolster and I. L. Singer, *ASLE Trans.* 24, 526 (1981).
13. I. L. Singer and J. S. Murday, *J. Vac. Sci. Tech.* 17, 327 (1980).
14. I. L. Singer, *ibid*, 18, 175 (1981).
15. I. Manning and G. P. Mueller, *Comp. Phys. Commun.* 7, 85 (1974).
16. F. Schulz and K. Wittmaak, *Rad. Effects* 29, 31 (1976).
17. R. P. Reed, *Acta Met.* 10, 865 (1962).

Section II.B

MECHANICAL AND MICROSTRUCTURAL PROPERTIES OF
BORON IMPLANTED BERYLLIUM

R. A. Kant and A. B. Knudson¹
K. Kumar²

¹Materials Modification and Analysis Branch
Condensed Matter and Radiation Sciences Division
Naval Research Laboratory

²Charles Stark Draper Laboratory
Cambridge, MA

This work was supported by the Office of Naval Research at Naval
Research Laboratory and at Draper Lab by ONR contract
#N0001477-C0388.

MECHANICAL AND MICROSTRUCTURAL PROPERTIES OF BORON IMPLANTED BERYLLIUM

R. A. KANT AND A. R. KNUDSON
Naval Research Laboratory, Washington, DC, 20375
K. KUMAR
Charles Stark Draper Laboratory, Cambridge, MA, 02139

ABSTRACT

High dose boron implantation into instrument grade I-400 beryllium has been found to produce a substantial increase of its wear resistance. A comparison of the friction and wear behavior resulting from two shapes of the boron depth distribution is made. The wear resistance provided by a boron layer of constant (flat) concentration was found to be superior to that of a gradually decreasing (graded) profile. Rutherford backscattering was used to determine the boron depth distribution profiles and transmission electron microscopy was used to examine the microstructure. Electron diffraction pattern analysis provides evidence for the formation of beryllium borides.

INTRODUCTION

A need to provide wear resistant surfaces for beryllium gas bearing components was the motivation for this study. Currently, hard coatings are being used, but an alternative is being sought because the coatings are difficult and expensive to machine and some problems with porosity and adhesion have been encountered. Previous experiments, reported elsewhere,^{1,2} with boron implanted beryllium showed that the hardness of the implanted surface increased with increasing dose. This increase was presumed to be due to the formation of beryllium borides. In the present study, evidence obtained by transmission electron microscopy suggests that borides have precipitated.

In addition, the friction and wear behaviors of two forms of boron depth distribution were investigated. The implantations were conducted using six different energies and the dose at each energy was adjusted to produce boron profiles which were either constant with increasing depth (flat), or which decreased with depth (graded). Rutherford backscattering was used in conjunction with computer modeling to determine the boron concentration profiles.

MATERIAL PREPARATION AND ION IMPLANTATION

The samples used in the mechanical tests were 19 mm diameter disks of instrument grade beryllium which were mechanically polished to a bright metallographic finish prior to ion implantation. They also received a stress relief anneal after being cut to size and before being polished. The samples used in the transmission electron microscopy study were 3 mm diameter disks of beryllium (99.95% pure). These were lapped to a thickness of 25 mm and lightly electropolished prior to implantation.

The ion implantation was conducted at a target chamber pressure of 10^{-6} Torr and the sample temperature never exceeded 160°C during implantation. The samples were firmly clamped to a water cooled holder and a thin sheet of indium was used to improve the thermal conduction at the sample/holder interface. The samples were held at low temperature in order to retard oxidation of the beryllium and to minimize the mobility of the implanted boron.

The samples used in the mechanical tests were subjected to one of two implantation treatments. One of these was designed to produce a reasonably flat

boron concentration profile extending from 100 nm to 650 nm beneath the surface. For the other, the doses were tailored to generate a graded boron concentration profile which peaked close to the surface and decreased gradually with increasing depth. The table is a list of the doses and ion beam energies used to produce the flat and graded distributions.

TABLE I
Boron doses ($\times 10^{17}$ B/cm²) and energies (keV) used to generate the flat and graded depth distributions.

	Energy (keV)					
	25	43	67	100	140	192
Flat	2.84	3.85	4.06	5.28	5.68	6.02
Graded	2.84	3.44	3.52	3.21	2.50	1.51

CONCENTRATION PROFILE MEASUREMENT

Rutherford backscattering was performed using 3 MeV alpha particles incident at 45 degrees to the surface normal and at 90 degrees to the detector. Because the kinematical scattering factors for boron and beryllium do not differ sufficiently to separate the signal due to the deeply buried boron from that due to the near surface beryllium, the determination of the boron profile involved more elaborate techniques. First, a spectrum from an unimplanted specimen was subtracted from the spectra of the implanted samples. The resulting difference spectrum has the advantage of being less sensitive to the choice of Be cross section. Then, a Rutherford backscattering simulation computer code³ was used to generate a theoretical difference spectrum which was compared to the observed difference spectrum. The matching process involves adjusting the concentration profile input to the code until the best fit to the observed data is achieved. The final form of the profiles for the flat and graded distributions are shown in figure 1.

It is estimated that the uncertainty in the boron concentration is 15 to 20% of the plotted values. The depth scale is less certain since the backscattering technique is sensitive only to the number of boron atoms per unit area and is insensitive to the local atomic density. It is expected, therefore, that the true distributions may differ from those in figure 1 by some expansion or contraction along the depth axis.

FRICTION, HARDNESS, AND WEAR TESTS

A Flex Pivot Wear Testor was used to evaluate the friction and wear. This is a pin-on-disk machine which is equipped with a means of measuring the torque necessary to hold the pin in position and thus gives a direct measure of the friction force. For both the wear and friction tests, a 1/8 inch diameter sapphire ball was loaded onto the samples with loads ranging from 20 to 60 grams and the sample was rotated under the pin at 100 rpm. A fresh spot on the ball and on the sample was used for each measurement. The friction coefficients were determined from the torque recorded during each run and the profiles of the wear tracks were obtained with a Dek Tak profilometer. No lubrication was used and the tests were performed dry in ambient air.

Figure 2 is a profile of a wear scar in unimplanted beryllium taken after ten minutes with a 20 gm load. This profile is to be compared with those obtained from the implanted samples (figure 3). In all cases, the profiles were taken after 10 minutes of wear. For both the flat and the graded boron distributions, no material removal was observed at the 20 gm load. While the flat distribution samples had no observable wear track at 20 gm, there was a track visible on the graded sample. The wear data for loads greater than 20 gm indicate that the samples with the flat

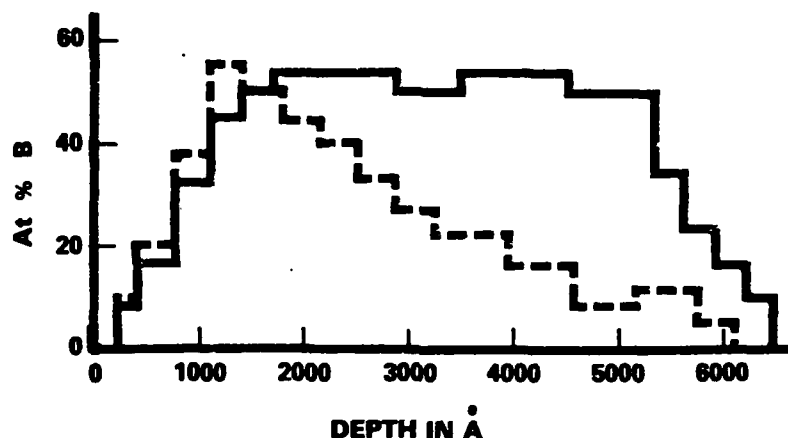


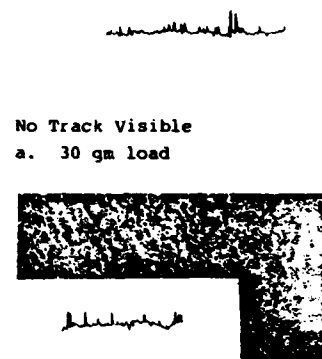
Fig. 1. Boron concentration as a function of depth for the flat distribution (solid line) and the graded distribution (dashed line).

distributions are able to withstand higher loads before the onset of catastrophic wear. The graded sample was able to withstand a 40 gm load without failing, whereas the flat boron distribution withstood a 50 gm load with little wear and 60 gm was required to produce substantial material removal.

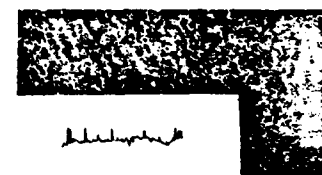


Fig. 2. Wear scar in unimplanted sample after 10 minutes at 20 gm load is 0.8 μm deep and 180 μm wide.

In addition to improving the wear resistance, ion implantation of boron also reduced the coefficient of friction. At the beginning of a run the friction of an implanted sample was typically about half that of the unimplanted samples. During the run it increased, usually with small intervals of rapid increase followed by long intervals of nearly constant value. Some stick-slip behavior was observed, and the variation of friction force during any small time interval within a run was about 12%. The variation from run to run, and at the same load, was somewhat

FLAT BORON DISTRIBUTION

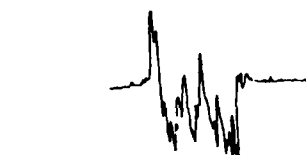
No Track Visible
a. 30 gm load



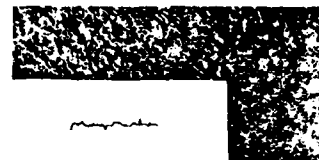
c. 40 gm load



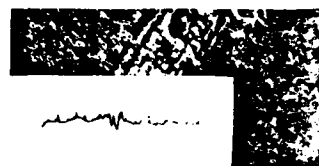
e. 50 gm load



g. 60 gm load

GRADED BORON DISTRIBUTION

b. 30 gm load



d. 40 gm load



f. 50 gm load

Fig. 3. Optical micrographs and profiles of wear tracks in B-implanted I-400 beryllium. The peak to peak variation is less than 200 nm for (a) through (e), 1.5 μm for (f), and 3 μm for (g). The horizontal scale is the same for all tracks. The scar in (g) is 150 μm wide.

larger, but the qualitative behavior of the coefficient with time was similar from run to run. The most consistently repeatable friction behavior was observed for the flat distribution samples with a 20 gm load. Here, the coefficient of friction remained at its initial value for the first minute, increased for the next 4 minutes, leveled off somewhat and then increased, but more slowly, throughout the remainder of the run. The graded samples exhibited more variation from run to run than the flat distribution specimens. For these specimens the friction increased slowly from its initial value for the first minute followed by 2 to 4 minutes of little or no increase. Then there was another interval of relatively rapid increase followed by a slower rate of increase until the end of the run.

Hardness measurements were made using a Knoop indenter with 2, 5, 10, 50 gm loads. Table II is a compilation of the results of these measurements. There is no significant difference between the hardness values obtained for the graded and flat boron distributions. This result is to be expected since the depth of penetration of the indenter is several times the thickness of the implanted layer even at the lowest load.

TABLE II
Knoop hardness data as a function of load.

Load (gm)	Knoop Hardness Number (Kg/mm^2)	
	Flat	Graded
50	356 \pm 20	341 \pm 4
10	542 \pm 75	762 \pm 75
5	1157 \pm 190	1211 \pm 190
2	1965 \pm 375	2233 \pm 390

ELECTRON MICROSCOPY

The samples used for transmission electron microscopy were implanted with boron at 25, 43, and 67 keV with the same doses used to produce a flat boron distribution (see table I). The higher energy implants were not performed because the boron which would have been introduced at the higher energies would have been removed during subsequent electropolishing. Figure 4a is a bright field micrograph of the unimplanted beryllium and 4b is the corresponding electron diffraction pattern. As expected, the only features observed in the unimplanted material are dislocations and grain boundaries. The implanted beryllium, on the other hand, contains additional contrast features (figures 4c and 4d). There is clear evidence that a second phase has precipitated. The portion of the unimplanted foil shown in figure 4a is 6.3 μm wide and 8 μm high and the micrograph of the B-implanted sample (figure 4c) covers a 12.7 μm x 16 μm region. The precipitates have a roughly circular cross section with a typical diameter of 50 nm.

Table III is a list of observed reflections and the beryllium compounds which may be present. An "x" indicates that the interplanar-spacing corresponding to an observed reflection is in agreement with a published value⁴ for the compound listed above. Since the second phase reflections do not appear as uniform rings, but instead are segments of rings, it is concluded that the precipitates exhibit preferential orientations. Thus, the absence of a reflection corresponding to a particular phase does not necessarily imply that that phase is not present. Since some reflections occur for each of the listed compounds, we must allow that each may be present. It is important to note that the borides also have strong reflections which would be too close to the central spot to be easily photographed. From the data listed in the table, the most likely compounds to have been



Fig. 4a-d. Bright field transmission electron micrographs and electron diffraction patterns of unimplanted beryllium (a and b), and B-implanted (c and d). The circular beryllium precipitates in c are typically 50 nm in diameter.

formed are Be_6B , Be_2B , and BeB_2 .

TABLE III

Beryllium compounds and observed inner planar spacing, $d(\text{\AA})$. An "x" indicates that the observed reflection is in agreement with a published d-value for the compound listed above.

$d(\text{\AA})$	Be	Be_6B	Be_2B	BeB_2	BeB_6	BeO
0.95	x		x			
1.12	x		x			
1.30			x			
1.33	x	x	x			x
1.57		x		x		
1.60		x	x	x		
1.72	x	x		x		
1.95	x	x		x		
2.06		x				
2.22		x		x	x	
2.32			x	x		
2.55				x		
2.60			x	x		

DISCUSSION AND CONCLUSION

Previous investigation of the mechanical properties of B-implanted beryllium have shown that in order to obtain reliable information about surface properties, it is highly desirable to perform a stress relief anneal of the as-machined specimens. Without this treatment, spontaneous changes occur which degrade the quality of the polished surfaces and increase the scatter in surface sensitive measurements. For this reason, all samples used in the mechanical tests were stress relieved after machining.

The Rutherford backscattering results indicate that peak boron concentrations of 50-55 atomic percent were generated and that the intended flat and graded profiles had been achieved. The measured boron profiles differ from what was expected in two respects. The peak concentrations are higher and profile widths are narrower than predicted by LSS. In performing the implants, the low energy doses were introduced first in order to use whatever sputtering occurs to bring the shallow boron as close to the surface as possible. However, no attempt was made, when applying the LSS calculations, to account for the effect of the presence of the boron implanted at low energy on the range of that implanted at high energy. Thus, it is reasonable that the resulting profiles are both narrower and higher than those predicted by an overly simplified application of the LSS range data.

The electron microscopy data provide conclusive evidence of second phase formation. Electron diffraction results suggest that more than one beryllium boride phase may be present. Since there is precipitation, it follows that the boron is mobile during implantation even though the temperature was intentionally held at low values. Thus the boron mobility must be the result of irradiation enhanced diffusion. The following is a possible sequence of events which could account for the presence of more than one boride phase. During the early stages of implantation, the boron-poor phases form and grow. But as the boron concentration increases, the boron-rich phases can begin to form. During the time that the boron-rich phases are forming, the original borides are likely to be dissolving; but if the dose rate is sufficiently high, the transformation to the boron-rich phases may not be completed before the implantation is finished. Of course, once the implantation process stops, the mobility of the boron reverts to the low value consistent with the temperature of the specimens. As a result, the non-equilibrium coexistence of different boride phases could occur.

Previous studies have shown that the hardness of boron implanted I-400 beryllium is increased by ion implantation, but from the results of the present investigation, it is clear that such measurements are not sufficiently sensitive to allow one to predict the differences observed in the wear behavior of the flat and graded boron distributions. The mechanical test results indicate that significant improvements of the wear resistance of I-400 beryllium have been produced by boron implantation. In addition, the samples with the flat boron distribution are able to withstand greater loads before the onset of catastrophic wear than are the graded samples.

ACKNOWLEDGEMENTS

This work was supported in part by the Office of Naval Research under contract N00014-77-C-0388.

REFERENCES

- 1 R. A. Kant, *Thin Solid Films*, 63(1979)27-30
- 2 D. Das, K. Kumar, E. Wettstein, J. Wollam, Materials Research For Advanced Inertial Instrumentation, Task 2: Gas Bearing Material Development, Technical Report R-1434, The Charles Stark Draper Laboratory, Inc., December 1980
- 3 J. F. Zeigler, R. F. Lever, and J. K. Hirvonen, "Ion Beam Surface Layer Analysis", editors, O. Meyer, G. Linker, and F. Kappler (Plenum, N.Y. 1976) p. 163
- 4 D. E. Sands, C. F. Cline, A. Zalkin and C. L. Hoenig, *Acta Cryst.* (1961) 14, 309

Section II.C

EFFECTS OF CARBON ON THE FRICTION AND WEAR OF
TITANIUM-IMPLANTED 52100 STEEL

I. L. Singer¹
R. A. Jeffries²

¹Surface Chemistry Branch
Chemistry Division
Naval Research Laboratory

²Geo-Centers, Inc.
Suitland, MD

This work was supported by the Office of Naval Research.

The Effect of Carbon on the Friction and Wear
of Titanium-Implanted 52100 Steel

I.L. Singer
Chemistry Division
Naval Research Laboratory
Washington, D.C. 20375

and

R.A. Jeffries
Geo-Centers, Inc.
4710 Auth Place
Suitland, MD 20746

Abstract

Auger spectroscopy, EDX and optical microscopy have been used to analyze friction and wear behavior of 52100 steel implanted with Ti to a fluence of $2 \times 10^{17}/\text{cm}^2$. Three implantation conditions were chosen to produce different C concentration profiles at the surface: disk 1 - Ti^+ implanted at 190 keV produced a partially carburized layer; disk 2 - Ti^+ at 190 keV followed by $\text{C}(2 \times 10^{17}/\text{cm}^2)$ at 50 keV produced equal and overlapping Ti and C profiles; disk 3 - Ti^+ implanted at 50 keV produced a more fully carburized layer than disk 1 but had less Ti and a smaller C/Ti ratio than disk 2. Disk 3 had the best tribological surface; the friction coefficient was $\mu=0.3$ and no wear was detected. Disk 2 displayed stick slip with an average $\mu=0.5$ and showed mild wear. Disk 1 showed high friction and severe wear. We conclude that the improved tribological surface of Ti-implanted steel results from vacuum carburization and not just the presence of excess C.

Effects of Carbon on the Friction and Wear of Titanium-Implanted Steel

Implantation of Ti at high fluences into Fe or steel creates a unique surface alloy (Ref. 1,2) with remarkable friction and wear behavior (Ref. 1,3-9). The alloy is a mixture of Fe-Ti-C (Ref. 1,2) with a microstructure shown to be amorphous (Ref. 2,3). Its friction coefficient in dry sliding contact against steel is typically half that of steel against steel (Ref. 1,3-5) and its wear resistance, both abrasive (Ref. 6,7) and adhesive, (Ref. 1,3-5,8,9) is increased significantly.

Improved tribological (i.e. friction and wear) behavior of Ti-implanted steel has been attributed to the Fe-Ti-C surface alloy, in particular to the excessively high concentration of C near the surface (Ref. 1,3). This unexpected constituent of the implanted surface enters the solid from the vacuum chamber, by a process which can be described as implant-assisted vacuum carburization (Ref. 3,10). During implantation, sputtering erodes the surface and uncovers implanted Ti, which reacts with residual gases in the vacuum chamber, producing surface carbide species. These carbon atoms then diffuse inwards producing a shallow carburized surface layer. It is not known, however, whether it is the presence of C itself or the process by which C enters the surface that is responsible for the formation of this remarkable tribological surface.

This study investigates the the friction and wear behavior of Ti-implanted steel in which the C concentration profiles were intentionally altered. Ti was implanted to a fluence of $2 \times 10^{17} \text{ Ti}^+/\text{cm}^2$ into three steel disks (AISI 52100-Fe/1.5 Cr/4C in at.%). Disk 1 was implanted at an energy of 190 keV. Previous studies have shown that surfaces implanted to this fluence at 190 keV were not fully carburized, which resulted in high friction and wear (Ref. 3,9). Disk 2 was implanted with Ti under identical conditions of

disk 1, and later implanted with C ($2 \times 10^{17} \text{C/cm}^2$) at 50 keV, chosen to produce similar implant profiles. Disk 3 was implanted with Ti to a fluence of $2 \times 10^{17} \text{Ti}^+/\text{cm}^2$, but at a lower energy of 50 keV. Implantation of Ti at lower energies enhances the carburization rate by placing Ti closer to the surface (Ref. 10), (i.e. the projected range decreases with energy). Results presented for each disk were obtained from two or more disks prepared on two separate occasions.

Composition vs. depth profiles of implanted disks were obtained by Auger profiling and interferometry; quantitative analyses of Auger data are based on reference compounds (Ref. 1,3). Fig. 1 presents composition profiles of Ti and excess C (the 4 at.% of C found in the bulk alloy has been subtracted out.) Fig. 1a (disk 1) shows a Ti profile which peaks at about 60 nm and a vacuum carburized layer about 50 nm deep. The non-Gaussian shape of the Ti profile indicates that the surface was sputtered during implantation (Ref. 11). Fig. 1b (disk 2) shows a similar Ti profile with implanted C and Ti overlapping one-to-one. (The concentration, of Ti in disk 2 is about 20% less than in disk 1 because implanted C dilutes the Fe-Ti alloy). Fig. 1c (disk 3) shows a Ti profile peaked nearer the surface and a more fully carburized layer than Fig. 1a.

Sputtering of the surface during implantation of 50 keV Ti ions not only enhances the carburization rate but also removes a greater percentage of implanted Ti as well. Energy dispersive X-ray analysis (EDX) of Ti in the three disks, presented in Table 1, confirms that a smaller percentage of Ti was retained in disk 3 than in disks 2 and 1. Retained Ti doses were also determined by graphical integration of Fig. 1 and agree to 15% with the EDX values in Table 1. Doses of incorporated C were also obtained by

graphical integration. The C to Ti dose ratios for the three disks are listed in Table 1. It is clear from Fig. 1 and Table 1 that although disk 3 was more carburized than disk 1, it had less C, less Ti and a smaller C/Ti ratio than disk 2.

The kinetic coefficients of friction (μ_k) of each of the surfaces were measured during low speed (0.1 mm/sec), dry sliding conditions in air. The geometry was a 1.27 cm diameter ball sliding against an implanted disk (both AISI 52100 steel of hardness $R_C \sim 60$). Strain gauges monitored friction and load (a constant 1 kg force, or 9.8N) for up to 20 passes, each 3 mm long, over the same track. Results of μ_k vs. number of passes are summarized in Fig. 2. All three disks had low μ_k values initially, although disks 1 and 2 displayed stick-slip, indicative of a somewhat higher adhesive contribution to the friction values. Disk 1 showed an increase to $\mu \sim 0.8$ before reaching a steady state value $\mu_k = 0.6$, that of steel-on steel. In the process, the partially carburized surface (50 nm thick) of disk 1 was sheared off, and upon reaching steady state, a considerable amount of debris covered the track (Ref.9).

The friction coefficient of disk 2 rose only to $\mu_k \sim 0.50$ and then leveled off. Stick-slip, however, continued in steady state. The wear track was not so severely scarred as that of disk 1. However, some mild wear had occurred as indicated by a track depth of ~ 20 nm measured by interferometry. Wear was also confirmed by EDX: the Ti/Fe ratio, inside the wear track was 10% less than the ratio outside the track, the equivalent of removing ~ 20 nm of the as-implanted surface (Fig. 1b).

The friction coefficient of disk 3, the low energy implant, leveled out at the low value of $\mu_k \sim 0.3$ and did not display stick-slip. This friction behavior is identical to that found on the fully carburized layer formed by a

fluence of 5×10^{17} Ti/cm² at 190 keV (Ref. 1,3,9). The 15-pass track of disk 3 showed no scarring or wear.

Friction and wear data show that disk 3, the low energy implant, had a tribological surface superior to that of the high energy dual implant, even though the latter had more C, more Ti, and a higher C/Ti ratio. The excess carbon in disk 3, however, resulted from vacuum carburization, which, as we suggested earlier (ref. 3) is responsible for the formation of a superior tribological surface. To date, the only explanation we can give for this effect is that the vacuum carburized Fe-Ti-C layer is amorphous. Miyoshi and Buckley recently investigated the friction behavior of Fe-based metallic glasses and found that amorphous foils had lower friction and greater wear resistance than recrystallized foils (Ref. 12).

Implantation of C (disk 2) did improve the tribological behavior of the Ti-implanted steel (disk 1). This improvement clearly indicates a synergistic effect of the dual implants since our experiments indicate that C alone (2 or 4×10^{17} /cm² at 50 keV) provides no substantial reduction in friction or wear. Implanted C in disk 2 probably increased the shear strength of the partially carburized layer, which without the extra C (e.g. in disk 1), sheared off after 8-10 passes. Stick-slip behavior of disk 2 is consistent with the enhanced adhesion (high friction) contact observed on Ti-alloyed Fe surfaces (Ref. 9). Adhesive contact was probably broken by shearing at the metal/oxide interface, producing the observed mild wear. The high concentration of C atoms at the dual-implant surface (~ 20 at %) may have promoted shear. Nevertheless, it is clear that implanted C in a Ti-implanted surface produced a surface that was tribologically inferior to a vacuum carburized surface, even though the C-implanted surface had more Ti and a larger C/Ti ratio.

We have also investigated the effect of reversing the order of implantation in the dual implant case: i.e. by implanting C-then-Ti. The friction and wear behavior was identical to disk 2 except that the friction coefficient for the C-then-Ti case was ~10% lower (stick-slip still occurred). We attribute this lower friction to the fact that the C-then-Ti implant had a slightly higher surface concentration of carbon than the Ti-then-C implant. Finally, we have also investigated dual implants of Ti^+ and B^+ (2 and $3 \times 10^{17} \text{ B}^+/\text{cm}^2$ at 50 keV). Friction was higher and wear more severe than for dual implants of Ti and C.

In summary, we have demonstrated that it is the vacuum carburized layer and not just the presence of carbon which creates the superior tribological surface of the Ti-implanted steel. The dose required to produce a fully carburized layer decreases as the energy of the implanted Ti decreases. This result is of great practical importance for the ion implantation processing of materials: lower fluences reduce production time and lower energies cut down beam heating problems. It also suggests that if sequential implants are to be performed at several energies (Ref. 4), e.g. to produce more uniform composition vs. depth profile, that the lowest energy implant should be done first. Also, for dual implants C should be implanted before Ti. Carbon implanted into Ti-implanted bearing steel had a secondary effect of reducing friction slightly, but may prove valuable in softer steels where friction reduction and solid solution strengthening might combine to improve tribological behavior.

Acknowledgments

We thank the Surface Modification and Analyses Branch at NRL for their support and cooperation with implantation.

References

1. C. A. Carosella, I. L. Singer, R. C. Bowers, and C. R. Gossett, Ion Implantation Metallurgy (Eds. C. M. Preece and J. K. Hirvonen, Metallurgical Society of AIME, Warrendale, Pa., 1980) p. 103.
2. J. A. Knapp, D. M. Follstaedt, and S. T. Picraux, Ibid., p. 152; Appl. Phys. Lett. 37 (1980) 330.
3. I. L. Singer, C. A. Carosella and J. R. Reed, Nucl. Inst. and Meth. 182/183 (1981) 923.
4. F. G. Yost, L. E. Pope, D. M. Follstaedt, J. A. Knapp and S. T. Picraux, Metastable Materials Formation by Ion Implantation (Eds. S. T. Picraux and W. J. Choyke, Elsevier, Amsterdam, 1982) p. 261.
5. T. E. Fischer, M. J. Luton, J. M. Williams, C. W. White and B. R. Appleton (ASME/ASLE Lubrication Conference, Washington, D.C. Oct. 1982) ASLE preprint No. 82-LC-3D-3.
6. I. L. Singer, R. N. Bolster, and C. A. Carosella, Thin Solid Films 73 (1980) 283.
7. R. N. Bolster and I. L. Singer, ASLE Transactions 24 (1981) 526.
8. J. K. Hirvonen, C. A. Carosella, R. A. Kant, I. L. Singer, R. Vardiman and B. B. Rath Thin Solid Films 63 (1979) 5.
9. I. L. Singer and R. A. Jeffries, J. Vac. Sci. Technol. March 1983 (to be published).
10. I. L. Singer, J. Vac. Sci. Technol. March 1983 (to be published).
11. F. Schulz and K. Wittmaack, Rad. Effects. 29 (1976) 31.
12. K. Miyoshi and D. H. Buckley, NASA Tech. paper 1991, March 1982.

Table 1

Retained Ti dose and C/Ti ratio for disks 1, 2 and 3

	<u>disk 1</u>	<u>disk 2</u>	<u>disk 3</u>
Retained Ti ($+1 \times 10^{16}/\text{cm}^2$) ^a	13	13	9
C/Ti ratio	0.060	1.0	0.23

- a. By EDX, calibrated against a Ti-implanted steel ($5 \times 10^{16} \text{Ti}/\text{cm}^2$ at 190 keV) for which the retention was observed to be almost 100%.

FRICTION COEFFICIENTS OF 52100 STEEL AGAINST Ti AND Ti+C IMPLANTED 52100 STEEL

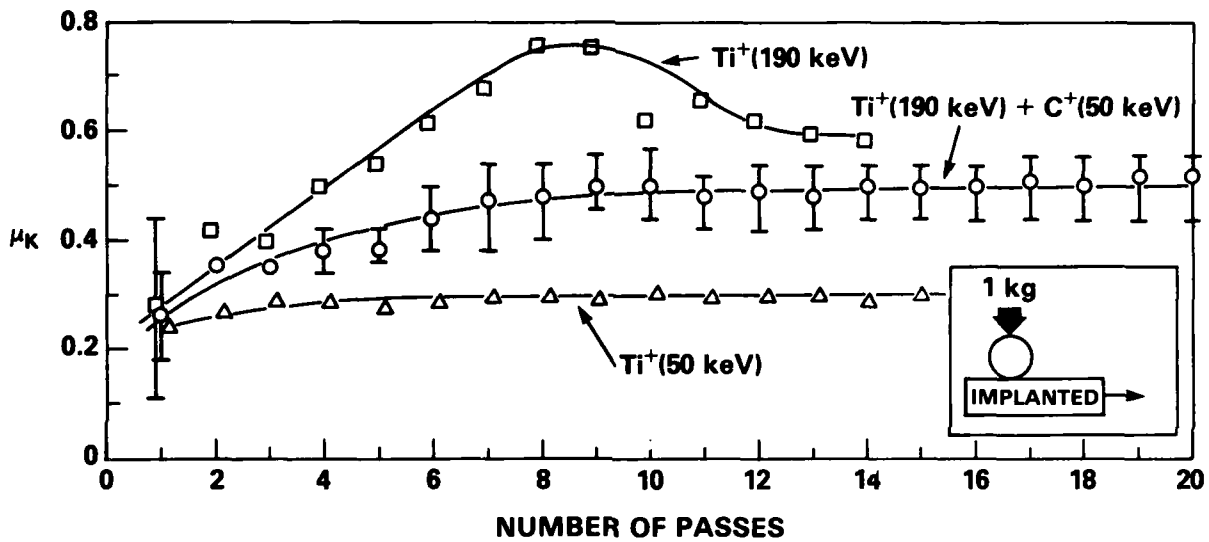


Figure 1. Auger composition vs. depth profiles of Ti and excess C (i.e. above bulk 4 at.%) in 52100 steel implanted to a fluence of $2 \times 10^{17}/\text{cm}^2$ with
 (a) disk 1 - Ti⁺(190 keV); (b) disk 2 - Ti⁺(190 keV) + C⁺(50 keV),
 (c) disk 3 - Ti⁺(50 keV).

CONCENTRATION PROFILES OF STEEL IMPLANTED TO $2 \times 10^{17}/\text{cm}^2$

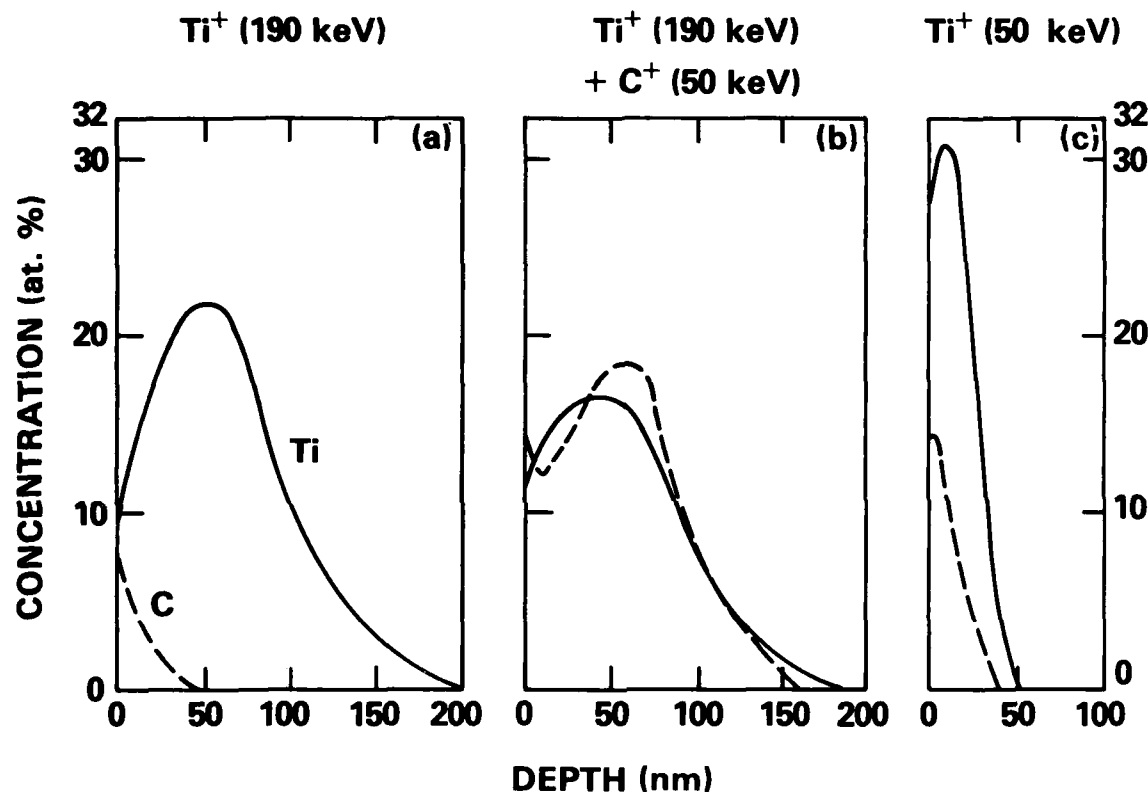


Figure 2. Coefficients of kinetic friction, μ_k , vs. number of passes over same track for: \square disk 1, \circ disk 2, Δ disk 3. Bar through data point indicates magnitude of stick slip. Inset. Schematic of sliding contact geometry.

Section II.D

A TECHNIQUE FOR STUDYING THE EFFECT OF ION IMPLANTATION ON
DISLOCATION STRUCTURES DEVELOPED DURING THE FATIGUE OF NICKEL

R. G. Vardiman

Physical Metallurgy Branch
Material Science and Technology Division
Naval Research Laboratory

This work was supported by the Office of Naval Research.

A TECHNIQUE FOR STUDYING THE EFFECT OF ION IMPLANTATION ON DISLOCATION STRUCTURES DEVELOPED DURING THE FATIGUE OF NICKEL

R. G. Vardiman

Introduction

Several recent studies (1-3) have shown that ion implantation can produce substantial increases in the fatigue life of a variety of metals and alloys. In some cases this improvement was attributed to a greater homogeneity of slip near the surface, reducing the size of surface slip steps which could develop into cracks. This mechanism was supported by surface examination in the SEM, but no direct observations of near surface dislocation configurations were made. For Ti-6Al-4V (1) the fatigue cracks were found to originate below the surface, well beneath the implanted layer. In this case the possibility has been raised (4) that the hard implanted layer actually increases the stress level required to produce a given amount of slip. The uncertainty in the actual microscopic mechanism for fatigue life improvement suggested the desirability of a study of near surface dislocation structure in fatigue specimens.

Transmission electron microscopy (TEM) is the best technique for dislocation structure studies. Ideally for near surface observations sections perpendicular to the surface should be taken. However, no techniques are available for producing thin area in the region of interest directly from such a transverse section. By plating the surface with a thick layer of the same or similar metal, it might be possible to make a TEM sample which had an area at the original surface thin enough for observation.

In order to facilitate development of a suitable technique, it was decided to do tension-tension fatigue on nickel wires. The usual preparation for plating which involves surface removal could not be used in this case, but it was hoped that plating the wires with nickel would give sufficient adhesion to allow surface preservation on thinning. A satisfactory technique has in fact been developed and will be described here. The initial results on pure nickel show only a small effect of implantation which can be understood in terms of the nature of the dislocation structure observed by TEM. Further work on a nickel alloy is currently in progress. The same experimental technique reported in this paper will be used in the alloy study.

Experimental Technique

Forty mil diameter nickel 200 (99.5% Ni) wire in the cold worked condition was obtained from a supplier. Sections were straightened by pulling in a tensile machine, then given a two

stage electropolish. First, a gauge length was prepared by masking all but a half inch length, and polishing in a solution of 60% H_3PO_4 - 40% H_2SO_4 at 8V to reduce the diameter to 32 mils. The principal object here is the even removal of material along the entire gauge length. The masking was then removed and a 2.5 inch length with the gauge section centered was polished in a solution of 37% H_3PO_4 , 56% glycerol, 7% H_2O at 35 V to remove an additional 1 to 2 mils. This left the entire length clean, with an excellent polish on the gauge section. The wires were then annealed 1/2 hour at 800°C in vacuum to produce a recrystallized grain structure of roughly 70 μ in size.

Ion implantation was performed on the NRL high current implanter. Carbon ions were implanted to a dose of 2×10^{17} atoms/cm² at a voltage of 125 keV. This produces a peak concentration of 17 atom pct. C at a depth of 150 nm. No precipitates are expected as nickel does not form carbides.

For the fatigue test, the ends of the wire are soldered into holes slightly larger than the wire diameter drilled into 0.25 in. diameter copper cylinders. These could then be slipped into specially designed holders attached to the test machine so that no undesired stresses were placed on the wires before testing. The test machine was hydraulically controlled, with maximum loads constant to better than +1%. The R value ($S_{\text{max}}/S_{\text{min}}$) was +0.1, the frequency 20 Hz. After testing, both the fracture surface and wire sides were examined in the SEM.

Specimens were prepared for plating by careful cleaning, then by being the anode (polishing) in a nickel chloride acid bath for a few seconds to remove the surface oxide layer. Current was immediately reversed in this bath for several minutes plating, then the specimen was moved directly to a nickel sulfamate bath to finish plating. The sulfamate solution produces a good plate at high current, and one which has a relatively low internal stress. Platings were made not only on representative fatigue specimens, but also on samples as annealed, as implanted, and tensile tested to typical fatigue stress levels.

15 mil slices of the plated specimens were cut on a thin slicing machine and mechanically polished to 4 mils. Thinning for TEM was done both electrolytically and in the ion mill. The former was found most satisfactory, as contrast effects from the surface damage produced in milling tended to obscure the underlying dislocation structure.

Results

Nickel is relatively soft; the yield strength of the wire used here is less than 10 ksi. To obtain fatigue lifetimes in the range of 10^5 - 10^6 cycles it is necessary to use stresses near

50 ksi (see Fig. 4). Consequently the specimen is markedly strained in the initial fatigue cycle. SEM examination shows slip markings on the surface and irregular movement between the grains (Fig. 1, left). In the TEM, a cellular dislocation structure is present after this initial cycle (Fig. 2). The density and cellular structure near the surface seem reduced (Fig. 3). Differences in either surface markings or dislocation structure are difficult to discern after fatiguing to fracture. Secondary cracks near the fracture surface seem to have some preference for grain boundaries (Fig. 1, right). Ion implanted specimens give essentially the same results, and fatigue lifetimes are only slightly greater than when unimplanted (Fig. 4).

Discussion

The extensive plastic deformation during the initial cycle probably severely disrupts the implanted layer, greatly reducing the influence of the implantation on the fatigue life. The cellular dislocation structure prevents the formation of persistent slip bands (PSB's) which could lead to surface cracks. Because of the relative movement of the grains, cracks are more easily developed in the grain boundaries, again minimizing the influence of implantation.

For these reasons the effect of ion implantation on fatigue should be much stronger for an alloy where solid solution strengthening greatly increases the yield strength. The fatigue endurance limit should then be below the yield point, PSB's will develop, and the effect of implantation on the slip mode and density should be more evident.

The technique described here seems satisfactory, so we have chosen a nickel-20 pct. chromium alloy for further study. Chromium is fully soluble to this amount, so the polishing and plating methods should carry over. It is hoped that work on this alloy will reveal some information on the mechanisms of implantation increased fatigue life.

References

1. R. G. Vardiman and R. A. Kant, J. Appl. Phys. 53, 690 (1982).
2. A. Kujore, S. B. Chakraborty, E. A. Starke, Jr., and K. O. Legg, Nucl. Inst. and Math., 182/183, 949 (1981).
3. H. Herman, *ibid.*, p. 887.
4. J. C. M. Li, private comm.



R-930

Figure 1

SEM micrographs of nickel wire: left, strained in tension to 50 ksi; right, fatigued 4×10^5 cycles at 50 ksi.

AD-A134 457

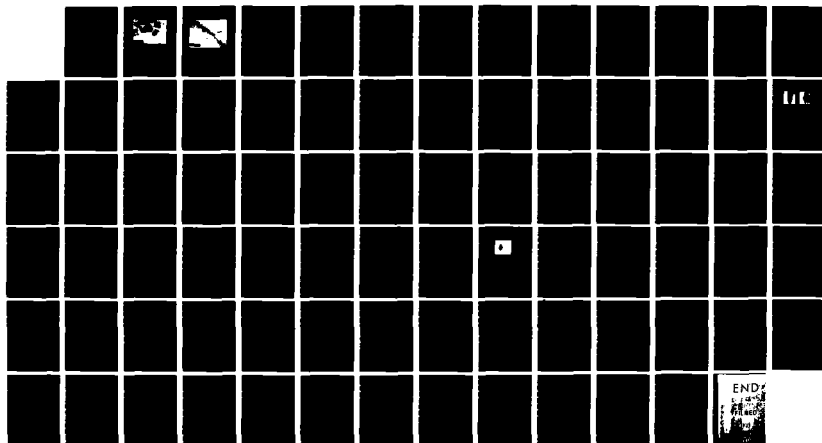
THE USE OF ION IMPLANTATION FOR MATERIALS PROCESSING
(U) NAVAL RESEARCH LAB WASHINGTON DC F A SMIDT
28 SEP 83 NRL-MR-5177

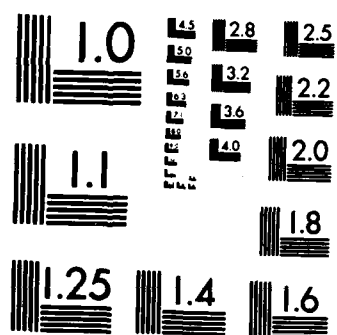
2/2

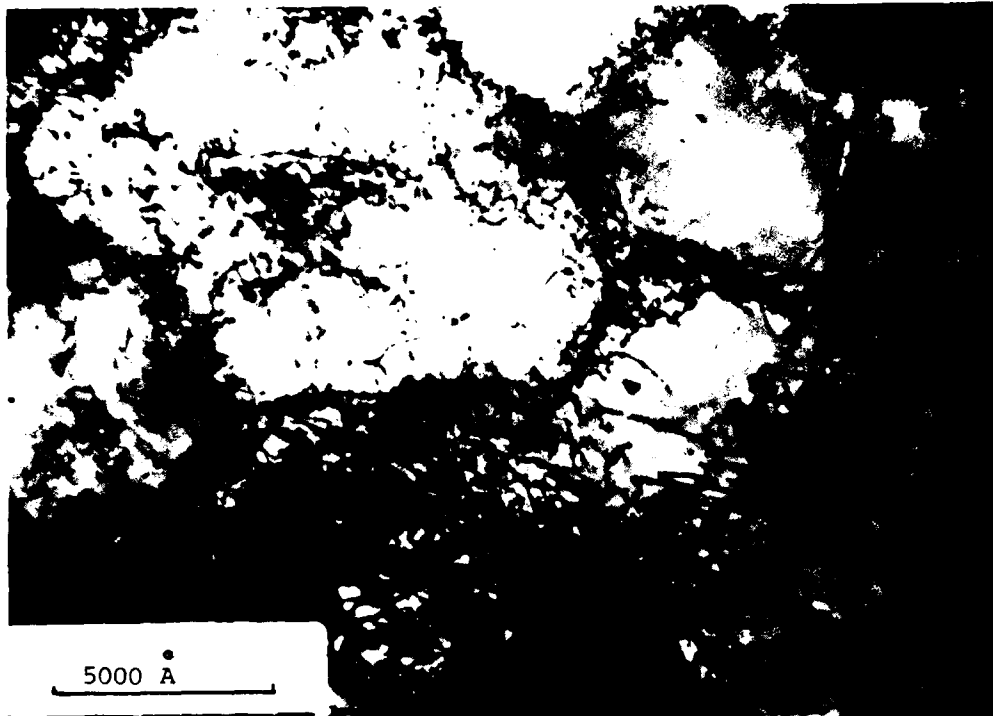
UNCLASSIFIED

F/G 20/8

NL



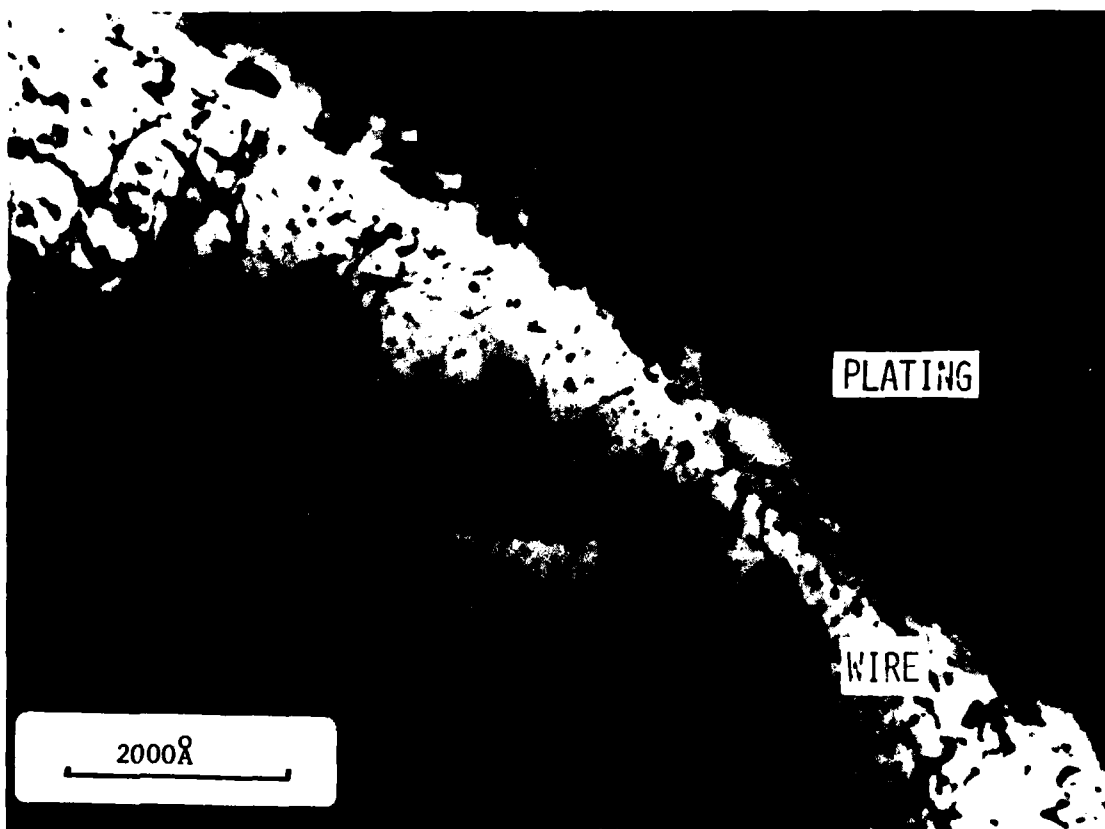




R-931

Figure 2

TEM micrograph of nickel wire strained in tension to 50 ksi (dark field).



R-932

Figure 3

TEM micrograph of nickel wire fatigued 4×10^5 cycles at 50 ksi (dark field).

Ni WIRE FATIGUE

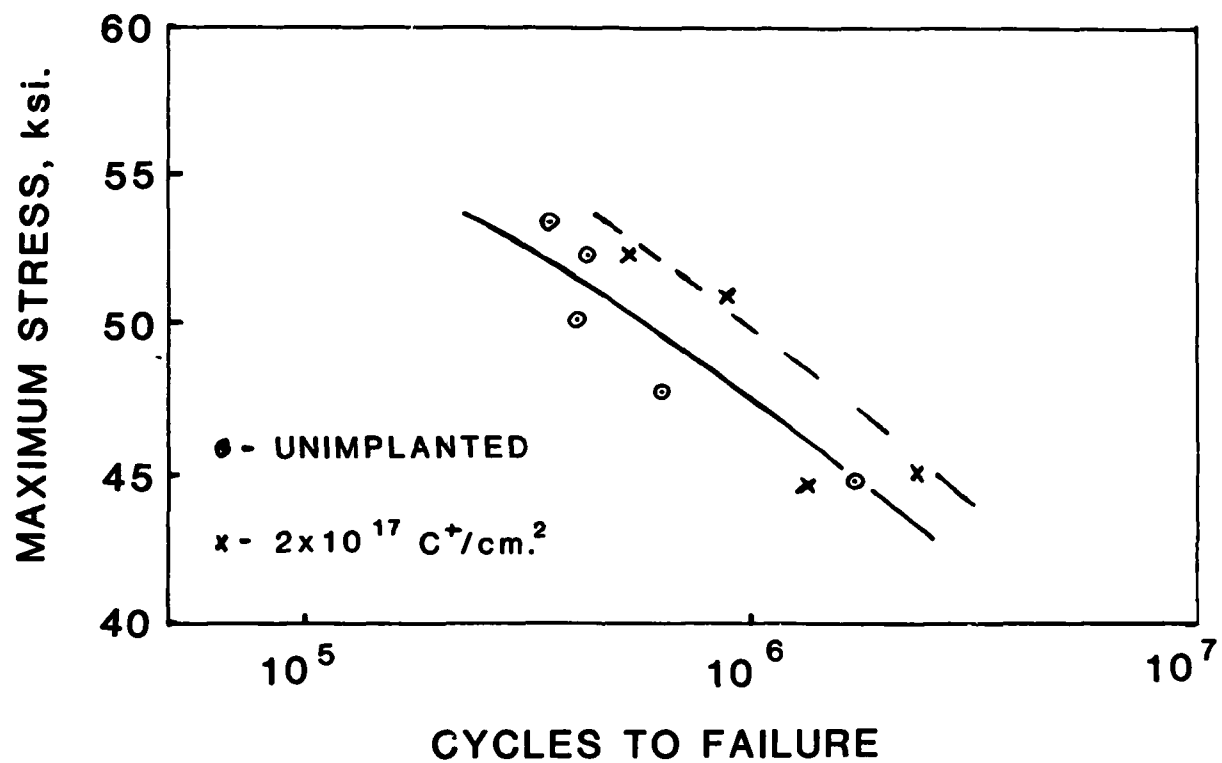


Figure 4

Cycles to failure vs maximum stress, Ni 200 wire, $R = 0.1$.

Section III.A

ION IMPLANTATION EFFECTS ON THE THERMAL OXIDATION OF METALS

K. S. Grabowski¹
L. E. Rehn²

¹Materials Modification and Analysis Branch
Condensed Matter and Radiation Sciences Division
Naval Research Laboratory

²Materials Science Division
Argonne National Laboratory
Argonne, Illinois

This work was supported by the Office of Naval Research at Naval Research Laboratory and by the Department of Energy at Argonne.

ION IMPLANTATION EFFECTS ON THE THERMAL OXIDATION OF METALS*

K. S. Grabowski
Naval Research Laboratory
Washington, DC 20375

L. E. Rehn
Materials Science Division
Argonne National Laboratory
Argonne, Illinois 60439

In the past decade, ion implantation has been shown to reduce oxide thicknesses up to tenfold in survey experiments on Ti, Zr, Ni, Cu, and Cr, and to enhance the long-term oxidation resistance of some high-temperature alloys. This review summarizes the major results of previous work. Important concepts are illustrated using recent experimental results obtained from a He-implanted Ni-1 at.% Pt alloy. Collectively, the results indicate that ion implantation has considerable potential for reducing oxidation, and as a research tool to investigate the mechanisms of thermal oxidation in metals. However, more thorough work needs to be done before the influences of ion implantation on the oxidation of metals can be understood.

*Portions of this work supported by the U.S. Department of Energy

Introduction

The effort invested during the last decade to determine the effects of ion implantation on the thermal oxidation of metals has been comprehensively reviewed from a chronological (1) and a mechanistic (2) viewpoint by Dearnaley, and more recently by Bennett (3). Research in this area was initially motivated by observations that ion implantation reduced the room-temperature tarnishing of some metals. A number of survey experiments on Ti, Zr, Ni, Cu, and Cr have shown that oxide thicknesses can be reduced by as much as a factor of ten by ion implantation. Implantation work on high-temperature alloys was initiated because alloying additions of Y, Ce, and Al are known to improve their oxidation resistance. By using ion implantation to allow only a thin surface layer, it was anticipated that oxidation resistance could be maintained using less of these additions, and without sacrificing desirable mechanical properties. Some success in this area, as well as a better understanding of how Y and Ce improve oxidation resistance, have been obtained (1-3).

The results suggest that ion implantation can be used to control the thermal oxidation of metals. They also show that implantation is a useful research tool for investigating the complex mechanisms of thermal oxidation. Measurements of the redistribution of implanted elements, and of their influence on oxidation kinetics and on oxide microstructure should help provide a better understanding of oxidation mechanisms (e.g., Berti et al.'s work on Zr (4,5) and a number of efforts on Fe, Ni, and their alloys, described in a recent conference session on high-temperature oxidation (6)), but to date the potential of this research tool has been underutilized.

This review summarizes the present understanding of the thermal-oxidation mechanisms of metals, and the major results of earlier ion-implantation work. Important concepts are illustrated using recent experimental results obtained from a He-implanted, Ni-1 at.% Pt alloy. More detailed reviews of the thermal oxidation of metals may be found in the literature (1,7-9).

Thermal Oxidation of Metals

Studies of metal oxidation frequently involve the rate of oxidation, since on thermodynamic grounds it is inevitable that most metals will oxidize. Interest in oxidation kinetics is especially pronounced at elevated temperatures, where the thermal-oxidation rate is often sufficiently fast to have significant engineering consequences. At present, the oxidation kinetics of very thin oxide films (≈ 10 nm) are not well understood, partly because complicated space-charge effects often control the growth process. The isothermal oxidation of thicker films, on the other hand, is frequently described by the classical expression first derived by Wagner (10):

$$x^2 = kt + x_0^2, \quad (1)$$

where x is the oxide thickness, t is the oxidation time and k is the parabolic-oxidation rate constant. Parabolic oxidation occurs when oxide growth is controlled by the diffusion of anions (O^{2-}) and/or cations (M^{+}) through a contiguous, thickening oxide film.

Significant departures from Equation 1 are observed if the protective oxide film is ruptured. Stresses generated in the oxide layer during its

growth may rupture the oxide and greatly enhance the oxidation rate. Stresses can be generated in a number of ways. Oxides which grow predominantly via anion diffusion (e.g., TiO_2 , ZrO_2 , and Al_2O_3), form new oxide at the metal/oxide interface which is constrained by the surrounding material. If the atomic volume of the oxide is larger than that of the metal, as is usually the case, large compressive stresses can be produced in the oxide film. Conversely, cation-diffusing oxides (e.g., NiO , Cu_2O , and Cr_2O_3) form new oxide at the unconstrained, gas/oxide interface. Nevertheless, stresses have been observed in the cation-diffusing oxides as Stringer (11) has indicated in his review on the subject. The mechanisms frequently proposed to explain the stresses include (i) a lattice-parameter mismatch between a coherent oxide layer and the underlying metal substrate, (ii) oxygen or lattice-defect dissolution into the underlying metal, or (iii) fresh oxide formation along pores, cracks, or grain boundaries within the oxide layer. Stresses are also generated in both anion- and cation-diffusing oxides following a temperature change, due to the difference in the thermal expansion of the metal substrate and its attached oxide film.

Additional departures from parabolic oxidation are caused by more subtle transformations in the oxide microstructure, which alter the rate-controlling diffusion mechanism. The formation of a protective alumina (Al_2O_3) or chromia (Cr_2O_3) layer on high-temperature alloys is one example of this effect. Another is the apparent gradual decrease in the density of short-circuit diffusion paths during the oxidation of Zr (12), and of Ni and Cu (13).

Even when parabolic-oxidation occurs, the oxide growth process may be complex. For many metals, the rate constant, k (Equation 1), depends on a variety of experimental parameters such as metal purity, sample heat treatment, and surface-polishing procedure. In addition, k does not exhibit a simple temperature dependence. In a manner analogous to diffusion in many metal oxides (14,15), there is a high-temperature oxidation regime where the growth rate is controlled by bulk diffusion, and a low-temperature regime where extrinsic defects and short-circuit pathways in the oxide enhance diffusion and consequently the oxide growth rate. As an example, the high and low-temperature regimes of Ni oxidation are illustrated in Figure 1. Above 900°C the activation energy for k equals that for Ni diffusion in bulk NiO. But, below 900°C the apparent activation energy is about 50% less than for Ni diffusion in bulk NiO. Smeltzer and Young (7) have argued that this apparent decrease in the activation energy is a common phenomenon (see Table I as taken from their review), and is caused by an increasing density of short-circuit diffusion pathways (grain boundaries and/or dislocations) with decreasing oxidation temperature. Figure 1 also shows that k depends strongly on the crystallographic orientation of the Ni substrate, being ten times larger on (100) surfaces than on (111) surfaces. A number of authors (13,16,17) have proposed that this anisotropy is caused by epitaxial relationships between the oxide and metal. For some metal orientations, pseudo single-crystal oxide films form, but for others two or more orientations of oxide crystallites are produced. As the number of oxide orientations increases, the incidence of incoherent or large-angle boundaries increases, and the density of short-circuit diffusion pathways in the oxide and the oxidation rate also increase. The metal orientation dependence can cause a threefold variation in the oxide thickness on a polycrystalline sample.

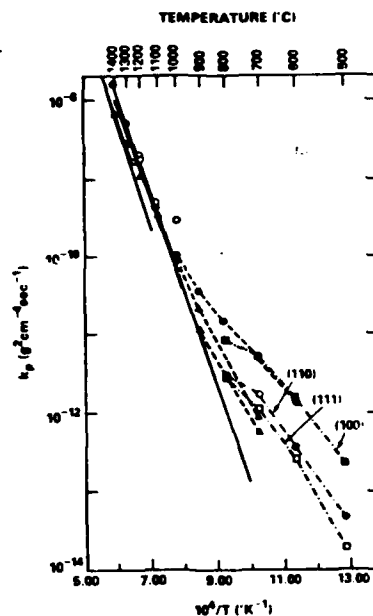


Figure 1. Parabolic-oxidation rate constant, k , for Ni as a function of temperature, as measured by various investigators. Low-temperature results for Ni single crystals are shown. (From Smeltzer and Young (7)).

Table I. Activation Energies for Parabolic-Oxidation Rate Constant and for Lattice Diffusion in Oxides

Metal	Oxide	Temperature Range (°C)	Oxidation E_o (kJ/mol)	Diffusion E_d (kJ/mol)	E_o/E_d
Cr	Cr_2O_3	700-1100	157	331	0.47
Ni	NiO	400-800	159	254	0.63
Cu	Cu_2O	300-550	84	151	0.56
Zn	ZnO	440-700	104	305	0.34
Ti	TiO_2	350-700	123	251	0.49
Zr	ZrO_2	400-860	134	234	0.57

From this brief summary, it is evident that ion implantation may reduce the oxidation rate by: (i) influencing the distribution of space charge within a thin oxide layer, (ii) producing a crystallographic phase having slower ionic-diffusion rates, (iii) reducing the density of short-

circuit diffusion pathways in the oxide, or (iv) preventing rupture of the oxide; for example by reducing or relieving the oxidation induced stresses, or by improving the mechanical strength of the oxide. Evidence for a number of these mechanisms has been obtained. These changes may be caused by the chemical influence of the implanted element (a chemical effect), or by the physical effects of the ion-implantation process. In this paper we consider the physical effects to include: (1) lattice damage, (2) surface contaminant removal and/or intermixing with the substrate, and (3) surface morphological changes induced by sputtering.

Ion-Implantation Effects on Thermal Oxidation

The ion implantations performed in the thermal-oxidation studies of pure elements and alloys have generally utilized the following conditions. The selected ions were implanted at ambient temperature (although some beam heating may have occurred), at pressures below 10^{-3} Pa, to ion doses between 5×10^{14} and 1×10^{17} cm $^{-2}$, and at energies near 100 keV. The peak concentrations of implanted elements and of induced lattice defects, of course, depend strongly on the particular implantation parameters. High-dose implantations of heavy ions produce near-saturation concentrations of the implanted atoms in the target. The saturation concentration depends upon the number of target atoms sputtered per ion incident on the target. In general, concentrations of 10 to 50 at.% were produced between the surface and the mean ion range in the target (typically ~ 100 nm). A large amount of lattice damage (many tens of dpa) was also produced. Light-ion implantations, which cause less sputtering, produce near-gaussian distributions of the implanted atoms in the target, centered about the mean ion range. Peak concentrations of ~ 10 at.% were produced at ~ 0.25 - 1.0 μ m beneath the surface in these cases. Intermediate-mass implantations and low-dose heavy-ion implantations produced intermediate distributions of the implanted ions. Of course, these distributions may have been substantially altered during thermal oxidation.

Pure Elements

The goal of the experiments on Ti, Zr, Ni, Cu, and Cr was to quantify the effects of ion implantation and to correlate these effects with certain properties of the implanted elements. After ion implantation and oxidation, the ratio (R) of the amount of oxygen on an ion-implanted region to that on an unimplanted region was measured typically using ion-beam analysis techniques. Because these techniques are limited to oxides thinner than ~ 2 μ m, oxidation temperatures generally could not exceed 800°C. The effects of ion implantation on the kinetics of oxidation were only studied in detail by Bentini et al. (18) for Zr. They observed nearly parabolic kinetics for a number of oxidation temperatures, enabling some extrapolation of their results to other oxidation conditions. The remaining surveys typically investigated oxidation at only one temperature and time.

Figure 2 identifies all the ions implanted into Ti, Zr, Ni, Cu, and Cr in the experiments whose results were published by October 1981. The influence of implanted ions on the oxidation rate of Ti and Zr is shown, but is qualified as potential because only limited experimental results are available. An ambivalent indication means that the result apparently depended upon the concentration of the implanted element. The influence of implanted ions on the oxidation rate of Ni, Cu, and Cr is not shown because the experimental results were extremely sensitive to the physical effects

(a) 30 IONS IMPLANTED INTO TITANIUM
PERIODIC TABLE OF THE ELEMENTS

(b) 21 IONS IMPLANTED INTO ZIRCONIUM
PERIODIC TABLE OF THE ELEMENTS

[illegible]

107

Titanium

Oxide thicknesses on Ti were reduced by as much as 40% by ion implantation. Surprisingly, even small quantities of the implanted element were effective. The reductions were somewhat correlated with ions having (i) a large ionic radius, (ii) a large enthalpy of oxide formation, and (iii) a limited solubility in Ti.

Dearnaley and coworkers (19-21) measured R values from 0.6 to 2.0 in Ti foils 3-50 μm thick; the most significant reductions were produced by Ba, Rb, and Cs implantations. The largest enhancements were produced by Ru, Ni, and Bi implantations. Because Ar and Ti implantations were observed to slightly increase R, all the implanted Ti foils were annealed at 850°C prior to oxidation to minimize the physical effects of ion implantation. The samples were subsequently oxidized in oxygen at 600°C for ~ 1 h, producing oxide films ~ 100 -200 nm thick.

In many foils a small amount of the implanted element was found on the opposite side of the foil after preoxidation annealing. Presumably, the element diffused rapidly through the foil along grain boundaries and dislocations. Consequently, similar oxidation results were usually observed on both faces of a foil, despite the much smaller average concentration on the unimplanted side. However, disparate results were obtained for the opposite faces of foils implanted with Ce, Au, and Lu ions.

Attempts to correlate the measured R values for Ti with properties of the implanted elements have met with limited success. The largest reductions were generally found for implanted elements with both a large ionic radius and a large enthalpy of oxide formation. Both Dearnaley (1,2) and Bennett (3) have argued that inhibiting elements may segregate to short-circuit diffusion pathways in the oxide due to their large size, trap fast diffusing oxygen, and thus inhibit oxidation. More recently, Galerie (22) has observed that insolubility of an implanted element in Ti, combined with its ability to form ternary oxides with Ti, correlate well with its ability to inhibit the thermal oxidation of Ti.

Clearly, additional investigations of Ti oxidation are needed. Measurements of segregation to grain boundaries in TiO_2 and its effect on oxygen diffusion, and measurements of the Ti oxidation rate at temperatures near the solvus for implanted elements would be particularly helpful.

Zirconium

Extensive experiments on Zr were undertaken to substantiate the results obtained from the closely related metal, Ti. However, while comparable reductions in oxide thicknesses were produced by ion implantation, a substantially different correlation between the results and the size of the implanted ion was observed. This disparity suggests that different mechanisms are responsible for the reductions of Zr and Ti oxidation. For Zr oxidation, the influence of implanted ions on oxide plasticity is believed to be important.

Dearnaley et al. (20) and Bentini et al. (18) measured R values from 0.7 to 6.0 in their extensive experiments; the best inhibitors were Co, Cu, Mo, Ni, and Sn. The greatest enhancements were produced by high-dose implantations ($5 \times 10^{16} \text{ cm}^{-2}$) of Cs and Eu. Zr specimens were implanted to ion doses between 5×10^{14} and $5 \times 10^{16} \text{ cm}^{-2}$ and oxidized between 380 and 550°C for up to 10 h in oxygen. Oxides up to 2- μm thick were produced, and

a negligible influence from the physical effects of implantation were reported. Bentini et al. (18) observed nearly parabolic kinetics for unimplanted and for Ni-, Cu-, and Ca-implanted specimens.

The dose dependence of R was also measured for 13 different ions (Al, Ca, Co, Cr, Cu, Eu, Fe, Mo, Nb, Ni, Sb, Sn, and V). Usually the influence of implantation increased monotonically with dose. However, some ions (Cr, Fe, Nb, Sb, and V) inhibited oxidation for doses below $1 \times 10^{16} \text{ cm}^{-2}$, but enhanced oxidation for higher doses. Precipitation of the implanted element at the higher doses may be responsible for this dose dependence.

An intriguing correlation was observed between the R value for low-dose implantations ($3-5 \times 10^{15} \text{ cm}^{-2}$) and the ionic radius of the implanted element, as is shown in Figure 3. For an ionic radius between 80 and 100% of Zr^{4+} , oxidation was inhibited by all the ions except Ti. Berti et al. (4,5) compared the oxides formed on Ti- and Ni-implanted Zr and observed marked differences in the lateral and depth distributions of O, Ti, and Ni. Whereas implanted Ni migrated to the oxide/metal interface during oxidation, implanted Ti migrated to the surface and became evenly distributed in the oxide. They also observed that Ni implantation prevented the preferential oxidation of Zr grain boundaries, but Ti implantation did not. Berti et al. (5) argued that correctly sized implanted ions may need to migrate to the metal/oxide interface to reduce Zr oxidation.

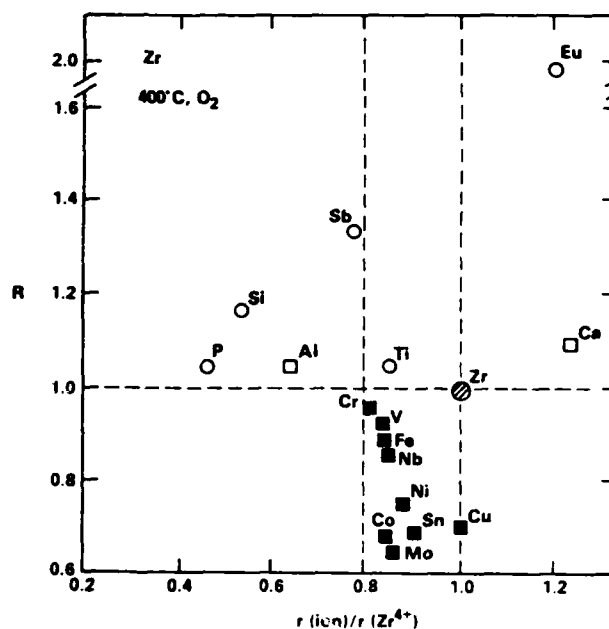


Figure 3. Ratio of oxygen uptake on low-dose implanted regions of Zr to that on unimplanted regions. Solid symbols show the beneficial effect of most ions with an ionic radius of 80-100% that of Zr^{4+} . (From Bentini et al. (13)).

Although its meaning is uncertain, this correlation with the ionic radius is consistent with results obtained from alloys prepared by conventional techniques. Dearnaley et al. (20) and Bentini et al. (18) both argued that appropriately undersize cations in ZrO_2 may increase the oxide plasticity, thus relieving oxidation induced stresses. The reduced stresses may either prevent oxide rupture or alter the oxide microstructure, thereby reducing the rate of oxidation. Measurements of the influence of implantation on oxidation-induced stress, and of the influence of applied stress on the oxidation of implanted Zr (e.g., as Bennett and coworkers (3) performed on a Ce-implanted steel) need to be performed.

Nickel

Ion implantation of Ni produced results quite different from those obtained from implanted Ti and Zr. The physical effects of ion implantation (i.e., lattice damage, or changes in the contamination or morphology of the surface) strongly influenced Ni oxidation, reducing oxide thicknesses by a factor of 5 at $\sim 600^\circ C$. The physical effects were similarly important in long term oxidations at $1100^\circ C$. Chemical effects of implanted elements also influenced Ni oxidation, both at ~ 600 and $1100^\circ C$, but the data were insufficient to establish any meaningful correlations between the results and properties of the implanted elements. Precipitate formation and oxide doping led to reduced oxidation rates at $1100^\circ C$.

The survey experiment by Goode (23) also indicates that physical effects of implantation can strongly influence Ni oxidation. Regardless of the ion implanted (see Figure 2c), he measured an R value of ~ 0.2 when the specimens were subsequently oxidized at $630^\circ C$. In all cases, a dose of $2 \times 10^{16} \text{ cm}^{-2}$ was used and oxides approximately 500-nm thick were produced during the 15-min exposure to oxygen.

To investigate the physical effects, 1 h annealing treatments were performed on Ni-implanted specimens prior to their oxidation. The results are shown in Figure 4. A maximum R value of 1.8 was obtained following preoxidation annealing at $370^\circ C$. Annealing in excess of $800^\circ C$ was required to completely remove the effect of self-ion implantation. Perhaps the onset of vacancy migration, or the dissolution of defect clusters in Ni causes the observed temperature response of R. Further evidence for a physical effect was found by annealing inert-gas implanted specimens at $370^\circ C$ prior to oxidation. R increased with the ion mass, in accordance with the expected increase in the energy deposited into atomic collisions.

Chemical effects of the implanted ions were also observed. For Ca, Bi, and Ce implantations, R values of 0.4 were obtained after preoxidation annealing at both 370 and $510^\circ C$. As these were the three largest implanted ions, there is a suggestion that large implanted ions inhibit the oxidation of Ni.

Recent experiments by Peide et al. (24) and by Stott et al. (25) on the oxidation of ion-implanted Ni at $1100^\circ C$ indicate that both chemical and physical effects are also important during high-temperature Ni oxidation. For oxidation times up to ~ 1 h, a strong chemical influence of implanted Cr or Li was observed. Initially, both elements formed ternary oxides with Ni which reduced the oxidation rate. Gradually, the Cr and Li dissolved into the surrounding NiO, thus altering the bulk diffusion of Ni^{2+} and

consequently the oxidation rate. After ~ 5 h of oxidation the dopants became sufficiently dilute in NiO, that microstructural changes induced in the oxide by the implantations dominated the oxidation rate. All the implanted ions (Li, C, Ar, Ni, and Cr) enhanced the oxidation rate of Ni to some extent for these times. This was attributed either to rapid diffusion of Ni through a higher density of oxide grain boundaries, or to O_2 migration through pores which were sometimes observed in the oxide.

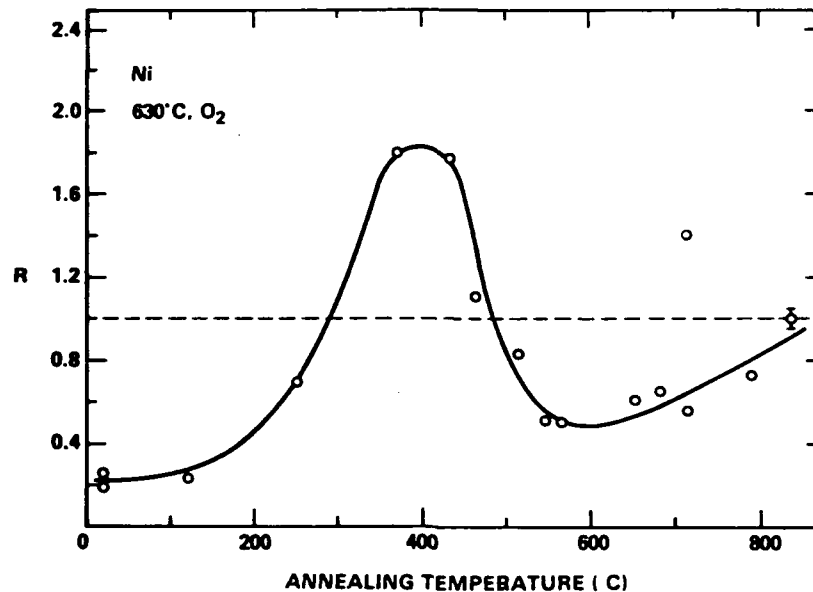


Figure 4. Oxygen-uptake ratio on self-ion implanted Ni, annealed at various temperatures prior to oxidation at 630°C. (From Goode (23)).

Copper

Several groups have investigated the effects of ion implantation on Cu oxidation, and have found up to fivefold reductions in oxide thicknesses. In general, small ions produced the greatest reductions while large ions enhanced the oxide thickness. The results were strongly sensitive to the physical effects of ion implantation and to the precise experimental procedures. Some of the results could be explained by the formation of an electrical-barrier layer in the oxide of ion-implanted specimens.

The earliest study, by Rickards (26), involved the effect of Al and Cu implantations on the oxidation of <110> single-crystal Cu at 320°C. Cu implantation produced an R value of ~ 3 , indicating a strong influence from the physical effects of implantation. Conversely, depending on the implantation energy and dose, R values of 0.2-0.7 were measured following Al implantation. The chemical influence of Al dominated the physical effects of implantation during the oxidation of Al-implanted Cu. On

unimplanted Cu, an oxide about 300-nm thick formed following the 20-min exposure to oxygen.

Svendson (27) investigated the effect of Al and Cr implantations on Cu oxidation at temperatures of 200-800°C. He found that Al reduced the Cu oxidation rate for temperatures up to 600°C. Similar studies of Cr-implanted Cu indicated that Cr was not as effective an inhibitor as Al.

In another study, Naguib et al. (28) implanted elements (B, C, N, and Ne) having a low solubility in Cu to doses between 1×10^{15} and 1×10^{17} cm⁻². R was found to depend significantly on the duration of oxidation for B and C implantations, and on the implanted dose for B and N. The dependence of R on both the implantation dose and the oxidation time reflects the complexity of the oxidation process, and indicates why the effects of ion implantation on thermal oxidation remain poorly understood. Samples were oxidized in oxygen at 200°C to produce an oxide on unimplanted Cu about 100-nm thick.

More extensive survey experiments by Dearnaley et al. (29) and by Morris et al. (30), covering the balance of the elements in Figure 2d, were helpful in understanding the effects of ion implantation on Cu oxidation. R values between about 0.2 and 1.6 were obtained, with the largest value produced by Xe and Cs implantations, and the smallest by C and Ti implantations. Both groups reported a tendency for the oxidation rate to increase with increasing ion size. Following an implantation dose of 2×10^{15} cm⁻² for all the ions, the samples were oxidized at 200°C for 1 h in oxygen. An oxide layer about 100-nm thick was produced on unimplanted Cu.

In the earlier survey of Dearnaley et al. (29), the influence of the physical effects of implantation were assessed by preoxidation annealing treatments of self-ion implanted specimens. Results comparable to those observed in Ni were obtained, but with a slight shift of the R-versus-T curve to lower temperatures. R for Cu went from about 1.2 to 0.4 to 1.0 as the annealing temperature was increased from 20 to 200 to 550°C, respectively. Again, physical effects of implantation significantly influenced metal oxidation.

The sensitivity of R to the precise experimental conditions was also demonstrated in the surveys by Dearnaley et al. and Morris et al. Their observed inhibition of oxidation by C ions is not consistent with the results previously obtained by Naguib et al. (28). Dearnaley, Morris, and coworkers (29,30) have argued that this discrepancy may be explained by differences in the sample polishing procedures. The purity of the oxidizing gas was also important, as the R value measured for Ti-implanted Cu was strongly dependent on the moisture content of the gas. In dry oxygen R was about 0.15, but in wet oxygen R jumped to about 1.5-2.0.

Another result of Morris et al.'s (30) survey was obtained from measurements of the electrical conductivity of the oxide layer on ion-implanted and oxidized Cu. Copper oxide normally converts irreversibly to a high-conductivity state when a sufficiently-high switching voltage (dependent on the oxide thickness) is applied. On all the implanted Cu specimens with $R < 1$, an additional 1.7 V was necessary to produce this high-conductivity state. Apparently, some of the implanted ions (Ti, C, Li, W, Bi, Ni, and Eu) were able to create an electrical-barrier layer in the oxide.

To explain the barrier layer, Morris et al. proposed that these ions produced a pn junction in the normally semiconducting Cu₂O. The junction

limits electron-hole diffusion and, consequently, the oxidation rate. Current versus low-voltage measurements performed on the oxidized samples support this interpretation. All the samples with $R < 1$ produced an asymmetrical current-versus-voltage curve (shown in Figure 5b), which is typical of a pn junction. All the $R \geq 1$ samples yielded a symmetrical curve (shown in Figure 5a), which is typical of a homogeneous semiconductor. While the electrical-property measurements suggest a mechanism by which ion implantation reduces the oxidation of Cu, they do not explain why in the other cases, the oxidation rate is enhanced. Apparently, multiple mechanisms influence the oxidation of ion-implanted Cu.

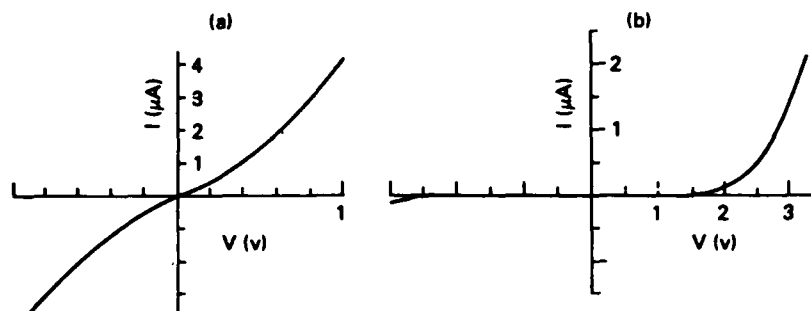


Figure 5. Current-versus-voltage curves measured on oxidized specimens of (a) unimplanted Cu and (b) Li-implanted Cu. (From Morris et al. (30)).

Chromium

Approximately 40% of the elements in the periodic table were implanted in the two survey experiments on Cr oxidation (see Figure 2e). Nearly all of these elements reduced oxide thicknesses up to a maximum reduction of 90%. However, no consistent correlation between properties of the implanted element and the oxidation results was observed. Physical effects of implantation strongly influenced Cr oxidation, and were well studied for this element. Their influence was complex, as indicated by a dependence of R on self-ion implantation energy and dose, and was persistent, as revealed by post-implantation annealing treatments. Segregation of implanted elements to the metal/oxide interface, and formation of precipitates in the oxide may have caused the reductions in oxide thickness.

In the survey by Muhl et al. (31), 13 different ions were implanted at two doses: 2×10^{15} and 2×10^{16} cm⁻². They observed R values between 0.4 and 1.4. Usually, the deviation of R from 1.0 was larger at the higher implantation dose, but for Xe, Mn, and Mg implantations, the deviations were smaller at the higher dose. Because Muhl et al. believed that radiation damage significantly influenced the oxidation rate, all the samples had been annealed at 800°C for 30 min prior to their oxidation. Subsequent exposure to oxygen at 750°C for 20 min produced oxides about 250-nm thick.

Collins et al. (32) also found important physical effects of implantation in their investigation. They implanted specimens with Cr, annealed them at various temperatures up to 800°C, and oxidized them for 20 min at 750°C. Apart from some anomalously high R values measured for a few annealing temperatures, an R value of about 0.8 was found for annealing temperatures up to 800°C. Similarly, in a preoxidation-annealing study of La-implanted Cr, a single R value of about 0.2 was found up to an annealing temperature of nearly 800°C. The physical effects of implantation were apparently quite persistent. These effects were monitored throughout their survey by frequently comparing the results of implanted samples which were either annealed or left in their as-implanted state. The annealing treatments were performed at 800°C following the implantation of $2 \times 10^{16} \text{ cm}^{-2}$ ions.

They found further evidence that the physical effects of implantation were important in the dose and energy dependence of R for Cr-implanted specimens (Figures 6a and b, respectively). The physical effects strongly influenced R, in a manner nonlinear with dose and with energy, and could enhance or inhibit the oxidation of Cr. A similar fluctuation of R with ion dose, but between values of 0.3 and 0.8, was observed for Ce-implanted specimens. Both chemical and physical effects were probably important in the latter specimens. The complex influence of the physical effects of implantation on Cr oxidation complicates analysis of the results.

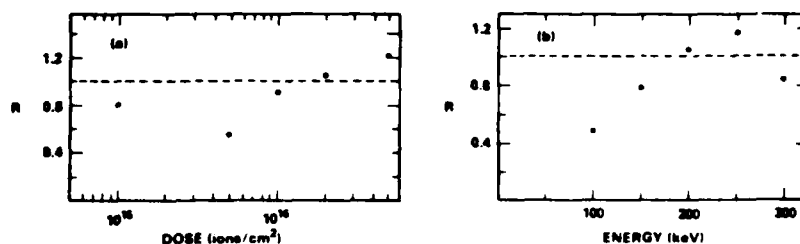


Figure 6. Dependence of the oxygen-uptake ratio of unannealed Cr samples on the dose and energy of Cr implantation. (From Collins et al. (32)).

Collins et al. implanted 35 elements besides Cr in their survey, and found only two (Pb and Sn) which increase the oxidation of Cr. The R values ranged from 0.1 to 1.2, with lanthanides and group-III elements being particularly effective at reducing oxidation. Ion microprobe analysis of Ho-, Pr-, and Ce-implanted specimens indicated that these oxidation inhibitors were concentrated at the metal/oxide interface. X-ray diffraction measurements of the oxide on Nd-, La-, and Dy-implanted specimens all indicated that a compound other than a simple binary oxide or a perovskite was present. Perhaps precipitates at the metal/oxide interface were able to block cation diffusion and hence slow the oxidation rate.

Summary

A number of trends are apparent from the results of these survey experiments:

(1) In cation-diffusing oxides (i.e., on Ni, Cu, and Cr), physical effects of implantation can enhance or inhibit the rate of oxidation by about a factor of 2-5. The direction and magnitude of the effect depend on the implantation energy and dose, the ion mass, the target material, and the temperature of any preoxidation annealing. A lesser influence from physical effects is observed for anion-diffusing oxides (i.e., on Ti and Zr).

(2) Chemical effects of the implanted species are also important. Oxides up to about 5 times thinner could be produced on the implanted portion of specimens which had been annealed to reduce the influence of the physical effects of implantation. The chemical influence of implanted elements can result from a change in the migration rate of anions and/or cations through the oxide. The implanted elements may reduce bulk diffusion through the oxide by (i) reducing the concentration of mobile defects in the oxide, (ii) forming a more protective secondary phase, or (iii) creating an electrical-barrier layer within the oxide. They may also reduce oxidation by reducing the density of short-circuit pathways through the oxide film, for example by (i) influencing the oxide grain size or epitaxy, (ii) trapping defects along available pathways, or (iii) improving the oxide plasticity, thereby preventing cracking of the stressed oxide. Further work is needed to identify the most important of these mechanisms.

(3) The effects of ion implantation usually correlate only weakly with fundamental parameters (e.g., the size) of the implanted element. A notable exception is Zr, where the ionic radius of the implanted element was found to be an important parameter. The solubility limits of the implanted element in the metal and in the oxide can also be important.

(4) Experimental conditions can strongly alter the influence of ion implantation. In particular, sample-polishing procedures, the purity of the oxidizing gas, the implantation dose, and the oxidation temperature and time are all important.

(5) More information about the microstructure of the implanted metal, and that of the grown oxide, is clearly needed.

Alloys

Alloys which form protective scales of either chromia (Cr_2O_3) or alumina (Al_2O_3) are better protected in an oxidizing environment at 700-1000°C when they also contain alloy additions of Y or a rare-earth element (e.g., Ce or Th). The additions decrease the oxidation rate somewhat, but more importantly they reduce the extent of oxide spallation during long term oxidations. Various mechanisms have been proposed to explain this result, but as Whittle and Stringer (33) indicated in their review, there is no consensus as to the most important of these mechanisms.

Ion-implantations of chromia and alumina-forming alloys were performed (i) to assess the ability of a thin alloy layer to prevent rapid oxidation of engineering alloys, and (ii) to investigate high-temperature oxidation mechanisms of these alloys. By analyzing the redistribution of implanted elements, and their influence on oxidation kinetics and on oxide microstructure, it was anticipated that high-temperature oxidation mechanisms might be better understood.

The alloys and the implanted ions which have been investigated are indicated in Table II. The sample weight gain and the amount of spalled oxide were monitored for periods of days in these investigations. Afterwards, samples were typically examined by optical and electron microscopy, and the composition of the scales was determined.

Table II. Ion Implantations of Alloys

Alloy (wt.%)	Ions	Reference
<u>Chromia-forming alloys</u>		
Fe-20Cr-25Ni(+Nb)	Y	34
"	Y, Kr, Nb	35
"	Pt, Si, Ce, Al, Al+Y	36
Ni-33Cr	Ar, Y	37
Fe-43Cr-27Ni	"	"
<u>Alumina-forming alloys</u>		
Fe-24Cr-1.45Al-0.09Y	Al	38
Fe-15Cr-4Al	Al, Al+Y, Y	39
Fe-15Cr-4Al	Y	35
Aluminized coatings	Ce, Y	35
Fe-41Ni-25Cr-10Al	Y	37

Chromia-Forming Alloys

Three chromia-forming alloys have been investigated, for oxidation times up to 6000 h. Both Y and Ce implantations reduced the oxidation rate (measured by weight gain) as well as conventional Y alloying did. After long-term oxidations, however, only implanted Ce prevented oxide spalling. The results suggest that a uniform distribution of the implanted element in the oxide may be necessary to prevent oxide spalling. Other implanted elements had virtually no effect on oxidation. The results indicate that Ce implantation may be able to protect chromia-forming alloys during long-term high-temperature oxidation, but the mechanism remains unknown.

Antill, Bennett, and coworkers (34-36) investigated the influence of various ions on the oxidation of an austenitic, Nb-stabilized stainless steel (see Table II). The sample weight gain and the amount of spalled oxide for implanted specimens was compared to that for unimplanted specimens in each investigation, and in two studies (34,35) to that of specimens alloyed with 0.13 and 0.41 wt.% Y. The distribution of oxide constituents was also determined (35,36) for some specimens. The samples were oxidized in CO₂ for nearly 6000 h at temperatures between 700 and 850°C.

They found that implanting Y and Ce reduced sample weight gain by an amount comparable to that produced by conventional Y alloying. Other implanted ions had essentially no effect, indicating that physical effects

of implantation had little influence on the alloy's oxidation. After long-term exposure the oxide of Ce-implanted specimens did not spall at all. However, the Y-implanted specimens were less resistant to oxide spallation than were Y-alloyed specimens. Further evidence that Ce implantation produces a tenacious oxide film was found by Bennett and coworkers (3), who recently observed enhanced creep of Ce-implanted specimens which were stressed in tension during oxidation at 825°C in CO₂. They attributed the enhancement to compressive stresses produced by unspalled oxide on the Ce-implanted specimens. The different behavior of Y- and Ce-implanted specimens may be associated with the depth distributions of Y and Ce which were measured after over 2400 h of oxidation. Implanted Ce was distributed throughout the oxide (36), while implanted Y was concentrated along the metal-oxide interface (35). Nb and Kr implantations slightly reduced oxide spallation, but the remaining ions had no effect.

Pivin et al. (37) implanted Ar and Y into Ni and Cr-based alloys (see Table II). They found that specimen weight gain during oxidation at 800-1000°C for up to 40 h in oxygen was considerably reduced by Y implantation, but was unaffected by Ar implantation. High-dose ($9 \times 10^{15} \text{ cm}^{-2}$) Y-implanted specimens also exhibited considerable resistance to oxide spalling during a thermal-cycling test. SIMS measurements revealed that Y was enriched at the metal-oxide interface in low-dose ($2 \times 10^{14} \text{ cm}^{-2}$) implanted specimens, but was distributed throughout the oxide layer in high-dose ($9 \times 10^{15} \text{ cm}^{-2}$) implanted specimens. The uniform distribution of Y at the high dose, where spallation resistance was observed, agrees well with the above mentioned Ce-implantation results of Bennett et al. (36). Apparently, a uniform distribution in the oxide of implanted Y or Ce can strongly inhibit oxide spalling. The mechanism for this protection is unknown. Pivin et al. (37) attributed the slower weight gain produced by Y implantation to reduced cation diffusivity in the oxide.

Alumina-Forming Alloys

Three alumina-forming alloys, and aluminized coatings on three Ni-based alloys have been investigated. Besides assessing the value of Y or Ce implantation, a few studies evaluated the benefits of Al implantation. Frequently, the standard 4 - 5 wt.% Al addition required to reduce oxidation excessively degraded mechanical properties. By implanting Al to alloy only a thin surface layer, it was hoped that both oxidation resistance and satisfactory mechanical properties could be produced. For short-term oxidations, it was found that alumina-forming alloys containing a substandard quantity of Al can be protected by Al implantation. Protection for longer periods, however, requires other additions to prevent oxide spalling. Cerium and Y implantations were unable to prevent oxide spalling during long-term oxidations. Implanted Y was observed to remain near the surface as oxidation progressed; eventually too small an amount resided near the metal/oxide interface to prevent spalling.

Bernabai et al. (38) implanted three different doses of Al into an alloy (Fe-24Cr-1.45Al-0.09Y) containing Y and a substandard amount of Al. The results of their oxidation at 1100°C for 24 h are shown in Figure 7. The highest implant dose produced an oxidation rate comparable to that of standard 4 - 5 wt.% Al alloys, even though the implanted layer was consumed within the first two hours of oxidation. Apparently, a large supply of Al is required to form a protective alumina layer, but considerably less is needed to sustain the protection for at least short additional periods.

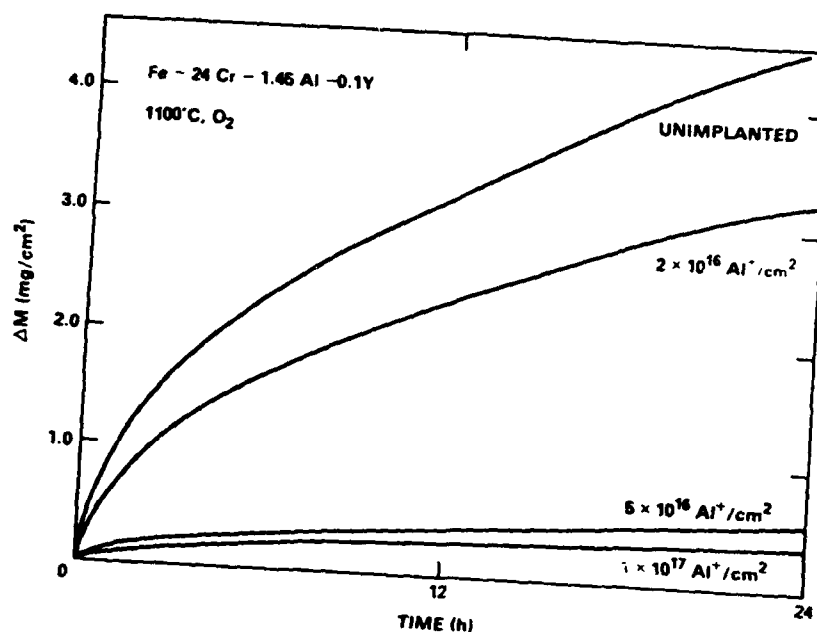


Figure 7. Weight gain measured during 1100°C oxidations of Fe-24Cr-1.45Al-0.09Y alloy, implanted with different doses of Al. (From Bernabai et al. (38)).

Bennett and coworkers implanted Al into two alloys: (i) an Al-free chromia-forming alloy, Nb-stabilized Fe - 20 wt.% Cr - 25 wt.% Ni (36), and (ii) a standard alumina-forming alloy, Fe - 15 wt.% Cr - 4 wt.% Al (39). Long-term oxidations of 30-3000 h duration did not show any reductions either in the oxidation rate or in the amount of spalled oxide. Dual implantations of Al+Y did prevent oxide spalling for a short time, but the benefit could be attributed solely to the presence of Y. These results suggest that although implantation of Al can reduce the initial oxidation rate of Al-containing alloys, it does not reduce long-term oxidation.

Antill, Bennett, and coworkers implanted Y into Fe - 15 wt.% Cr - 4 wt.% Al (35,39), and into aluminized coatings on 3 different Ni-based alloys (35). The former investigations compared Y implantations with 0.86 wt.% Y alloy additions, for oxidations at 1100-1200°C. Alloyed Y prevented oxide spalling for up to 4000 h, whereas implanted Y barely reduced spalling, indicating that for alumina-forming alloys a continuous bulk supply of Y is needed to prevent oxide spalling for long oxidation times. Neither Ce nor Y implantations improved the oxidation resistance of the aluminized coatings either. The coatings were oxidized at 1100°C for up to 1500 h.

Pivin et al. (37) implanted Y into Fe - 41 wt.% Ni - 25 wt.% Cr - 10 wt.% Al, and found little oxidation improvement during 40 h oxidations at

800°C. SIMS analysis showed that most of the Y resided at the interface between an outer mixed-oxide layer and an inner Al_2O_3 layer, indicating that the alumina layer grew by anion diffusion. This shows the usefulness of ion implantation as a tool to study oxidation mechanisms, and explains why implanted Y is unable to prevent oxide spalling of alumina-forming alloys. Implanted Y remains near the surface as the oxide grows, until too little resides near the metal/oxide interface to prevent spalling. When spalling finally does occur, all of the implanted Y is lost.

Oxidation of He-implanted Ni-1 at.% Pt⁺

A number of general concepts which were presented earlier in this review, are illustrated by recent experimental results obtained from a He-implanted Ni-1 at.% Pt alloy. A Ni-base alloy was selected because (i) pure-Ni oxidation has been so widely investigated, (ii) only one oxide phase (NiO) forms on Ni, and (iii) oxygen has a limited solubility in Ni (730 appm at 600°C). These latter two conditions simplified specimen analysis using RBS. Platinum was selected as an alloy component because (i) it has a high solubility in Ni, (ii) it has a high resistance to oxidation, (iii) it is expected to have a limited solubility in NiO, and (iv) as a heavy atom, it was well suited for RBS depth-profile analysis. Platinum was expected to be rejected from the growing NiO layer and, thus, to be enriched in the alloy just beneath the oxide/metal interface. By measuring the Pt distribution, it was expected that information on the oxidation rate and on the mobility of Pt in the alloy could be obtained.

Experimental procedure

Samples were prepared using the following procedures. Ni-1 at.% Pt ingots, fabricated using inert-gas arc melting, were reduced about 90% by cold-rolling them into 0.3-mm-thick sheets. Analyses for impurities indicated that C, Fe, Al, and Cu concentrations of about 300, 40, 20, and 10 appm, respectively, were present in the sheets. Rectangular (13 x 4 mm) and transmission electron microscopy (TEM) disk (3-mm diameter) specimens were spark cut and punched, respectively, out of the sheets. Both types were annealed for 2 h at 700°C in Ar, producing a grain size of < 100 μm . The specimens were mechanically polished down to 0.05- μm γ alumina, electropolished at -60°C in a solution of 30% nitric acid in methanol, and well rinsed with alcohol. A similar electropolishing solution was used to back-thin TEM specimens after oxidation.

Five rectangular specimens were each implanted with 300-keV-He⁺ ions, one end with $1 \times 10^{15} \text{cm}^{-2}$, the other end with $1 \times 10^{17} \text{cm}^{-2}$. A central region remained unimplanted. The implantations were designed to produce a near-gaussian distribution of He in the specimens, centered 720 nm below the surface with about a 79-nm standard deviation. The thickest oxides produced in this study penetrated less than one-third of this distance into the samples. The high-dose implantations produced a calculated peak He concentration of about 5.5 at.% and about 0.5 displacements per atom of radiation damage at the surface.

Four of the samples were oxidized in pairs to check for reproducibility. They were oxidized at 550°C for 3 h in flowing (about 2 ml/s) high-purity oxygen at atmospheric pressure. The fifth specimen remained unoxidized. Following oxidation, the unimplanted regions appeared brown, the low-dose implanted regions blue, and the high-dose implanted

⁺ This work was supported by the U.S. Department of Energy.

regions were nearly indistinguishable from the unimplanted regions. Color variations between metal grains were evident in each of the regions. Unimplanted TEM specimens were oxidized for 6 min at 550°C to permit microstructural examination of the oxide film.

Rutherford-backscattering analysis was performed on each specimen using a 1-mm-diameter beam of 3.08-MeV He⁺ ions and a 135° scattering angle. The samples were tilted 30° with respect to the ion beam, causing backscattered He to exit the surface at a 15° grazing angle, which was accurately measured using reflection of a laser beam. This technique produced a depth resolution of about 6 nm of NiO at the sample surface, and easily enabled the Pt distribution to be determined within the first 160 nm of NiO.

Results

In Rutherford-backscattering (RBS) analysis, the intensity of ions backscattered from each element in an alloy is proportional to the concentration of that element in the alloy; the energy of backscattered ions decreases with increasing sample depth. Consequently, a measured intensity-versus-energy distribution, for ions backscattered from a particular element in an alloy, represents that element's concentration-versus-depth profile in the alloy. However, alloys contain a number of elements, and the backscattered-ion energy increases with increasing target-atom mass. Consequently, the intensity-versus-energy distributions measured for alloys contain overlapping concentration-versus-depth profiles from each element present in the alloy.

Figure 8 compares RBS data obtained from the unimplanted region of oxidized and unoxidized Ni-1 at.% Pt specimens. The limits of variation among four oxidized specimens are indicated by the dashed lines. The contributions from surface atoms of O, Ni, and Pt appear at 1.28, 2.44, and 2.87 MeV, respectively. Depth scales for the Ni and Pt distributions were calculated assuming a surface composition of NiO. Note that the Pt signal is free from interference for about the first 160 nm of NiO. The Ni intensity from a surface layer of NiO is indicated in the figure. Of course, the Pt surface signal would be zero for a surface layer of pure NiO.

Upon examining the Ni distribution in Figure 8, it is clear that a uniformly thick layer of stoichiometric NiO did not form on Ni-1 at.% Pt when oxidized at 550°C. If it had, a sharp step change in the RBS intensity, from that of NiO to that of Ni, would have been observed at an NiO depth equal to the oxide thickness. Since stoichiometric NiO is the only oxide which forms on Ni, the RBS data indicate that an oxide layer of nonuniform thickness was present on the analyzed area of the sample. This result was somewhat expected. Typically, more than 100 metal grains were simultaneously analyzed over the lateral extent ($\approx 1 \text{ mm}^2$) of the ion beam. Since the oxidation rate of Ni is highly anisotropic at 550°C (as shown in Figure 1), a variety of oxide thicknesses was expected to form on the different metal grains analyzed. However, the variations were larger than expected. From Figure 1, the parabolic oxidation rate was expected to vary approximately tenfold at 550°C, producing threefold variations in oxide thicknesses at a given time. Instead, nearly tenfold variations in oxide thicknesses were observed. Due to these large thickness variations, it was impossible to determine if Pt was completely rejected from the growing oxide film, or to determine the extent of Pt enrichment beneath the metal/oxide interface.

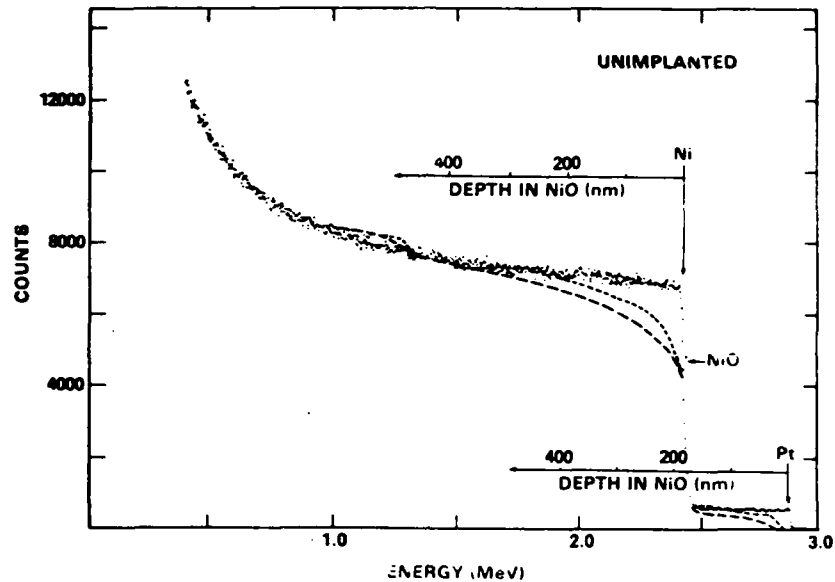


Figure 8. RBS data from the unimplanted region of oxidized and unoxidized Ni-1 at.% Pt. The limits of variation among four oxidized specimens are indicated by the dashed lines. The oxidations were performed at 550°C for 3h.

Figure 9 shows two additional variations in oxide thickness which were observed on unimplanted samples by electron microscopy. An oxidized sample was jet electropolished from the back to the front surface. The metal/oxide interface is only visible in the central portion of the images shown in Figure 9. Some roughness at the metal/oxide interface is evident, indicating that variations in oxide thickness occurred over a given metal grain. Also evident is an oxide protrusion which had grown into a metal grain boundary during oxidation. Such protrusions were frequently observed, and they occasionally attained lengths of nearly 0.5 μm . Caplan et al. (40) also observed such protrusions in their studies of Ni oxidation at 700°C. They argued that the protrusions formed by the oxidation of cavities, which were produced along metal grain boundaries earlier in the oxidation. Cavity formation was found to require a moderate level of C in the Ni (~ 65 appm), so they suggested that C, segregated at Ni grain boundaries, had promoted the nucleation of cavities during grain-boundary sliding. The sliding was generated by the decrease in metal volume which accompanies Ni oxidation. The Ni-1 at.% Pt alloy used in this work contained 300 appm C.

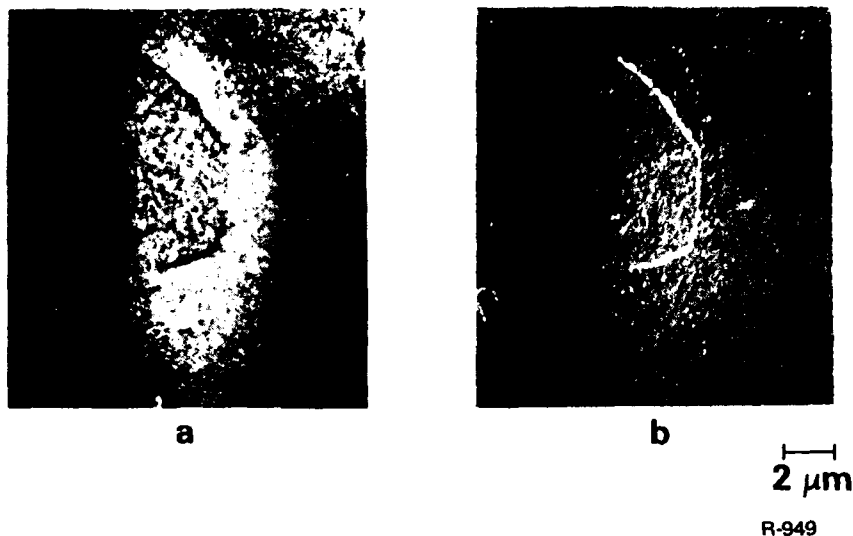


Figure 9. Electron micrographs of metal/oxide interface side of back-thinned unimplanted sample. Both scanning transmission image (a) and secondary electron image (b) show a thick oxide protrusion at the previous location of a metal grain boundary.

The deep penetration of oxide along grain boundaries may have contributed considerably to the thick portion of oxide which was measured using RBS. Berti et al. (4) observed similar behavior in their RBS investigations of Ti-implanted Zr oxidation. By using a tightly collimated microanalysis beam (a few μm diameter), they were able to separately analyze individual metal grains and even metal grain boundaries. Each analysis location exhibited a uniformly thick layer of stoichiometric oxide, with the thickest layers observed at metal grain boundaries. When the analysis-beam diameter was expanded, RBS data similar to that shown in Figure 8 was observed. Having examined many separate regions, they concluded that the thick portion of oxide measured on Zr using RBS was directly caused by deep penetrations of oxide along metal grain boundaries.

Figure 10 shows the effect of low-dose ($1 \times 10^{16} \text{ cm}^{-2}$) He implantation on the alloy's oxidation. A thinner and more uniformly thick oxide, which was also more reproducible, developed on the low-dose implanted regions of the samples. This behavior is evident from both the Ni and Pt distributions shown in Figure 10.

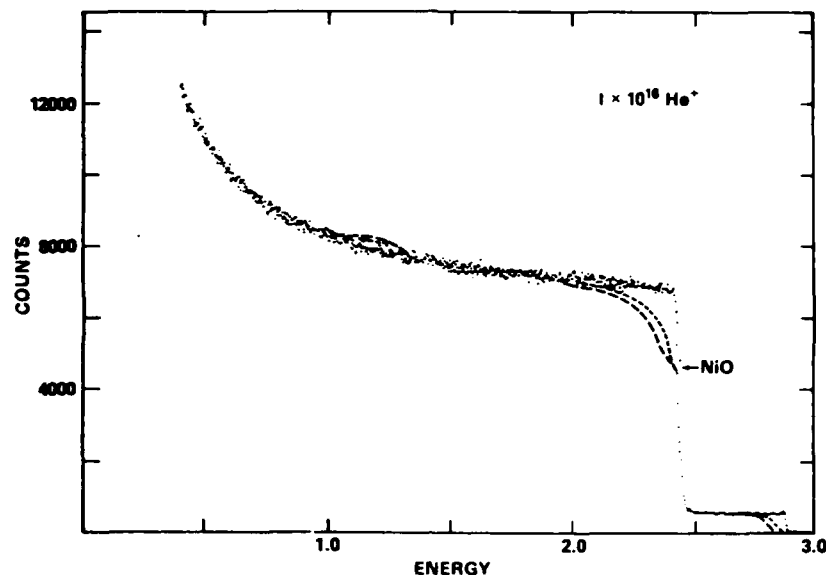


Figure 10. RBS data from oxidized and unoxidized Ni-1 at.% Pt specimens, implanted with a low dose ($1 \times 10^{16} \text{ cm}^{-2}$) of He prior to oxidation. The limits of variation among four oxidized specimens are again indicated. Note the reduction in oxide thicknesses on these implanted specimens.

The total oxygen uptake on the low-dose implanted region was reduced about 40%, largely because of a reduction in the quantity of thick oxide which formed. This reduction could have been caused by a reduction in the quantity of deep oxide penetrations along metal grain boundaries or, perhaps, by a reduction in the anisotropy of oxidation. The actual extent of each of these possibilities was not determined. However, Berti et al. (4) did observe both of these effects in their investigation of Ni-implanted Zr.

The benefits gained by low-dose He implantations, and perhaps more, were lost as a result of high-dose ($1 \times 10^{17} \text{ cm}^{-2}$) He implantations of Ni-1 at.% Pt (see Figure 11). The oxidation behavior after high-dose implantation is quite similar to that of the unimplanted alloy. A compact nature of the oxide layer found after low-dose implantation is clearly lost.

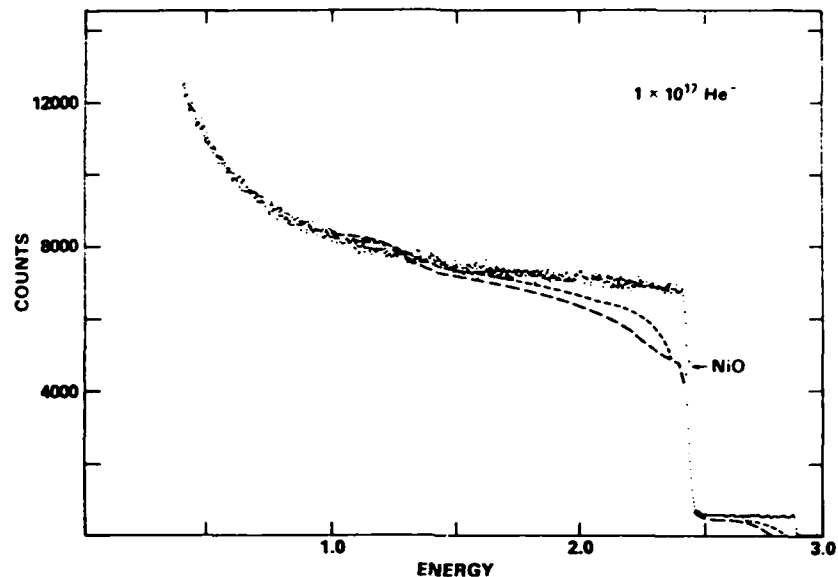


Figure 11. RBS data from oxidized and unoxidized Ni-1 at.% Pt specimens, implanted with a high dose ($1 \times 10^{17} \text{ cm}^{-2}$) of He prior to oxidation. The limits of variation among oxidized specimens are again indicated. Note the closer similarity to unimplanted specimens (Figure 8) than to low-dose implanted specimens (Figure 10).

Discussion of Ni-1 at.% Pt results

The results of Ni-1 at.% Pt oxidation illustrate well a number of general features of thermal oxidation. The variation in oxide thickness between different metal grains (observed by optical microscopy) is typical for the low-temperature regime of oxidation, where anisotropic oxidation rates occur. Such variations diminish with increasing oxidation temperature. The roughness observed at the oxide/metal interface is usually present for all oxidation temperatures, with its lateral dimension corresponding to the oxide-crystallite size. The penetrations of oxide observed along alloy grain boundaries probably occur in other metals and at higher oxidation temperatures; Caplan et al. (40) showed that such penetrations persist up to 1270°C in Ni and are probably caused by C in the metal. The specimen to specimen variation in oxide thicknesses are believed to reflect subtle differences in the contamination and/or microstructure of the sample surface, and in the oxidation conditions. These are common problems in thermal oxidation experiments at low temperatures.

The influence of He implantation on the oxidation of Ni-1 at.% Pt can be large and is poorly understood, much like the results of other ion-implantation investigations. The 40% reduction in oxygen uptake observed in low-dose He-implanted specimens, was similar to the earlier investigations of Ni oxidation at 630°C by Goode (23). He argued that the

physical effects of implantation (including of He^+) reduced oxide thicknesses by about 80%. The difference in thickness reduction might be explained by the slightly different experimental conditions. No depth-dependent information was reported by Goode. The new information provided by the present study shows that most of the reduction occurs by a decrease in the quantity of thick oxide, and suggests that the low-dose He implantations may prevent the rapid growth of oxide along metal grain boundaries. If this is true, it is possible that He implantation prevented the formation of grain boundary cavities, perhaps by minimizing grain-boundary sliding or by eliminating C segregation at the boundaries.

Although a higher implantation dose would be expected to produce greater physical effects in the metal (i.e., more lattice damage, more surface sputtering, and more intermixing/cleansing of surface contaminants), a lesser effect on oxidation was observed in the present experiment. This result suggests that implanted He chemically influences the oxidation of Ni-1 at.% Pt. The defect structure in low-dose implanted specimens may have trapped C and prevented cavity formation along metal grain boundaries, whereas in the high-dose implanted specimens, a different defect structure allowed C to migrate to the grain boundaries. However, this explanation requires that C trapping depends on the lattice-defect structure, and it is not clear that such a dependency exists.

The chemical effect of He is difficult to substantiate because the He concentration in oxidized specimens was not measured. Although one might expect to find more He in high-dose implanted specimens, this may not have been the case. Biersack et al. (41) found that He, implanted at 300 keV to a dose of $\sim 1 \times 10^{16} \text{ cm}^{-2}$ into various metals (Ag, Au, Cu, and Pt), was retained by specimens after isochronal-annealing at temperatures up to at least 700°C. However, samples which initially contained larger concentrations of He were found to thermally release their He beginning at 300°C, and to have lost over 90% of their initial concentration by 700°C. Their results indicate that the strength of He traps does depend on the defect microstructure. In the present investigation, high-dose implanted He may have been detrapped, whereas low-dose implanted He may not have been, during the 550°C oxidation.

In conclusion, this investigation of Ni-1 at.% Pt oxidation at 550°C has shown that:

- (1) Low-dose ($1 \times 10^{15} \text{ cm}^{-2}$) He implantation can reduce the alloy oxidation rate by about 40%, but high-dose ($1 \times 10^{17} \text{ cm}^{-2}$) He implantation has less effect. Dose-dependent detrapping of He at the oxidation temperature may have produced this dose-dependent behavior.
- (2) Large variations in oxide thicknesses occur for this alloy as a result of (i) anisotropic oxidation rates and (ii) the penetration of oxide along metal grain boundaries, probably due to the presence of C in the alloy. Smaller variations are caused by oxide roughness associated with oxide polycrystallinity.
- (3) Low-dose He implantation may have minimized grain-boundary oxidation of the alloy, since most of the oxidation reduction occurred by a decrease in the quantity of thick oxides.

Discussion

Although ion implantation produces only a thin alloy layer near the surface, large and occasionally long-term effects on thermal oxidation have been observed. For all the pure elements reviewed (Ti, Zr, Ni, Cu, and Cr), some implanted elements were found which reduced oxide thicknesses by a factor of 2-10. In most of these investigations, however, the oxidations were at low enough temperatures and for short enough times, that significant amounts of the implanted element were still present in the metal substrate, and in the oxide film. Perhaps long-term, high-temperature exposures would dilute the implanted elements sufficiently that their benefits will be eliminated. Evidence to the contrary was exhibited by the large reductions in oxide thicknesses which were produced on the back surfaces of ion-implanted Ti foils. These surfaces contained only a small quantity of the implanted elements, as a result of post-implantation annealing. The idea that in some cases, small quantities of the implanted element are sufficient is supported by observations on implanted high-temperature alloys. Chromia-forming alloys can be protected from oxide spalling for nearly 6000 h at 825°C by Ce implantation, a better benefit than provided by the conventional technique of alloying with Y. Good oxidation resistance is also provided by Y implantation, but not for as long a duration. It is therefore possible to create coatings which remain resistant to oxidation for long times by using ion implantation. Additionally, Dearnaley (2) has indicated that ion implantation can produce coatings resistant to both oxidation and mechanical stresses. He reported significant improvements in fretting-fatigue resistance, sliding-wear resistance, and high-temperature erosion resistance of metals as a result of ion implantation.

A number of mechanisms may be responsible for the effects produced by ion implantation. The pure-element work showed that physical effects of implantation (i.e., lattice damage, surface contaminant cleansing or intermixing, and changes in surface morphology) can influence oxidation rates by about a factor of 2-5, at least for cation-diffusion oxides and at intermediate temperatures. The mechanisms for these effects are not yet understood. Implanted elements can chemically influence oxidation rates by altering the normal mechanisms of transport through the oxide film. They may reduce transport through bulk oxide by (i) reducing the concentration of mobile defects in the oxide, (ii) forming a more protective secondary phase, or (iii) creating a space-charge barrier within the oxide. Oxidation can also be reduced if the implanted elements reduce short-circuit transport in the oxide, for example by (i) decreasing the density of pathways by increasing oxide grain size, or by influencing grain-boundary orientations, (ii) trapping fast-diffusing ions along the available pathways, or (iii) preventing oxide fracture by relieving or preventing the oxidation-produced stresses, or by strengthening the oxide against such stresses. Evidence for most of these chemical effects has been obtained but there is little understanding of how or why they occur. The mechanisms most likely to provide long-term high-temperature protection against oxidation are obviously those which require only a small quantity of the implanted element; e.g., the blockage of short-circuit-diffusion pathways, the formation of a tenacious barrier layer, or the mitigation of oxidation-produced stresses by segregation of the implanted element to the metal/oxide interface.

The thin alloy layer produced by ion implantation makes ion implantation a useful research tool for the investigation of thermal-oxidation mechanisms. By analyzing the redistribution of implanted elements, considerable information about atomic migration during oxidation

can be obtained. Recent work on the thermal oxidation of metals (6) has demonstrated this usefulness. Ion implantation should also prove useful as a research tool in the selection of candidate alloy elements for the improvement of oxidation resistance, since many elements can be easily and reproducibly implanted.

Future investigations of ion-implantation effects on thermal oxidation will probably differ considerably from the earlier work discussed in this review. Ion implantation is now known to significantly influence metal oxidation, but little is known about the mechanisms for these effects. Future work will investigate these mechanisms more thoroughly by measuring oxidation kinetics, and by analyzing the composition, microstructure, and morphology of oxidized specimens. High-resolution analysis techniques will be required for these investigations, to differentiate between metal grains and their boundaries, and between the front and back surfaces of the oxide.

In conclusion:

(1) Ion implantation can have large effects on the thermal oxidation of metals; reductions in oxide thicknesses of up to 90% for pure elements, and the elimination of oxide spalling for nearly 6000h for a chromia-forming alloy were observed.

(2) The mechanisms for these effects are poorly understood. Both physical effects of the implantation process, and chemical influences of the implanted species can contribute to the effect; although, the physical effects appear to be more important for cation-diffusing oxides (e.g., NiO, Cu₂O, Cr₂O₃), and at low oxidation temperatures. More thorough investigations of oxidation kinetics, and of oxide composition, microstructure, and morphology are needed to understand the mechanisms by which ion implantation reduces oxidation.

(3) Ion implantation can provide long-term, high-temperature oxidation protection by, probably, only a few mechanisms. In these mechanisms, small quantities of the implanted element provide protection, perhaps by (i) blocking short-circuit diffusion through the oxide, (ii) forming a protective barrier layer in the oxide, or (iii) segregating to the metal/oxide interface where they mitigate oxidation produced stresses, thus, preventing rupture of the oxide.

(4) Ion implantation is a useful research tool to investigate atomic migration during oxidation, and to select candidate elements for conventional alloying for oxidation protection.

The authors are indebted to J. K. Hirvonen for his ideas and suggestions in the writing of this review, and to H. Wiedersich for his support and for many illuminating discussions during the experimental work. We also thank P. Baldo for his skillful help with the measurements.

References

1. G. Dearnaley, "Thermal Oxidation," pp. 257-320 in Ion Implantation, Treatise on Materials Science and Technology, Vol. 13, J. K. Hirvonen, ed.; Academic Pr., New York, NY, 1980.

2. G. Dearnaley, "The Alteration of Oxidation and Related Properties of Metals by Ion Implantation," Nucl. Instrum. Methods, 182/183 (1981) pp. 899-914.
3. M. J. Bennett, "The Role of Ion Implantation in High-Temperature Oxidation Studies," paper presented at NACE Int. Conf. High Temperature Corrosion, San Diego, March 1981, (AERE-R 10082).
4. M. Berti, A. Carnera, A. V. Drigo, A. Armigliato, G. G. Bentini, and G. Dearnaley, "Thermal Oxidation of Ion Implanted Polycrystalline Zirconium: Effects of Implanted Species on Grain Boundary Oxidation," pp. 171-180 in Ion Implantation Metallurgy, C. M. Preece and J. K. Hirvonen, eds.; AIME, New York, NY, 1980.
5. M. Berti, A. Carnera, A. V. Drigo, A. Armigliato, A. DeSalvo, and R. Rosa, "Oxygen and Implanted Ion Profiles in Oxidized Zirconium," Nucl. Instrum. Methods, 182/183 (1981) pp. 215-222.
6. Int. Conf. Modification of the Surface Properties of Metals by Ion Implantation, Manchester, UK, June 1981, (to be published as Ion-Implantation into Metals, V. Ashworth, W.A. Grant, and R.P.M. Procter, eds., Pergamon Pr., 1982).
7. W. W. Smeltzer and D. J. Young, "Oxidation Properties of Transition Metals," Prog. Solid-State Chem., 10 (1975) pp. 17-54.
8. K. R. Lawless, "The Oxidation of Metals," Rep. Prog. Phys., 37 (1974) pp. 231-316.
9. Per Kofstad, High-Temperature Oxidation of Metals; John Wiley and Sons, Inc., New York, NY, 1966.
10. C. Wagner, "Beitrag zur Theorie des Anlaufvorgangs," Z. Phys. Chem. 21B (1933) pp. 25-41.
11. J. Stringer, "Stress Generation and Relief in Growing Oxide Films," Corros. Sci. 10 (1970) pp. 513-543.
12. W. W. Smeltzer, R. R. Haering, and J. S. Kirkaldy, "Oxidation of Metals by Short Circuit and Lattice Diffusion of Oxygen," Acta Metall. 9 (1961) pp. 880-885.
13. S. Matsunaga and T. Homma, "Influence on the Oxidation Kinetics of Metals by Control of the Structure of Oxide Scales," Oxid. Met. 10 (1976) pp. 361-376.
14. P. J. Harrop, "Self-Diffusion in Simple Oxides (A Bibliography)," J. Mater. Sci. 3 (1968) pp. 206-222.
15. R. Freer, "Bibliography: Self-diffusion and Impurity Diffusion in Oxides," J. Mater. Sci. 15 (1980) pp. 803-824.
16. N. N. Khoi, W. W. Smeltzer, and J. D. Embury, "Growth and Structure of Nickel Oxide on Nickel Crystal Faces," J. Electrochem. Soc. 122 (1975) pp. 1495-1503.
17. J. V. Cathcart, G. F. Petersen, and C. J. Sparks, Jr., "The Structure of Thin Oxide Films Formed on Nickel Crystals," J. Electrochem. Soc. 116 (1969) pp. 664-668.

18. G. G. Bentini, M. Berti, A. Carnera, G. Della Mea, A. V. Drigo, S. Lo Russo, P. Mazzoldi, and G. Dearnaley, "The Thermal Oxidation of Ion-Implanted Zirconium," Corros. Sci. 20 (1980) pp. 27-39.
19. G. Dearnaley, P. D. Goode, W. S. Miller, and J. P. Turner, "The Influence of Ion Implantation Upon the High-Temperature Oxidation of Titanium and Stainless Steel," pp. 405-414 in Int. Conf. Ion Implantation in Semiconductors and Other Materials, B. L. Crowder, ed.; Plenum Pr., New York, NY, 1973.
20. G. Dearnaley, J. D. Benjamin, W. S. Miller, and L. Weidman, "The Use of Ion Implantation in a Comparison of the Thermal Oxidation of Titanium and Zirconium," Corros. Sci. 16 (1976) pp. 717-728.
21. J. D. Benjamin and G. Dearnaley, "Further Investigations of the Effects of Ion Implantation on the Thermal Oxidation of Titanium," pp. 141-146 in Int. Conf. Applications of Ion Beams to Materials, 1975, G. Carter, J. S. Colligon, and W. A. Grant, eds.; Institute of Physics, London, UK, 1976.
22. A. Galerie, "High Temperature Oxidation of Ion Implanted Metals," paper presented at Int. Conf. Modification of the Surface Properties of Metals by Ion Implantation, Manchester, UK, June 1981.
23. P. D. Goode, "The Influence of Ion Implantation on the Oxidation of Nickel," pp. 154-159 in Int. Conf. Applications of Ion Beams to Materials, 1975, G. Carter, J. S. Colligon, and W. A. Grant, eds.; Institute of Physics, London, UK, 1976.
24. Zhou Peide, F. H. Stott, R. P. M. Procter, and W. A. Grant, "The Early Stages of Oxidation of Ion-Implanted Nickel at High Temperature," Oxid. Met. 16 (1981) pp. 409-426.
25. F. H. Stott, Zhou Peide, R. P. M. Procter, and W. A. Grant, "The Oxidation of Ion-Implanted Nickel at High Temperatures," paper presented at Int. Conf. Modification of Surface Properties of Metals by Ion Implantation, Manchester, UK, June 1981.
26. J. Rickards, "Ion Implantation and Backscattering from Oxidized Single-Crystal Copper," pp. 101-109 in Int. Conf. Application of Ion Beams to Metals, S. T. Picraux, E. P. EerNisse, and F. L. Vook, eds.; Plenum Pr., New York, NY, 1974.
27. L. G. Svendsen, "A Comparison of the Corrosion Protection of Copper by Ion Implantation of Al and Cr," Corros. Sci. 20 (1980) pp. 63-68.
28. H. M. Naguib, R. J. Kriegler, J. A. Davies, and J. B. Mitchell, "Effect of B, C, N, and Ne Ion Implantation on the Oxidation of Polycrystalline Cu," J. Vac. Sci. Technol. 13 (1976) pp. 396-400.
29. G. Dearnaley, J. R. Morris, and R. A. Collins, "The Role of Ion-Implanted Impurities on the Thermal Oxidation of Copper," pp. 955-958 in Proc. Int. Vac. Congr., 7th, R. Dobrozemsky et al. eds.; R. Dobrozemsky, Vienna, 1977.
30. J. R. Morris, R. A. Collins, and G. Dearnaley, "The Influence of Ion Implantation on the Thermal Oxidation of Copper," J. Phys. F: Met. Phys. 8 (1978) pp. 1333-1342.

31. S. Muhl, R. A. Collins, and G. Dearnaley, "The Effect of Ion-Implanted Impurities on the Oxidation of Chromium," pp. 147-153 in Int. Conf. Applications of Ion Beams to Materials, 1975, G. Carter, J. S. Colligon, and W. A. Grant, eds.; Institute of Physics, London, UK, 1976.
32. R. A. Collins, S. Muhl, and G. Dearnaley, "The Effect of Rare Earth Impurities on the Oxidation of Chromium," J. Phys. F: Met. Phys. 9 (1979) pp. 1245-1259.
33. D. P. Whittle and J. Stringer, "Improvements in High Temperature Oxidation Resistance by Additions of Reactive Elements or Oxide Dispersions," Phil. Trans. R. Soc. Lond. A295 (1980) pp. 309-329.
34. J. E. Antill, M. J. Bennett, G. Dearnaley, F. H. Fern, P. D. Goode, and J. F. Turner, "The Effects of Yttrium Ion Implantation upon the Oxidation Behaviour of an Austenite Stainless Steel," pp. 415-422 in Int. Conf. Ion Implantation in Semiconductors and Other Materials, B. L. Crowder, ed.; Plenum Pr., New York, NY, 1973.
35. J. E. Antill, M. J. Bennett, R. F. A. Carney, G. Dearnaley, F. H. Fern, P. D. Goode, B. L. Myatt, J. F. Turner, and J. B. Warburton, "The Effect of Surface Implantation of Yttrium and Cerium upon the Oxidation Behaviour of Stainless Steels and Aluminized Coatings at High Temperatures," Corros. Sci. 16 (1976) pp. 729-745.
36. M. J. Bennett, G. Dearnaley, M. R. Houlton, R. W. M. Hawes, P. D. Goode, and M. A. Wilkins, "The Influence of Surface Ion Implantation upon the Oxidation Behaviour of a 20%Cr-25%Ni, Niobium Stabilized Austenitic Stainless Steel, in Carbon Dioxide, at 825°C," Corros. Sci. 20 (1980) pp. 73-89.
37. J. C. Pivin, C. Roques-Carmes, J. Chaumont, and H. Bernas, "The Influence of Yttrium Implantation on the Oxidation Behaviour of 67Ni-33Cr, Fe-43Ni-27Cr and Fe-41Ni-25Cr-10Al Refractory Alloys," Corros. Sci. 20 (1980) pp. 947-962.
38. U. Bernabai, M. Cavallini, G. Bombara, G. Dearnaley, and M. A. Wilkins, "The Effects of Heat Treatment and Implantation of Aluminum on the Oxidation Resistance of Fe-Cr-Al-Y Alloys," Corros. Sci. 20 (1980) pp. 19-25.
39. M. J. Bennett, M. R. Houlton, and G. Dearnaley, "The Influence of the Surface Ion Implantation of Aluminum and Yttrium upon the Oxidation Behaviour of a Fe-15%Cr-4%Al FeCrAlloy Stainless Steel, in Air, at 1100°C," Corros. Sci. 20 (1980) pp. 69-72.
40. D. Caplan, R. J. Hussey, G. I. Sproule, and M. J. Graham, "Effect of Carbon on Cavity Formation During High-Temperature Oxidation of Ni," Oxid. Met. 14 (1980) pp. 279-299.
41. J. P. Biersack, D. Fink, R. A. Henkelmann, and K. Muller, "Range Profiles and Thermal Release of Helium Implanted into Various Metals," J. Nucl. Mater. 85/86 (1979) pp. 1165-1171.

Section III.B

ELECTROCHEMICAL AND A.E.S. STUDIES OF Fe-Cr SURFACE ALLOYS
FORMED ON A.I.S.I. 52100 STEEL BY ION BEAM MIXING

W. K. Chan and C. R. Clayton¹
R. G. Allas, C. R. Gossett and J. K. Hirvonen²

¹Department of Materials Science and Engineering
State University of New York
Stony Brook, NY

²Materials Modification and Analysis Branch
Condensed Matter and Radiation Sciences Division
Naval Research Laboratory

This work was supported by the Office of Naval Research at
the Naval Research Laboratory and at SUNY by ONR Contract
#N0001477-C0424

ELECTROCHEMICAL AND A.E.S. STUDIES OF Fe-Cr SURFACE ALLOYS FORMED ON AISI 52100 STEEL BY ION BEAM MIXING

W.K. CHAN and C.R. CLAYTON

Dept. of Materials Science and Engineering, State University of New York, Stony Brook, NY, 11794, USA

R.G. ALLAS, C.R. GOSSETT and J.K. HIRVONEN

Naval Research Laboratory, Washington, D.C., 20375, USA

Fe-Cr surface alloys have been formed on AISI 52100 steel by ion beam mixing in order to improve localized corrosion resistance. Three implant species were considered in this work, namely: Cr^+ , Xe^{2+} and Kr^{2+} . Ion implantation was carried out on Cr surface layers, of 30 and 50 nm, deposited onto 52100 steel coupons. The resulting surface alloys were chemically characterized by Auger electron spectroscopy. Electrochemical pitting studies were carried out in deaerated 0.01 M NaCl solution buffered to pH 6. Each of the surface alloys formed by the ion beam mixing technique exhibited a significantly higher resistance to localized corrosion compared to 52100 steel. The possible influence on the localized corrosion resistance of the surface alloys of oxidation, carbide formation and sputtering, resulting from the ion implantation treatments, is discussed.

1. Introduction

Bearing corrosion is a serious problem in military aircraft propulsion systems. Commonly, corrosion takes the form of localized pitting along the contact region between the rollers and racers [1]. Corrosion is also responsible for severely lowering the shelf-life of replacement bearings, independent of the type of bearing alloy. In a previous paper we have considered the use of high dose ion implantation to dope the surface region of 52100 bearing steel with Cr in order to improve localized corrosion resistance [2]. In this note we report the use of ion beam mixing as an alternative means of forming Fe-Cr surface alloys on 52100 steel for the purpose of improving localized corrosion resistance.

2. Experimental

AISI 52100 bearing steel is a martensitic steel containing very little Cr. The composition is given in table 1. Samples of $7 \times 7 \times 1$ mm were cut from rod stock. Polishing was then carried out up the grades finishing with a $1 \mu\text{m}$ diamond polish finish. Samples were then degreased in methanol, rinsed in distilled water and finally dried. Cr was then deposited by E-beam evaporation onto the sam-

Table 1
Composition (wt.%) of AISI 52100

C	Cr	Mn	Si	P	S	Fe
0.96	1.36	0.36	0.22	0.010	0.012	Bal.

ples. Two thicknesses were used in this preliminary study: 30 and 50 nm. Ion beam mixing was then carried out using the ion implantation parameters given in table 2. During implantation the samples were clamped to a water-cooled copper heat sink in order to ensure that the sample temperature did not exceed 70°C .

The composition of the surface alloys was determined by Auger electron spectroscopy. Depth profiling was carried out using a V.G. Scientific

Table 2
Implantation parameters for ion beam mixing studies

Ion species	Energy (keV)	Fluence (ions cm^{-2})	Cr layer thickness (nm)
Cr^+	150	2×10^{17}	30
Xe^{2+}	300	3×10^{16}	30
Cr^+	150	5×10^{16}	50
Kr^{2+}	300	5×10^{16}	50

Scanning Auger Microprobe mounted onto a V.G. Scientific ESCA 3MKII which is fitted with an hemispherical electrostatic analyzer. Auger measurements were carried out in a vacuum of better than 10^{-9} Torr using a rasterable electron gun operating at 3 keV and a beam current of 50 μ A. The modulating voltage used was 3 V. In the initial stage of this work, which was concerned with the ion beam mixing of 30 nm Cr films, ion etching was carried out intermittently using an Ar^+ ion gun operating at 4 keV accelerating potential in a background pressure of 10^{-6} Torr. Profiling studies of the intermixed 50 nm Cr films were carried out using Xe^+ ion etching at 1.5 keV in order to improve depth resolution. Auger profiling in this case was carried out in a continuous etching mode in order to minimize surface adsorption or hydrocarbons.

In preparation of the polarization experiments, coupons of $7 \times 7 \times 1$ mm were mounted onto a "plexiglas" backed electrochemical probe. Epoxy was used to seal the edges of the samples. The electrolyte used for pitting studies was a deaerated 0.01 M NaCl (pH 6 acetate buffer) solution. The samples were initially cathodically polarized for 30 min at a sufficiently negative potential to yield a cathodic current of 5 mA in order to cathodically reduce the air formed oxide films. The samples were then left at open circuit potential for 3–5 min prior to potentiodynamic anodic polarization. The scan rate used was 1 mV s^{-1} . All electrode potentials were measured against a Saturated Calomel Electrode (S.C.E.).

3. Results

In this preliminary investigation we compared the use of inert gas implantation (Xe^{2+} and Kr^{2+}) and self-ion (Cr^+) implantation for ion beam mixing of Cr into 52100 steel. In the first set of experiments Xe^{2+} and Cr^+ implantation was carried out on a 30 nm Cr film and the results were compared. The Auger depth profiles, obtained by Ar etching, are shown in figs. 1 and 3.

It can be seen from fig. 1 that Xe^{2+} implantation has led to some interdiffusion of Fe and Cr. However, by far the most distinguishing feature of the profile is the formation of a relatively thick oxide film formed apparently during the implantation process. In a previous Auger depth profile

analysis of the unimplanted Cr film, only a very thin oxide layer was found on the surface of the Cr film, and the bulk of the Cr layer was found to be relatively clean of carbon and oxygen impurities. It is also seen from fig. 1 that a trace of Fe is observed within the oxide film, following implantation. The shape of the KLL Auger spectra for carbon was found to vary throughout the profile indicating the presence of adsorbed hydrocarbons and chromium carbide, as indicated by the inserts 1, 2 and 3 in fig. 1. The four primary carbon KLL Auger spectral shapes observed in this work are given in fig. 2.

The profile obtained following Cr^+ -implantation (fig. 3), by contrast shows evidence of very little oxidation. A considerably greater sputter removal of the Cr film, however, has apparently taken place. The original interface between the Cr film and 52100 steel substrate, which was indicated by the presence of a polish formed oxide film, has been completely removed. Again the presence of chromium carbide is found throughout the surface regions of the alloy.

The electrochemical pitting behavior of the two surface alloys is compared with that of the 52100 steel in fig. 4 and table 3. Both treatments have resulted in a considerable positive shift in the breakdown potential, which indicates a significant improvement in localized corrosion resistance. The Cr implantation treatment led to the greatest improvement observed.

In a second stage of this work Kr^{2+} and Cr^+ ion beams were used to intermix a 50 nm Cr film deposited onto 52100 steel. In this work, the Cr fluence was lower, i.e. 5×10^{16} ion cm^{-2} , than the previous experiment in order to reduce the amount of Cr film removed by sputtering. The profiles were again obtained by Auger spectroscopy, but in this work Xe etch profiling was carried out in order to enhance depth resolution.

The Auger depth profiles of the unimplanted 50 nm Cr film and the Kr and Cr intermixed surface alloys are presented in figs. 5, 6 and 7, respectively. Since the Nuclear Reaction Analysis (NRA) technique to profile depth distributions of various elements is nondestructive it was chosen to supplement the Auger depth profiles. Comparison of the yield of reaction particles from the selected reaction for the sample and for a stoichiometric reference produces the concentration profile. The same sample was depth profiled for ^{12}C and ^{16}O both

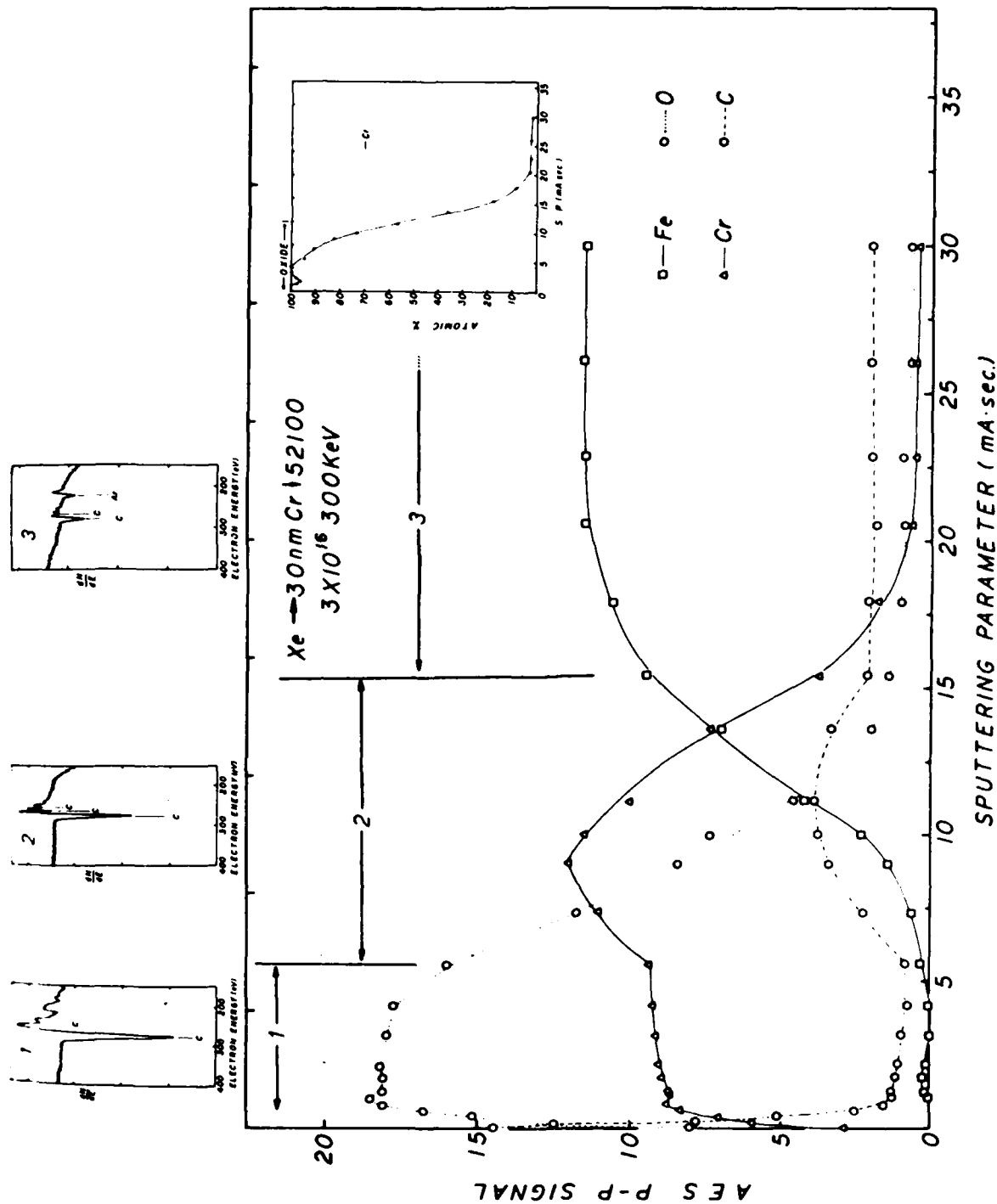


Fig. 1. Auger depth profiles of Fe, Cr, O and C following Xe ion beam mixing of 30 nm Cr film on 52100 steel (profiled with Ar at 4 keV).

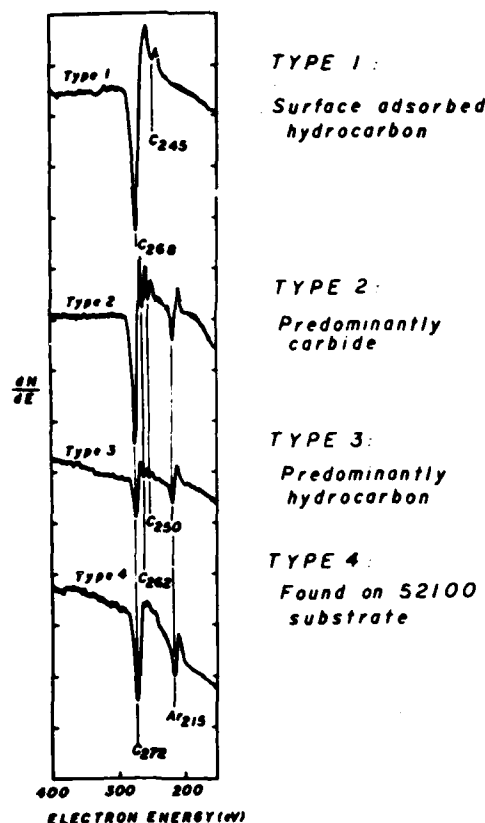


Fig. 2. Four commonly observed configurations of carbon KLL Auger spectra.

before and after the Kr bombardment. We used a method developed by one of us (CRG) involving a (^3He , p) reaction for ^{12}C profiling and a (^3He , α) reaction for ^{16}O profiling. The results for ^{16}O are shown in fig. 8. The ^{12}C case did not have sufficient statistics to unfold a reasonably detailed profile.

By comparing the slopes of the Fe and Cr profiles of figs. 5, 6 and 7, it can readily be seen that some considerable inter-diffusion has taken place in both of the surface alloys. However, it can be seen from fig. 6, that Kr implantation has resulted in considerable surface oxidation. The Cr implantation treatment by contrast shows only the presence of a very thin airformed surface oxide film, and the oxide film at the original surface of 52100 steel. Inspection of the oxygen profile of fig. 6 reveals three major concentrations of oxygen. In addition to a thickened surface oxide film, the oxygen associated with the oxide film on the 52100 steel interface is seen to extend towards the surface of the Cr film forming an intermediate concentration maximum. The results are also reflected in the NRA data of fig. 8. The Cr profile of fig. 6 also shows three maxima. The outermost maximum is clearly associated with the surface oxide film. The remaining two maxima do not appear to be exclusively associated with oxygen. Since the carbon profile is largely made up of carbides, it is conceivable that carbide formation may lead to a significant change in the Auger electron cross-section. Hence, the undulations in the Cr profile may be the result not only of variations in concentration, but also spectral sensitivity.

On comparing the profiles of the Cr^+ ion beam mixed surface alloys, shown in figs. 3 and 7, it can be seen that the excessive sputtering of the Cr film initially observed in the 30 nm Cr film with 2×10^{17} ions cm^{-2} fluence has been successfully avoided by the use of a thicker, 50 nm film and a lower Cr^+ ion fluence. In the latter case the outer portion of the Cr film has not been mixed with Fe, even through considerable inter-diffusion is observed in this surface alloy. It can also be seen

Table 3
AISI 52100 pitting data in deaerated 0.01 M NaCl (buffered pH = 6) solution

Sample	Cathodic treatment	Open circuit pot. (mV)	Breakdown pot. (mV)	Passive current density ($\mu\text{A cm}^{-2}$)
52100 untreated	45 min @ 25 mA	-675	-648	23
Xe \rightarrow 30 nm Cr 3×10^{16} , 300 keV	30 min @ 5 mA	-650	-10	38
Cr \rightarrow 30 nm Cr 2×10^{17} , 150 keV	30 min @ 5 mA	-710	+135	45

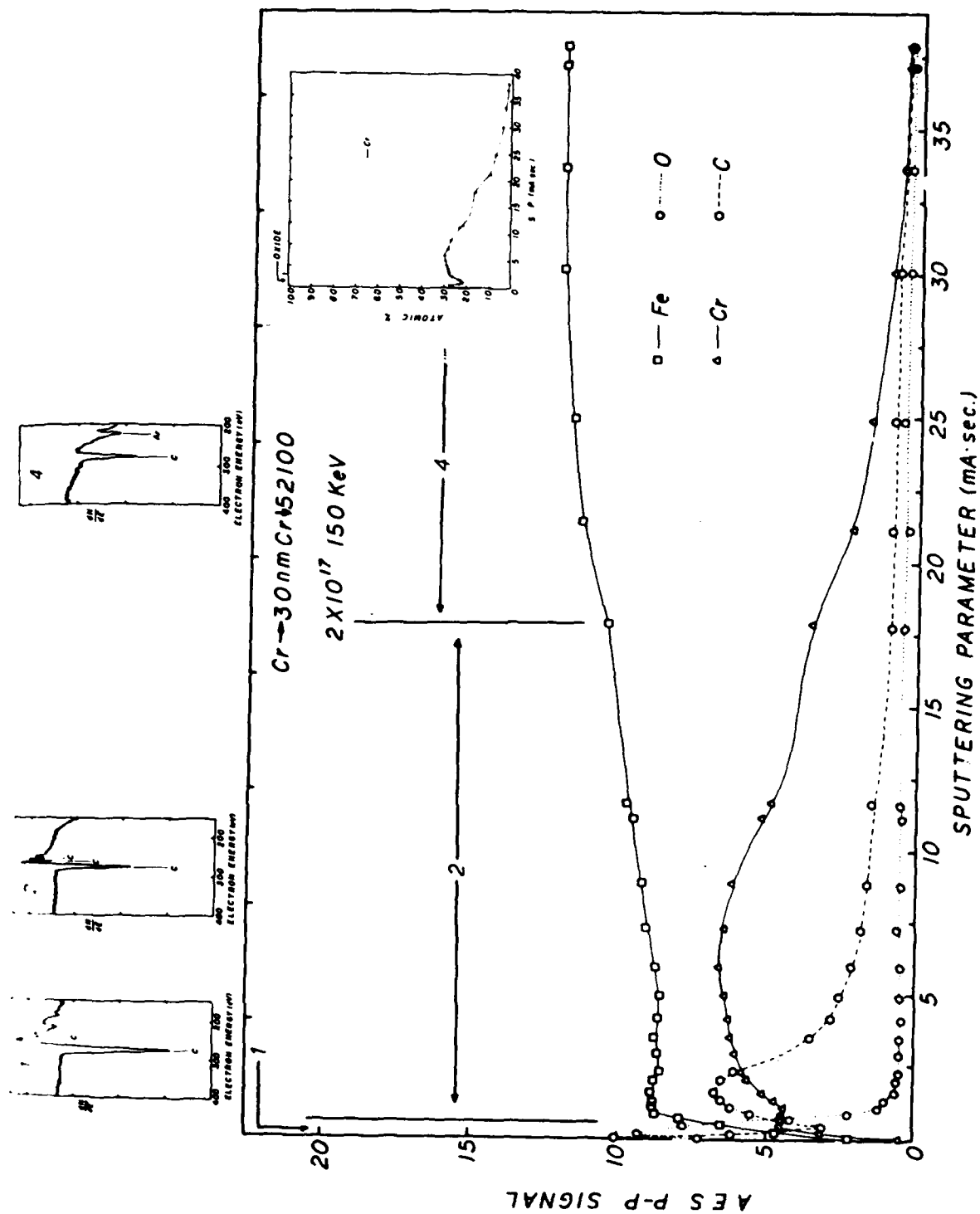


Fig. 3. Auger depth profiles of Fe, Cr, O and C following Cr ion beam mixing of 30 nm Cr film on 52100 steel (profiled with Ar at 4 keV).

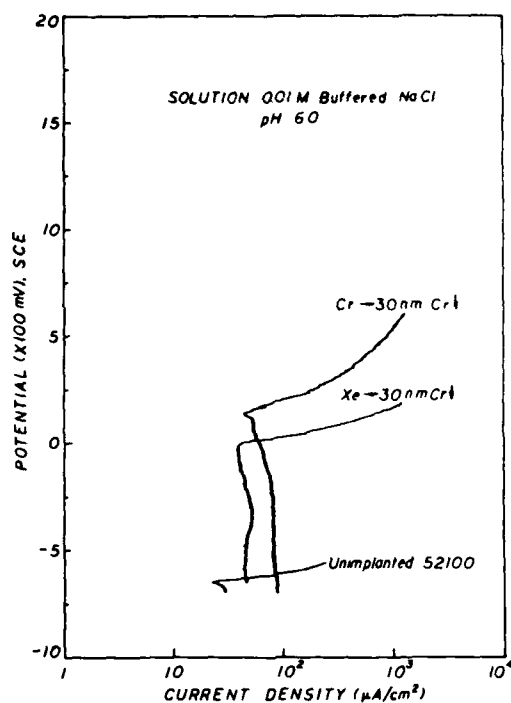


Fig. 4. Anodic polarization plots of 52100 steel and ion beam mixed surface alloys in deaerated 0.01 M NaCl solution buffered at pH = 6 with cathodic pretreatment.

from fig. 7, that carbide formation is again observed, especially in the vicinity of the original oxide film of the 52100 steel.

The electrochemical behavior of the Kr and Cr intermixed surface alloys, in the pitting solution can be seen from fig. 9 and table 4. Both surface alloys exhibit a more noble breakdown potential than 52100 steel. The improvement in breakdown potential for Kr was 550 mV and for Cr 725 mV. The passivation current density was found to be

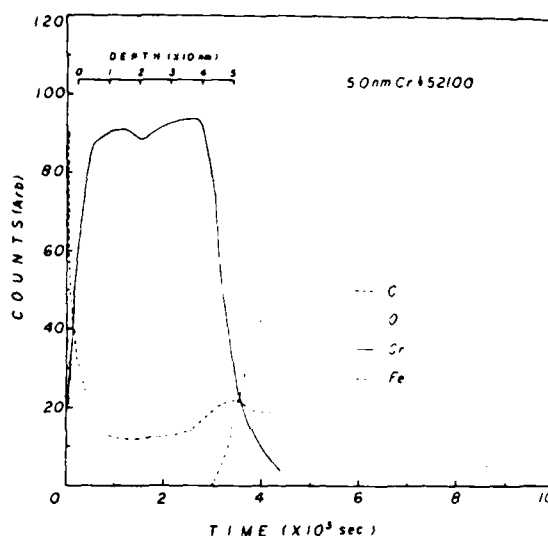


Fig. 5. Auger depth profiles of Fe, Cr, O and C of 50 nm Cr film E-beam deposited on 52100 steel.

significantly lower in this work compared to the two previous surface alloys tested.

4. Discussion

In both of the inert gas implantation experiments considerable surface oxidation took place apparently during the implantation process. The NRA depth profiles confirm the Auger depth profiling data. The possibility exists that radiation enhanced oxidation may have taken place during implantation. Oxidation during implantation would require that the arrival rate of adsorbates containing oxygen exceeds the rate of sputtering. The ion beam current densities, in the $\mu\text{A cm}^{-2}$

Table 4
AISI 52100 pitting data in deaerated 0.01 M NaCl (buffered pH = 6) solution

Sample	Cathodic treatment	Open circuit potential (mV)	Breakdown potential (mV)	Passive current density ($\mu\text{A cm}^{-2}$)
52100 untreated	45 min @ 25 mA	-675	-648	23
Kr → 50 nm Cr ↓ 5×10^{16} 300 keV	30 min @ 5 mA	-570	-125	4
Cr → 50 nm Cr ↓ 5×10^{16} 150 keV	30 min @ 5 mA	-570	+50	8

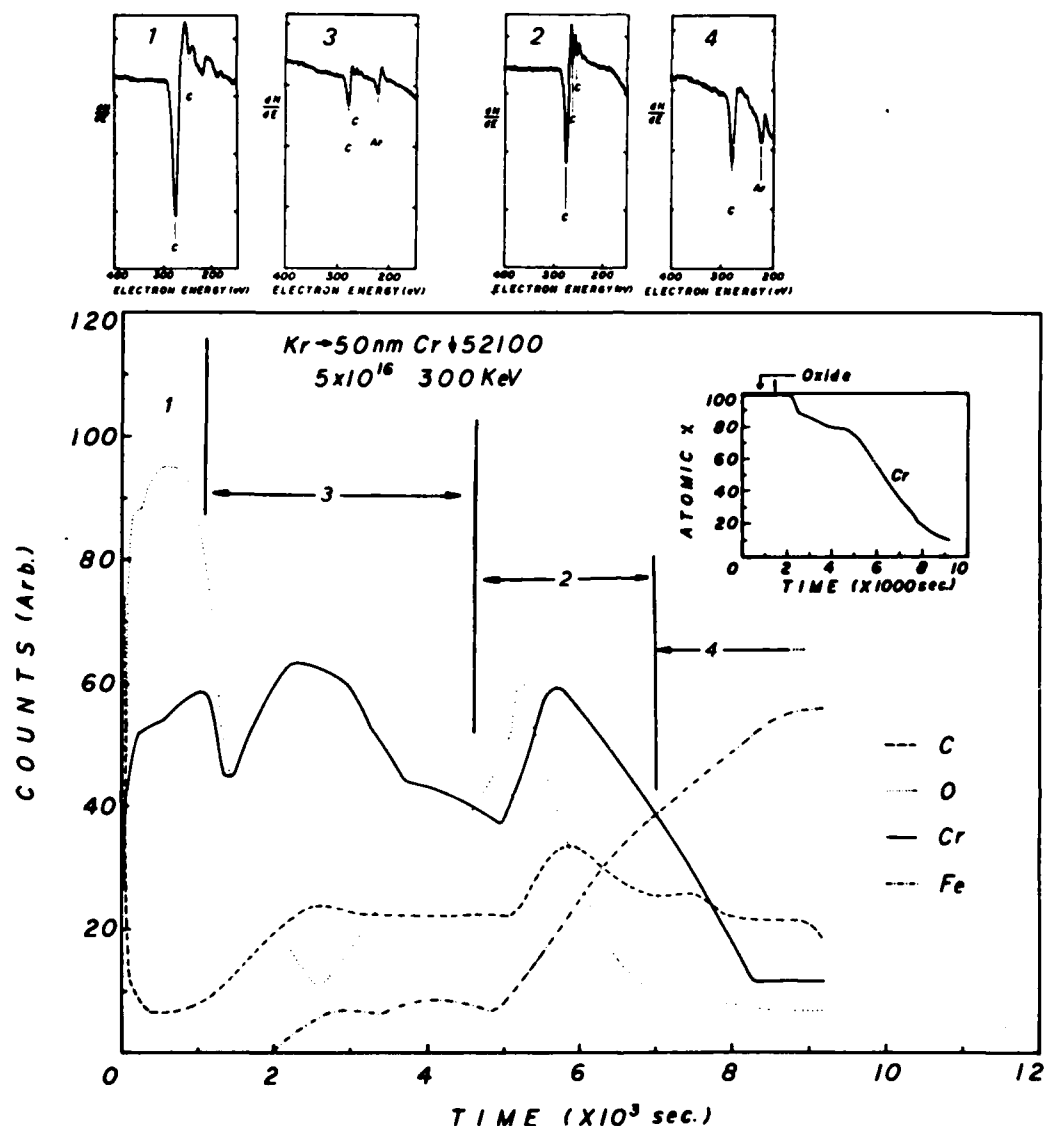


Fig. 6. Auger depth profiles of Fe, Cr, O and C following Kr ion beam mixing of 50 nm Cr film on 52100 steel (profiled with Xe at 1.5 keV).

range, used in the inert gas implantations apparently met this condition, resulting in considerable oxide growth by radiation enhanced oxidation. During the chromium implantation experiments beam currents varied between 300–800 $\mu\text{A cm}^{-2}$ – a condition that would not be expected to favor surface oxidation.

The formation of such an oxide film during intermixing is not desirable since it interferes with the intermixing process by tending to immobilize the Cr and rendering less metallic chromium avail-

able for passivation. The resulting oxide layer will perform as a protective barrier on exposure to an aqueous environment, but will not have the unique chemical and mechanical properties normally associated with Cr-rich ultra-thin (~ 1.5 nm) passive films.

The corrosion behavior of the surface alloys studied in this paper is superior to 52100 steel. The addition of Cr to 52100 steel, by ion-implantation or ion beam mixing is carried out in order to form a Cr-rich passive film. Cr-based passive films are

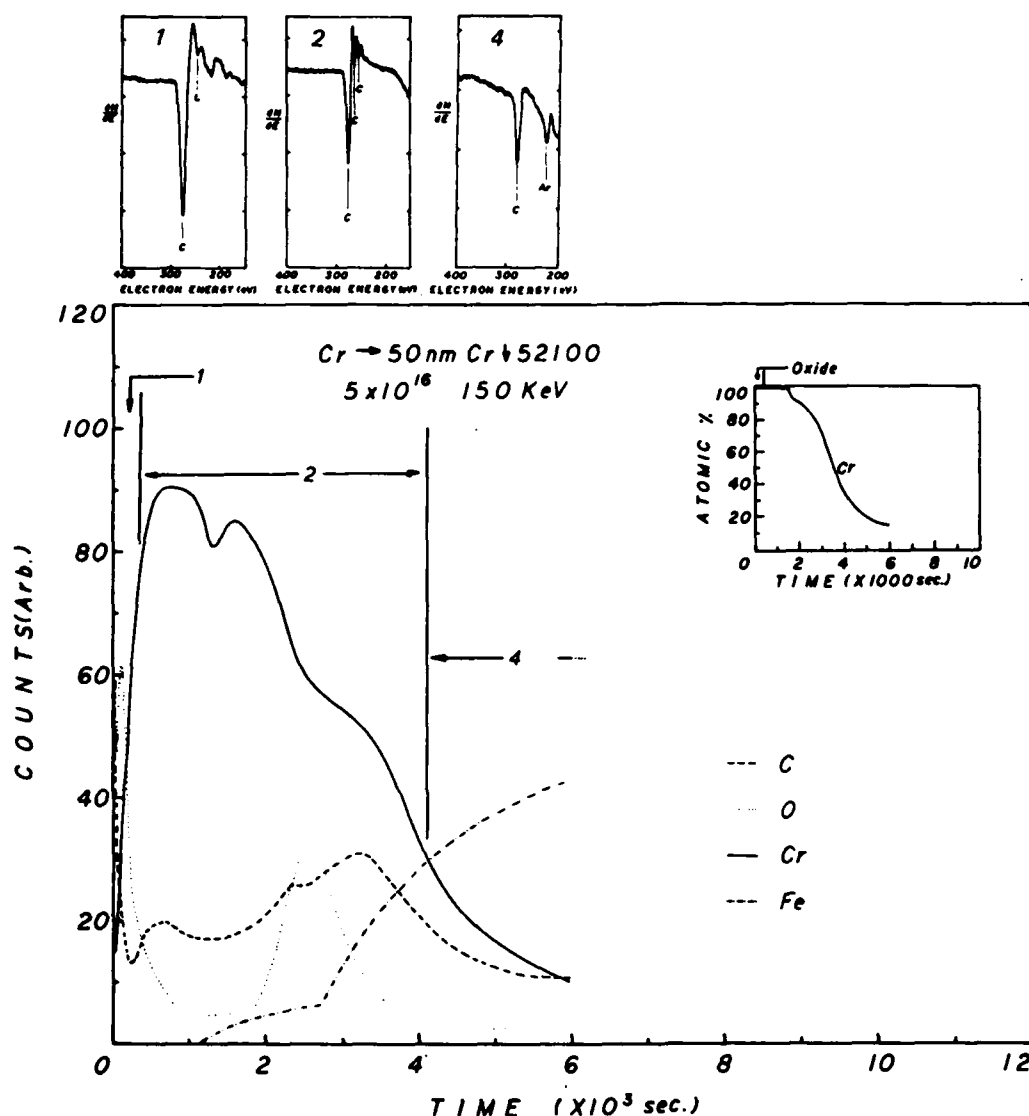


Fig. 7. Auger depth profile of Fe, Cr, O and C following Cr ion beam mixing of 50 nm Cr film on 52100 steel (profiled with Xe at 1.5 keV).

generally more stable over a greater variety of environmental conditions than an Fe-based passive film. In a previous paper we have shown that Cr-implantation into 52100 steel results in considerably improved passivation behavior and pitting resistance [2]. However, the full potential of the Fe-Cr surface alloys to resist pitting corrosion was not realized owing to the formation of surface carbides which tend to disrupt coverage of the alloy by the passive film. Pitting may, therefore, take place along the interface between the carbide

phase and the Fe-Cr matrix. Since carbides have been observed in each of the surface alloys discussed in this paper, it is likely that pitting of these surface alloys may be associated with the presence of carbides. In particular we note that of the two surface alloys formed by Cr^+ ion beam mixing, the surface alloy rich in Cr showed the poorer resistance to pitting. It follows from the above discussion that this may be due to the significantly higher chromium carbide content present in the surface alloy of higher chromium content.

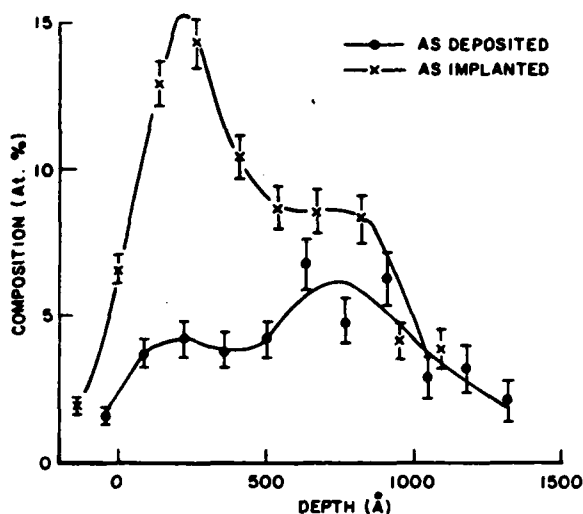


Fig. 8. Nuclear reaction analysis of 50 nm Cr film deposited on 52100 steel, before and after Kr ion beam mixing ($^3\text{He}, \alpha$) reaction was used to profile ^{16}O .

The source of carbon for carbide formation is well known to be the product of hydrocarbon cracking during ion implantation [3,4]. Three sources of hydrocarbons are available for cracking:

- 1) Vacuum contamination.
- 2) Surface hydrocarbons from the atmosphere and organic solvents.
- 3) The hydrocarbon layer on the original oxide surface of 52100 steel, having similar origin as 2).

Systematic reduction in the surface and interfacial hydrocarbon layers and improvement in vacuum conditions are, therefore, important prerequisites to the formation of highly corrosion resistance surface alloys formed by the ion beam mixing technique.

5. Conclusions

- Fe-Cr surface alloys have been formed on 52100 steel by ion beam mixing Cr films with Kr^{2+} , Xe^{2+} and Cr^+ .
- The surface alloys so formed exhibited superior resistance to pitting in 0.01 M NaCl (buffered to pH 6) compared to 52100 steel.
- Kr^{2+} and Xe^{2+} ion beam mixing was accompanied by severe surface oxidation.
- Carbide formation resulted from ion beam mixing by Kr^{2+} , Xe^{2+} and Cr^+ .
- The presence of carbides was found to lower the pitting resistance of the surface alloys.
- For the production of highly corrosion resistant surface alloys using ion beam mixing, hydrocarbon contamination must be reduced as far as possible.

This work was sponsored by the U.S. Office of Naval Research, Arlington, Virginia under Contract No. N0001477CO424. The V.G.S. Electron Spectrometer and V.G.S. 1000 data system was acquired from equipment awards DMR7718319 and DMR8117321 from the National Science Foundation, Washington, D.C.

References

- [1] R. Valori and G.K. Hubler, NRL Memorandum Report 4527, June (1981) p. 100.
- [2] W.K. Chan, C.R. Clayton and J.K. Hirvonen, in: Corrosion of Metals Processed by Directed Energy Beams, Eds., C.R. Clayton and C.M. Preece (TMS-AIME, New York) in press.
- [3] J.A. Knapp, D.M. Follstaedt and S.T. Picraux, in: Ion Implantation Metallurgy, Eds., C.M. Preece and J.K. Hirvonen (TMS-AIME, New York, 1980) p. 152.
- [4] I.L. Singer, C.A. Carosella and J.R. Reed, Nucl. Instr. and Meth. 182/183 (1981) 923.

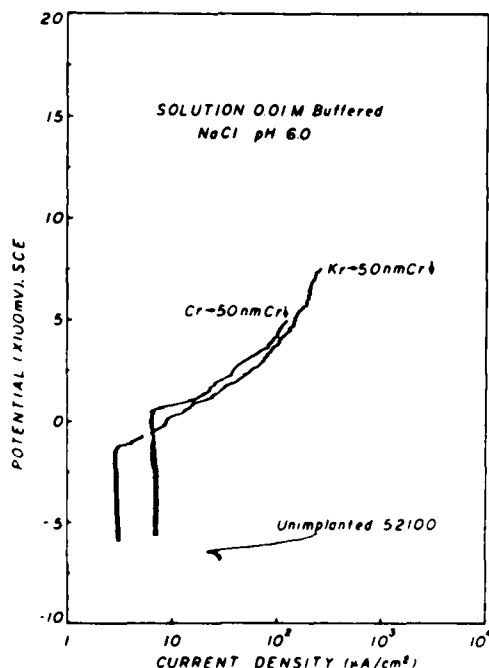


Fig. 9. Anodic polarization plots of 52100 steel and ion beam mixed surface alloys in deaerated 0.01 M NaCl solution buffered at pH = 6 with cathodic pretreatment.

Section III.C

RHEED, AES and XPS STUDIES ON THE PASSIVE FILMS
FORMED ON ION IMPLANTED STAINLESS STEEL

C. R. Clayton, K. G. K. Doss and Y-F. Wang¹
J. G. Warren²
G. K. Hubler³

¹Department of Materials Science and Engineering
State University of New York
Stony Brook, NY

²Brookhaven National Laboratory
Upton, NY

³Materials Modification and Analysis Branch
Condensed Matter and Radiation Sciences Division
Naval Research Laboratory

This work was supported by the Office of Naval Research Contract
#N0001477C0424 at SUNY, by the Department of Energy at Brookhaven
and by ONR at the Naval Research Laboratory.

RHEED, AES AND XPS STUDIES OF THE PASSIVE FILMS FORMED ON ION IMPLANTED STAINLESS STEEL

C. R. Clayton*, K. G. K. Doss*, Y-F. Wang*, J. B. Warren** and G. K. Hubler***

*Department of Materials Science and Engineering, State University of New York, Stony Brook, N.Y. 11794, USA

**Brookhaven National Laboratory, Upton, N.Y. 11973, USA

***Naval Research Laboratory, Washington, D.C. 20375, USA

ABSTRACT

P-implantation (10^{17} ions cm^{-2} , 40 Kev) into 304 stainless steel (ss) has been carried out, and an amorphous surface alloy was formed. Polarization studies in deaerated 1N H_2SO_4 + 2% NaCl showed that P-implantation improved both the general and localized corrosion resistance of 304 ss. A comparative study has been carried out between the implanted and unimplanted steel to determine what influence P-implantation has upon the properties of the passive film formed in 1N H_2SO_4 . The influence of Cl ions on pre-formed passive films was also studied. RHEED, XPS and AES were used to evaluate the nature of the passive films formed in these studies.

KEYWORDS

Ion implantation, X-ray Photoelectron Spectroscopy, Auger Electron Spectroscopy, Reflection High Energy Electron Diffraction, passivity.

INTRODUCTION

In a previous study (1) TEM analysis was carried out on pre-thinned 3 mm. diameter discs of 304 (ss) which had been implanted with 10^{17} P+ ions cm^{-2} at 40 Kev. The microstructure of the surface alloy showed a mottled structure which could be interpreted as evidence of microcrystallinity with grains of ca. 50 Å in diameter. Electron diffraction analysis produced a single diffraction halo, indicative of either an amorphous or microcrystalline surface alloy. The electrochemical behavior of the surface alloy was studied in deaerated 1N H_2SO_4 and in 0.1 N NaCl solution. Little improvement was found in the active-passive behavior in the acid, and poor resistance to pitting was observed in the chloride solution. This behavior was not typical of the ultra-high corrosion resistance which has been observed in amorphous Cr bearing ferrous alloys (2,3), and was taken as further evidence that the surface alloy was indeed microcrystalline.

Recently we have improved the heat sinking of 304 ss samples during ion implantation with P, by bonding the samples with silver adhesive to a water-cooled copper plate. This has resulted in significant improvements in the

passivation behavior of the P-implanted 304 ss in deaerated 1N H₂SO₄ and 1N H₂SO₄ + 2% NaCl solution. This study is concerned with the compositional and structural nature of the passive films formed on P-implanted and unimplanted 304 ss.

EXPERIMENTAL

The composition of the stainless steel used in this work is given in Table 1.

Table 1. Composition of 304 Stainless Steel

% Cr	% Ni	% Mn	% Si	% Mo	% C	% N	% S	% P
18.18	8.48	1.75	0.5	0.36	0.055	0.05	0.005	0.028

Sample preparation was the same as that reported earlier (1). As mentioned above, heat sinking was improved to insure that the power input (1 watt cm⁻²) during implantation did not raise the temperature of the sample to above 50°C. A composition depth profile was carried out using Auger Electron Spectroscopy (AES) with Ar⁺ ion etching (6 Kev, 15 μ A cm⁻²). This profile, which is given in Fig. 1, indicates that > 90% of the P is distributed within a depth of ca. 120 Å and that the peak distribution is located at ca. 40 Å from the surface. In agreement with the previous work (1) in which X-ray Photoelectron Spectroscopy (XPS) was used to profile the surface alloy, no sign was found of the redistribution of Fe, Cr or Ni due to selective sputtering or radiation enhanced segregation. However, the second maxima found in the P-profile of the previous work was not observed in this study.

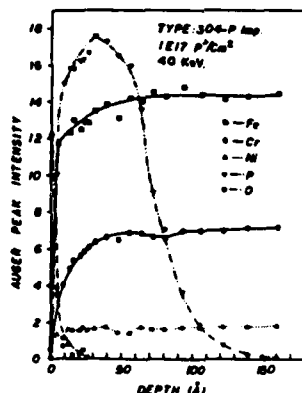


Fig. 1. AES composition depth profile of P⁺-implanted 304 stainless steel.

ELECTROCHEMICAL ANALYSIS

The details of the technique of anodic polarization used in this study have been published earlier (1). In this work the active-passive behavior was observed in a deaerated solution of 1N H₂SO₄ + 2% NaCl. All electrode potentials were measured against the Saturated Calomel Electrode (SCE). Fig. 2 shows the polarization curves for 304 and P-implanted 304 ss. In this electrolyte a marked lowering of the passivation potential and a decrease in the critical and passive current densities due to P-implantation was

observed. A second anodic current maximum was also observed at -50 mV. Whereas no pits were observed in the implanted steel, pitting did occur on the unimplanted steel where breakdown of passivity took place transpassively.

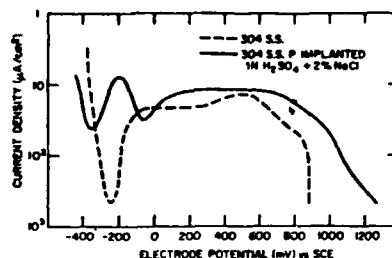


Fig. 2. Anodic polarization curves of 304 ss and P^+ -implanted 304 ss in 1N H_2SO_4 + 2% NaCl.

PASSIVE FILM ANALYSIS

To study the nature of the passive films formed on the implanted and unimplanted steels, structural analysis was carried out using RHEED (Reflection High Energy Electron Diffraction), compositional depth profiles were obtained by AES coupled with Ar^+ ion sputtering and the chemical states of the constituents of the films was determined by XPS.

In order to prepare the passive films for analysis, samples were first cathodically pre-treated (-1000 mV, $10^3 \mu A cm^{-2}$, 15 mins.) in deaerated 1N H_2SO_4 to remove the air formed oxide followed by potentiostating at either +250 or +550 mV (Vs. SCE) for 1 hour. Immediately following the passivation treatment samples were cleaned in doubly distilled water, dried with a jet of argon and quickly transferred to the electron microscope or electron spectrometer. Separate, freshly prepared samples were used for structural and compositional analysis.

In order to compare the effect of Cl^- ions on the passive film formed at +550 mV and +250 mV (Vs. SCE) in deaerated 1N H_2SO_4 , a Cl^- ion inoculation treatment was carried out following passivation for 1 hour. The inoculation treatment consisted of the addition of a small amount of concentrated H_2SO_4 and NaCl solution in order to make up a bulk solution of 1N H_2SO_4 and 2% NaCl. The samples were then passivated for a further 10 minutes, in a solution of 1N H_2SO_4 + 2% NaCl, during which time no pitting took place. The samples were then washed and prepared for analysis as before.

RHEED ANALYSIS

All the RHEED patterns were obtained using a Phillips EM300 electron microscope. A summary of the data is given in Tables 2 and 3. The crystalline films formed on the unimplanted steel were seen to modify with increase in anodic potential (4) and with exposure to the Cl^- ions. The films formed on the implanted steel were found to be amorphous yielding halos as shown in Fig. 3. A single ring was observed between the halos in three of the samples analyzed. In order to determine the possible origin of this ring, we assumed that two other rings were superimposed on the halos. We approximated the possible position of the two other rings and determined their

radii. The calculated 'd' spacings which resulted from this approximation matched those of CrPO_4 and $\text{Fe}(\text{PO}_3)_3$.

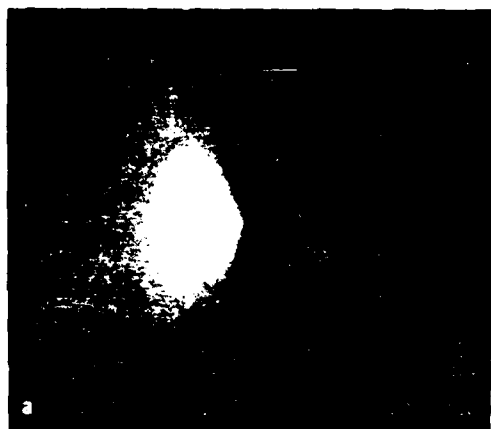


Fig. 3. RHEED halos of the anodic film formed on P^+ -implanted 304ss in 1N H_2SO_4 at +550 mV SCE.

Table 2. Calculated Interplanar Spacings of the Passive Films Formed in 1N H_2SO_4 at +550 mV and +250 mV for 1 Hr.

Potential	Steel	d Spacing	Phase
+550 mV SCE	304	3.23, 2.73, 2.35, 2.18 1.88, 1.69, 1.43, 1.19	$\gamma\text{-FeOOH}$ CrOOH
	304-P	2.65, 1.98, 1.44	$\text{Fe}(\text{PO}_3)_3$ CrPO_4
	304	3.54, 3.21, 2.85, 2.46, 2.21 1.88, 1.70, 1.60, 1.31	Green Rust II* $\text{Fe}(\text{OH})_2$ CrOOH
+250 mV SCE	304-P	2 diffuse Rings	—

*Green Rust II (GR II): $2\text{Fe}(\text{OH})_2 \cdot 4\text{Fe}(\text{OH})_3 \cdot \text{FeSO}_4 \cdot x\text{H}_2\text{O}$, Ref (5).

Table 3. Calculated Interplanar Spacings of the Passive Films Formed in 1N H_2SO_4 for 1 Hr. and continued passivation in 1N H_2SO_4 + 2% NaCl for 10 Min.

Potential	Steel	d Spacing	Phase
+550 mV	304	3.33, 3.06, 2.64, 2.20, 1.80 1.75, 1.64	γ -FeOOH $Cr(OH)_3$
	304-P	2.65, 1.98, 1.44	$Fe(PO_3)_3$ $CrPO_4$
+250 mV	304	3.91, 3.30, 2.97, 2.64, 2.40 2.03, 1.89, 1.76, 1.70, 1.57, 1.42	Green Rust I* $Cr(OH)_3$
	304-P	3 Diffuse Rings 2.70, 2.16, 1.49	$Fe(PO_3)_3$ α - $CrPO_4$

*Green Rust I (GR I): $Fe_{3.6}^{2+} Fe_{0.9}^{3+} (O, OH, Cl)_9$ Ref. (6)

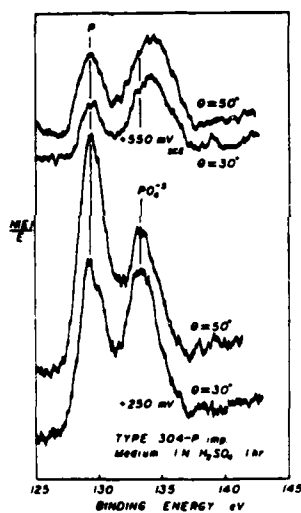


Fig. 4a

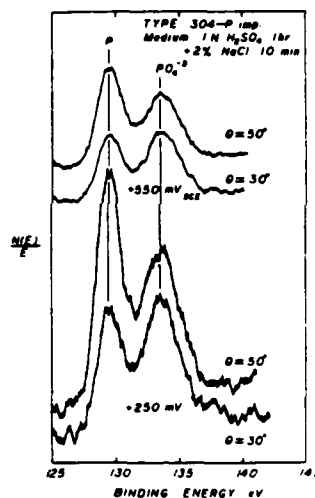


Fig. 4b

Fig. 4. The phosphorus 2P photoelectron spectra measured for anodic films formed on P^+ -implanted 304 ss under various conditions.

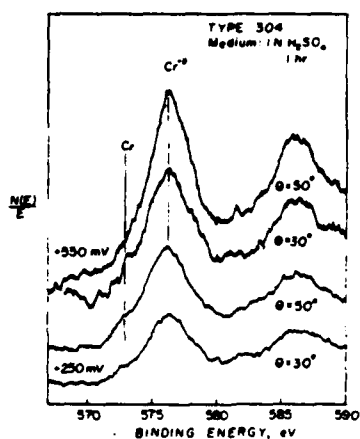


Fig. 5a

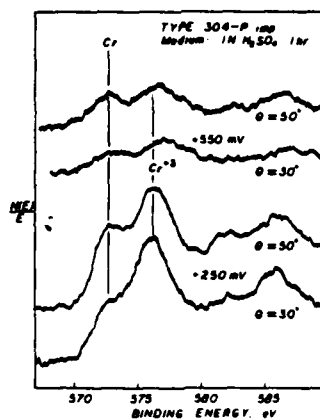


Fig. 5b

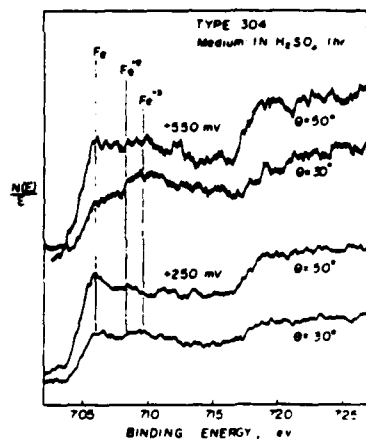


Fig. 5c

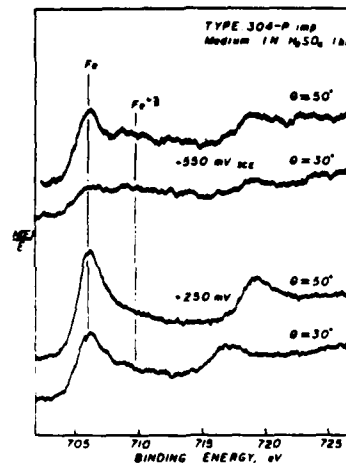


Fig. 5d

Fig. 5. Cr 2p and Fe 2p photoelectron spectra measured for anodic films formed on 304 ss and P⁺ implanted 304 ss in 1N H₂SO₄ at +550 mV and +250 mV SCE.

XPS AND AES ANALYSIS

A non-destructive analysis was first carried out using XPS, varying the angle of electron take off in order to differentiate between the outer and inner layers of the passive films. XPS showed the presence of Cr³⁺, Fe³⁺ and Ni²⁺ cations and SO₄²⁻ anions in all the films studied. Phosphate anions were also observed in the films formed on the surface alloy. As shown in Figs. 4 and 5 the chemically shifted peaks of the cations were lower and the metallic signals higher in the film formed on the surface alloy indicating that the surface alloy formed a thinner passive film. The phosphate peaks (P 2p) were broadened by charge shifting in the case of the film not

exposed to Cl^- ions. This indicates that the film is more insulating in nature.

The depth profiles obtained by AES (Figs. 6 and 7) revealed that the thickness of the films was slightly increased on exposure to Cl^- ions. The passive films formed on the unimplanted samples increased from 17-22 Å while those formed on the P-implanted steel increased from 6-10 Å at +550 mV and remained almost unchanged at +250 mV. The extra film growth coincided with the depth to which Cl^- ions were detected and to a plateau in the distribution of the sulphur (SO_4^{2-}) peaks. The low level of Ni^{2+} detected by XPS and AES accounts for the absence of the nickel phase in the RHEED analysis. The composition profiles also indicated a build-up of Cr^{3+} in the inner layer of the passive film in each of the cases studied.

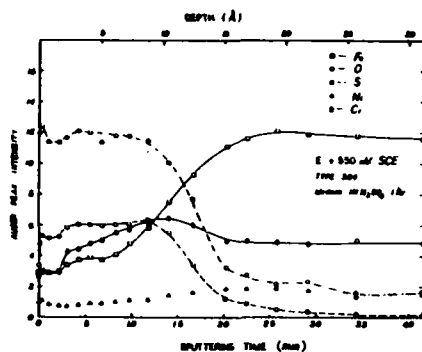


Fig. 6a

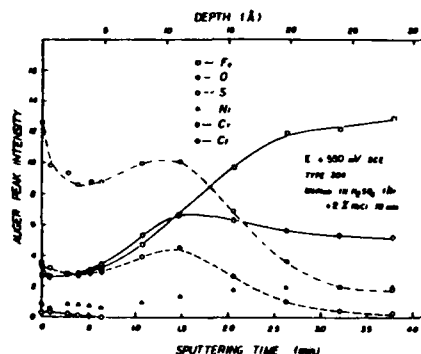


Fig. 6b

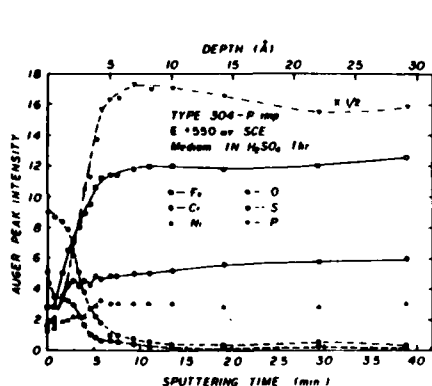


Fig. 6c

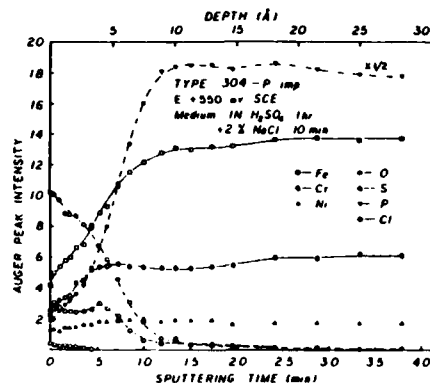


Fig. 6d

Fig. 6. AES composition profiles of the anodic films formed on 304 ss and P^+ -implanted 304 ss in 1N H_2SO_4 at +550 mV SCE with and without the addition of Cl^- ion.

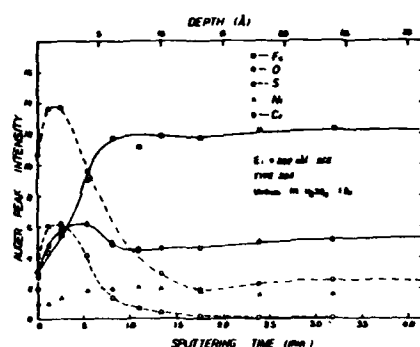


Fig. 7a

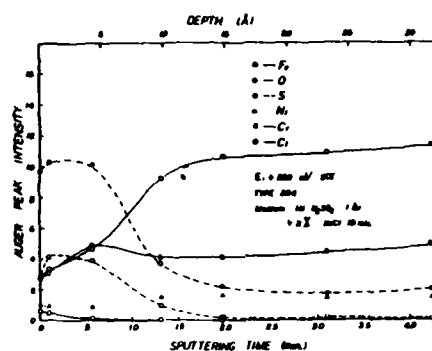


Fig. 7b

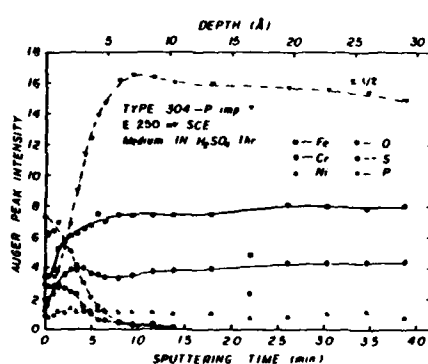


Fig. 7c

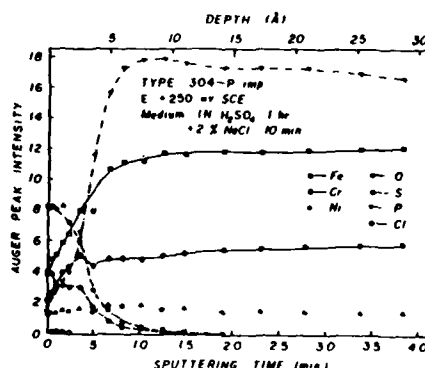


Fig. 7d

Fig. 7. AES composition profiles of the anodic films formed on 304 ss and P⁺-implanted 304 ss in 1N H₂SO₄ at +250 mV SCE with and without the addition of Cl⁻ ion.

DISCUSSION OF RESULTS

Electrochemical analysis in deaerated acidic-chloride solution shows that the P-implanted amorphous surface alloy produces a more extensive range of passive potential accompanied by a lower passive current density. Compositional analysis indicates that the film is much thinner than is formed on unimplanted steel.

The structural modification of the passive films formed on the unimplanted 304 ss resulting from Cl⁻ attack has not resulted in pitting. The containment of Cl⁻ ions to the outer regions of the passive film appears to be due to the formation of β -FeOOH at +550 mV and G.R.I. at +250 mV which are only formed in the presence of Cl⁻ ions (5). Indeed G.R.I. incorporates Cl⁻ ions into the crystal structure. The role of Cr(OH)₃ is less understood, since it has been shown that the hydroxyl group of metallic hydroxides is more easily displaced by Cl⁻ ions than in the case of oxyhydroxides (7). An

important point which must be emphasized is that the RHEED analysis carried out in this work gave no evidence of the existence of the phases formed in the passive film prior to Cl^- ion exposure. Since the AES profiles indicate that only the outer portions of the passive films are modified by Cl^- ion exposure it is reasonable to assume that the new phases which are formed are only present in the outer region of the passive film. It is, therefore, thought that the diffraction patterns from the inner portions of the passive film are too weak to be detected.

The ability of the amorphous passive film to resist Cl^- ion penetration and structural modification is probably due to (a) the difficulty with which diffusion may take place in the passive film and (b) the inhibitive action of the phosphate anions. It is apparent from the AES composition depth profiles that the phosphate anions are generally incorporated into the amorphous passive film. However, the trace of crystalline phosphates detected by RHEED in the high potential film may have resulted from precipitation from the solution.

The effectiveness of phosphates to resist Cl^- ion attack may be indicated by the ease with which phosphate anions may be displaced. Some evidence of the displacement of phosphate anions by Cl^- is seen in the high potential passive film. It is evident from the 30° P 2p spectra from +550 mV film (Figs. 4a and 4b) that the elemental P 2p peak from the surface alloy and the phosphate P 2p peak from the film are of approximately equal height following 10 minutes exposure to Cl^- ions. However, before exposure to the Cl^- ions, the 30° spectra show that the peaks from the phosphate anions are higher than for the elemental P. Since exposure to the acidic-chloride solution leads to film thickening one would normally expect the phosphate peak to be higher than the elemental peak due to (a) increased attenuation of the elemental P peak from the alloy and (b) the increase in the total number of phosphate ions in the film. It is, therefore, possible that Cl^- ions may have begun to displace phosphate ions incorporated in the outer regions of the original passive film. In contrast to this observation, the films formed at +250 mV did not show any significant change in the relative heights of the elemental P and phosphate 2p peaks resulting from Cl^- ion exposure. This is consistent with the limited penetration of Cl^- as indicated by Fig. 7d and the undetectable level of film growth resulting from Cl^- ion exposure.

CONCLUSIONS

Ion implantation may be used to produce an amorphous surface alloy on a commercial stainless steel, and, thereby, enhance considerably the corrosion resistance of that steel. The removal of grain boundaries and other imperfections in the substrate is expected to improve the general and localized corrosion resistance of the steel, because such defects disrupt the coverage of the passive film at these active sites in the crystalline substrate. A further effect of the amorphous structure of the surface alloy is to promote the formation of an amorphous passive film having superior resistance to Cl^- ion attack in acidic media. The stability of the passive films in acidic-chloride solution is probably due to (a) the effectiveness of an amorphous film to act as a diffusion barrier, (b) the corrosion inhibitor properties both of the phosphates contained within the amorphous passive film, and, the layer of crystalline phosphates which are assumed to have been deposited from solution on to the outer surface of the passive film.

ACKNOWLEDGEMENTS

We gratefully acknowledge the U.S. Office of Naval Research for support of this work under contract #N0001477C0424 and the National Science Foundation for an equipment award for the VGS ESCA3MK11 spectrometer. Portions of this work was supported under U.S. Department of Energy Contract DE-AC02-76-CH00016.

REFERENCES

1. Clayton, C. R., K.G.K. Doss, H. Herman, S. Prasad, Y.F. Wang, J.K. Hirvonen and G.K. Hubler, Ion Implantation Metallurgy, Ed. C.M. Preece and J.K. Hirvonen, TMS-AIME 1980.
2. Asami, K., K. Hashimoto, T. Masumoto and S. Shimodaira, Corros. Sci. 16, 909 (1976).
3. Hashimoto, K., M. Naka, J. Noguchi, K. Asami and T. Masumoto. Passivity of Metals, Ed. R.P. Frankenthal and J. Kruger (Proc. of Fourth Int. Symp. on Passivity, 1977) p. 56. The Electrochem. Soc. Inc., Princeton, N.J. (1978).
4. Doss, K.G.K., C.R. Clayton and J.B. Warren, Spring Meeting, The Electrochem. Soc., Minneapolis, Minnesota, May 1981, Extended Abstracts.
5. Misawa, T., K. Hashimoto and S. Shimadaira, Corros. Sci. 14, 131 (1974).
6. Bernal, J.D., D.A. Das Gupta and A.L. Mackay, Clay Minerals Bulletin 4, 15 (1959).
7. Saito, H., T. Shibata and G. Okamoto, Corros. Sci. 19, 693 (1979).

Section IV.A

INFRARED STUDIES OF ISOTHERMAL ANNEALING OF ION-IMPLANTED SILICON:
REFRACTIVE INDICES, REGROWTH RATES, AND CARRIER PROFILES

C. N. Waddell¹
W. G. Spitzer²
G. K. Hubler³
J. E. Fredrickson⁴

¹Physics and Materials Science Departments
University of Southern California
Los Angeles, CA
and

Materials Modification and Analysis Branch
Condensed Matter and Radiation Sciences Division
Naval Research Laboratory

²Physics and Materials Science Departments
University of Southern California
Los Angeles, CA

³Materials Modification and Analysis Branch
Condensed Matter and Radiation Sciences Division
Naval Research Laboratory

⁴Physics-Astronomy Dept.
California State University
Long Beach, CA

This work was supported by the Office of Naval Research and Joint
Services Electronics Program monitored by the Air Force
Office of Scientific Research.

Infrared studies of isothermal annealing of ion-implanted silicon: Refractive indices, regrowth rates, and carrier profiles

C. N. Waddell and W. G. Spitzer

Physics and Materials Science Departments, University of Southern California, Los Angeles, California 90007

G. K. Hubler

Naval Research Laboratory, Washington, D.C. 20375

J. E. Fredrickson

Physics-Astronomy Department, California State University, Long Beach, California 90840

(Received 22 February 1982; accepted for publication 30 March 1982)

A model-dependent computer analysis technique developed previously has in this work been applied to the infrared reflection data of a number of $\langle 111 \rangle$ and $\langle 100 \rangle$ oriented Si samples which were implanted with high fluences of Si or P ions and then taken through an isothermal annealing process. The physical properties deduced from this analysis are: (i) Dielectric properties including the frequency dependent refractive indices of the recrystallized Si and of the α -Si as a function of annealing temperature and time; (ii) structural information including the amorphous layer depth, widths of transition regions, and the epitaxial regrowth rates; and (iii) electrical properties including the depth profile of the carrier density, the carrier mobility near the maximum carrier density, and the carrier activation efficiency. The physical interpretation of the results is discussed and, where possible, comparisons with results of other experiments are made.

PACS numbers: 78.20.Dj, 61.70.Tm, 61.40. — a, 78.65.Jd

I. INTRODUCTION

There have been a number of studies of high fluence, ion-implanted Si, GaAs, and GaP semiconductors by means of infrared reflection and/or transmission methods.¹⁻¹⁶ Various investigators have attempted to explain the nature of the interference effects observed in the reflection (transmission) as a function of frequency by using dielectric layer models. These models generally attempt to approximate the changes in the dielectric properties produced by ion implantation by using one or more layers overlying the undisturbed bulk material. In some recent studies it was demonstrated that the interference spectra observed for implanted Si could be calculated very accurately with such a model if one incorporated a sufficient number of features to adequately approximate the physical situation.^{9,15} This model gave good nonlinear least-squares fits to the measured reflection for a large number of as-implanted Si samples.⁹ It also fit well the spectrum of an annealed sample¹⁵ which had been implanted with P⁺ ions if one included the effects of the spatial distribution of the free carriers¹⁰ on the dielectric properties of the epitaxially recrystallized material. Some earlier studies^{2-8,10,11} had also incorporated plasma effects; however, generally physically unrealistic simplifying assumptions were used which resulted in much less satisfactory fits to the data. The more realistic model,¹⁵ to be discussed briefly, has also been used recently to study the changes in the dielectric constant of amorphous Si(α -Si) produced by isothermal annealing of implanted layers.¹⁶ In the present work, this model and analysis are applied to the infrared reflection measurements of a number of $\langle 111 \rangle$ and $\langle 100 \rangle$ oriented Si samples which were implanted with high fluences of Si or P ions and then taken through an isothermal annealing process. The model dependent physical properties deduced from this analysis are:

- (i) Dielectric properties including the frequency depen-

dent refractive indices of the recrystallized Si and of the α -Si as a function of annealing temperature and time;

- (ii) structural information including the amorphous layer depth, widths of transition regions, the epitaxial regrowth rates; and

- (iii) electrical properties including the depth profile of the carrier density, the carrier mobility near the maximum carrier density, and the carrier activation efficiency. For each case the physical interpretation of the results is discussed and, where possible, comparisons with results of other experiments are made.

II. BACKGROUND

The model to be used for the analysis of the present measurements has been discussed in detail in a previous paper.¹⁵ Therefore, it will be reviewed here only briefly with an emphasis on the interpretation of the model's parameters. When Si crystals are heavily implanted, the frequency-dependent infrared reflection has interference fringes produced by the presence of a layer of material having implantation-induced changes in the dielectric constant. This interference effect was first reported by Crowder and co-workers.¹⁷ The model used here approximates the modifications of the material according to the illustrative curves shown in Fig. 1, which are repeated from Ref. 15. The curves of Figs. 1(a) and 1(b) show the depth profiles for the high frequency refractive index and extinction coefficient in the damaged or amorphous layer (D), the recrystallized layer (R) which will be present in annealed samples, and the crystalline substrate (S). High frequency refers to the frequency interval below E_g/\hbar , where E_g is the energy gap, and well above the free carrier plasma frequency. The relative positions of the interfaces are dependent upon the past annealing conditions. The transition regions between the three layers

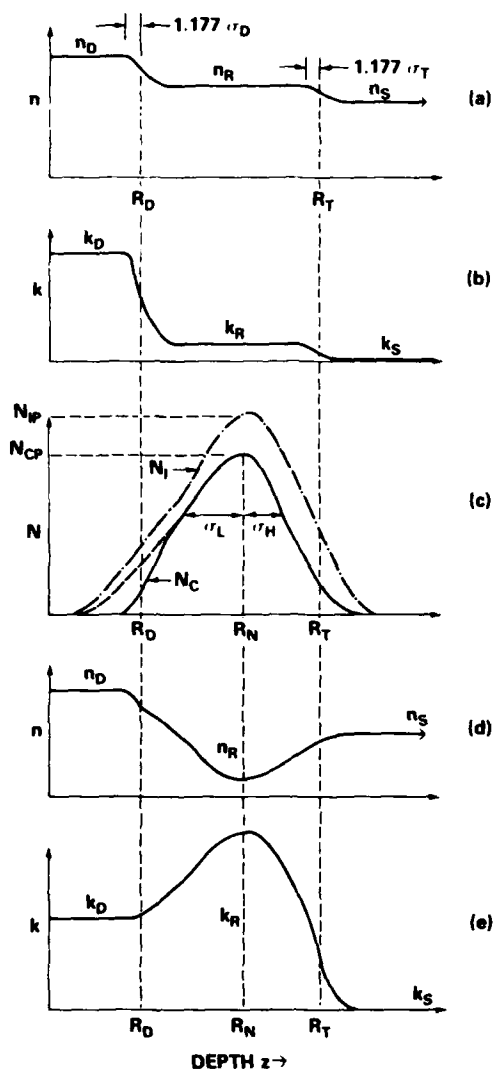


FIG. 1. A schematic representation of the model used to calculate infrared reflection spectra. (a) and (b) show the depth profiles for the high frequency refractive index and extinction coefficient in the damaged surface layer (n_D, k_D), the recrystallized region (n_R, k_R), and the crystalline substrate ($n_S, k_S = 0$). (c) illustrates the impurity distribution (dash-dot) and carrier distribution (solid line) in the recrystallized region represented by a truncated skewed Gaussian. (d) and (e) illustrate the depth profiles of the refractive index and extinction coefficient due to the free carrier plasma in the recrystallized region for a frequency near the plasma frequency.

have been approximated by half-Gaussians. The dash-dot curve of Fig. 1(c) illustrates the implanted impurity distribution while the carrier density is given as the solid line which is a truncated, skewed Gaussian. Experiments show that the carrier density in the amorphous region is very small,¹⁰ which is the reason for the difference between the solid and dashed curves, the latter being the carrier density expected when the recrystallization extends to the sample surface. When the frequency of measurement decreases to values which are comparable to the free carrier plasma frequency for the region of highest carrier density, then one has depth

profiles for the refractive index and extinction coefficient of the type illustrated by Figs. 1(d) and 1(e). These curves differ from those of Figs. 1(a) and 1(b) primarily through the frequency-dependent contribution of the free carriers to the complex dielectric constant.

The reflection expected from a sample approximated by the model of Fig. 1 is obtained from computer calculation by using the thin-film equations of Heavens.¹⁶ A computer code calculates the reflection for an arbitrary number of layers of specified refractive index, extinction coefficient, and thickness. At each frequency, these quantities are calculated from Sellmeier equations for the various refractive indices, and where appropriate, the plasma contribution to the dielectric constant is also included. For the frequency range covered, the measured extinction coefficient in the amorphous layer is found to have a negligible effect and is usually taken to be zero. In regions where the refractive index is changing rapidly with depth, e.g., the transition layers or where the carrier density is changing, the region is divided into a number of layers, each of uniform properties. The layer thickness is typically $\sigma/10$, where σ is the standard deviation of the approximating Gaussian. The details of the procedure including the sensitivities of both the magnitude and spectral character of the calculated reflection to variations of each of the model parameters have been discussed previously.¹⁵

III. EXPERIMENTAL

Samples of chemically polished, undoped, (111) and (100) oriented, single crystal Si were ion implanted using procedures described previously.⁸ The (111) samples were implanted with P^+ ions having energies of 200, 300, 1600, or 2700 keV or with 300 keV ions of Si^+ . The fluences ranged from 1 to 10×10^{16} ions/cm². Some (111) samples were maintained at 200 K during implantation and subsequently allowed to warm to room temperature while others were simply clipped in contact with a room temperature cooling fixture. The implantation parameters for each (111) sample are given in Table I. The sample designation is by implanted ion, incident ion energy in MeV, fluence in units of 10^{16} ions/cm², and A, B, etc., if there is more than one such sample. Thus, P-2.7-1.7-A is a P ion-implanted Si sample, where the P ion energy is 2.7 MeV, the fluence is 1.7×10^{16} /cm², and "A" indicates that there is more than one such implanted sample and that this sample is the first one labeled. The (100) samples were all implanted with a fluence of 0.5×10^{16} /cm² of 380 keV ions of Si^{++} , and these samples were all kept at 200 K during implantation. The implantation parameters for all (100) samples are given in Table II. All of the samples were implanted at an angle of 8° to minimize channeling, and the entire implanted depth from the front surface to somewhat beyond the ion range was amorphous.

Most of the post-implantation anneals were done at 500 °C, the exceptions being one sample at 550 °C and a few at 600 °C. The anneals were almost all isothermal, and the anneal times t_a and temperatures T_a are given in Tables I and II, where the t_a values refer to the total time of anneal at the specified T_a . The term "nonannealed" refers to a sample which has not been raised above room temperature. In most

TABLE I. (111) oriented samples.

Sample ^a	Anneal temp/time [T_A (C)/ t_A (h)]	R_T (μm)	σ_T (μm)	R_D (μm)	R_N (μm)	σ_L/σ_H ($\mu\text{m}/\mu\text{m}$)	f_D	f_R	N_D (10^{18} cm^{-2})	F_T	χ^2 (10^{-1})
P-2.7-1.7-A ^b	none	2.52	0.041	2.52 (2.58) ^d/...	1.00	0.008
	500/10	2.42	2.17	.../0.13	0.97	1.00	80	1.00	0.021
	500/20	2.39 (2.5) ^d	2.18	.../0.13	0.96	1.00	154	1.00	0.014
	500/30	2.59	...	2.32	2.26	.../0.11	0.97	1.02	115	1.07	0.019
	500/50	2.56	...	2.04 (2.0) ^d	2.23	0.39/0.11	0.95	1.02	124	0.67	0.15
	500/70	2.51	...	1.80 (1.6) ^d	2.20	0.33/0.14	0.97	1.04	116	0.77	0.099
	500/100	2.48	...	1.60	2.35	0.38/0.11	0.95	1.05	131	1.00	0.16
	500/150	2.54	...	1.37	2.24	0.36/0.17	0.95	1.04	105	0.82	0.16
	500/250	2.49	...	0	2.16	0.30/0.16	...	1.02	86	0.87	0.070
	500/750	2.52	...	0	2.22	0.36/0.14	...	1.02	68	0.78	0.020
P-2.7-1.7-B ^b	none	2.54	0.035	2.54/...	1.00	0.017
	600/10	2.48	...	0	2.28	0.33/0.12	...	1.01	98	0.56 ^c	0.10
P-2.7-10.0 ^b	none	2.61	0.032	2.61/...	1.00	0.023
	500/30	2.59	...	2.43	2.33	.../0.08	0.96	1.01	692	0.17 ^c	0.22
P-1.6-1.6 ^b	none	no measurements				
	600/10	1.90	...	0	1.65	0.40/0.10	...	0.99	62	0.64 ^c	0.026
Si-0.30-1.0	none	0.569	0.040	0.569/...	1.00	0.010
	500/5	0.569	...	0.526/...	0.97	1.03	0.009
	500/30	0.569	...	0.518/...	0.96	1.01	0.009
P-0.30-1.0-A	none	0.507	0.037	0.507/...	1.00	0.007
	500/30 ^c	0.507	...	0.456/...	0.97	1.00	0.008
	600/5	0.507	...	0	0.39	0.14/0.09	...	1.00	62	1.75	0.016
P-0.30-1.0-B	none	0.506	0.035	0.506/...	1.00	0.006
	500/10 ^c	0.506	...	0.464/...	0.97	1.01	0.010
	500/20 ^c	0.506	...	0.468/...	0.96	1.01	0.025
	500/30 ^c	0.506	...	0.472	0.39	.../0.04	0.97	1.01	1035	0.46 ^c	0.024
	500/50 ^c	0.506	...	0.456/...	0.97	1.01	0.007
	500/50 ^c	0.506	...	0.438/...	0.96	1.01	0.013
	500/50 ^c	0.506	...	0.439	0.39	.../0.04	0.95	1.02	835	0.82 ^c	0.076
Si-0.30-3.0-A	none	0.611	0.041	0.611/...	1.00	0.008
	500/5	0.611	...	0.568/...	0.97	1.03	0.008
	500/10	0.611	...	0.562/...	0.97	1.03	0.010
	500/15	0.611	...	0.562/...	0.97	1.03	0.014
	500/20	0.611	...	0.562/...	0.96	1.02	0.017
	500/30	0.611	...	0.552/...	0.96	1.02	0.016
	500/50	0.611	...	0.527/...	0.95	1.00	0.010
	500/70	0.611	...	0.497/...	0.93	1.00	0.024
Si-0.30-3.0-B	none	0.624	0.030	0.624/...	1.00	0.006
	500/16	0.624	...	0.565/...	0.97	1.03	0.010
P-0.20-1.0	none	0.408	...	0.408/...	1.00	0.014
	600/5	0	0.25	0.11/0.08	...	1.00	84	0.92 ^c	0.016

^a Sample designation is as follows: Implanted ion-ion energy (MeV)-fluence in units of 10^{16} cm^{-2} -A,B, etc., if more than one such sample.

^b Implantation temperature of 200 K, others done at room temperature.

^c Fit to data points for $\nu > 3000 \text{ cm}^{-1}$.

^d Optical microscope measurements.

^e Value for $\gamma = \text{constant}$ in units of 10^{14} sec^{-1} .

cases the anneals were done with the sample sealed in a cleaned, evacuated quartz ampoule. In one case, Si-0.38-0.5-D of Table II, the anneals were carried out in a vacuum chamber where the pressure was 10^{-6} – 10^{-7} Torr.

The room temperature, near normal incidence, infrared reflection of the implanted surface was measured for all samples at all anneal stages specified in Tables I and II. The frequency range of measurement was generally

$7600 > \nu > 250 \text{ cm}^{-1}$, although in some cases, the measurements were extended to 9000 cm^{-1} . The reflection measurements were made with the back surface coarsely ground to prevent multiple reflections. In this case, the simplifying assumption that the substrate is infinitely thick can be made in the calculations. The energy reflected from the sample was compared to that reflected either by a good quality front surface Al mirror¹⁹ or a chemically polished, high purity,

TABLE II. (100) oriented samples.

Sample ^a	Anneal temp/time [T_a (C)/ t_a (h)]	R_T (μm)	σ_T (μm)	R_D (μm)	σ_D (μm)	f_D	f_R	χ^2
Si-0.38-0.5-A	none	0.707	0.040	0.707	0.040	1.00	...	0.007
	500/2	0.577	...	0.96	1.00	0.006
	500/4	0.516	...	0.96	1.00	0.003
	500/8	0.404	...	0.96	1.00	0.007
	500/12	0.343	...	0.96	1.00	0.004
	500/16	0.091	...	0.93	1.00	0.0005
	500/20	0.105	...	0.91	1.00	0.0007
Si-0.38-0.5-B	none	0.701	0.044	0.701	0.044	1.00	...	0.004
	550/0.17	0.605	0.046	0.98	1.00	0.010
	550/0.33	0.565	0.034	0.97	1.00	0.010
	550/0.50	0.528	0.014	0.96	1.00	0.002
	550/0.83	0.421	0.027	0.96	1.00	0.004
	550/1.08	0.367	0.010	0.96	1.00	0.002
	550/1.33	0.324	0.024	0.96	1.00	0.003
	550/1.83	0.220	0.033	0.96	1.00	0.010
	550/2.08	0.176	0.039	0.96	1.00	0.010
	550/2.33	0.123	0.014	0.96	1.00	0.0006
	550/2.58	0.078	...	0.94	1.00	0.001
	550/2.83	0.019	...	0.90	1.00	0.002
	550/3.08	0	1.00	...
Si-0.38-0.5-C	none	0.753	0.038	0.753	0.038	0.99	...	0.008
	500/2	0.610	0.024	0.96	1.00	0.020
	500/4	0.541	...	0.95	1.00	0.020
	500/8	0.423	0.025	0.96	1.00	0.008
	500/12	0.359	...	0.96	1.00	0.010
	500/16	0.092	0.026	0.93	1.00	0.0002
Si-0.38-0.5-D	none	0.716	0.048	0.716	0.048	1.01
	500/1	0.650	0.033	0.97	1.00	...
	500/2	0.626	0.032	0.96	1.00	...
	500/3	0.597	0.026	0.96	1.00	...
	500/4	0.576	0.023	0.96	1.00	...
	500/5	0.552	0.027	0.97	1.00	...
	500/6	0.537	0.016	0.96	1.00	...
	500/8	0.496	0.024	0.95	1.00	...
	500/10	0.461	0.028	0.96	1.00	...
	500/12	0.426	0.032	0.96	1.00	...
	500/15	0.367	0.034	0.96	1.00	...
	500/18	0.294	...	0.95	1.00	...
	500/19	0.268	0.025	0.94	1.00	...
	500/20	0.230	0.060	0.94	1.00	...
	500/21	0.204	0.074	0.93	1.00	...
	500/23	0.215	0.088	0.90	1.00	...
	500/24	0.201	0.111	0.92	1.00	...
	500/28	0.229	0.109	0.90	1.00	...
Si-0.38-0.5-E	none	0.723	0.045	0.723	0.045	1.00	...	0.002
	500/20	0.269	0.036	0.97	1.00	0.0005
	500/40	0.195	0.090	0.89	1.00	0.004

^a Sample designation: Same as in Table I.

nonimplanted Si sample.

For sample P-2.7-1.7-A of Table I, the thickness of the amorphous layer was also measured²⁰ by making use of the fact that amorphous Si (α -Si) and crystalline Si (c -Si) have different visual appearances. A region near one edge of the implanted surface was beveled at an approximate angle of 20 mrad by using a chemical polish to expose the amorphous-crystalline (α - c) interface. A microscope was used to determine the width of the milky appearing amorphous layer and the bevel angle was measured interferometrically.

The phosphorus impurity depth distribution for sample P-2.7-1.7-B was measured by means of the $^{31}\text{P}(p,\alpha)^{28}\text{Si}$ resonant nuclear reaction at a proton energy of 1.514 MeV. The

reaction product α particles were counted in a position-sensitive solid-state detector placed in the focal plane of a magnetic spectrometer, which was at a 135° angle with respect to the proton beam. Details of this impurity profiling technique can be found elsewhere.²¹

IV. EXPERIMENTAL RESULTS AND DISCUSSION

Reflection data for some of the implanted samples being studied here have already appeared in prior papers.^{9,10,15,16} Several examples of these measurements are given in Fig. 2, primarily for illustrative purposes. Tables I and II summarize the parameter values obtained from com-

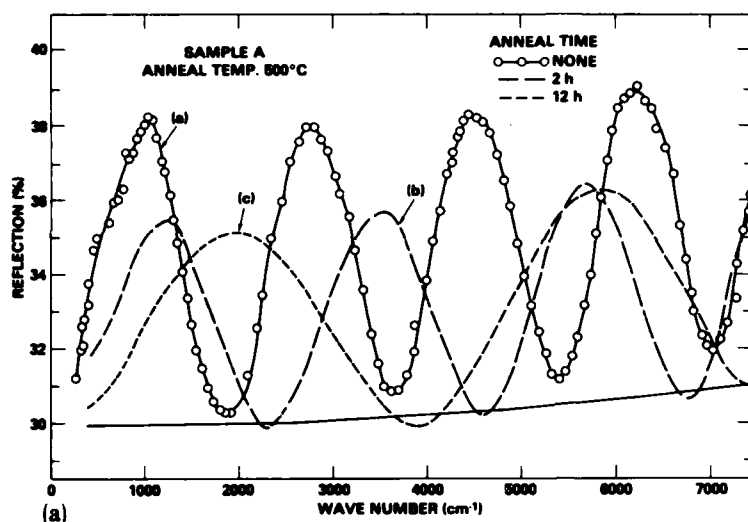


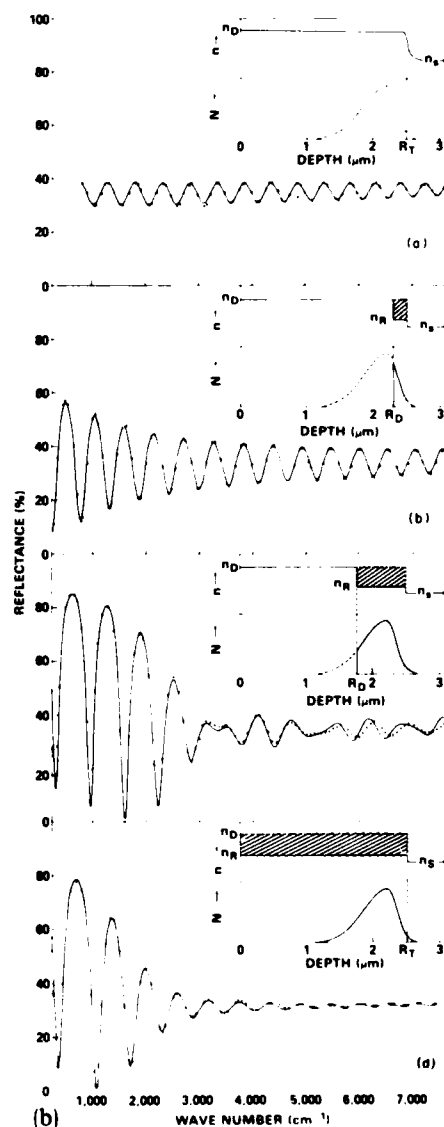
FIG. 2. (a) Measured infrared reflection spectra of Si implanted with 380 keV Si to a fluence of 5×10^{15} ions/cm² (sample Si-0.38-0.5-A of Table II). Data points are shown for the as-implanted case and smooth lines have been drawn through the data points for the annealed cases. They are very close to the best-fit calculations with the parameters given in the table. The solid curve at the base of the others is the reflectivity of crystalline Si given by $(n_s - 1/n_s + 1)^2$. (b) Measured infrared reflection spectra of Si implanted with 2.7 MeV P⁺ ions to a fluence of 1.7×10^{16} ions/cm² (sample P-2.7-1.7-A of Table I). Data and best fit calculated curves are shown for the as-implanted case (a), and three different anneal stages: (b) 500 °C/30 h, (c) 500 °C/70 h, and (d) 500 °C/750 h. The inserts are schematics indicating the depth dependence for the high frequency refractive index n and the carrier density N_c . The shaded areas in the n curves are those regions which changed by recrystallization and those similar areas in N_c indicate the region where carriers are observed. The dashed portion of the N_c curve is the carrier density that will be present after recrystallization.

puter fits to reflection data such as those given in Fig. 2(b). The parameters f_D , f_R , and F_T will be defined in the discussion which follows. Computer fits to the data¹⁵ yield reduced χ^2 values, which are typically 10^{-5} to 10^{-6} , indicating that the average value of $|R_{\text{calc}} - R_{\text{meas}}|$ is about 0.1–0.3%. This is less than the experimental accuracy of measurement, $\pm 0.5\%$ reflection. In the tables, a dash given in place of a parameter value either indicates that the parameter does not enter into the calculation or that the calculation is insensitive to the parameter value.

The results of the model analyses given in Tables I and II have a number of interesting features which are discussed in the following sections.

A. Depth of the amorphous layer

The depth of the amorphous layer in a nonannealed sample is called R_T and the depth after annealing is R_D —see Fig. 1(a). The high energy P⁺ ion-implanted (111) sample P-2.7-1.7-A of Table I was one of those studied in the greatest detail. In the analysis, the refractive index of the recrystallized region n_R is generally close to the substrate index



and is represented by $n_R = f_R n_S$, where n_S is the index for nonimplanted *c*-Si.¹⁵ Since for the most anneal stages, the best fit for this sample required $f_R > 1.00$, the calculation is sensitive to R_T which was kept as an adjustable parameter. The average of the 8 values given in Table I for R_T is $2.53 \mu\text{m}$ with a deviation of $0.03 \mu\text{m}$. The values for samples P-2.7-1.7-B and P-2.7-10.0, where $f_R > 1.00$, show a similar reproducibility for R_T . Therefore, in the remaining calculations of Table I, where $f_R \neq 1.00$, the R_T was frozen at the value obtained from the fit to the as-implanted data. The $f_R \neq 1.00$ cases are all $\langle 111 \rangle$ oriented samples and in all cases save one, $f_R > 1.00$ indicating that the refractive index of the recrystallized silicon has not fully returned to that for the pre-implanted, single-crystal material. It has been established²²⁻²⁴ that initially $\langle 111 \rangle$ material, when heavily implanted and epitaxially recrystallized in the temperature range used here, contains a large residual damage concentration which is not present in $\langle 100 \rangle$ annealed samples. It is this damaged region which has $f_R > 1.00$. However, it has also been found that there is some residual damage in the $\langle 100 \rangle$ material as well. Recent studies using electron stereomicroscopy²⁵ show that when $\langle 100 \rangle$ Si is implanted with Si^+ ions (200 keV and 1×10^{16} ions/cm²) and then annealed at 600 or 800 °C, the recrystallized layer still has a 500–600 Å residual damage layer located near the original *a-c* interface position. This layer has a high density of small defect clusters in the 600 °C annealed samples. From Table II it is apparent that the change in refractive index for such a layer is not sufficient to be detected in the reflection interference spectrum. Trial calculations indicate that a Δn of about 0.05 in a 500–600 Å layer at or near R_T should be detected.

It is noted that increasing the fluence while holding all other implantation parameters constant causes R_T to increase slightly as expected, [e.g., in Table I, compare P-2.7-1.7-A (or B) with P-2.7-10.0 and Si-0.30-1.0 with Si-0.30-3.0-A (or B)]. Increasing the fluence moves the *a-c* interface further out on the implanted impurity distribution curve, and the optical measurements are sensitive to this change.

The depth of the *a-c* interface for sample P-2.7-1.7-A was measured visually for several anneal stages and the results given in Table I are in reasonable agreement with the value of R_D from the infrared measurements. Regrowth rates deduced from Tables I and II are compared to previous studies in Sec. IV D.

B. The transition regions

The presence of a transition region between the *a*-Si and *c*-Si regions in as-implanted samples is indicated by a decrease in the amplitude of the high frequency interference fringes.^{9,15} The width σ_T of the transition region was found to be about $0.03\text{--}0.05 \mu\text{m}$.⁹ When the samples are annealed, the width of the transition region σ_D becomes less than the minimum detectable width of about $0.02 \mu\text{m}$, even for the shortest anneal times. Therefore, σ_D was set equal to zero for the analyses of annealed samples presented in Table I. In a similar manner, it was found that σ_T values for annealed samples were unnecessary. The σ_D values listed for the annealed $\langle 100 \rangle$ samples in Table II are believed to be an artifact of the particular fitting procedure used and their significance is discussed in the next section.

The values of the transition widths, $\sigma_T \sim 0.03\text{--}0.05 \mu\text{m}$, for the nonannealed samples could be considered surprising since transmission electron microscopy (TEM) measurements have shown *a-c* interfaces which are much sharper.^{25,26} The TEM values appear to be well below our minimum detectable value of σ_T (about $0.02 \mu\text{m}$). There are several possible contributions to the σ_T observed here. While TEM measurements indicate a sharp transition, for high fluence implantation cases they also show that a crystalline but heavily damaged region extends beyond the *a-c* interface.²⁵ In another TEM study of a nonannealed sample, a width of about $0.025 \mu\text{m}$ was reported.²⁶ These TEM observations are in substantial agreement with the results of a recent study of the thermal redistribution of oxygen during solid-phase regrowth of As-implanted Si.²⁷ TEM examination of unannealed, $\langle 111 \rangle$ implanted samples in this latter study also showed a narrow region of small clustered defects in the *a-c* transition region and these defects were largely annihilated by annealing at 400 °C for 1–4 h. In the present study, it is observed that the nonannealed $\langle 111 \rangle$ samples have the σ_T values mentioned above and also that σ_T and σ_D both become less than our minimum detectable value of about $0.02 \mu\text{m}$ after the shortest anneal time used at 500 °C. Thus, the source of the transition width σ_T could be a heavily damaged but crystalline region.

It is also possible that the transition layer could actually be a region of mixed *c*- and *a*-Si and thus have an average index varying between n_D and n_S . A similar suggestion was used²⁸ in an earlier study of solid-phase epitaxial recrystallization of amorphous films which were deposited on atomically clean and well-ordered Si surfaces. This approach was also employed in an ellipsometry measurement of the damage profile of P^+ -implanted material where a transition layer was taken into account.²⁹

A third possibility for the σ_T values observed here is that the interface is not planar and that σ_T reflects the variation in depth over the area measured by the infrared beam (about 10^{-1}cm^2). While this latter effect might make some contribution, it is unlikely to be a dominant factor because both σ_T and σ_D become less than the minimum detectable value after the shortest annealing time employed. To avoid such nonuniformities, the ion beam is raster-scanned over the surface during the implantation.

C. Refractive index of amorphous material

Refractive index results for these samples have already been discussed in a prior letter.¹⁶ In that work, it was observed that the refractive index of the as-implanted amorphous layer, called n_D , decreased with annealing to a new value, n'_D . Although the dispersions of n_D and n'_D are slightly different,¹⁶ it was found that quite reasonable fits could be obtained by using the simplifying assumption $n'_D(\nu) = f_D n_D(\nu)$, where f_D is a frequency independent fitting parameter. It is seen from Tables I and II that prior to annealing, $f_D = 1.00 \pm 0.01$ for all samples indicating a high degree of reproducibility in the measurement of n_D . After annealing for a short time at either 500 or 550 °C, all cases require $f_D = 0.96$ in order to give a good fit to the measured reflection. It was suggested that $f_D = 0.96$ corresponds to an

"anneal-stabilized" state, and it was shown that $n'_D(\nu)$ is in good agreement with values obtained in a recent study³⁰ of CVD films of Si deposited on fused silica substrates held between 550 and 650 °C.

In a few cases the value of f_D for the annealed α -Si drops below 0.96. With one exception, these cases are the $\langle 100 \rangle$ samples, where the annealing time has been sufficiently long such that $R_D \leq 0.2 \mu\text{m}$. None of the $\langle 111 \rangle$ samples was measured in this state. Values of f_D as low as 0.93 and 0.90 are given in Table II. One may note from previous work^{15,16} that if we set $n_S = f_D n_D(\nu)$, then $f_D \approx 0.89$. The 0.93 and 0.90 values indicate that the index has annealed most of the way back to the pre-implantation crystalline value. It is also noted in Table II that these lower f_D values are associated with anneals where R_D is changing very slowly with increased anneal time t_A and usually σ_D becomes large. In such cases the small value for R_D as well as the f_D values close to 0.89 mean that the reflection curves have very little structure and are close in magnitude to the crystalline, nonimplanted curve. Hence, the fitting procedure is subject to greater relative inaccuracies for the parameters in these cases. Nevertheless, these results indicate that the region close to the surface is not annealing by a continuation of the uniform epitaxial process, but that the α - c interface becomes quite nonuniform with possible polycrystalline nucleation and grain growth. The large σ_D and the $f_D \rightarrow 0.89$ are both consistent with the interpretation that the surface region has become a mixture of c -Si and α -Si.

In Table II it is seen that most of the samples have σ_D of about 0.02–0.04 μm in the different anneal stages before the large σ_D values described above are obtained. As mentioned earlier, these σ_D values for annealed samples are largely an artifact and are present because the fitting procedure is using $n'_D = f_D n_D$ rather than calculating n'_D from the Sellmeier equation with best fit values for the parameters. Since n'_D has less dispersion than n_D , the program compensates by increasing σ_D . The fits of the annealed $\langle 111 \rangle$ samples of Table

I are less sensitive to this effect because of the stronger interference effects due to the plasma in the P-implanted samples and reflections from the recrystallized-crystalline interface since $f_R > 1.00$.

D. Regrowth rates

As expected from previous studies the regrowth behavior of the amorphous layers on the $\langle 111 \rangle$ and $\langle 100 \rangle$ oriented samples are substantially different,^{22–24,31,32} and therefore they will be discussed separately.

1. $\langle 100 \rangle$ regrowth

If one neglects any change in Si density upon recrystallization, then $R_T - R_D$ is the thickness of the regrown layer. In Figs. 3 and 4, $R_T - R_D$ versus annealing time t_A have been plotted from the results given in Table II. All of the 500 °C annealed samples show an initial period of 1–2 h of rapid regrowth. This is the same period when the α - c interface width is greatly reduced and f_D changes from 1.00 to near 0.96. Sample Si-0.38-0.5-B, which was annealed at 550 °C, shows a similar behavior except that the time periods are shorter. For all of the samples, there are extended periods in which the regrowth rates are approximately constant. This is illustrated in Fig. 5 by the plot of the average regrowth rate during each anneal interval as a function of the regrowth layer thickness for sample Si-0.38-0.5-D (open circles in Fig. 3). For those samples annealed at 500 °C, the average rates in the approximately uniform rate periods are 2.2, 2.3, and $2.0 \times 10^{-2} \mu\text{m/h}$ for samples Si-0.38-0.5-A, C, and D, respectively. The average of these values is about $2.2 \times 10^{-2} \mu\text{m/h}$ or 3.7 Å/min. This is about a factor of 2½ below the rate determined by Csepregi *et al.* from ion channeling measurements for 500 °C anneals of Si-implanted, $\langle 100 \rangle$ oriented samples.^{22,23,32} This same difference is observed for 550 °C annealing where the present rate is $2.0 \times 10^{-1} \mu\text{m/h}$ (34 Å/min) compared to the Csepregi *et al.*

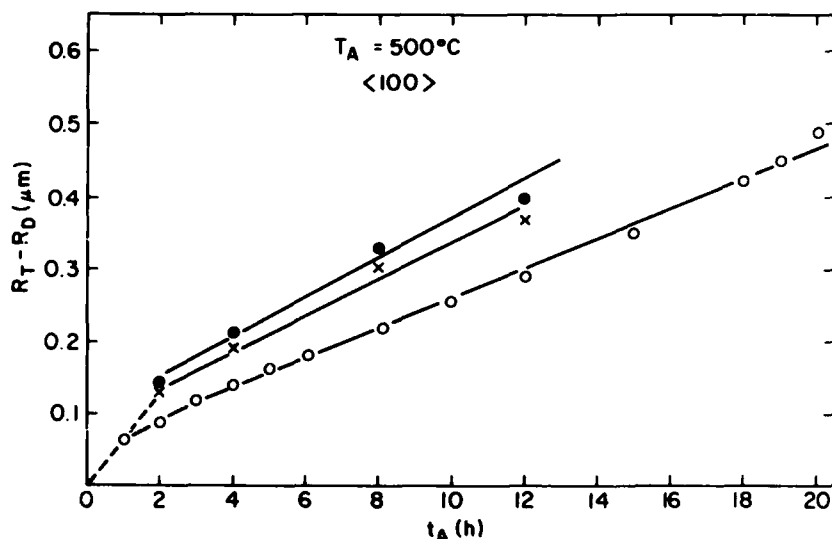


FIG. 3. Width of the regrown layer, $R_T - R_D$, as a function of anneal time t_A for three $\langle 100 \rangle$ Si-implanted samples annealed at 500 °C. (x) is sample Si-0.38-0.5-A, (●) is Si-0.38-0.5-C, and (○) is Si-0.38-0.5-D.

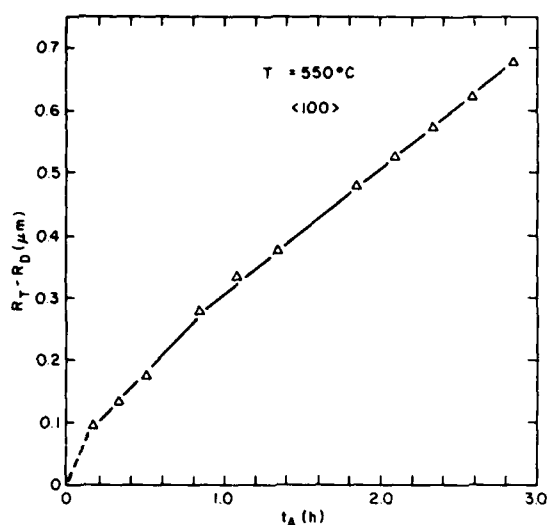


FIG. 4. Width of the regrown layer, $R_T - R_D$, as a function of anneal time t_A for the $\langle 100 \rangle$ sample Si-0.38-0.5-B annealed at 550 °C.

value of about 85 Å/min. In the study of Blood *et al.*,²⁴ which also used channeling measurements, the $\langle 100 \rangle$ regrowth rate was not measured; however, it was stated that complete regrowth was observed in times predicted by the Csepregi *et al.* rate. It is of interest to note, however, that a recent determination³³ of the regrowth rate for $\langle 100 \rangle$ material by measuring the reflection versus t_A at a single frequency in the visible gives about 30 Å/min at 550 °C, which is in good agreement with the present value and also lower than the previous measurements.

Although there are several mechanisms which could produce changes in the measured regrowth rates, the present

authors are unable to present convincing arguments that any of them are responsible for the differences between the present rates and those given previously. The present measurements are optical ones while the earlier results were from ion channeling. However, where the optical and ion channeling measurements of R_D have been compared directly,⁹ they are in good agreement. The regrowth rate is a function of substrate orientation with the $\langle 100 \rangle$ value being the largest. From previous measurements,³² a decrease of a factor of 2 $\frac{1}{2}$ in rate would require the present samples to be more than 20° off the proper orientation. Laue diffraction patterns show our samples to be within 2° of the $\langle 100 \rangle$ orientation. It is also known³⁴ that certain impurities such as O, C, and N, if present in sufficiently large concentration, can substantially reduce the regrowth rate. However, secondary ion mass spectroscopy (SIMS) measurements³⁵ of some of the present implanted samples indicated that the concentrations for these impurities are approximately an order of magnitude or more below those required to produce the lower regrowth rates.

2. $\langle 111 \rangle$ regrowth

Previous studies have demonstrated that the $\langle 111 \rangle$ regrowth process is more complicated than that for the $\langle 100 \rangle$ case. In their study of Si⁺ implanted Si, Csepregi *et al.*^{22,23} found two different annealing behaviors in the regrowth of $\langle 111 \rangle$ Si at an anneal temperature, $T_A = 550$ °C. For a short anneal time the regrowth is relatively slow, the rate ≈ 2.9 Å/min, and the a - c interface remains uniform. For $t_A > 4$ h, the rate increases to ≈ 10 Å/min and the interface becomes very nonuniform. In the later work of Blood *et al.*,²⁴ the $\langle 111 \rangle$ regrowth rates at 550 °C after In⁺ and Sb⁺ implants were measured and were 3.0 and 3.8 Å/min, respectively. In these cases there was no change in rate for $t_A < 9$ h. The anneal for the $\langle 111 \rangle$ cases was viewed as an epitaxial process producing a crystalline layer containing twins and defect clusters. If the

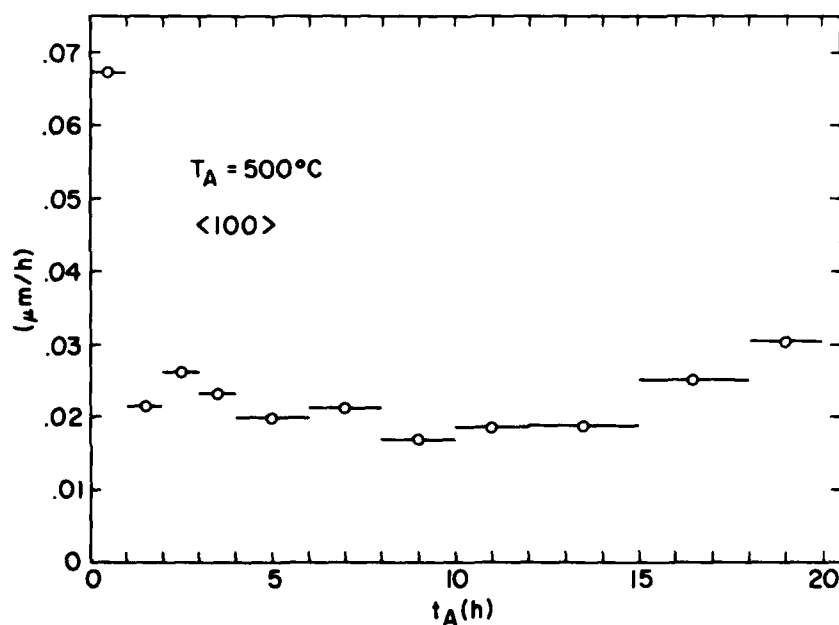


FIG. 5. Average regrowth rate for $\langle 100 \rangle$ sample Si-0.38-0.5-D of Table II for most of the anneal intervals given in the table.

annealing is done at a substantially higher temperature, such as $T_A = 900^\circ\text{C}$, then the epitaxial regrowth process is no longer dominant and the layer recrystallizes primarily by nucleation and growth of polycrystalline grains. However, if the 900°C anneal is preceded by a short 550°C anneal, then a much improved quality of single-crystal regrowth is observed.²³

The most complete data in Table I for a $\langle 111 \rangle$ sample implanted with Si^+ are for Si-0.30-3.0-A, and these data are shown in Fig. 6(a). There is an initial short period of relatively rapid regrowth followed by a period of very slow regrowth and finally a more extended period of intermediate rate. Omitting the first two regions, the data indicate an average rate of about $0.23 \text{ \AA}/\text{min}$ for $T_A = 500^\circ\text{C}$. This value is in reasonable agreement with the 500°C value of $0.3 \text{ \AA}/\text{min}$ calculated from the data of Csepregi *et al.*³¹ by using their activation energy of 2.3 eV and their regrowth rate of $3 \text{ \AA}/\text{min}$ measured at 550°C . However, the behavior of the implanted samples observed here for $t_A < 20 \text{ h}$ is different than that of Blood *et al.*²⁴ and Csepregi *et al.*^{22,23}

The most complete regrowth data in Table I for a P^+ -implanted $\langle 111 \rangle$ sample are for P-2.7-1.7-A, and these data are plotted in Fig. 6(b). Because of the large incident ion energy, R_T is large and R_D can be followed over a large range of values. Again, it appears that one cannot fit the data by one regrowth rate for all t_A . Three regions are required. In this case the intermediate region is the one of largest regrowth rate. When R_D is in the range $R_N + \sigma_H > R_D > R_N - \sigma_L$, where R_N is the depth of maximum carrier concentration and σ_L and σ_H are the standard deviations on either side of the peak as shown in Fig. 1, then the regrowth is taking place in the region of high P concentration. This rate is $2.1 \text{ \AA}/\text{min}$ or about 9 times that for the Si^+ -implanted sample Si-0.30-3.0-A. The rates for the deepest implanted region, $R_T > R_D > R_N + \sigma_H$, and the shallow region, $R_D < R_N - \sigma_L$, appear similar and are about $0.9 \text{ \AA}/\text{min}$. The measurements for the shallow region are too limited in range and too few in number to conclude that this rate characterizes the entire $R_D < R_N - \sigma_L$ region. The enhancement of the regrowth rate in regions of high P concentration has been reported by Mayer and co-workers as part of a more extensive investigation of the dependence of regrowth rates on impurity type and concentration.^{31,34} They noted that a concentration of P ions of about $2 \times 10^{20} \text{ cm}^{-3}$ produced by implantation in a $\langle 111 \rangle$ sample increased the 550°C regrowth rate by a factor of 5–6 with respect to that observed for a Si ion implant, an increase similar to that observed here for a similar P concentration.

It is of interest to note that the P impurity enhancement effect will be reversed for very high impurity concentrations. Sample P-2.7-1.7-A discussed above was implanted with a fluence of $1.7 \times 10^{16} \text{ P}^+/\text{cm}^2$ and the regrowth was completed by 250 h at 500°C (see Table I). Sample P-2.7-10.0 was implanted under the same conditions but with a fluence of $10 \times 10^{16} \text{ P}^+/\text{cm}^2$. By $t_A = 30 \text{ h}$, the R_D was 2.43 \AA compared to $R_T = 2.59 \text{ \AA}$, but the regrowth rate was reduced to essentially zero. Subsequent anneals at 500°C to $t_A = 750 \text{ h}$ (not listed in Table I) showed almost no change in the reflection spectrum and, hence no change in any of the pa-

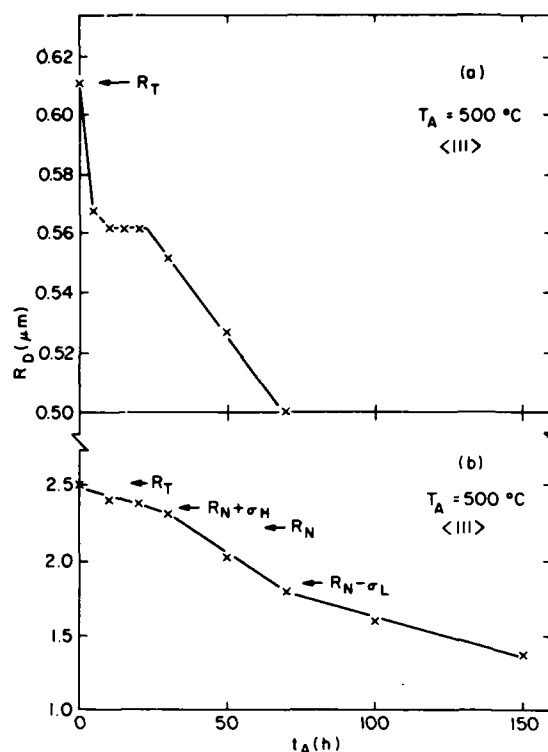


FIG. 6. Depth of the a-c interface as a function of anneal time. (a) is for $\langle 111 \rangle$ sample Si-0.30-3.0-A, (b) is for $\langle 111 \rangle$ sample P-2.7-1.7-A, both of Table I. The anneal temperature is 500°C for both samples.

rameters including R_D . This reduction of the regrowth rate by a high concentration of implanted ions was noted previously for Sb implantations³⁶ and for Pb and As implantations³⁷ in $\langle 100 \rangle$ oriented Si.

E. Carrier density profile

If diffusion effects are negligible and if the carrier activation efficiency is independent of depth, then the peak position of the carrier density curve R_N will be the same as the peak position of the implanted impurity distribution. Using the same assumptions the two standard deviations, σ_L and σ_H , will represent the widths of both the carrier density and the impurity distribution. The use of two half-Gaussians to approximate a distribution which deviates from a Gaussian shape, as in Fig. 1(c), has been investigated by Gibbons and Mylroie.³⁸ If σ_L and σ_H were equal then R_N would be the same as the first moment of the implanted distribution which is generally called R_p , the projected range. Since $\sigma_L \neq \sigma_H$ for the P implants of Table I, the R_N values are not expected to equal R_p but must be modified according to the expression³⁸ $R_p = R_N - 0.8(\sigma_L - \sigma_H)$. In Fig. 7, the R_p values calculated from this expression and the fitting parameters of Table I are compared with a plot of the theoretically calculated projected range as a function of ion energy for P-implanted Si as given by Smith.³⁹ Other tabulated calculations of the projected range³⁸ are close to those of Smith but are not ex-

tended above 1.00 MeV where some of the present data lie. Note in Fig. 7 that our values of R_p measured by infrared reflection are in very good agreement with measured values reported in the literature^{40,41} and that all measured values lie somewhat below the calculated curve.

In order to check the validity of the optical values for R_p at the highest energy, 2.7 MeV, where other data are not available for comparison, the impurity concentration was also measured by means of the $^{31}\text{P}(p,\alpha)^{28}\text{Si}$ resonant nuclear reaction for two annealing states of the high energy implanted sample P-2.7-1.7-B. The projected range of the P-impurity distribution was measured to be $R_p = 2.1 \pm 0.2 \mu\text{m}$, in excellent agreement with the first moment of the carrier distribution measured by the optical method of $2.01 \pm 0.04 \mu\text{m}$. The P-impurity profile was found to be well represented by a symmetric Gaussian shape with a straggling parameter $\Delta R_p = 0.20 \mu\text{m}$. This is entirely consistent with the asymmetry found in the carrier distribution by the optical method as will now be discussed.

The p,α reaction impurity profile is calculated from the raw data by an iterative method wherein an assumed Gaussian profile is folded with a resolution function which is composed of three contributions—(i) Energy straggling of the protons, (ii) energy width of the proton beam, and (iii) resonance width of the p,α reaction. The parameters of the Gaussian impurity profile are varied until the folded profile is in agreement with the raw data profile. Because the asymmetry measured by the optical method (and calculated by range theories) is approximately equal to or less than the effective depth resolution ($0.3 \mu\text{m}$) of the p,α method, only the first and second moments of the impurity distribution can be measured. This was demonstrated by folding a trial impurity distribution having the same area ($\sigma_L = 0.3 \mu\text{m}$,

$\sigma_H = 0.1 \mu\text{m}$ versus $\sigma_L = \sigma_H = 0.2 \mu\text{m}$) with the resolution function with the result that the generated data points were indistinguishable within the errors of the measurement.

The values of the straggling of the carrier distributions measured here can be compared with the calculations of Gibbons *et al.*³⁸ for P^+ implantations at energies of 0.2 and 0.3 MeV which are $\Delta R_p = 0.078$ and $0.102 \mu\text{m}$, respectively. The corresponding values calculated by Smith³⁹ are 0.101 and $0.132 \mu\text{m}$. These values compare favorably with the mean values, $(\sigma_L + \sigma_H)/2$, measured here which are 0.095 and $0.115 \mu\text{m}$, respectively. Moreover, the 3rd moment ratios, also calculated by Gibbons *et al.*,³⁸ are in reasonable agreement with those calculated from σ_L and σ_H and indicate that $\sigma_L > \sigma_H$, in agreement with our experimental values.

Gibbons⁴² has also developed an expression for the 4th moments in terms of the 3rd moments which have been tabulated.³⁸ Therefore, the implanted impurity distribution can be calculated including the 4th moment and Gibbons⁴³ has done this for 2.7 MeV ions of P^+ in Si by using an extrapolation technique from lower energies. The calculation gives a projected range of $2.67 \mu\text{m}$. This is somewhat larger than the value calculated by Smith of $2.45 \mu\text{m}$ and our experimental values of $2.0\text{--}2.1 \mu\text{m}$. The impurity distribution widths are $\sigma_L = 0.34 \mu\text{m}$ and $\sigma_H = 0.20 \mu\text{m}$ which compare well with the values in Table I. Again the measured asymmetry, $\sigma_L/\sigma_H > 1$, agrees with the calculation.

When R_D is larger than R_N , all but the lowest frequency portion of the reflection interference spectrum is relatively insensitive to the plasma-related parameters. This is illustrated by sample P-0.30-1.0-A of Table I, where equally good fits could be obtained to data for $\nu > 3000 \text{ cm}^{-1}$ by omitting the plasma term completely—see the fitting parameters for anneals superscripted with *c*. In particular, values of N_{cp} [the peak carrier density—see Fig. 1(c)] given in Table I should be regarded with caution when $R_D > R_N$. In the early anneal stages, when $R_T > R_D > R_N$, the fitting procedure has only the tail of the implanted distribution, where the carriers have been activated by the recrystallization, upon which to base the calculations of R_N , σ_H , and N_{cp} . In such cases, small relative changes in R_N or σ_H can introduce large relative changes in N_{cp} . An example of this behavior is the $500^\circ\text{C}/20 \text{ h}$ anneal of sample P-0.30-1.0-B where $N_{cp} = 1.04 \times 10^{21} \text{ cm}^{-3}$ when $R_D = 0.472 \mu\text{m}$ and $R_N = 0.39 \mu\text{m}$. Sample P-0.30-1.0-A, which has the same implantation conditions but was annealed to an $R_D = 0$ condition, had N_{cp} more than an order of magnitude less than the above value.

The doping efficiency is given by the expression

$$\text{Efficiency} = (\pi/2)^{1/2} N_{cp} (\sigma_L + \sigma_H) / \Phi,$$

where Φ is the fluence. With the values of N_{cp} , σ_L , σ_H , and Φ given in Table I for P^+ ion implantation and taking only those cases where the sample has been annealed sufficiently that $R_D < R_N$, one obtains average doping efficiencies for the recrystallized region in the range of 0.17–0.41.

One effect not understood by the authors is the decrease in N_{cp} with increasing t_A seen for sample P-2.7-1.7-A in cases where $R_D < R_N$. There is no corresponding trend for σ_L and

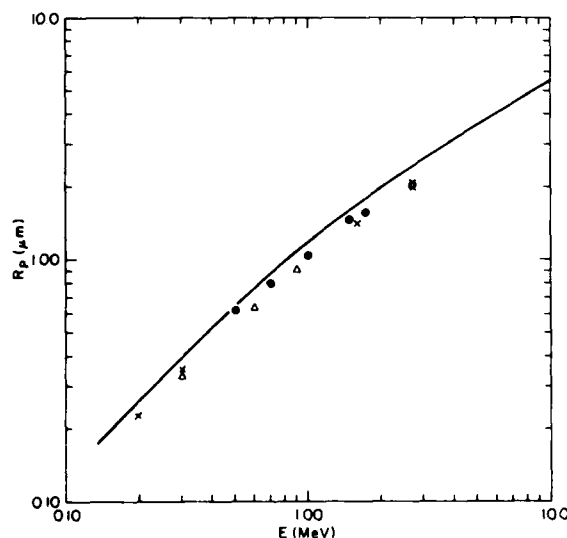


FIG. 7. Curve is the projected range as a function of incident ion energy for P-implanted Si calculated by B. Smith—see Ref. 37. The \times points are the R_p values obtained in the present study by using $R_p = R_N - 0.8(\sigma_L - \sigma_H)$. The Δ points are from Ref. 39 and the \bullet from Ref. 40. The \circ point is from the p,α measurement described in the text.

σ_H to increase so that bulk diffusion does not appear to be the cause. Indeed, for sample P-2.7-1.7-B which was annealed at 600 °C, an even higher temperature, the p, α measurement showed no increase in ΔR_p . Although we are unable to offer evidence to establish a mechanism for this decrease in N_{cp} , one could speculate that P-impurity segregation at defects in the regions of large residual damage concentrations, which we have previously discussed for the $\langle 111 \rangle$ samples, might lower the concentration of electrically-active P doping. It would be interesting to perform the same experiments in $\langle 100 \rangle$ samples where the residual damage concentration is much lower. Phosphorus segregation to regions of high damage in $\langle 111 \rangle$ Si has been observed by means of cross-sectional TEM measurements by Sadana *et al.*⁴⁴ after annealing at 750 °C. However, their samples were implanted at low fluences (3×10^{14} ions/cm²) so that only a thin buried amorphous layer was created—a situation which is known to produce different damage structure than for regrowth of a completely amorphous implanted layer.²⁶ In the present work, the observed decrease in N_{cp} for sample P-2.7-1.7-A causes the conversion efficiency to drop from 0.41 at $t_A = 150$ h to 0.25 after 750 h.

The significance of F_γ has been previously discussed.¹⁵ It is a fitting parameter used in the equation $\gamma = N_c e^2 / m^* \sigma F_\gamma$, where σ is the conductivity for a carrier density N_c taken from electrical studies. It is worth noting that, with few exceptions, the values of F_γ are within a factor of 2 of 1.0 which means that the best fit damping constant F_γ is close to that predicted from dc conductivity and Hall effect measurements of samples having carrier densities equal to our best fit values. The values in the F_γ column of Table I which are superscripted with (e) are not F_γ but values of $\gamma = \text{constant}$, independent of depth, given in units of 10^{14} sec^{-1} . Examples are the values for samples P-2.7-1.7-B and P-0.20-1.0 which are $\gamma = 0.56$ and $0.92 \times 10^{14} \text{ sec}^{-1}$. These are close to about 0.70 and $0.75 \times 10^{14} \text{ sec}^{-1}$, respectively, as given by mobility measurements⁴⁵ for the N_{cp} for each case.

V. SUMMARY

Measured infrared reflection spectra of 15 samples of heavily implanted Si in both nonannealed and annealed states have been fitted by calculations employing a model detailed in a previous work and reviewed here. The calculations yield values for (1) the as-implanted a - c interface depth, (2) the annealed sample's a - c interface depth, (3) the width of the transition regions between the amorphous, recrystallized, and substrate regions, (4) the refractive indices of the amorphous, annealed-amorphous, and recrystallized regions, (5) the peak carrier density and its position, (6) the carrier density standard deviations on either side of the peak density, and (7) the plasma damping constant. In all cases where comparisons can be made, the values obtained here are in reasonable agreement with those deduced from other measurements or from calculations. From these results epitaxial regrowth rates are deduced for both $\langle 100 \rangle$ and $\langle 111 \rangle$ orientations which are compared with values obtained previously, primarily from backscattering studies. Significant differences in $\langle 100 \rangle$ regrowth rates are observed and discussed.

Based on the results of this study and two earlier ones,^{9,15} it appears that the infrared measurements are a useful, nondestructive technique for characterizing samples which have been implanted with fluences sufficiently large to significantly alter the dielectric properties. It is clear that this technique is most useful when used with other methods of analysis, particularly those which give microstructural information.

ACKNOWLEDGMENTS

Three of the authors (CNW, WGS, and JEF) were supported in part by the Joint Services Electronics Program, monitored by the Air Force Office of Scientific Research. The authors wish to thank P. R. Malmberg for high energy phosphorus implantations, C. R. Gossett for the p, α nuclear reaction measurement of the phosphorus impurity profile, and K. L. Dunning for the computer calculation to unfold the nuclear reaction profile data.

- ¹E. C. Baranova, V. M. Gusev, Yu. V. Martynenko, C. V. Starinin, and I. B. Haibullin, *Radiat. Eff.* **18**, 21 (1973).
- ²A. H. Kachare, W. G. Spitzer, F. K. Euler, and A. Kahan, *J. Appl. Phys.* **45**, 2938 (1974).
- ³A. H. Kachare, J. M. Cherlow, T. T. Yang, and W. G. Spitzer, *J. Appl. Phys.* **47**, 161 (1976).
- ⁴E. C. Baranova, V. M. Gusev, Yu. V. Martynenko, and I. B. Haibullin, *Radiat. Eff.* **25**, 157 (1975).
- ⁵A. H. Kachare, W. G. Spitzer, and J. E. Fredrickson, *J. Appl. Phys.* **47**, 4209 (1976).
- ⁶T. E. Seidel, G. A. Pasteur, and J. C. C. Tsai, *Appl. Phys. Lett.* **29**, 648 (1976).
- ⁷A. H. Kachare, W. G. Spitzer, J. E. Fredrickson, and F. K. Euler, *J. Appl. Phys.* **47**, 5347 (1976).
- ⁸W. G. Spitzer, C. N. Waddell, H. Narayanan, J. E. Fredrickson, and S. Prussin, *Appl. Phys. Lett.* **30**, 623 (1977).
- ⁹G. K. Hubler, C. N. Waddell, W. G. Spitzer, J. E. Fredrickson, S. Prussin, and R. G. Wilson, *J. Appl. Phys.* **50**, 3294 (1979).
- ¹⁰W. G. Spitzer, C. N. Waddell, J. S. Ko, G. K. Hubler, and J. E. Fredrickson, *J. Appl. Phys.* **50**, 3775 (1979).
- ¹¹Sook-Il Kwun, W. G. Spitzer, C. L. Anderson, H. L. Dunlap, and K. V. Vaidyanathan, *J. Appl. Phys.* **50**, 6873 (1979).
- ¹²G. K. Hubler, P. R. Malmberg, and T. P. Smith III, *J. Appl. Phys.* **50**, 7147 (1979).
- ¹³W. Wesch and G. Gotz, *Radiat. Eff.* **49**, 137 (1979).
- ¹⁴G. K. Hubler, P. R. Malmberg, C. A. Carosella, T. P. Smith III, W. G. Spitzer, C. N. Waddell, and C. N. Phillippi, *Radiat. Eff.* **48**, 81 (1980).
- ¹⁵G. K. Hubler, P. R. Malmberg, W. G. Spitzer, and C. N. Waddell, *Radiat. Eff.* **60**, 35 (1982).
- ¹⁶J. E. Fredrickson, C. N. Waddell, W. G. Spitzer, and G. K. Hubler, *Appl. Phys. Lett.* **40**, 172 (1982).
- ¹⁷B. L. Crowder, R. S. Title, M. H. Brodsky, and G. D. Pettit, *Appl. Phys. Lett.* **16**, 205 (1970); also see M. H. Brodsky, R. S. Title, K. Weiser, and G. D. Pettit, *Phys. Rev. B* **1**, 2632 (1970).
- ¹⁸O. S. Heavens, *Optical Properties of Thin Solid Films* (Academic, New York, 1955).
- ¹⁹H. E. Bennett, M. Silver, and E. J. Ashley, *J. Opt. Soc.* **53**, 1089 (1963).
- ²⁰The authors wish to express their appreciation to S. Prussin for his help with these measurements.
- ²¹J. W. Mayer, L. Eriksson, and John A. Davis, *Ion Implantation in Semiconductors* (Academic, New York, 1970), p. 146.
- ²²L. Csepregi, J. W. Mayer, and T. W. Sigmon, *Phys. Lett. A* **54**, 157 (1975); also see L. Csepregi, J. W. Mayer, and T. W. Sigmon, *Appl. Phys. Lett.* **29**, 92 (1976).
- ²³L. Csepregi, W. K. Chu, H. Mueller, J. W. Mayer, and T. W. Sigmon, *Radiat. Eff.* **28**, 227 (1976).
- ²⁴P. Blood, W. L. Brown, and G. L. Miller, *J. Appl. Phys.* **50**, 173 (1979).
- ²⁵L. D. Glowinski, K. N. Tu, and P. S. Ho, *Appl. Phys. Lett.* **28**, 312 (1976).

- ²⁶D. K. Sadana, M. C. Wilson, G. R. Booker, and J. Washburn, *J. Electrochem. Soc.* **127**, 1589 (1980).
- ²⁷T. J. Magee, C. Leung, H. Kawayoski, R. Ormond, B. K. Furman, C. A. Evans, Jr., and D. S. Day, *Appl. Phys. Lett.* **39**, 413 (1981).
- ²⁸J. A. Roth and C. L. Anderson, *App. Phys. Lett.* **31**, 689 (1977).
- ²⁹T. Motooka and K. Watanabe, *J. Appl. Phys.* **51**, 4125 (1980).
- ³⁰M. Janai, D. D. Allred, D. C. Booth, and B. O. Seraphin, *Solar Energy Mater.* **1**, 11 (1979).
- ³¹L. Csepregi, E. F. Kennedy, T. J. Gallagher, J. W. Mayer, and T. W. Sigmon, *J. Appl. Phys.* **48**, 4234 (1977).
- ³²L. Csepregi, E. F. Kennedy, and J. W. Mayer, *J. Appl. Phys.* **49**, 3906 (1978).
- ³³G. L. Olson, S. A. Kokorowski, J. A. Roth, R. S. Turley, and L. D. Hess, *Proc. Soc. Photo-Opt. Inst. Eng.* **276**, 128 (1981).
- ³⁴E. F. Kennedy, L. Csepregi, J. W. Mayer, and T. W. Sigmon, *J. Appl. Phys.* **48**, 4241 (1977).
- ³⁵Measurements made by Charles Evans & Associates, San Mateo, California 94402.
- ³⁶Y. Tammimga and W. J. M. J. Josquin, *Appl. Phys. Lett.* **32**, 13 (1978).
- ³⁷J. S. Williams and R. G. Elliman, *Appl. Phys. Lett.* **37**, 829 (1980).
- ³⁸J. F. Gibbons and S. W. Mylroie, *Appl. Phys. Lett.* **22**, 568 (1973); also see J. F. Gibbons, W. S. Johnson, and S. W. Mylroie, *Projected Range Statistics in Semiconductors and Related Materials* (Halsted, Stroudsburg, PA, 1975).
- ³⁹B. Smith, *Ion Implantation Range Data for Silicon and Germanium Device Technologies* (Research Studies Press, Forest Grove, Oregon, 1977).
- ⁴⁰V. G. K. Reddi and J. D. Sansbury, *J. Appl. Phys.* **44**, 2951 (1973).
- ⁴¹D. Eirug Davies, *Can. J. Phys.* **47**, 1750 (1969).
- ⁴²J. F. Gibbons (private communication).
- ⁴³The authors wish to express their appreciation to Prof. J. F. Gibbons for performing this calculation and sending us the results.
- ⁴⁴D. K. Sadana, M. Strathman, J. Washburn, C. W. Magee, M. Maenpaa, and G. R. Booker, *Appl. Phys. Lett.* **37**, 615 (1980).
- ⁴⁵J. C. Irvin, *Bell Syst. Tech. J.* **41**, 387 (1962); also see J. L. Moll, *Physics of Semiconductors* (McGraw-Hill, New York, 1964).

Section IV.8

PROPERTIES OF AMORPHOUS SILICON PRODUCED BY ION IMPLANTATION:
THERMAL ANNEALING

W. G. Spitzer¹
G. K. Hubler and T. A. Kennedy²

¹Departments of Materials Science and Physics
University of Southern California
Los Angeles, CA

²Materials Modification and Analysis Branch
Condensed Matter and Radiation Sciences Division
Naval Research Laboratory

This work was supported by the Office of Naval Research.

PROPERTIES OF AMORPHOUS SILICON PRODUCED BY ION IMPLANTATION: THERMAL ANNEALING

W.G. SPITZER *, G.K. HUBLER and T.A. KENNEDY

Naval Research Laboratory, Washington, DC 20375, USA

The refractive index, electron paramagnetic resonance (EPR) signal strength and density of amorphous silicon were measured as a function of 500°C isothermal annealing time. The EPR signal was found to be correlated with two distinct optical states of amorphous silicon that were previously reported. One state is the as-implanted state which has a refractive index 12% larger than crystalline silicon. The other state is stabilized after thermal annealing and has a refractive index 8% larger than crystalline silicon and an EPR signal strength a factor of three smaller than the first state. This state is stable until epitaxial recrystallization occurs. No correlation is found with the amorphous silicon density.

1. Introduction

Recently, careful measurements of the refractive index profile of amorphous Si (a-Si), prepared by Si- or P-ion implantation into single crystal Si, demonstrated that two well-defined states of the a-Si could be identified [1]. The as-implanted a-Si was in one state with an index $n_D(\nu)$ that is about 12% larger than for crystalline Si (c-Si) [1-4]. The second state had a refractive index, $n'_D(\nu)$, that is about 8% larger than the refractive index of c-Si, $n_c(\nu)$, and was produced by annealing as-implanted samples for 2 h at 500°C in vacuum. The second state was stable upon further isothermal annealing until the material recrystallized. Both states, as characterized by $n_D(\nu)$ and $n'_D(\nu)$, were stable over a wide range of ion fluence (5×10^{15} to 10^{17} atoms/cm²), ion energy (200 keV to 2.7 MeV) and substrate implantation temperature (200 K to 300 K). It was suggested in the prior study [1] that the as-implanted state was in a "defect saturated" condition [4] and the annealed state was a "thermally stabilized" state [5].

In related work, Shimada et al. used electron diffraction, ion channeling, and density measurements to identify two states of disorder in ion-implanted GaP [6]. For fluences of 10^{16} /cm² of nitrogen ions, they found an as-implanted state

with a density 3% smaller than for c-GaP and the state had no short- or long-range order. After annealing at 400°C they measured a sharp transition to a new state with a density 1% smaller than c-GaP and which possessed short-range order as indicated by the appearance of diffuse rings in electron diffraction patterns. In this work we compare electron paramagnetic resonance (EPR) and density data with the refractive index measurements of as-implanted and annealed Si samples to determine if the two states observed in our refractive index measurements of Si correlate with other physical parameters, as observed by Shimada et al. for GaP. We find that the EPR spin density decreases in accordance with the decrease in refractive index upon annealing for 2 h at 500°C, and that the EPR measured spin density is stable with further annealing until the amorphous layer recrystallizes. However, within the errors of our measurements, there is no correlation between the density of amorphous material and the refractive index or EPR spin density. To our knowledge, this is the first study of amorphous Si to compare the thermal annealing behavior of the macroscopic quantities of refractive index and density with the microscopic quantity of EPR spin density.

2. Experimental

Several <100> oriented, 15 to 25 Ω cm, p-type Si samples were implanted at 200 K with a total fluence of 9.1×10^{15} ions/cm² of ²⁹Si at an ion

* On leave from the Departments of Materials Science and Physics, University of Southern California, Los Angeles, CA 90007, USA.

III. NEW PHASES

Table 1
Implantations of ^{29}Si

Ion energy (keV)	Fluence (10^{15} ions/cm 2)
50	0.23
100	0.45
150	0.56
200	1.13
250	2.25
325	2.25
400	2.25
total fluence = 9.1×10^{15}	

flux which never exceeded $0.7 \mu\text{A}/\text{cm}^2$. The implantation schedule of energies and fluences is given in table 1 and was used to ensure that all portions of the layer were heavily damaged and made amorphous. The ^{29}Si was used rather than ^{28}Si in order to avoid contamination by implantation of $^{14}\text{N}_2^+$. The samples were mounted about 8° off-axis with respect to the beam in order to minimize channeling. Post-implantation annealing was carried out in a tube furnace with a dry argon atmosphere.

The measurements made on the samples were infrared reflection, room temperature EPR, and step height between non-implanted and implanted regions on the sample surface (swelling). The infrared reflection measurements were made by using a double beam spectrometer covering the frequency region $250 < \nu < 4000 \text{ cm}^{-1}$. The reflected intensity varies with frequency because of the interference effect produced by the reflection from the amorphous-crystalline interface [2,4]. These measurements were used primarily to determine the thickness of the amorphous layer. The refractive index behavior of the a-Si with annealing was taken from prior measurements [1,3] which were more accurate and covered almost twice the frequency range measured here.

The EPR measurements were made at room temperature with a Varian E3 spectrometer at 9 GHz. The EPR signal of a-Si is known to have an isotropic g value equal to 2.0055 and is generally attributed to dangling bonds in the material [7]. A line having the same g value is reported for all undoped a-Si, independent of the method of preparation, and is also observed for sample surfaces [8]. Measurements were made on non-im-

planted, as-implanted, and fully recrystallized samples as well as samples in various annealing stages. Absolute values of the spin density were made by comparison of the intensity of the EPR of the as-implanted sample with that of the Varian pitch-in-KCl standard. The non-implanted and fully recrystallized samples had EPR signals which were negligible compared to the implanted samples having an a-Si layer. Since the same surface preparation was used for all samples, it was concluded that the effects to be discussed are not surface related.

A mask protected a small portion of the surface of each sample during the implantation and the resulting non-implanted-implanted boundary was used to measure the swelling introduced by the implantation. The measurements were made by using a DECTAK profilometer and are similar in nature to some previously reported [9,10]. Each value given here is the average of at least three different measurements with an estimated accuracy of each measurement of $\pm 25 \text{ \AA}$ and a reproducibility within 25 \AA . If the step height is small compared to the total a-Si layer thickness, then the crystalline to amorphous density ratio, (ρ_c/ρ_a) , is approximately $1 + (\text{step height}/\text{a-Si layer thickness})$. An unexpected difficulty of the present measurements was that the step heights obtained were a factor of 2 to 3 smaller than those suggested by the previous data [9,10] for similarly implanted samples. The infrared measurement indicated that the implanted layer was totally amorphous [4]. The accuracy and reproducibility of the DECTAK profilometer data compared to the total step height for a large number of as-implanted samples, typically 160 \AA , seemed to preclude such a large discrepancy. The DECTAK profilometer calibration was checked by measuring two samples with an interferometer and, within the experimental accuracy of about $\pm 25 \text{ \AA}$, the two types of measurements agreed in their step-height values.

3. Results and discussion

The results of all measurements are listed in table 2, and the data are also plotted in fig. 1. The refractive index values, taken from previous work and given in the form $n(\nu)/n_D(\nu) = f_D$, show a drop of f_D from 1.0 to 0.96 after 2 h of annealing

Table 2
Samples, anneal stages, and measurements

Sample No.	Anneal stage	a-Si layer thickness (μm)	a-Si volume (cm^{-3})	ESR (arbitrary units)	Spin density (arbitrary units)	Step height per unit a-Si layer thickness ($\text{\AA}/\mu\text{m}$)
26	non-implanted sample	-	-	0.6	-	-
7	none	0.73	0.34×10^{-4}	120	353	210
17	none	0.73	0.37×10^{-4}	155	419	230
11	500°C/2h	0.62	0.28×10^{-4}	38	136	210
11	500°C/4h	0.56	0.25×10^{-4}	32	128	200
9	500°C/6h	0.51	0.24×10^{-4}	23	96	180
9	500°C/8h	0.45	0.21×10^{-4}	19.5	93	170
12	500°C/6h + 560°C/3h	0	0	0.8	-	-

at 500°C and the constancy of f_D and hence $n(\nu) = n_D(\nu)$ with further annealing. The EPR measurements (adjusted for the change in a-Si layer thickness with annealing time, in column 6 of table 2) are proportional to the spin density attributable to dangling bonds and show a behavior very similar to the refractive index. The spin density has a large drop, a factor of approximately 3, during the first 2 h of annealing at 500°C and has little, if any, decrease with further annealing. The apparent decrease between 2 h and 8 h annealing

times is at most 40%; however, this change lies within the experimental errors. This result supports the existence of a "thermally stabilized" state for the implantation-produced a-Si layer.

It is of interest to note that the EPR measurements bear some similarity to others reported for annealed a-Si layers. In a recent detailed study of ultrahigh vacuum deposited a-Si layers onto pure fused silica substrates, Thomas et al. [7] measured isochronally annealed samples and some samples directly annealed at 450°C and about 560°C. The

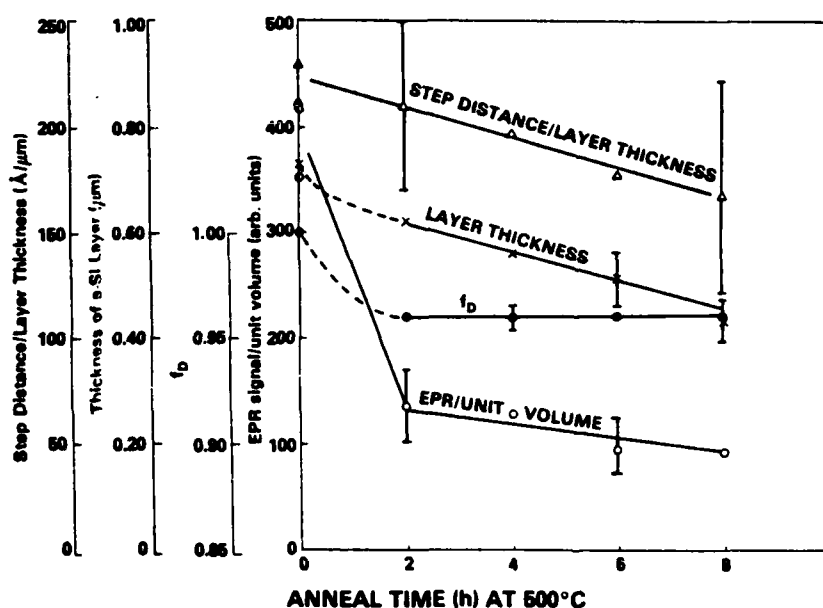


Fig. 1. Dependence of the step distance per unit layer thickness (Δ) (a measure of density change), amorphous layer thickness (\times), refractive index (\odot), and EPR signal per unit volume (\circ) as a function of annealing time at 500°C for amorphous silicon. The solid and dashed lines are only a guide to the eye.

annealing times were two hours and they reported a total decrease in spin density of a factor of 3.5 prior to recrystallization. In an earlier study, Ohdomari et al. [11] show some EPR data for isochronally annealed, heavily Ar-ion implanted layers and again the decrease in signal by 500°C is about a factor of 3. There is also a suggestion of a plateau in the temperature region near 500 to 600°C in their data.

The a-Si density, ρ , appears to behave differently with annealing. No significant drop in swelling is observed in the first two hours and very little decrease, if any, with further annealing. So, within the limits of accuracy of the ρ measurement, there is no correlation of density with the refractive index and EPR signals during the transition between the two states. This differs from the GaP case where an increase in density was noted at the transition temperature. In ref. 1 it was found that for a 7000 Å amorphous layer on <100> Si, the layer thickness decreased by about 1200 Å in the first two hours of a 500°C anneal. It is unclear if this decrease is caused by an accelerated regrowth rate during the initial stages of epitaxy, or if it is caused by a density change when the thermally stabilized phase is formed, or both. A rough estimate of this effect can be made. After the two hour anneal, the regrowth rate stabilized at a value of 3.7 Å/min which would give only 440 Å of regrowth for two hours. If the remaining 760 Å thickness is caused by a density change, then we would expect only an approximately 20 Å decrease in the step height - a value that we would be unable to reliably measure.

Although not indicated in fig. 1, it is seen from table 2 that the swelling in the fully recrystallized sample No. 12 is not detectable. From the values given in table 2, the ρ_c/ρ_a is approximately 1.02. This value is lower than the lowest value given by Brodsky et al. [12] and is close to their estimate of $\rho_c/\rho_a = 1.01$ for "void-free" material. They give an estimated error of 2%. This result supports the view [1] that the a-Si produced by ion implantation is essentially "void free" and our estimate of the dangling bond spin density of about $2 \times 10^{19} \text{ cm}^{-3}$ for the non-annealed samples is consistent with the values of $2\text{--}6 \times 10^{19} \text{ cm}^{-3}$ given by Thomas et al. [7] for high-purity, void-free, a-Si. We conclude, therefore, that the spins here are not

associated with voids. Brodsky et al. [12] made a similar observation in that some of their samples had a much higher spin density than one would expect from the density change.

The simplest interpretation of the present results is that the change from the as-implanted amorphous state to the thermally stabilized state is accomplished through network reorganization and dangling bond reduction within the framework of a continuous random network model. This interpretation implies that the spins are essentially randomly distributed which is consistent with the conclusion of Thomas et al. [7] for their pure a-Si samples. No large change in density with annealing would be expected until recrystallization takes place.

Initial X-ray diffraction experiments for an as-implanted sample with $n = n(\nu)_D$, and for an annealed sample with $n = n(\nu)_D$ show no difference in the amorphous ring pattern between the two samples. This work is continuing with samples implanted at high energy in order to obtain thicker layers which will improve the sensitivity to both X-ray diffraction and density measurements.

References

- [1] J.E. Fredrickson, C.N. Waddell, W.G. Spitzer and G.K. Hubler, *Appl. Phys. Lett.* 40 (1982) 172.
- [2] G.K. Hubler, P.R. Malmberg, C.N. Waddell, W.G. Spitzer and J.E. Fredrickson, *Rad. Effects* 60 (1982) 35.
- [3] C.N. Waddell, W.G. Spitzer, G.K. Hubler, P.R. Malmberg and J.E. Fredrickson, *J. Appl. Phys.* 53 (1982) 5851.
- [4] G.K. Hubler, C.N. Waddell, W.G. Spitzer, J.E. Fredrickson, S. Prussin and R.G. Wilson, *J. Appl. Phys.* 50 (1979) 3294.
- [5] M. Janai, D.D. Allred, D.C. Booth and B.O. Seraphin, *Solar Energy Mat.* 1 (1979) 11.
- [6] T. Shimada, Y. Kato, Y. Shiraki and K.F. Komatsubara, *J. Phys. Chem. Solids* 37 (1976) 305.
- [7] P.A. Thomas, M.H. Brodsky, D. Kaplan and D. Lepine, *Phys. Rev. B* 18 (1978) 3059; and references therein.
- [8] D. Haneman, *Phys. Rev.* 170 (1968) 705.
- [9] R.E. Whan and G.W. Arnold, *Appl. Phys. Lett.* 17 (1970) 378.
- [10] K.N. Tu, P. Chaudhari, K. Lal, B.L. Crowder and S.I. Tan, *J. Appl. Phys.* 43 (1972) 4262.
- [11] I. Ohdomari, M. Ikeda, H. Yoshimoto, N. Onoda, Y. Tanabe and T. Itoh, in: *Ion implantation in semiconductors*, eds., F. Chermow, J.A. Borders and D.K. Brice (Plenum Press, New York, 1976) p. 39.
- [12] M.H. Brodsky, D. Kaplan and J.F. Ziegler, *Appl. Phys. Lett.* 21 (1972) 305.

BIBLIOGRAPHY

1. E. A. Wolicki, C. R. Gossett, K. W. Marlow, and M. E. Toms, "Capabilities for Nonnuclear Applications with Nuclear Facilities at NRL," NRL Report 6599, 17 October 1967.
2. I. Manning and D. Padgett, "Transport Theory of Penetration by Heavy Ions," NRL Memorandum Report 2631, August 1973.
3. I. Manning and G. P. Mueller, "Depth Distribution of Energy Deposition in Ion Bombardment," *Comp. Phys. Comm.* **7**, 85 (1974).
4. G. P. Mueller, "Total Cross-Section Corresponding to the Differential Cross-Section of Lindhard, Nielsen and Scharff," *Radiat. Eff.* **21**, 253 (1974).
5. J. W. Butler, "Ion Implantation and Tribology," Proceedings of ONR-NRL Tribology Workshop, Washington, DC, 14-16 October 1975.
6. H. W. Kugel, L. Eytel, G. K. Hubler, and D. E. Murnick, "The Temperature Dependence of Hyperfine Fields at Rare Earth Nuclei in Iron and Nickel," *Phys. Rev. B* **13**, 3697 (1976).
7. J. W. Butler, "Ion Implantation and Wear," Reports, Memoranda and Technical Notes of the Materials Research Council Summer Conference, La Jolla, CA (University of Michigan Document 005020, 1976) p. 255.
8. Irwin Manning, Mervine Rosen, and J. E. Westmoreland, "Adaptation of a Program for Depth Distribution of Energy Deposition by Ion Bombardment: Calculation of Ion Lateral Ranges," *Comp. Phys. Comm.* **12**, 335 (1976).
9. I. Manning, M. Rosen, and J. E. Westmoreland, "Computer Code for the Calculation of Lateral Range of a PKA," NRL Memorandum Report 3358, September 1976.
10. J. M. Poate, J. A. Borders, A. G. Cullis, and J. K. Hirvonen, "Ion Implantation as an Ultrafast Quenching Technique for Metastable Alloy Production: The Ag-Cu System," *Appl. Phys. Letters* **30**, 365 (1977).
11. G. P. Mueller and Mervine Rosen, "A Boltzmann Transport Code for Ion Penetration in Matter," NRL Memorandum Report 3556, July 1977.
12. J. K. Hirvonen, "Spinodal Decomposition in Amorphous Au-Implanted Pt," *Appl. Phys. Letters* **32**, 25 (1978).
13. A. G. Cullis, J. A. Borders, J. K. Hirvonen, and J. M. Poate, "Metastable Alloy Layers Produced by Implantation of Ag⁺ and Ta⁺ Ions into Cu Crystals," *Phil. Mag.* **B32**, 615 (1978).
14. J. K. Hirvonen, "Ion Implantation in Tribology and Corrosion Science," *J. Vac. Sci. Technol.* **15**, 1662 (1978).
15. Wen-Wei Hu, C. R. Clayton, H. Herman, and J. K. Hirvonen, "Fatigue-Life Enhancement by Ion Implantation," *Scri. Met.* **12**, 697 (1978).

16. E. McCafferty and G. K. Hubler, "Electrochemical Behavior of Palladium-Implanted Titanium," *J. Electrochem. Soc.* **125**, 1892 (1978).
17. J. W. Butler, "Some Effects of Ion Implantation on Fluid-Solid Surface Interactions," Proceedings of the Fourth Symposium on Fluid-Solid Surface Interactions, sponsored by the U.S. Department of the Navy and the West Germany Federal Ministry of Defense, 18-20 October 1978, National Bureau of Standards, Gaithersburg, MD, p. 267.
18. J. K. Hirvonen, C. A. Carosella, R. A. Kant, I. L. Singer, R. Vardiman, and B. B. Rath, "Improvement of Metal Properties by Ion Implantation," *Thin Solid Films* **63**, 5 (1979).
19. G. K. Hubler, P. R. Malmberg, and T. P. Smith, III, "Refractive Index Profiles and Range Distributions of Silicon Implanted with High-Energy Nitrogen," *J. Appl. Phys.* **50**, 7147 (1979).
20. G. K. Hubler, C. N. Waddell, W. G. Spitzer, J. E. Fredrickson, S. Prussin, and R. G. Wilson, "High-Fluence Implantations of Silicon: Layer Thickness and Refractive Indices," *J. Appl. Phys.* **50**, 3294 (1979).
21. R. A. Kant, J. K. Hirvonen, A. R. Knudson, J. S. Wollam, "Surface Hardening of Beryllium by Ion Implantation," *Thin Solid Films* **63**, 27 (1979).
22. W. G. Spitzer, J. S. Ko, C. N. Waddell, G. K. Hubler, and J. E. Fredrickson, "Plasma Region in High-Fluence Implants of Phosphorus in Amorphized Silicon," *J. Appl. Phys.* **50**, 3775 (1979).
23. Y. F. Wang, C. R. Clayton, G. K. Hubler, W. H. Lucke, and J. K. Hirvonen, "Applications of Ion Implantation for the Improvement of Localized Corrosion Resistance of M50 Bearing Steel," *Thin Solid Films* **63**, 11 (1979).
24. J. K. Hirvonen, "Implantation Into Metals - Mechanical Property Changes," Proceedings of the 1st Conference on Ion Beam Modification of Materials, eds., J. Gyulai, T. Lohner, and E. Pasztor, Central Research Institute for Physics, H-1525, Budapest 114 POB 49, Hungary, Vol. III, p. 1753 (1979).
25. J. K. Hirvonen and J. W. Butler, "Improved Corrosion and Mechanical Behavior of Alloys by Ion Implantation," 1978 Science and Engineering Symposium Proceedings (Joint Air Force and Navy), Vol. IV (Basic Research), Navy Material Command and Air Force Systems Command, p. 981 (1979).
26. J. K. Hirvonen, J. W. Butler, T. P. Smith, III, R. A. Kant, and V. C. Westcott, "Sliding-Wear Reduction by Ion Implantation," Proceedings of the 1st Conference on Ion Beam Modification of Materials, eds., J. Gyulai, T. Lohner, and E. Pasztor, Central Research Institute for Physics, H-1525, Budapest 114, POB 49, Hungary, Vol. III, p. 1973 (1979).
27. J. K. Hirvonen, J. M. Poate, Z. L. Liao, and J. W. Mayer, "Sputtering Limitations for High-Dose Implantations," Proceedings of the 1st Conference on Ion Beam Modification of Materials, eds., J. Gyulai, T. Lohner, and E. Pasztor, Central Research Institute for Physics, H-1525, Budapest 114, POB 49, Hungary, Vol. III, p. 1519 (1979).

28. G. K. Hubler, P. R. Malmberg, C. A. Carosella, T. P. Smith, III, W. G. Spitzer, C. N. Waddell, and C. N. Phillippi, "Optical Effects Resulting from Deep Implants of Silicon with Nitrogen and Phosphorus," Proceedings of the 1st Conference on Ion Beam Modification of Materials, eds., J. Gyulai, T. Lohner, and E. Pasztor, Central Research Institute for Physics, H-1525, Budapest 114, POB 49, Hungary, Vol. II, p. 1323 (1979).
29. W. W. Hu, C. R. Clayton, H. Herman, J. K. Hirvonen, and R. A. Kant, "Fatigue-Life Enhancement of Steel by Nitrogen Implantation," Proceedings of the 1st Conference on Ion Beam Modification of Materials, eds., J. Gyulai, T. Lohner, and E. Pasztor, Central Research Institute for Physics, H-1525, Budapest 114, POB 49, Hungary, Vol. III, p. 1977 (1979).
30. D. J. Land, D. G. Simons, J. G. Brennan, M. D. Brown, and J. K. Hirvonen, "Range Distribution for 25-100 keV $^{14}\text{N}^+$ Ions," Proceedings of the 1st Conference on Ion Beam Modification of Materials, eds., J. Gyulai, T. Lohner, and E. Pasztor, Central Research Institute for Physics, H-1525, Budapest 114, POB 49, Hungary, Vol. I, p. 93 (1979).
31. E. McCafferty, G. K. Hubler, and J. K. Hirvonen, "Corrosion Control by Ion-Implantation," Proceedings of the 1978 Tri-Service Conference on Corrosion, ed. by M. Levy and J. Brown, Materials and Ceramics Information Center, Battelle, OH, p. 435, May 1979.
32. R. G. Vardiman, R. A. Kant, and T. W. Crooker, "The Effect of Ion Implantation on Fatigue Behavior of Ti/6Al/4V Alloy," Report of NRL Progress, p. 4, May 1979.
33. I. Manning, "Use of Range Distributions to Approximate Energy Distributions," F. A. Smidt and L. A. Beach, Coordinators, Cooperative Radiation Effects Simulation Program (Annual Progress Report) NRL Memorandum Report 4080 (October 1979), p. 2.
34. I. Manning, "Approximation for Energy Deposition in Ion Beam Bombardment," F. A. Smidt and L. A. Beach, Coordinators, Cooperative Radiation Effects Simulation Program (Annual Progress Report) NRL Memorandum Report 4080 (October 1979), p. 8.
35. M. Zamanzadeh, A. Allan, H. W. Pickering, and G. K. Hubler, "Effect of Helium-, Iron-, and Platinum-Ion Implantation on Permeation of Hydrogen Through Ion Membranes," ONR Technical Report No. 10 (Contract No. N00-14-75-C-0264), July 1979.
36. G. K. Hubler and E. McCafferty, "The Corrosion Behaviour and Rutherford Backscattering Analysis of Palladium-Implanted Titanium," Corros. Sci. **20**, 103 (1980).
37. R. N. Bolster and I. L. Singer, "Surface Hardness and Abrasive Wear Resistance of Nitrogen-Implanted Steels," Appl. Phys. Letters **36**, 208 (1980).
38. I. L. Singer and J. S. Murday, "The Chemical State of Ion-Implanted Nitrogen in $\text{Fe}_{18}\text{Cr}_8\text{Ni}$ Steel," J. Vac. Sci. Technol. **16**, 330 (1980).
39. G. P. Mueller, "New Analytical Calculation of Displacement Damage," Nucl. Instr. and Methods **170**, 389 (1980).

40. G. P. Mueller, "Differential Cross Section and Related Integrals for the Moliere Potential," *Radiat. Eff. Letters* **50**, 87 (1980).
41. W. N. Allen, P. Brant, C. A. Carosella, J. J. DeCorpo, C. T. Ewing, F. E. Saalfeld, and D. C. Weber, "Ion Implantation Studies of $(\text{SN})_x$ and $(\text{CH})_x$," *Synthetic Metals* **1**, 151 (1979/80).
42. L. Buene, J. M. Poate, D. C. Jacobson, C. W. Draper, and J. K. Hirvonen, "Laser Irradiation of Nickel Single Crystals," *Appl. Phys. Lett.* **37**, 385 (1980).
43. J. K. Hirvonen, J. M. Poate, A. Greenwald, R. Little, "Pulsed Electron Beam Irradiation of Ion Implanted Copper Single Crystals," *Appl. Phys. Lett.* **36**, 564 (1980).
44. G. K. Hubler, P. R. Malmberg, C. A. Carosella, T. P. Smith, III, W. G. Spitzer, C. N. Waddell, and C. N. Phillippi, "Optical Effects Resulting from Deep Implants of Silicon with Nitrogen and Phosphorus," *Radiat. Eff.* **48**, 81 (1980).
45. G. K. Hubler and E. McCafferty, "The Corrosion Behavior and Rutherford Backscattering Analysis of Pd-Implanted Titanium," *Corrosion Science* **20**, 103 (1980).
46. M. Zamanzadeh, A. Allam, H. W. Pickering, and G. K. Hubler, "Effect of Helium, Iron, and Platinum Implantation on the Absorption of Hydrogen by Iron," *J. Electrochem. Soc.* **127**, 1688 (1980).
47. C. A. Carosella, I. L. Singer, R. C. Bowers, and C. R. Gossett, "Friction and Wear Reduction of Bearing Steel via Ion Implantation," *Ion Implantation Metallurgy*, eds. C. M. Preece and J. K. Hirvonen, (The Metallurgical Society of AIME, 1980), p. 103.
48. C. R. Clayton, K. G. K. Doss, H. Herman, S. Prasad, Y-F. Wang, J. K. Hirvonen, and G. K. Hubler, "Modification of the Corrosion Behavior of 304 Stainless Steel by Phosphorus Implantation," *Ion Implantation Metallurgy*, eds. C. M. Preece and J. K. Hirvonen, (The Metallurgical Society of AIME, 1980), p. 65.
49. J. K. Hirvonen, "Introduction," *Ion Implantation*, Treatise on Materials Science and Technology **18**, 1-16, Academic Press (1980).
50. J. K. Hirvonen, ed., *Ion Implantation*, Treatise on Materials Science and Technology **18**, Academic Press (1980).
51. J. W. Mayer, S. S. Lau, B-Y Tsaur, J. M. Poate, and J. K. Hirvonen, "High-Dose Implantation and Ion-Beam-Mixing," *Ion Implantation Metallurgy*, eds., C. M. Preece and J. K. Hirvonen, (The Metallurgical Society of AIME, 1980), p.37.
52. W. W. Hu, H. Herman, C. R. Clayton, J. Kozubowski, R. A. Kant, J. K. Hirvonen, and R. K. MacCrone, "Surface-Related Mechanical Properties of Nitrogen-Implanted 1018 Steel," *Ion Implantation Metallurgy*, eds. C. M. Preece and J. K. Hirvonen, (The Metallurgical Society of AIME 1980), p.92.
53. C. M. Preece and J. K. Hirvonen, Editors, *Ion Implantation Metallurgy*, (The Metallurgical Society of the AIME, 1980).

54. I. L. Singer, R. N. Bolster, and C. A. Carosella, "Abrasive Wear Resistance of Ti and N Implanted 52100 Steel Surfaces," *Thin Solid Films* **73**,283(1980).
55. G. K. Hubler, J. K. Hirvonen, I. L. Singer, R. C. Bowers, C. R. Gossett, M. R. Weller, C. R. Clayton, and Y. A. Wang, "Application of Ion Implantation for the Improvement of Localized Corrosion Resistance of M50 Steel Bearings," *NAPC Progress Report*, Mar 1980.
56. I. L. Singer, J. S. Murday, H. Ravner, J. K. Hirvonen, and N. L. Jarvis, "New Opportunities in Tribology," *Naval Research Reviews* **32**,4(1980).
57. I. L. Singer and R. N. Bolster, "Surface Hardness and Abrasive Wear Resistance of Nitrogen-Implanted Steels," *Ion Implantation Metallurgy*, eds. C. M. Preece and J. K. Hirvonen, The Metallurgical Society of AIME, p.116,(1980).
58. J. H. Harding and R. H. Bassel, "A Theoretical Study of the Defect Structure of Praseodymium Chromite," TP.862, Theoretical Physics Division, AERE Harwell, Oxfordshire, United Kingdom, July 1980.
59. F. A. Smidt, "The Use of Ion Implantation for Materials Processing," Semi-annual Progress Report for Period 1 Oct. 1979 - 31 Mar. 1980, NRL Memorandum Report 4341, Oct 6,1980.
60. L. Buene, D. C. Jacobson, S. Nakahara, J. M. Poate, C. W. Draper, and J. K. Hirvonen, "Laser Irradiation of Ni: Defect Structures and Surface Alloying," pp. 583-590 in *Laser and Electron-Beam Interactions and Materials Processing*, eds. Gibbons, Hess, Sigmon, Elsevier North Holland, Inc., 1981.
61. G. K. Hubler, "Use of Ion Beam Analysis in Metal Modification By Means of Ion Implantation," *Nucl. Instrum. Methods* **191**,101(1981).
62. F. A. Smidt, "The Use of Ion Implantation for Materials Processing," Semi-annual Progress Report for the Period 1 Apr. 1980 - 30 Sept. 1980, NRL Memorandum Report 4527, June 24,1981.
63. F. A. Smidt, J. K. Hirvonen, and S. Ramalingam, "Preliminary Evaluation of Ion Implantation as a Surface Treatment to Reduce Wear of Tool Bits," NRL Memorandum Report 4616, Naval Research Laboratory, 25 Sep 1981.
64. M. Rosen and G. P. Mueller, "Calculation of Self Sputtering of High Energy Copper Ions," 1981 NRL Review. pp.152-154.
65. R. G. Allas, A. R. Knudson, J. M. Lambert, P. A. Treado, and G. W. Reynolds, "Self-Ion Sputtering Yields for Copper, Nickel, and Aluminum," *Nucl. Instrum. Methods* **194**,615(1982).
66. P. Trzaskoma, E. McCafferty, G. K. Hubler, and I. L. Singer, "Electrochemical Behavior of an Amorphous Fe-Ti-C Surface in Titanium-Implanted Steel," *Ion Implantation into Metals*, eds., V. Ashworth, W. A. Grant, and R. P. M. Proctor, Pergamon Press, NY, pp.24-34, (1982).
67. R. G. Vardiman, D. Creighton, G. Saliver, A. Effatian, and B. B. Rath, "The Effect of Ion Implantation on Fretting Fatigue in Ti-6Al-4V," in STP 780 Symposium on

Materials Evaluation Under Fretting Conditions, Ed. S. R. Brown, American Soc. for Testing and Materials, Philadelphia, Pa, p.138, (1982).

68. J. E. Fredrickson, C. N. Waddell, W. G. Spitzer, and G. K. Hubler, "Effects of Thermal Annealing on the Refractive Index of Amorphous Silicon Produced by Ion Implantation," Appl. Phys. Lett., **40**, 172 (1982)
69. G. K. Hubler, P. R. Malmberg, C. N. Waddell, W. G. Spitzer, and J. E. Fredrickson, "Electrical and Structural Characterization of Implantation Doped Silicon by Infrared Reflection," Radiat. Eff., **60**, 35 (1982).
70. R. G. Vardiman, R. N. Bolster, and I. L. Singer, "The Effect of Nitrogen Implantation on Martensite in 304 Stainless Steel," in Metastable Materials Formation by Ion Implantation, Eds. S. T. Picraux and W. J. Choyke, Elsevier Science Publishing Co., NY, p. 269, (1982)
71. R. G. Vardiman and R. A. Kant, "The Improvement of Fatigue Life in Ti-6Al-4V by Ion Implantation," J. Appl. Physics **53**, pp. 690-694 (1982).
72. C. N. Waddell, W. G. Spitzer, G. K. Hubler, and J. E. Fredrickson, "Infrared Studies of Isothermal Annealing of Ion-Implanted Silicon: Refractive Indices, Regrowth Rates, and Carrier Profiles," J. Appl. Phys. **53**, P. 5851-5862 (1982).
73. C. R. Clayton, K. G. K. Doss, Y-F. Wang, J. B. Warren, and G. K. Hubler, "RHEED, AES, and XPS Studies of the Passive Films Formed on Ion-Implanted Stainless Steel," Ion Implantation into Metals, eds., V. Ashworth, W. A. Grant, and R. P. M. Procter, Pergamon Press, NY, pp. 67-76, (1982).
74. C. R. Gossett, "Near Surface Analysis with Energetic Ion Beams," in ACS Symposium Series, No. 199, Industrial Applications of Surface Analysis, eds. L. A. Casper and C. J. Powell, American Chemical Society, Washington, DC, pp. 49-68, (1982).
75. K. S. Grabowski and L. E. Rehn, "Ion Implantation Effects on the Thermal Oxidation of Metals," in Corrosion of Metals Processed by Directed Energy Beams, eds. C. R. Clayton and C. M. Preece, The Metallurgical Society of AIME, p. 23, (1982).
76. G. K. Hubler, "DOD Applications of Implantation-Modified Materials," in Metastable Materials Formation by Ion Implantation, eds., S. T. Picraux and W. J. Choyke, North Holland, NY, pp. 341-354, (1982).
77. F. A. Smidt, "The Use of Ion Implantation for Materials Processing," Annual Progress Report for the Period 1 Oct. 1980 - 30 Sept. 1981, NRL Memorandum Report 4821, 2 July 1982.
78. R. A. Kant, A. R. Knudson, and K. Kumar, "Mechanical and Microstructural Properties of Boron Implanted Beryllium," in Metastable Materials Formation by Ion Implantation, eds., T. Picraux and W. J. Choyke, Elsevier Science Publishing Co., NY, pp. 253-259, (1982).
79. E. McCafferty, P. G. Moore, J. D. Ayers, and G. K. Hubler, "Effect of Laser Processing and Ion Implantation on Aqueous Corrosion Behavior," in Corrosion of Metals Processed by Directed Energy Beams, eds., C. R. Clayton and C. M. Preece, AIME, (1982).

80. G. W. Reynolds, F. R. Vozzo, R. G. Atlas, A. R. Knudson, and J. M. Lambert, "The Surface Behavior of a Binary Alloy by Ion Implantation," in Metastable Materials Formation by Ion Implantation, eds., S. T. Picraux and W. J. Choyke, Elsevier Science Publishing Co., NY, pp. 51-57, (1982).
81. W. K. Chan, C. R. Clayton, R. G. Atlas, C. R. Gossett, and J. K. Hirvonen, "Electrochemical and A. E. S. Studies of Fe-Cr Surface Alloys Formed on AISI 52100 Steel by Ion Beam Mixing," Conference on Ion Beam Modification of Materials, Grenoble, France, 6-10 September 1982.
82. E.N. Kaufmann, R. G. Musket, J. J. Truhan, K. S. Grabowski, C. R. Gossett, and I. L. Singer, "High-Temperature Oxidation of Ion-Implanted Tantalum," Conference on Ion Beam Modification of Materials, Grenoble, France, 6-10 September 1982.
83. K. S. Grabowski, F.D. Correll, J. K. Hirvonen, J. A. Sprague, W. H. Lucke, and G. K. Hubler, "The Influence of Ba, Pt, and Ti Implantations on the Thermal Oxidation of Ti, Ti-6Al-4V, and Ti-6Al-2Sn-4Zr-2Mo," Conference on Ion Beam Modification of Materials, Grenoble, France, 6-10 September 1982.
84. M. Rosen and G. P. Mueller, "Computer Study of Self Sputtering of Cu and Ni at 90 KeV," Conference on Ion Beam Modification of Materials, Grenoble, France, September 6-10, 1982.
85. K. S. Grabowski and R. A. Kant, "Methods to Control Target Heating During Ion Implantation," Fourth International Conference on Ion Implantation: Equipment and Techniques, Berchtesgaden, Germany, 13-17 September 1982.
86. G. K. Hubler, D. Popgoshev, and R. Valori, "Ion Implantation of Bearing Surfaces for Corrosion Resistance," ASME/ASLE 1982 Lubrication Conference, Washington, DC, 5-7 October 1982.
87. J. M. Lambert, P. A. Treado, D. Trbojevic, R. G. Atlas, A. R. Knudson, G. W. Reynolds, and F. R. Vozzo, "Sputtering Analysis with PIXE," 1982 Conference on the Application of Small Accelerators in Research and Industry, Denton, TX, 8-10 November 1982.
88. G. W. Reynolds, R. G. Atlas, J. M. Lambert, and P. A. Treado, "Sputtering from Binary Alloys - A Technique for Evaluating Change in Surface Binding Energy," Seventh Conference on the Application of Accelerators in Research and Industry, Denton, TX, 8-10 November 1982.

